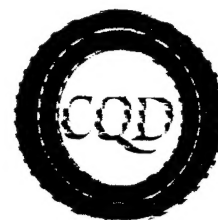


REPORT DOCUMENTATION PAGE			Form Approved OMB No. 0704-0188	
<small>Public reporting burden for this collection of information is estimated to average 1 hour per response, including the time for reviewing instructions, searching existing data sources, gathering and maintaining the data needed, and completing and reviewing the collection of information. Send comments regarding this burden estimate or any other aspect of this collection of information, including suggestions for reducing this burden, to Washington Headquarters Services, Directorate for Information Operations and Reports, 1215 Jefferson Davis Highway, Suite 1204, Arlington, VA 22202-4302, and to the Office of Management and Budget, Paperwork Reduction Project (0704-0188), Washington, DC 20503.</small>				
1. AGENCY USE ONLY (Leave blank)		2. REPORT DATE 1/96		3. REPORT TYPE AND DATES COVERED Final Report 3/93-12/95
4. TITLE AND SUBTITLE InGaAsP Diode Laser for Nd:YAG Pumping			5. FUNDING NUMBERS DAAH04-93-G-0044	
6. AUTHOR(S) M. Razeghi				
7. PERFORMING ORGANIZATION NAME(S) AND ADDRESS(ES) Northwestern University Center for Quantum Devices 2225 N. Campus Drive, MLSB Room 4051 Evanston, IL 60208-3118			8. PERFORMING ORGANIZATION REPORT NUMBER	
9. SPONSORING/MONITORING AGENCY NAME(S) AND ADDRESS(ES) U.S. Army Research Office P.O. Box 12211 Research Triangle Park, NC 27709-2211			10. SPONSORING/MONITORING AGENCY REPORT NUMBER ARO 31108.20-PH	
11. SUPPLEMENTARY NOTES The views, opinions and/or findings contained in this report are those of the author(s) and should not be construed as an official Department of the Army position, policy, or decision, unless so designated by other documentation.				
12a. DISTRIBUTION/AVAILABILITY STATEMENT Approved for public release; distribution unlimited				
13. ABSTRACT (Maximum 200 words) <p>The objective of this contract has been to develop reliable, inexpensive, high-power diode lasers emitting at 808nm. Main application of such devices is to replace the currently used AlGaAs lasers as diode laser pumps for Nd:YAG solid state lasers. The principal advantage of aluminium-free InGaAsP material is the absence of degradation mechanisms limiting the lifetime of AlGaAs lasers and the overall reliability of the diode-pumped systems.</p> <p>By the end of 1995, all the target results of the contract were achieved as well as several extra major achievements in laser development. Output power above 7 Watts in pulse and 4.5 Watts in continuous wave has been obtained from single-stripe laser diode. Laser bars operated up to 70 Watts in quasi-CW mode. No degradation has been observed for the diodes operating at the temperature as high as 60°C with uncoated facets at the continuous wave output power of 1 Watt.</p> <p>World-class results (<math>T_0 = 350K</math>, COD limit above 6MW/cm<sup>2</sup> for uncoated facets, 800mW output power at 100°C) have been obtained for 980 nm laser diodes.</p>				
14. SUBJECT TERMS			15. NUMBER OF PAGES	
			16. PRICE CODE	
17. SECURITY CLASSIFICATION OF REPORT UNCLASSIFIED		18. SECURITY CLASSIFICATION OF THIS PAGE UNCLASSIFIED		19. SECURITY CLASSIFICATION OF ABSTRACT UNCLASSIFIED
				20. LIMITATION OF ABSTRACT UL



*InGaAsP Diode Laser for Nd:YAG Pumping*

*ARPA/US Army Project # DAAH04-93-G-0044*

*Principal Investigator: Manijeh Razeghi*

*Center for Quantum Devices  
Northwestern University, Evanston, IL 60208*

*Final Report - 1995*

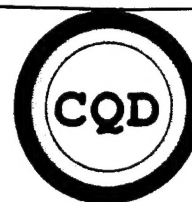
## TABLE OF CONTENTS

### CHAPTER

I. INTRODUCTION .....	1
II. MATERIAL GROWTH AND CHARACTERIZATION.....	2
1. Growth and Characterization of 808nm InGaAsP/InGaP/GaAs .....	2
2. Growth and Characterization of 980nm InGaAs/InGaP/GaAs .....	7
III. FABRICATION TECHNOLOGY AND PROCESSING OF 808nm .....	18
InGaAsP/GaAs Laser Structures	
1. Processing of InGaAsP/InGaP/GaAs Lasers .....	18
a. Introduction	
b. Wafer Preparation	
c. Metallization of p <sup>+</sup> Contacts	
d. Photolithography	
e. Annealing of p <sup>+</sup> Contacts	
f. Lapping/Polishing of n <sup>+</sup> Contacts	
g. Evaporation and Annealing of n <sup>+</sup> Contacts	
h. Cleaving of Laser Bars	
i. Bonding of Laser Diodes	
IV. LASERS DIODE CHARACTERIZATION .....	45
1. Studies of Radiative Efficiency of 0.8 $\mu$ m InGaAsP laser Material	
2. Uniformity of MOCVD Grown InGaAsP/GaAs Structure	
3. Optimization of Laser Structure Parameters	
V. THEORETICAL ANALYSIS OF 808nm InGaAsP/GaAs LASERS .....	90
1. Introduction	
2. Radiative Recombination Efficiency of InGaAsP/GaAs Lasers Grown by MOCVD	
3. Dependence of Minority Carrier Leakage on Active Layer Volume for the InGaAsP Lasers	

4. Comparison of Gain and Threshold Current Density for Diode with Differential QW Thickness
5. Temperature Dependence of Laser Characteristics
6. Strain Effect on 808nm Lasers
7. Beam Propagation in MOPA
8. Conclusion

VI. 808nm InGaAsP/GaAs Buried Ridge Lasers .....	128
1. Introduction	
2. Growth Characterization of GSMBE Regrowth	
a. GSMBE Regrowth Review	
3. Experimental Studies of Buried Ridge	
a. Growth Structure	
b. Buried Ridge Processing	
4. Device Characterization	
5. Summary	
VII. PRESS RELEASES AND ARTICLES .....	152
VIII. PATENTS .....	153
IX. PUBLICATION LISTS.....	154



## **InGaAsP Diode Laser for Nd:YAG Pumping**

**ARPA/US Army Project #: DAAH-04-93-G-0044**

**1993 - 1995**

### **Scientific Personnel:**

#### **Staff:**

**Dr. L.J.Wang  
Dr.D.Garbuzov  
Dr.J.Xu**

### **Material Growth Characterization:**

#### **Staff**

**Dr. E. Kolev  
J. Gwilliam**

#### **Students**

**X. He  
S.Kim  
M.Erdtmann  
D.Wu**

### **Laser Processing and Measurements:**

#### **Staff**

**Dr. L.J. Wang  
Dr. D. Garbuzov  
Dr. J. Xu**

#### **Students**

**G. Lucas  
J. Diaz  
I. Eliashevich  
A. Rybaltowski**

**Theoretical Calculation: H.-J. Yi**

## CHAPTER I

### Introduction

InGaAsP/GaAs quantum well lasers operating in the wavelength range of 0.8  $\mu\text{m}$  to 1.0  $\mu\text{m}$  are useful for pumping of erbium doped fiber amplifier and Nd:YAG lasers. At present, AlGaAs/GaAs quantum well lasers are commonly used for these purposes, but there are several problems involved in these structures; oxidation of AlGaAs layers which prevent further regrowth or device fabrication, higher growth temperature which is not compatible with monolithic integration, and the presence of dark line defects causing degradation in device performance. Most of these problems are attributed to Al and hence an alternative material is necessary. InGaAsP material is an alternative to AlGaAs and has been already shown a lot of promise for the above applications.

The main objective of this contract under ARPA/US Army #DAAH-04-93-G-0044 is to develop and demonstrate 0.8 $\mu\text{m}$  high power laser based on InGaAsP material system for pumping of Nd:YAG lasers. In order to achieve this goal there are three major considerations: (1) growth and fabrication of GaInAsP/GaAs heterostructures lasers, (2) packaging and device testing, and (3) the reliability assessments of these structures. This report summarizes the results of experimental research work that the Center for Quantum Devices have accomplished under this contract.

## *CHAPTER II*

### *MATERIAL GROWTH AND CHARACTERIZATION*

## CHAPTER II

### Material Growth and Characterization

#### 1. Growth and Characterization of 808nm InGaAsP/InGaP/GaAs

##### a. Introduction

After series of InGaAsP/InGaP/GaAs growth structures, two changes have been made in the growth. The first change is the decrease of  $\text{PH}_3$  from 450 cc/min to 300 cc/min, and the second change is the decrease of growth temperature from 530°C to 510°C. It was found that lower  $\text{PH}_3$  flow rate into the reactor chamber improves the quality of InGaP as well as saves the source material. The lower growth temperature is intended to increase the bandgap of InGaP carrier confinement layer, which will give better carrier confinement and laser performance. It also fits in our efforts to grow laser on Si substrate.

In accordance to the above two changes, the growth conditions of all layers were readjusted. It is found that the III/V ration has a large effect on the optical quality of the quaternary. The optimum conditions for the InGaAsP waveguide and active layers were determined. The n-type doping by silane and p-type doping by DEZn at 510°C were calibrated. After the above optimization of the growth conditions, approximately twenty-five 808nm laser wafers have been grown (see Table 1). The laser wafers grown under new conditions were discovered to have far stronger room temperature photoluminescence than that of the best laser sample (#228) grown before.

Table 1.  
Growth and Characterization Results

Wafer #	Substrate	Waveguide growth time	Wavelength (nm) PL (EL)	Mismatch
331	Sumitomo	8'	805.8	-0.1%
334	Sumitomo	8'	812.5	-0.07%
335	Sumitomo	8'	808	0.0%
336	Sumitomo	8'	808	0.0%
337	Amer. Xtal	8'	808	0.0%
338	Amer. Xtal	8'	808	0.0%
339	Sumitomo	8'	808	0.0%
340	Sumitomo	8'	804.7	-0.06%
341	Sumitomo	8'	808	0.0%
342	Sumitomo	8'	808 (815)	0.0%
343	Sumitomo	8'	809.4	-0.05%
344	Sumitomo	8'	808 (813)	0.0%
345	Sumitomo	8'	808 (813)	0.0%
356	Amer. Xtal	8'	808	0.0%
357	Amer. Xtal	8'	802.0	0.1%
358	Sumitomo	8'	808	0.0%
359	Sumitomo	8'	808	0.0%
360	Amer. Xtal	8'	809.0	Broad
361	Amer. Xtal	8'	799.0	0.1%
364	Sumitomo	8'	799.0	-0.2%
367	Sumitomo	6'	809.0	-0.1%
384	Sumitomo	12'	808	0.06%
385	Sumitomo	8' (2 wells)	808	0.06%
386	Sumitomo	8' (3 wells)	808	0.06%
387	Sumitomo	10'	808	0%

#### b. Optimization of InGaAsP Quality

Except for the two pre-conditions: the growth temperature is 510°C and PH<sub>3</sub> flow rate is 300 cc/min, the only remaining adjustment freedom is on the III/V ratio.

In our study, we use photoluminescence (PL) as the main tool to evaluate the quality of the film, since optical quality is the major concern of the laser wafers. The partial pressure of group V element is unchanged during the study. Only partial pressure of group III element is changed to study the III/V ratio effect on the optical quality. Figure 1.1 shows the dependence of photoluminescence full width at half maximum (FWHM) and integrated intensity on the relative change of the group III flow rates for InGaAsP ( $E_g \sim 1.53\text{eV}$ ). Apparently, there is an optimum group III flux value for the material, at which the photoluminescence is strong and sharp. By the simpler interpolation of the data in Figure 1.1, the optimum growth conditions were obtained. Similar optimization of III/V ratio was also performed for InGaAsP ( $E_g \sim 1.77\text{eV}$ ). Results of the above study indicate that the optimization of the III/V ratio is crucial to the optical quality of InGaAsP layer.

Although the optical quality of the InGaAsP grown under the optimized conditions at 510°C is not as good as that grown at 530°C in the sense of PL FWHM, the PL of the separate confinement heterostructure (SCH) is comparable to that grown at 530°C. Another restriction at 510°C is that the highest InGaAsP bandgap obtainable with the present AsH<sub>3</sub> mass flow controller (MFC) is 1.53 eV. A 0.02eV higher bandgap is required to insure the lasing wavelength at 0.808 $\mu\text{m}$ . However, a 5°C increase of the growth temperature should get the work done.

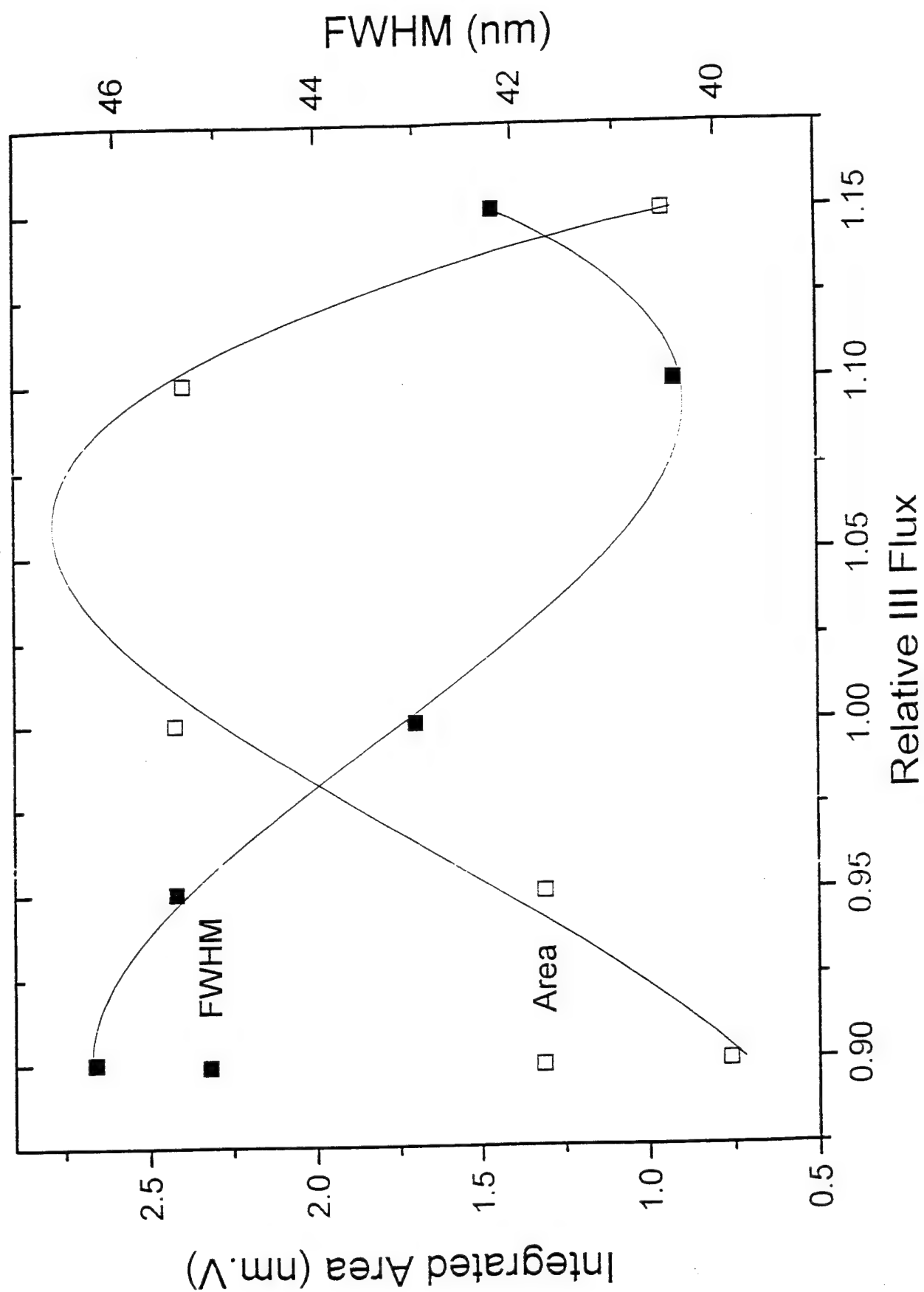


Figure 1.1

### c. Improvement of Wafer Homogeneity and Morphology

The homogeneity of the wafer is improved by choosing a susceptor holder that has about  $1^\circ$  larger tilt angle than the old susceptor holder. With the old susceptor holder, it was found that the layer at downstream of the susceptor had far larger mismatch in Ga rich side than that at upstream. The sensitive temperature dependence of the indium incorporation in the layer is attributed to the larger mismatch fluctuation of the layer on the old susceptor. The upstream has lower temperature than downstream with the old susceptor holder. Larger tilt angle gives rise to better homogeneity due to two reasons. Firstly, the downstream is farther away from the center of the heating coil where the maximum heating power presents. Hence, the temperature is lower than the temperature on the old susceptor at that point. Secondly, the gas flow speed at the down-stream is faster for the larger tilted susceptor, it will bring away heat at the down-stream faster. In addition to the temperature uniformity over the susceptor, the gas flow patterns also affect the homogeneity of the layer.

Figures 1.2 (a-c) shows the x-ray and photoluminescence mapping of a InGaAsP/InGaP/GaAs double heterostructure grown by using new susceptor holder. InGaP has less mismatch fluctuation over the susceptor than InGaAsP. The photoluminescence from InGaAsP is relative independent to the mismatch of InGaAsP layer. Except the larger mismatch and fluctuation of photoluminescence wavelength at the edge of the susceptor, which is due to the gas flow pattern effects there, approximately 70% excellent quality (mismatch  $< 0.1\%$ ,  $\Delta\lambda < 5\text{nm}$ ) film can be obtained under the proper growth conditions.

In order to assure the reproducible wafer quality after each tube cleaning, a tube gauge is invented to track the mounting positions of the tube and susceptor. The

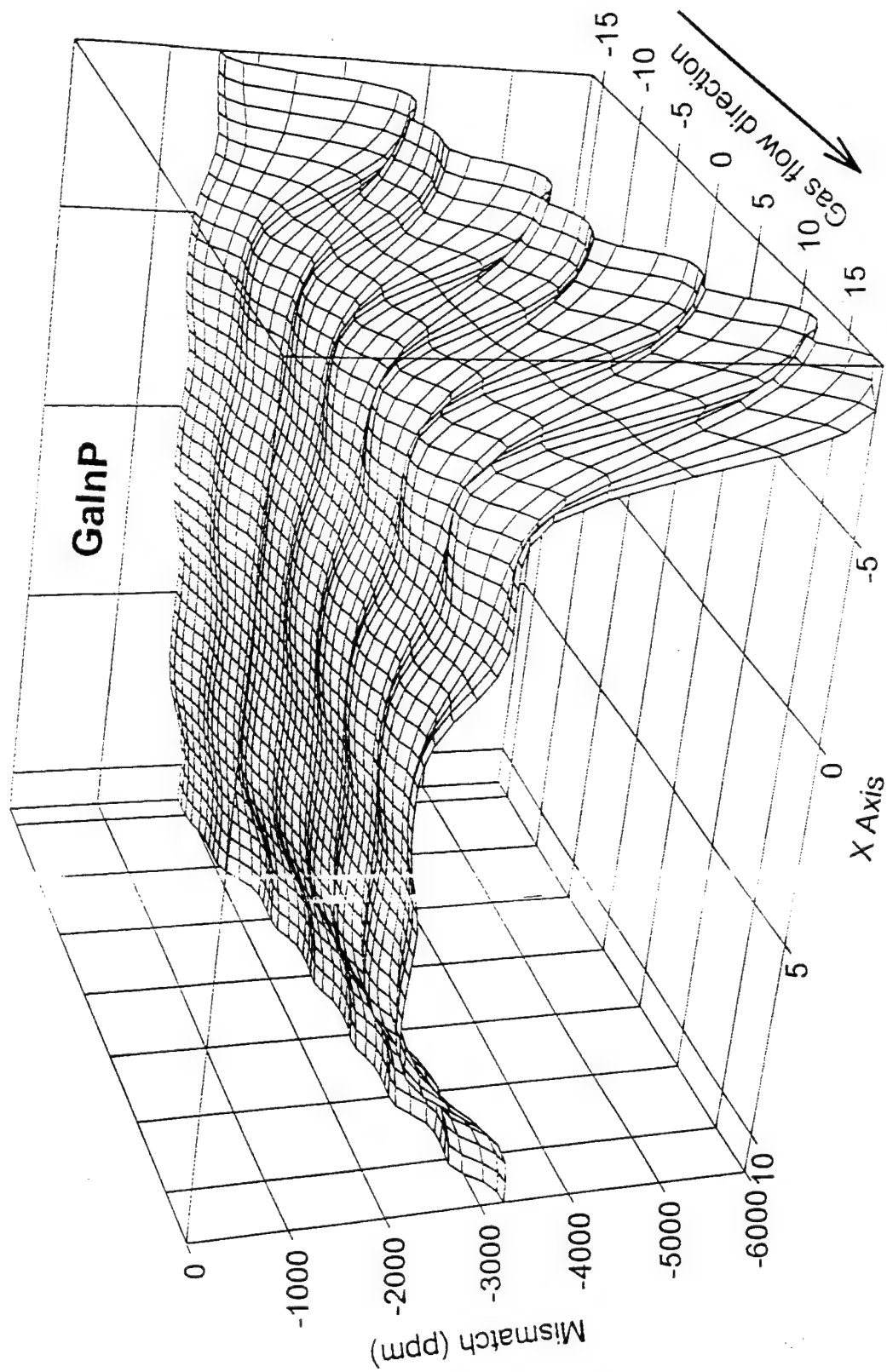


Figure 1.2 (a)

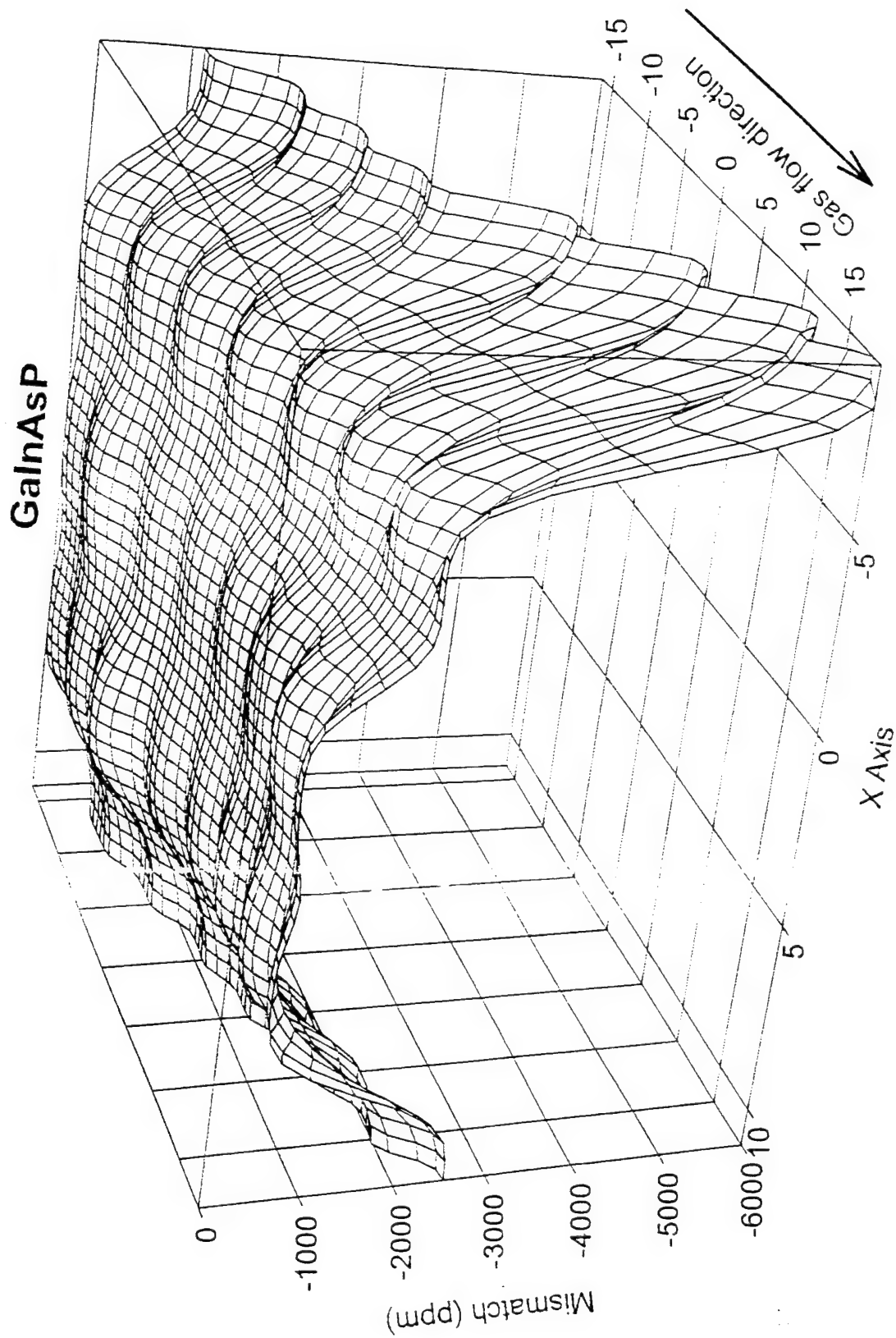


Figure 1.2 (b)

## Wavelength distribution

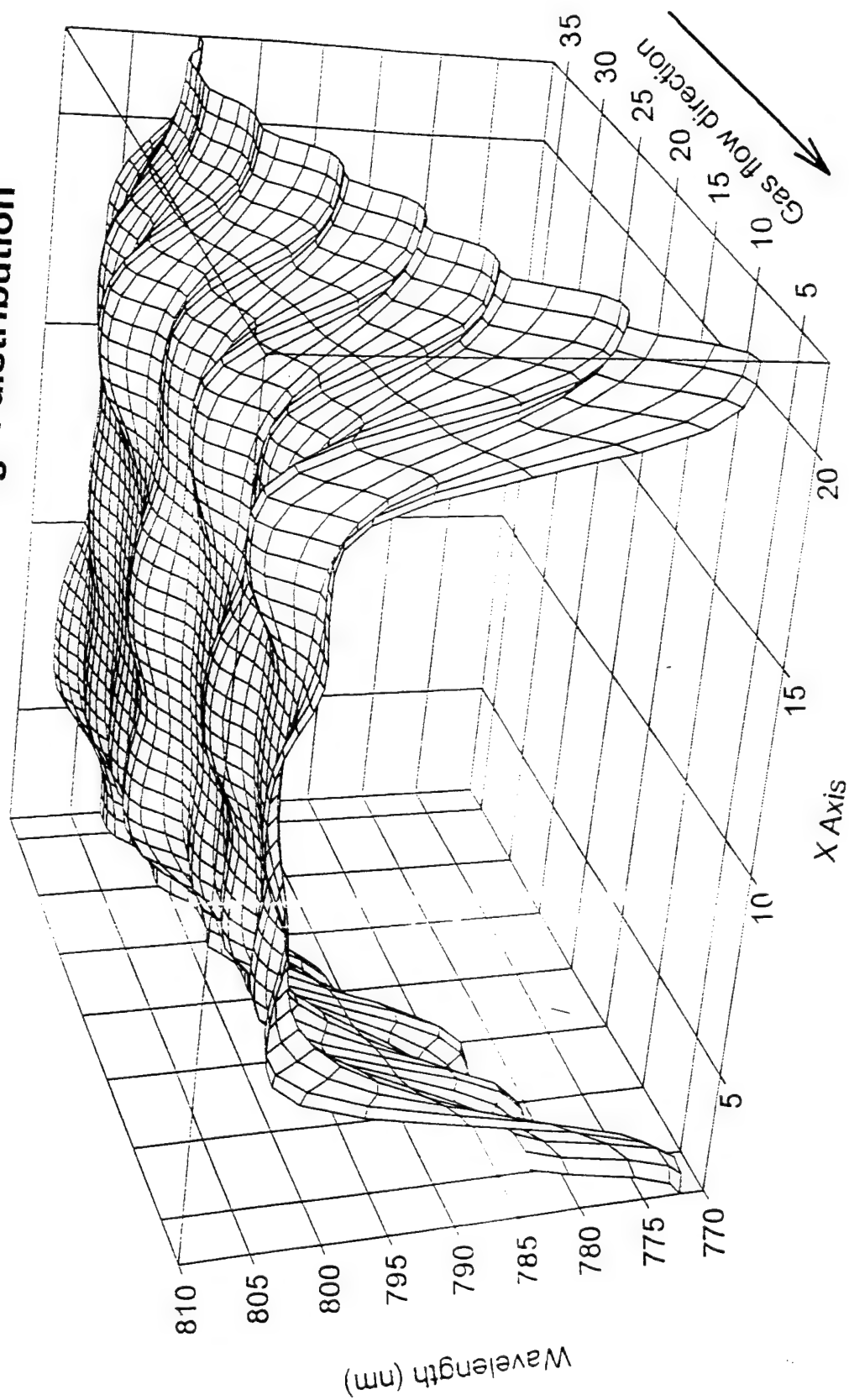


Figure 1.2 (c)

homogeneity of the film can be fine tuned by slightly adjustment of the mounting positions of the reactor tube and the susceptor holder rolling angle.

The surface defects have long been a perplexing problem for the InGaP containing layer. The defects on the wafers were reduced or removed by the good cleaning of the reactor tube, the effectively minimizing the oscillation of the system and the proper cleaving and loading of the substrate. It is found that the InGaP containing film is very vulnerable to the particles and dirtiness on the substrate surface prior to the growth. The proper cleaving can avoid the microcrystal splashing from the cleaving edge. It is found that the major defect source comes from the inside of the reactor tube due to the oscillation of the system and the improper cleaning of the reactor tube after each growth run. Better in-situ cleaning of the reactor is achieved by introducing an appropriate tube cleaning procedure. A stable system is most important to the reduction of growth defect density. To stable the system, the most unstable source, that is DEZn, is turned on 45 seconds before it is used. The oscillation between the switching of the valves is minimize by carefully balancing the reactor chamber pressure and vent line pressure. With the above precautions, a far improved sample surface morphology is obtained for the laser wafer grown at 510°C.

#### d. Doping Calibration

The doping at 510°C is calibrated through the profiling of a stair doped sample by electrochemical capacitance-voltage (ECV) profiler. The relation between the flow rate of silane and the donor concentration in GaAs is shown in Figure 1.3. No saturation or compensation has been observed in the studied doping range. The doping level increases linearly with silane flow rate. Similar calibrations were done for InGaP:Si and InGaAsP:Zn. A laser structure is grown after the calibration of doping and optimization of the material. In comparison with the doping profile of the lasers grown at 530°C, the p-n junction is more close to the center of the active and waveguide region and the doping

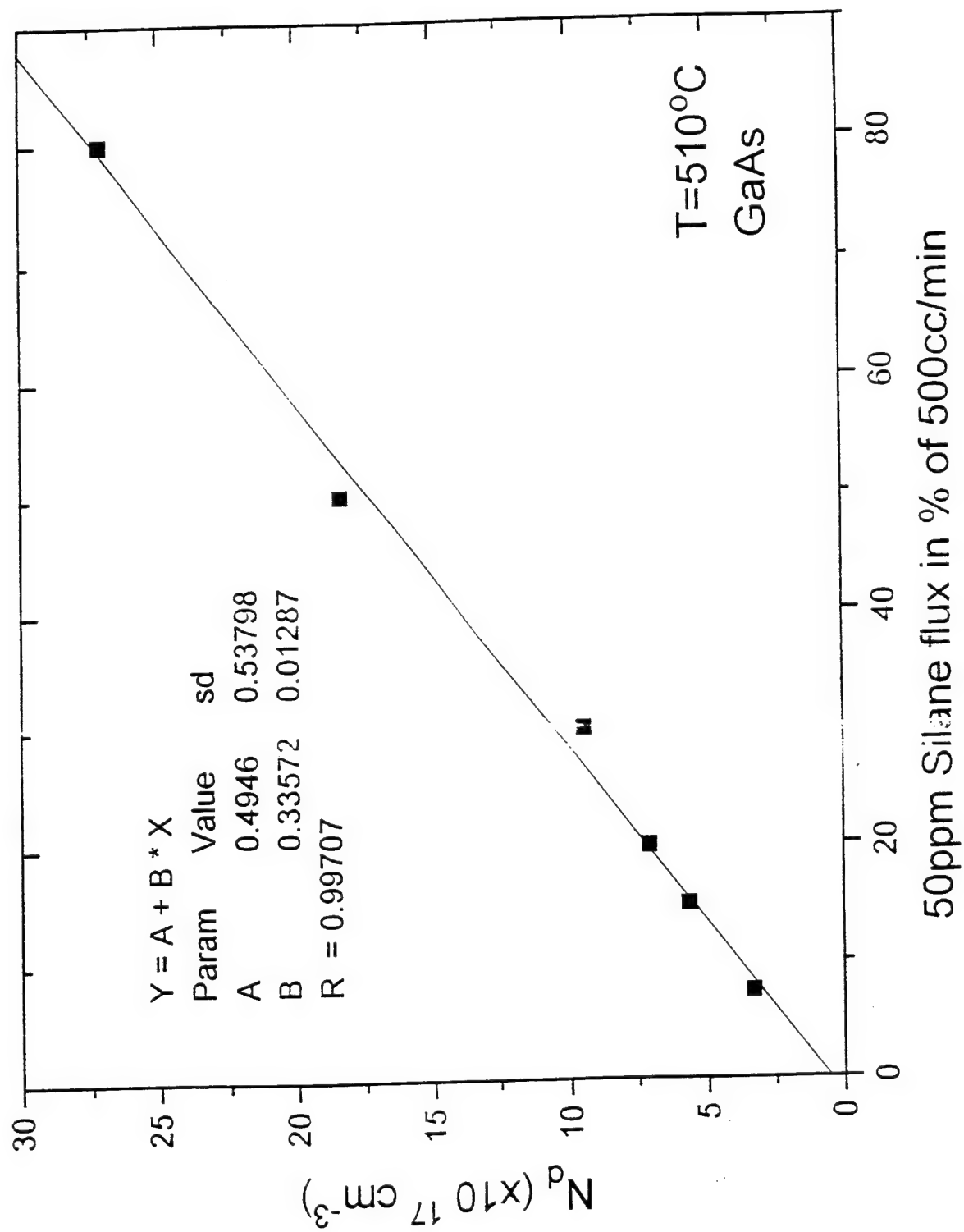


Figure 1.3

transition between undoped waveguide layer and doped carrier confinement layer is more abrupt. It may come out of the less diffusion of dopants, especially Zn, at lower growth temperature.

#### e. Laser Wafer Quality Evaluation

Figure 1.4 shows the photoluminescence of the sample grown at 510°C and the best sample grown at 530°C (#228). It indicates that the photoluminescence of the sample grown with the new growth conditions is approximately three times of that of the best sample grown at 530°C. The improved optical quality is due to the higher quality InGaP layer. The active layer quaternary grown at 530°C has been measured to have approximately 100% spontaneous emission quantum efficiency, which indicates that there is no further improvement for the quaternary, the stronger photoluminescence is due to the better quality of the InGaP carrier confinement layers. This was evidenced from the fact that the photoluminescence intensity is similar for the samples grown at 510 °C and 530 °C when a focused beam is used as an excitation. When the focused beam is used as excitation, the photoluminescence is less affected by the InGaP quality because electron-hole pairs are generated in a far smaller volume.

Structures grown at 510°C have larger bandgap (1.90eV) than that grown at 530°C (1.86eV). It has been reported that the bandgap of InGaP depends strongly on the growth temperature. Larger InGaP bandgap will improve the carrier confinement efficiency in the laser structure. Figure 1.5 shows the photoluminescence spectra of the two samples grown at two sets of temperatures. For the sample grown at 530°C, a photoluminescence peak from waveguide quaternary is clearly observed in the spectra. However, no photoluminescence peak from the waveguide was observed in the spectrum. In previous studies, it is found that weaker photoluminescence intensity from the waveguide region indicates better carrier confinement, therefore, contributes to better laser performance.

FIG1-6.XLC

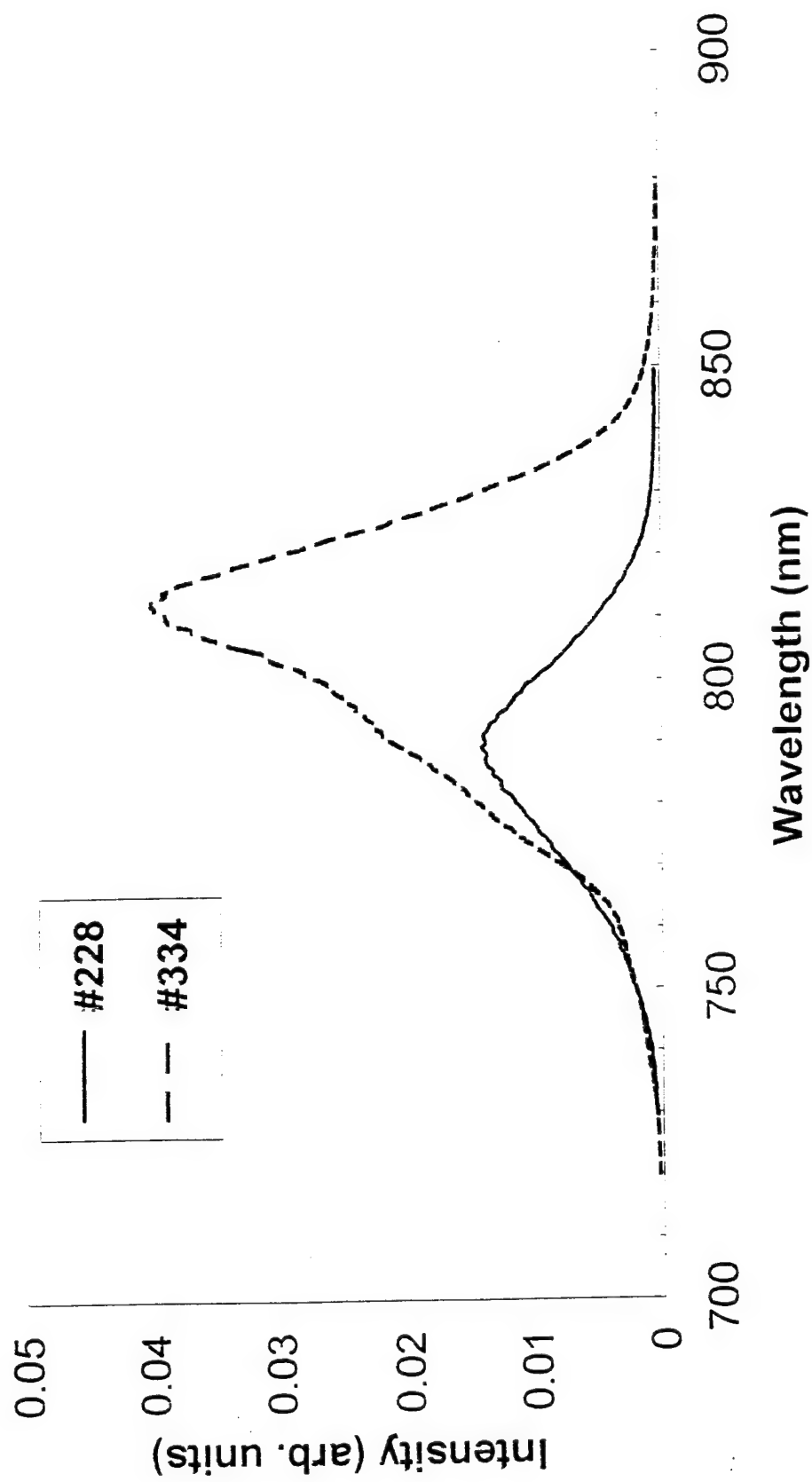


Figure 1.4

FIG1-7.XLC

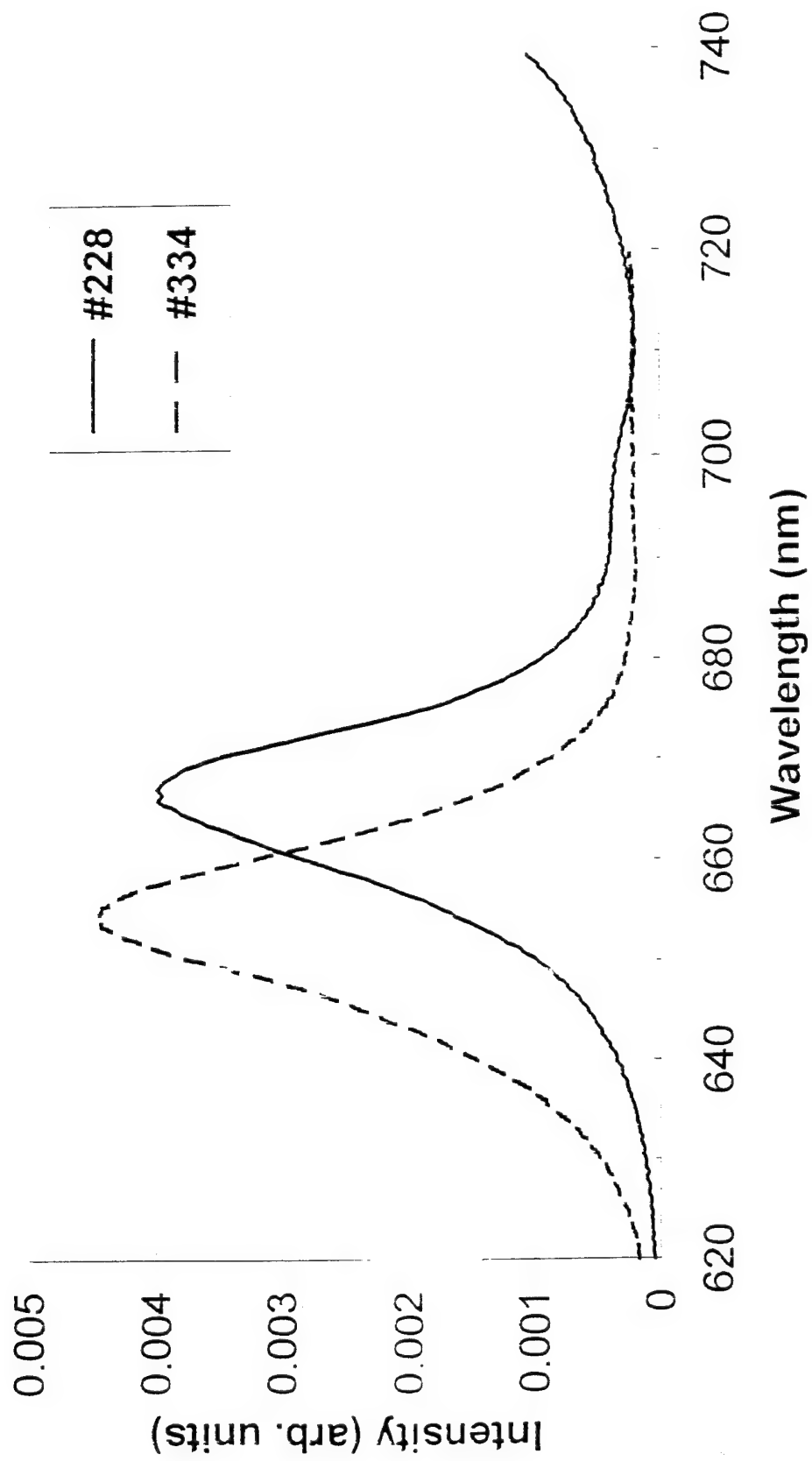


Figure 1.5

## 2. Growth and Characterization of 980nm InGaAs/GaAs

### a. Introduction

980 nm strained  $\text{In}_{1-x}\text{Ga}_x\text{As}$  quantum well laser has special importance for pumping  $\text{Er}^{3+}$  doped fiber amplifier which are very attractive devices for single mode fiber communications systems in the  $1.3\ \mu\text{m} - 1.5\ \mu\text{m}$  wavelength band instead of  $1.49\ \mu\text{m}$  because of lower noise, high power conversion efficiency.

Instead of the conventional GaAs/AlGaAs system with AlGaAs serving as the cladding layer, the Al-free 980 nm laser was attempted to improve 1) the laser reliability, 2) less surface oxidation during the fabrication process and device operation, 3) improve the optical characteristics of the material by lowering the growth temperature, 4) achieve the uniformity and reproducibility of the material.

The improved material quality can promise the obtaining the lower threshold current density, higher differential quantum efficiency and higher power output with less temperature sensitivity. We can expect the long life time and narrow far field in the fundamental transverse mode.

### b. Growth conditions

Separate confinement InGaP/GaAs/InGaAs and InGaP/InGaPAs/InGaAs heterostructures have been grown by low pressure metalorganic chemical deposition (LP-MOCVD). The epitaxial layers were grown on a  $n^+$  silicon doped GaAs substrate (100) with a  $2^\circ$  miscut. The process of growth was carried out at pressure of 78 torr in a horizontal reactor at a substrate temperature of  $510^\circ\text{C}$ .

Trimethylindium (TMIN) and Triethylgallium (TEGa) were used as sources of In and Ga while pure arsine ( $\text{AsH}_3$ ) and phosphine ( $\text{PH}_3$ ) provide As and P respectively. Hydrogen ( $\text{H}_2$ ) was used as a carrier gas.  $\text{SiH}_4$  and diethylzinc (DEZn) were used as n-type and p-type dopants, respectively. The structure of the grown material is shown in Figure 2.1.

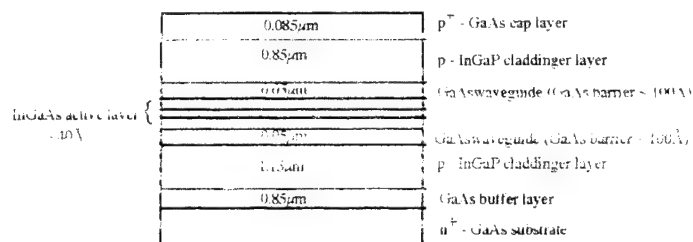


Figure 2.1. 980nm InGaP/InGaAs/GaAs Laser Structure  
It is well known that when strain is induced, the critical thickness of the epilayer is

important factor to determine the optical properties of the material. In lattice mismatched  $\text{In}_x\text{Ga}_{1-x}\text{As}$  on GaAs, the internal compressive or tensile strain can be expected and it is important how to grow the multiquantum wells to compromise this kind of deformation.

The high resolution x-ray diffraction measurements of the grown laser sample (Figure 2.2) shows the very fine peaks. It means that the sample has sharp interface of each layer. The interface can be improved by finding the appropriate growth rate of each layer and growth temperature. The growth temperature for these lasers is 510°C.

Table 1. Growth rate of each layer

Layer	InGaP	GaAs	InGaAs
Growth rate	178 Å/min	162 Å/min	135 Å/min

The real growth rates (Table 1) are lowered than the expected value. It comes from the doping effects in case of InGaP. The relationship between the growth rate and optical properties in multi-quantum well has not been examined at this time.

#### c. Optical Properties with Photoluminescence

By the strain, there is energy shift in the light hole valence bandedge and heavy hole valence bandedge and this energy shift strongly depends on the In amount and the thickness of the well. It's already calculated that  $x=0.19$  for  $\text{In}_x\text{Ga}_{1-x}\text{As}$  is the most probable value for the 980 nm laser.

The formula for the energy gap  $E_g = 1.424 - 1.614x + 0.54x^2$  and the calculated band offset  $\Delta E_c/\Delta E_g = 0.65$ .

The shift in the PL peak energy is due to the biaxial elastic strain and to the quantum size effects. Elastic strain results from the epilayer maintaining registry with the substrate such that the lattice mismatch is accommodated entirely by elastic strain.

## X-RAY RESULTS

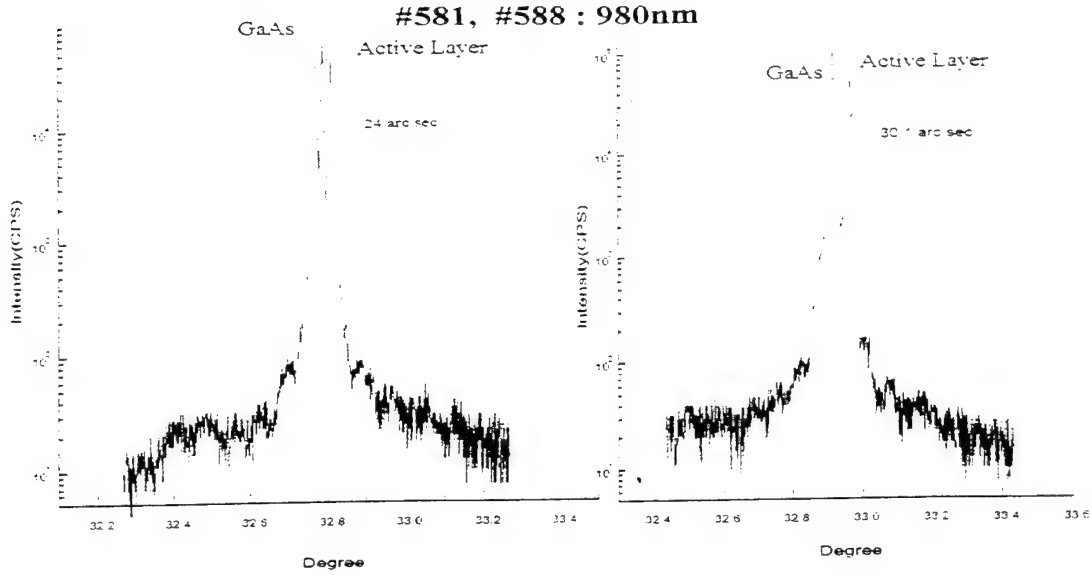


Figure 2.2. High Resolution X-Ray Diffraction Measurements of 980nm laser structure.

After correcting for quantum size effects, the PL peak is expected to be at a constant strain shifted position for epilayer thickness less than the critical thickness. The correction term of quantum size effect should be considered in case of specific multi-quantum wells.

We obtained good PL spectrum of the material with FWHM of 14.43 meV at 77K (Figure 2.3) and 15 meV at 300K (Figure 2.4).

The results of the grown samples are shown in Table 2:

Table 2. Summarized PL results of three laser samples

	Sample	#580	#581	#588
Peak position	77K		912nm	918nm
	300K	968nm	970nm	973nm
FWHM	77K		14.43 meV	16.02 meV
	300K	16 meV	15 meV	23 meV

This results shows that the PL peaks nearly has constant values that is the composition rate is stable during the growth and the growth condition is successfully optimized for 980 nm lasing wavelength.

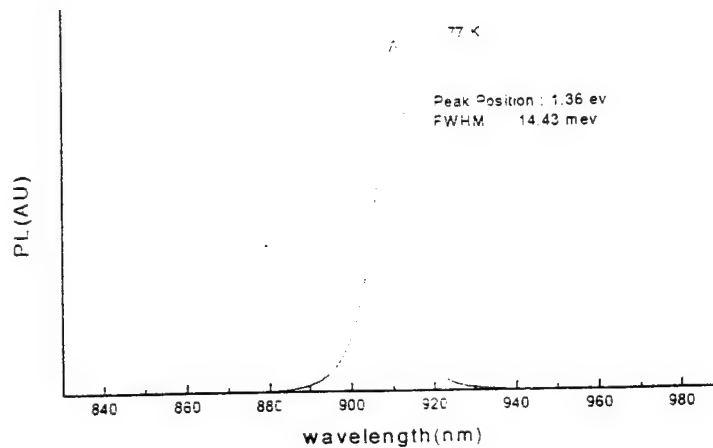


Figure 2.3. The spectrum of the Photoluminescence of the laser structure at 77K.

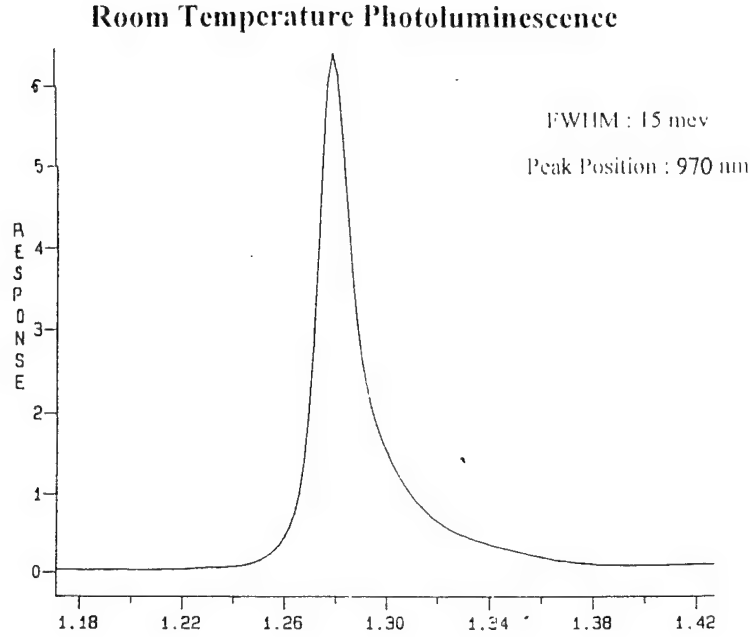


Figure 2.4. The spectrum of the Photoluminescence of the laser structure at 300K.

#### InGaP/In<sub>1-x</sub>Ga<sub>x</sub>AsP<sub>1-y</sub>/InGaAs Multiquantum Well Structures

There are two main reasons for InGaAsP instead of GaAs as confinement layers: 1) InGaAsP confinement layer give better carrier confinement and consequently, higher external quantum efficiency compared with GaAs confinement layers. Quantum efficiency strongly depends on not only the cavity wavelength but also on the energy gap of the confinement layer because of the effective carrier confinement. There are some results shows that 1.72eV InGaAsP exhibit higher  $\eta_d$  than the lasers with 1.57eV InGaAsP.

Secondly, InGaAsP alloys lattice matched to GaAs are attractive because they cover the band gap range of 1.91 eV to 1.42 eV at room temperature. In order to obtain high coupling power into a single mode fiber, narrow beam divergence and circular beam is indispensable. The large difference of refractive index between GaAs and InGaP which was measured as  $\Delta n_r = 0.32$  ( $n_r = 3.49$  for GaAs,  $n_r = 3.17$  for InGaP) at a wavelength of  $0.98\mu\text{m}$  by ellipsometry, gives wide transverse beam divergence. The optimized InGaP/In<sub>1-x</sub>Ga<sub>x</sub>As<sub>y</sub>P<sub>1-y</sub>/InGaAs can contribute for suppressing the heterointerface spikes and narrowing the transverse beam divergence.

High resolution x-ray diffraction results shows ambiguous state of the sample. It is expected that the strain induced interface same as the GaAs/InGaAs structure but it shows the possibility that quaternary has effect on the accommodation of the internal strain. As shown in Figure 2.5, the PL display the transition of 1.21eV which is lower than the expected energy gap.

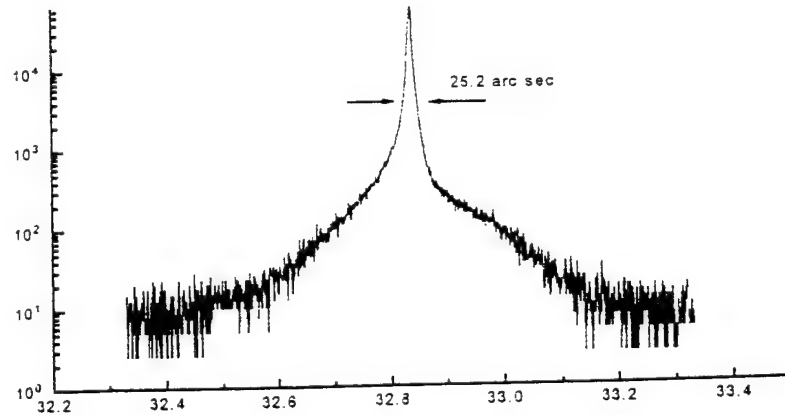


Figure 2.5. X-Ray Diffraction Measurement of InGaAs/GaAs laser structure.

The InGaP has the effect on the condensation of the InGaAsP layer. We can see the relaxation of the mismatch without the InGaP layer in many cases. Without InGaP layer, the quaternary of the waveguide has a mismatch of 0.13%. When InGaP layer is grown, the mismatch is decreased to 0.052% as shown in Figure 2.6.

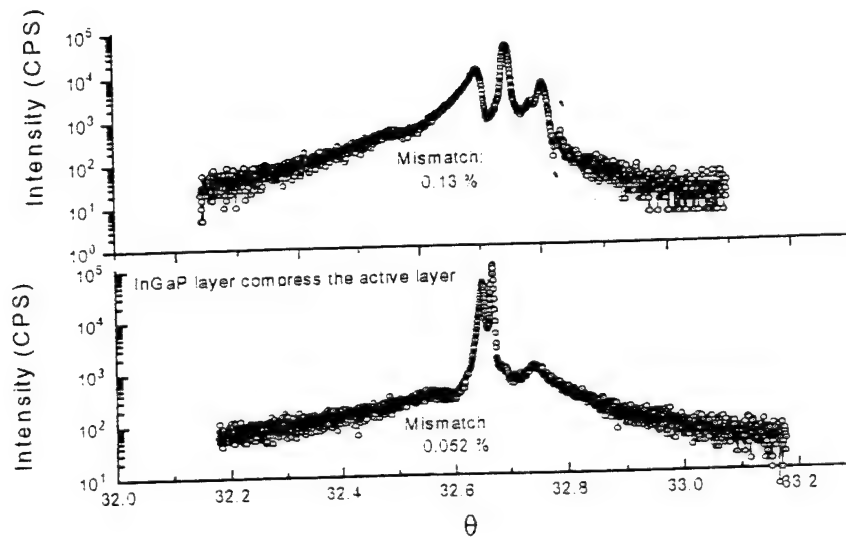


Figure 2.6. Relaxation of the internal strain of the laser structure

#### *Optical properties with photoluminescence*

According to earlier works, the single quantum well laser is ideal for obtaining a very high output power and good far field for efficient fiber coupling, and the multi-quantum well lasers exhibit very high external quantum efficiency and launch high

power at low drive currents. Several samples were grown to compare the optical properties between SQW and MQW structures. Using a 514nm line spectra physics Ar<sup>+</sup> laser and a Carl Zeiss microscope with a photodetector mounted in the collimator, photoluminescence experiments were carried out. At room temperature, a PL peak was measured at 1.02 $\mu$ m and at 0.960  $\mu$ m with a FWHM is 15 meV (Figure 2.7) for the MQW structure. For the SQW structure, the luminescent wavelength is increased to 1.03  $\mu$ m (Figure 2.8). The energy shift resulted from 15 meV to 88 meV. Compared to InGaAs/GaAs peak obtained at 970nm ~ 973 nm, the InGaAsP/InGaAs structure should be optimized for 980 nm lasing wavelength to decrease the energy shift. Now the shift range is from 13 meV to 76 meV. As we see in the case of single quantum well, the thickness and the number of quantum well must be optimized. Table 3 summarizes room temperature PL studies for MQW and SQW structures.

Table 3. Photoluminescence results at 300K

Sample	#582	#583	#584
Peak Position	1.02 $\mu$ m	0.960 $\mu$ m	1.026 $\mu$ m
	0.966 $\mu$ m		1.028 $\mu$ m
FWHM	39 meV	15 meV	29 meV
	15 meV		33 meV
Structure	MQW	MQW	SQW

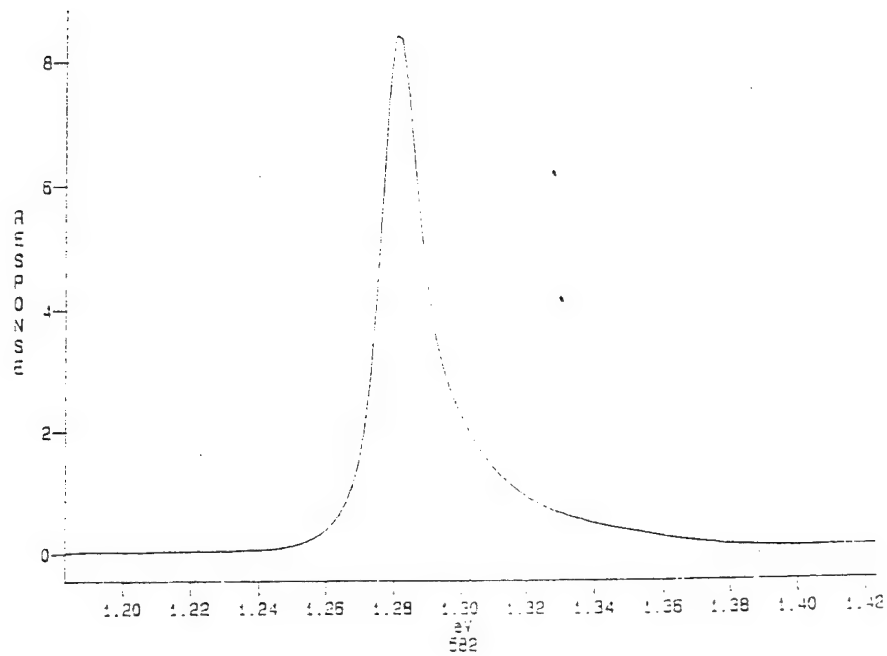


Figure 2.7. Room temperature photoluminescence of the modified laser structure with MQW with FWHM of 15 meV.

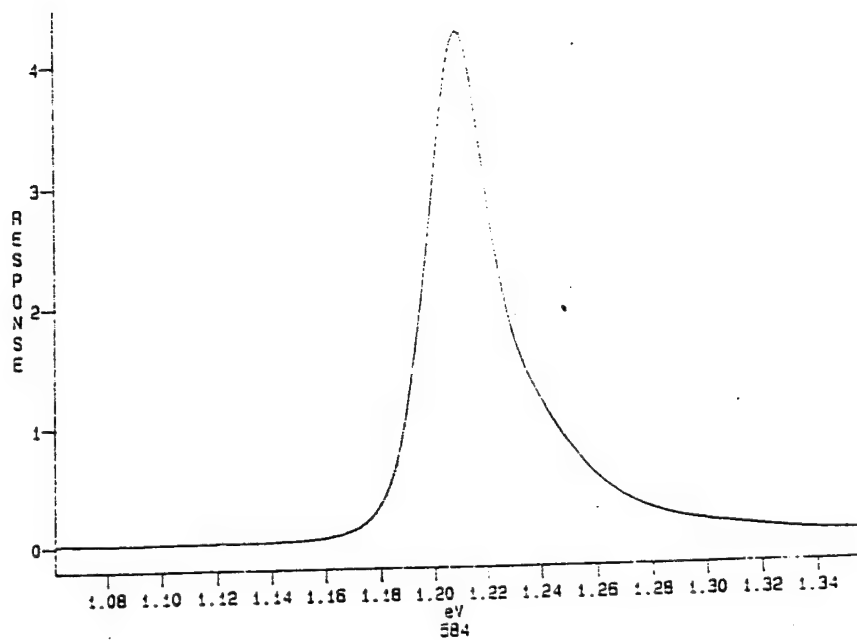


Figure 2.8. Room temperature photoluminescence of the SQW with energy shift and broad peak.

## *CHAPTER III*

### *FABRICATION TECHNOLOGY and PROCESSING OF 808NM InGaAsP/GaAs LASERS*

## CHAPTER III

### Fabrication Technology and Processing of 808nm InGaAsP/GaAs Lasers

#### 1. Processing of InGaAsP/InGaP/GaAs Lasers

##### a. Introduction

The design structure of a SCH laser diode is to achieve both maximum carrier confinement and efficient optical confinement. The SCH lasers, as proposed in 1973 by Thompson and Kirby, consists of five layers such that the center composition step between the active layer and the waveguide layers gives an energy band discontinuity to confine injected carriers within the active layer, and the outer step in the refractive index between the waveguide and cladding layers confine the light within the optical cavity. Separate optical and electrical confinement ensures moderate beam divergence and optical power density at the laser mirror, while preserving fundamental transverse mode operation and low threshold current density for lasers with thin active layers. Quantum well lasers takes advantage of the quantization effects on carriers confined in a thin heterostructure, with active regions on the order of 50-200 Å. The preference of quantum well lasers offers (i) high differential gain to attain low threshold current density; (ii) small optical confinement factor, and (iii) a small variation of threshold current with temperature.

The light emitting area of a laser diode is confined by a stripe contact resistance of some width,  $W$ , in which most current will flow through the ohmic contact region. The stripe contacts are created by the combination of metallization and photolithographic techniques. The processing of 0.808  $\mu\text{m}$  broad area laser diodes follows ten sequential steps. These steps are explained in detail in the following subsections.

### b. Wafer Preparation

The sequence for fabricating broad area  $0.808\mu\text{m}$  InGaAsP/GaAs laser diodes begins with the preparation of the wafers, that is, all laser samples undergo a chemical degreasing of trichloroethane (to remove wax and grease residues), acetone (to remove polymer particules), methanol and propanol (to remove particles from previous steps or water content) for seven minutes. The laser wafers are then immersed in 1% hydrofluoric (HF) solution for ten seconds to remove any interfacial native oxides from the semiconductor surface prior to metal deposition. The preparation of semiconductor surface prior to metal film deposition is very important not only to the processing of the laser device but it can degrade the electrical characteristics of the device as well as contribute to reliability problems. The most aspect of all chemical processing is to obtain chemicals of the highest practical purity. Heavy metals ions in processing chemicals may stick to the semiconductor surface and modify its properties. Recent studies have been investigated in the preparation of the semiconductor surfaces by the use of bombardment with low energy  $\text{Ar}^+$  ion (60eV) as compared to chemically precleaned prior to the deposition of contacts. From the practical point of view, the use of ion-beam etching is a compromise solution since it ensures the removal of the native oxides. However, such application can introduce radiation damages in the disordered subsurface layer and effect the electrical performance of the contacts.

### c. Metallization of $\text{P}^+$ Contacts

The metal patterning of stripe contacts to a  $\text{p}^+$ -type doped GaAs layer begins with a metal film layer. This metal film is comprised of properties that are essential to the behavior of devices. Such properties are: ohmic contact, quality of adhesion, and temperature resistance. The ohmic contact is an important component particular for GaAs devices because it can strongly influence the electrical properties of device operation. The term "ohmic contact" is essentially defined as a metal/semiconductor (M/S) contact that has current-voltage characteristics which approximates a straight line through an origin and extends over the entire range of voltages and currents to which the contact regions are subjected.

The most widely technique to create ohmic contacts is to deposit metals containing an amount of dopants onto a GaAs layer, and allow the metal dopant to diffuse into the GaAs near the surface region by a subsequent annealing at elevated temperatures. These dopants occupy either n- or p-type sites and supply additional donors or acceptors at the GaAs interface. The doping level at the M/S interface locally increases. This technique is called alloying in which the metal melts during annealing and reacts with GaAs. The two common methods used for fabricating ohmic contacts or metal films are vacuum evaporation (electron beam evaporation) and sputtering. A significant difference exists between these techniques in producing films due to the different vacuum conditions which exists. In vacuum evaporation, the metal films are deposited in vacuums of  $10^{-6}$  to  $10^{-8}$  torr ( $1 \text{ atm} = 760 \text{ torr}$ ), while sputtering films are produced at pressures of  $10^{-1}$  to  $10^{-2}$  torr. In today's technology, the simplicity of depositing films is generally done by vacuum deposition as shown in Figure 3.1.

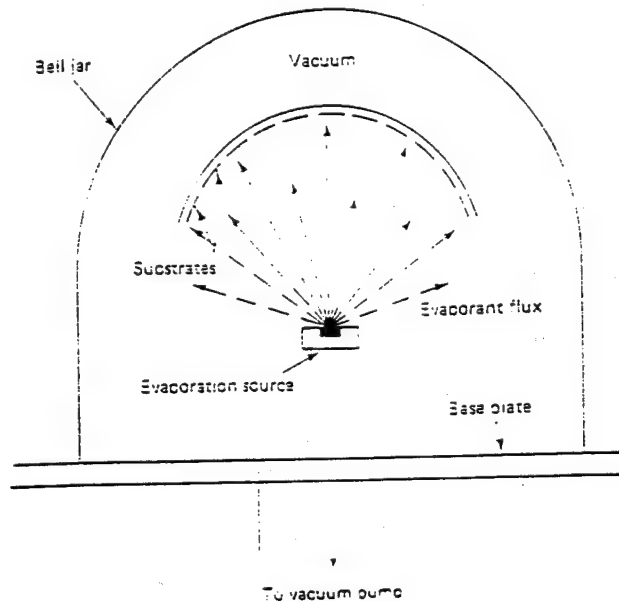


Figure 3.1 Schematic diagram of a vacuum evaporator.

As indicated earlier, the light emitted area of a laser diode is confined by a stripe metal contact. The metal contact is formed by depositing first a metal film containing dopants onto the  $p^+$ -GaAs layer. The most common metallization system to form ohmic contacts to  $p$ - and  $n$ -type GaAs are AuZn and AuGe/Ni systems, respectively. Since Ge and Zn are donors and acceptor dopants, respectively, their incorporation into GaAs would result in a doped surface region.

The  $p^+$  contact metal layer used for InGaAsP/GaAs laser diodes is Au/AuZn/Au systems. The multilayer structure of Au/AuZn/Au is deposited by a resistance-heated evaporation, consisting of 300 Å of Au, 500 Å of AuZn (16 % Zn by weight), and 1800-2300 Å of Au. The first Au layer provides good adhesion between the AuZn and the GaAs surface, since AuZn alloy shows very poor adhesion to GaAs. The thickness of this layer, 140 Å, was chosen to provide a reasonable surface uniformity and also permit easy penetration of Zn into the GaAs layer during alloying. A final layer of Au (1800-2000 Å) is required for the top surface layer of the contact in order to act as a bonding pad and to provide additional uniformity to the alloyed surface. In addition to ohmic characteristics, a smooth surface and strong adhesion between the contact metal and the GaAs are required. The contact morphology to the GaAs surface is highly influenced by the evaporation rate. If the evaporation rate is extremely high, there is only a limited time for the atoms on the surface to rearrange and combine into clusters before the next monolayer is deposited. Hence, rapidly deposited films contain a large number of islands, whereas slowly deposited films initially contain a few islands. These islands can be encountered during device fabrication as shown in Figures 3.2. These metal islands are more pronounced during gold and GaAs etching between the stripe contacts as shown in Figure 3.2 (a) and (b). In order to eliminate these gold islands, a suitable deposition rate must be used. A low deposition rate of 90-200 Å/min is found to reduce the incidence of metal islands, as shown in Figures 3.3 (a) and (b). The operator should keep in mind that the evaporation rate is highly dependant upon the type of

evaporation system being used. The presence of gaseous impurities in both the source material and the films can have a pronounced effect on the surface uniformity.

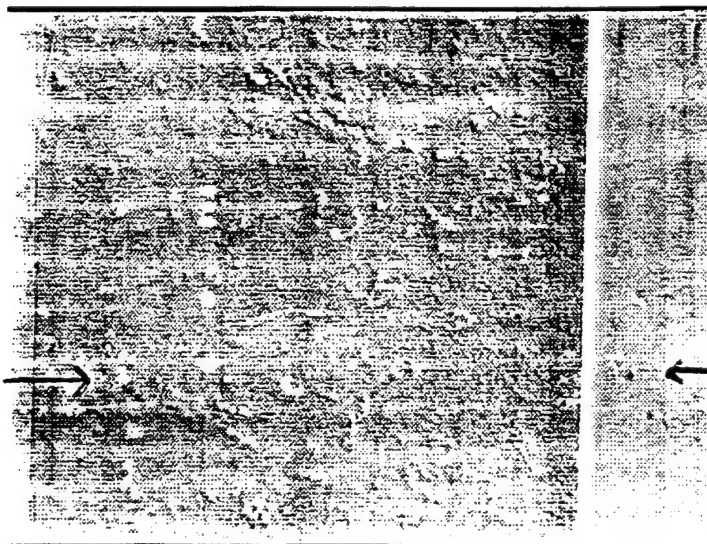
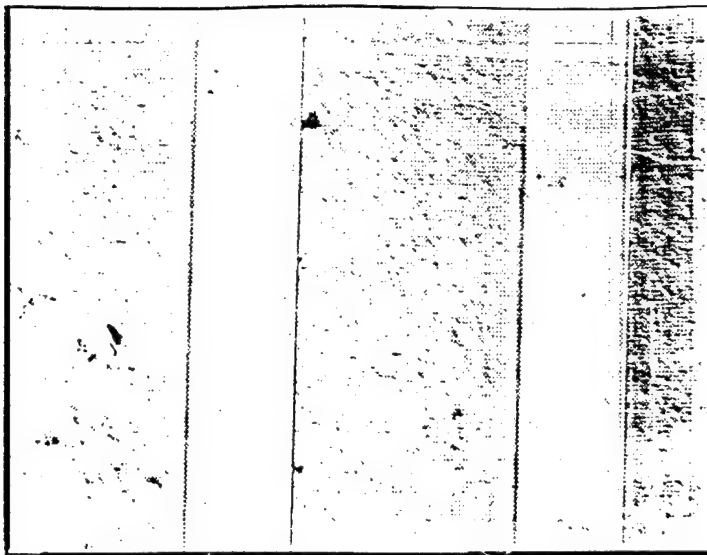


Figure 3.2 Metal islands due to high depoition rate which contributes defects onto the InGaAsP layer upon removing Au and GaAs layer between the stripe contacts.

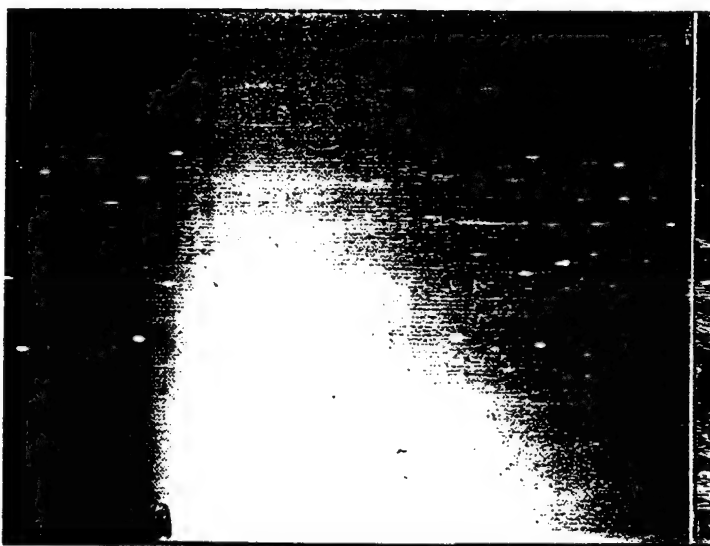
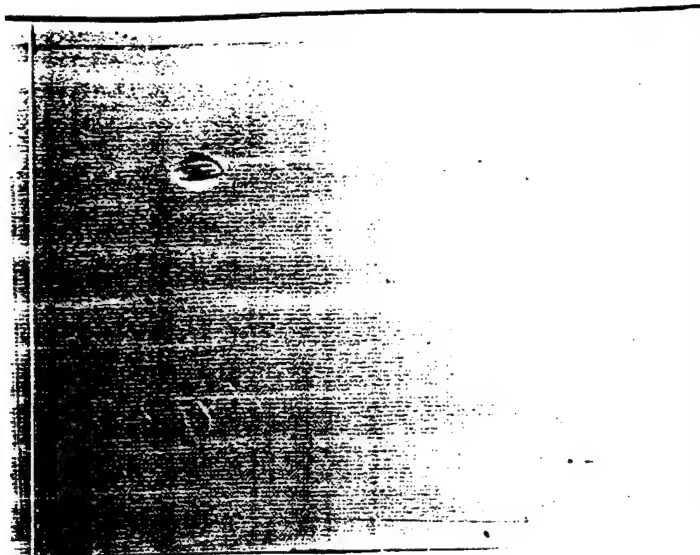


Figure 3.3 The elimination of metal islands on the  $p^+$ -GaAs layer by reducing the deposition rate.

The deposition of Au/AuZn/Au by electron-beam evaporator is accomplished by inserting the precleaned samples into a vacuum chamber as indicated earlier. The pressure in the chamber is reduced to the range of about  $2 \times 10^{-6}$  to  $10^{-7}$  torr this ensures that virtually all the evaporant flux will reach the semiconductor surface, and to prevent any undesirable chemical reactions between the evaporant molecules and the residual gases in the vacuum chamber. The evaporated material is placed in a water cooled crucible in which a focused beam of very high power density is directed at the surface of the material. This causes a small region of the material to heat up to a very high temperature and to start to vaporize. The evaporated molecules that hit the semiconductor surface will condense there and form a thin-film coating. As indicated earlier, the metal composition for the  $p^+$ -GaAs laser contact consists of Au(300Å)/AuZn(500Å)/Au(1800-2300Å). The evaporation of AuZn film is completely done by a resistance-heated evaporator rather by an electron beam evaporator to prevent any dopant mixture between the two material, AuZn and AuGe, within the vacuum chamber. The thickness of the deposited film can be monitored during the evaporation process by a quartz crystal film thickness monitor that is situated about 35 cm above the water-cooled crucible. As the film thickness builds up on the exposed face of the quartz crystal, it increases the net mass of the crystal. When the required film deposition has been reached, the evaporant material can be shut off automatically by means of a shutter that is placed in front of the evaporation source. Immediately, following the evaporation, all laser wafers should undergo a pre-heat treatment process. This extra step insures better adhesion of the metal film to the GaAs surface during photolithography and to sustain any chemical etching. The recommended pre-heat treatment is 330°C for two minutes under controlled forming gas ambient of 10% H<sub>2</sub>-N<sub>2</sub>.

The amount of time and temperature for this heat treatment is critical, since AuZn alloys at high temperatures are close to 400°C. The extend of time and temperature can create problems when removing unwanted gold from the semiconductor surface. All heat

treatments are carried out by conventional tube furnace. The formation of stripe contacts are completely done by photolithographic techniques.

#### d. Photolithography

Photolithographic techniques are universally used in transferring device patterns onto semiconductor materials. The photolithographic processing of broad area lasers consists of ten steps. These processing steps are explained briefly below:

1) Photoresist Application: Photoresist is a chemical substance containing a light-sensitive material in suspension in a solvent. The light-sensitive material is selected so that it responds to a intense blue-violet produced by a mercury arc lamp, but does not respond to the red or yellow light commonly in use in darkrooms or photoresist application areas. Photoresist comes in two distinct types:

- i. Positive resist: The light from the exposure step increases the solubility of the resist in the developing solution, by depolymerizing the resin.
- ii. Negative resist: The light from the exposure step causes polymerization to occur in the resist, reducing the solubility in the developing solution. This type of resist may be thought of as light-hardened.

The photoresist is characterized by four parameters that effect its performance. These four parameters are adhesion, etch resistance, resolution, and photosensitivity.

The application of photoresist onto a semiconductor surface is accomplished by dispensing the positive resist (Shipley's S1350J) through a 0.2  $\mu\text{m}$  filtering hypodermic syringe to remove polymerized particles before it is placed onto the center of the sample. The sample which is held down by vacuum chuck is rapidly accelerated to 5000 rpm for 25 seconds to obtain a resist thickness of about 1  $\mu\text{m}$ . The thickness of the resist coating depends upon the viscosity of the resist and the rate of acceleration of the spinner. Control over the

thickness and uniformity of the resist is very important in controlling the pattern dimension during exposure. Typical resist thickness is in the range of 0.5-1.0  $\mu\text{m}$

2) Pre-Exposure Soft Bake: Soft baking is necessary to prevent solvent trapping and possible bubbling or peeling of the resist. Resist adhesion to the substrate is improved with increased drying time. This is usually carried out on a hot chuck or in a conventional oven which heats the substrate and the resist film to a temperature of 90°C. Improper baking can result in hardening of the resist surface prior to the removal of all residual solvent which can result in pin holes and poor uniformity of the imaged dimensions.

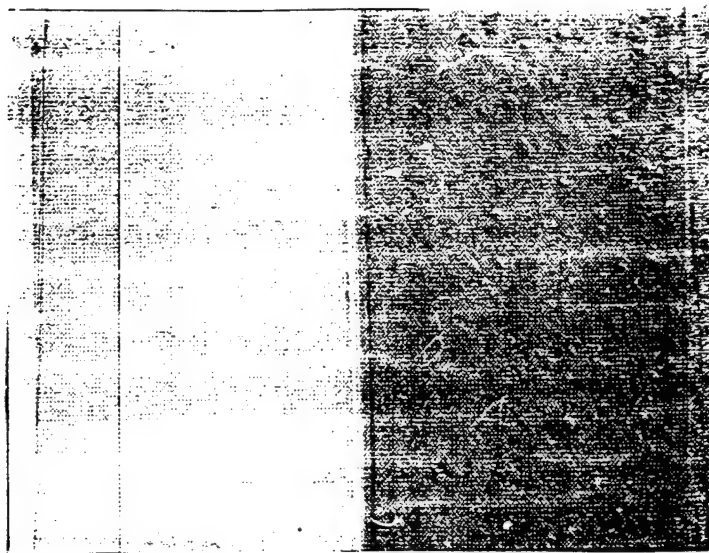
3) Alignment and Exposure: Alignment and Exposure are the most critical and significant part of the photolithographic process. The exposure method used in this processing consists of an apparatus called a "mask aligner" by Karl Suss that exposes the photoresist film to ultra violet light. The proximity of the coated wafer to a photomask ranges from 25 to 125  $\mu\text{m}$ . The relative position of the wafer and the photomask are adjusted such that the photomask is correctly lined up with the edges of the wafer. After proper alignment has been achieved, the wafer is brought into direct contact with the photomask of the pattern to be transferred onto the wafer, in this case, a 100  $\mu\text{m}$ -wide stripe. The areas of wafer that are not shielded by the opaque areas from the photomask are exposed to high intensity ultra violet light. The exposure time ranges from 4 to 10 seconds and is dependent on the age of the photoresist and the excitation lamp.

4) Development: The development of photoresist is accomplished by immersing the wafer in a developer solution of a ratio of four to one of deionized water to developer for a predetermined amount of time. This developer dissolves the exposed areas of the photoresist, while the unexposed areas remain insoluble and remain on the substrate. This process of replication transfers the photomask pattern onto the semiconductor substrate.

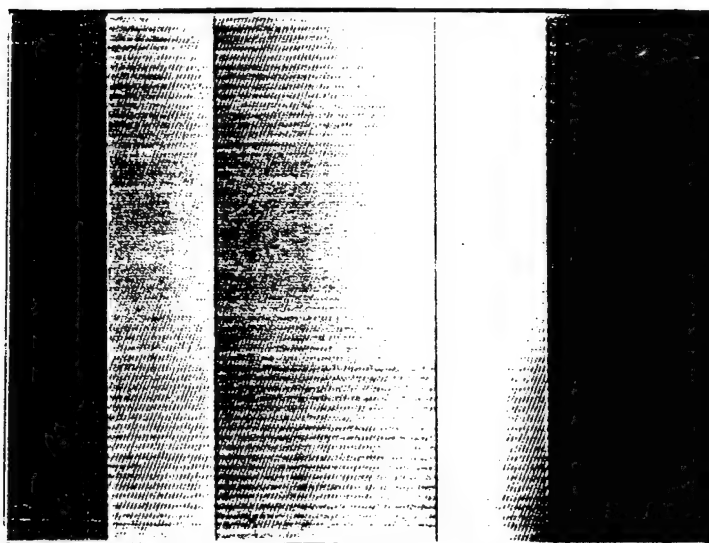
5) Post-Baking: After development, a post-bake treatment is used to dry the resist and to increase the adhesion of the resist to the substrate in order to withstand the subsequent

processing. The heat treatment is done by using a conventional oven at temperature of 120°C for 30 minutes.

6) Etching: Wet chemical etching is used extensively in the semiconductor processing to delineate patterns and to open windows. In the processing of lasers, the Au and the GaAs layer between the patterned stripes are selectively etched using KI(40grams):I<sub>2</sub>(3grams):H<sub>2</sub>O(100ml) for ten seconds and NH<sub>4</sub>OH:H<sub>2</sub>O<sub>2</sub>:H<sub>2</sub>O (Hydrogen Peroxide/Ammonium Peroxide/Water) for thirty-five minutes, respectively, to define the contact stripes and to confine the current uniformly along the 100 μm contact stripe. The removal of GaAs material can be accomplished by a variety of etching solutions. However, two possible chemical etchants were investigated to etch the GaAs cap layer without damaging the InGaP cladding layer, H<sub>2</sub>SO<sub>4</sub>:H<sub>2</sub>O<sub>2</sub>:H<sub>2</sub>O (Sulfuric/Hydrogen Peroxide) and NH<sub>4</sub>OH:H<sub>2</sub>O<sub>2</sub>. The GaAs etching using H<sub>2</sub>SO<sub>4</sub>:H<sub>2</sub>O<sub>2</sub>:H<sub>2</sub>O solution resulted in surface irregularities and surface pitting rather than NH<sub>4</sub>OH:H<sub>2</sub>O<sub>2</sub> as shown in Figure 3.4 (a). The best candidate to remove GaAs material is NH<sub>4</sub>OH:H<sub>2</sub>O<sub>2</sub> solution (PH=7, with an etch rate of 0.2 μm/min.) without attacking the underlying InGaP layer and the photoresist, as shown in Figure 3.4 (b). Once the Au and GaAs layers between the 100 μm stripes are removed completely, the photoresist is removed by rinsing in acetone and the stripe contacts are ready to proceed with a annealing.



(a)



(b)

Figure 3.4 (a) The appearance of surface irregularities when removing the GaAs layer between the stripe contacts with  $\text{H}_2\text{SO}_4:\text{H}_2\text{O}_2:\text{H}_2\text{O}$  etching solution, and (b) the effect of no surface irregularities using  $\text{NH}_4\text{OH}:\text{H}_2\text{O}_2$  solution.

The conventional method of reproducing stripe contacts is accomplished by following the photolithographic steps as mention earlier as shown in Figure 3.5. In Figure 3.5, the following steps are (a) the application of photoresist layer onto the GaAs substrate surface, (b) the photomask exposure of the  $100\mu\text{m}$  stripe, (c) the developing of the exposed regions, and (d) the etching of the metal and the GaAs cap layer combined.

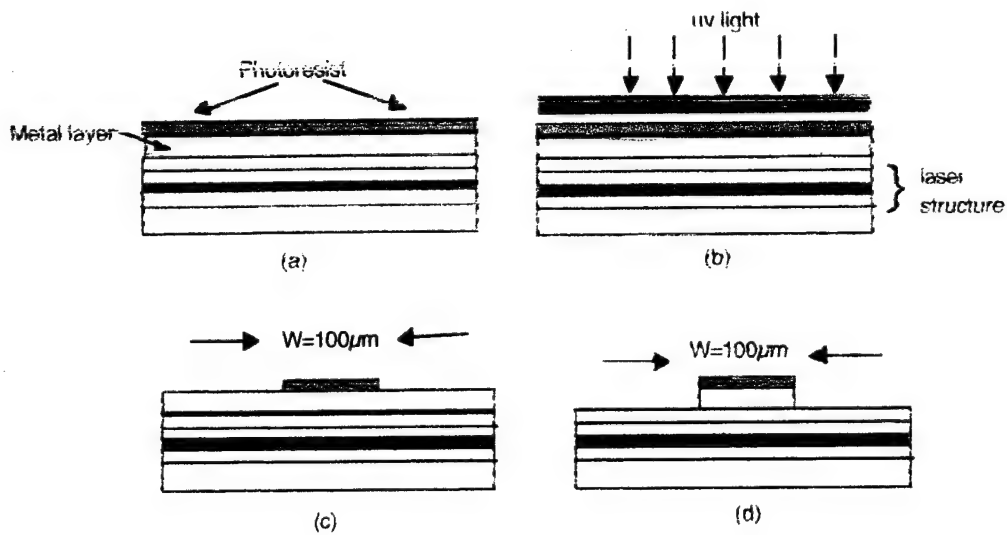


Figure 3.5 Photolithography steps used in processing broad-area lasers. (a) resist applied to metal layer, (b) expose  $100\mu\text{m}$  pattern onto resist, (c) develop resist and obtain  $100\mu\text{m}$  resist, and (d) etch away metal layer and GaAs cap layer.

e) Annealing of  $p^+$  contacts

The alloy formation of Au/AuZn/Au to the p-GaAs layer is accomplished by a heat treatment of 440°C - 448°C for approximately two to three minutes in controllable forming gas ambient of 10%  $H_2$ - $N_2$ . To obtain ohmic properties and low contact resistance values, it is necessary to alloy such contacts at high temperatures above 400°C. The alloy treatment is required to form a metallurgical bond between the metal and the semiconductor material, thus forming an ohmic contact. During this heat treatment of contacts, a strong interaction between the AuZn and the semiconductor interface exist. The amount of such interactions cannot be accounted at this time. Due to the amount of high controllability of the metal composition and good adhesion of Au/AuZn/Au, the contact resistance is reproducible in the present method. Once the  $p^+$ - contacts are annealed, the wafers are prepared for lapping and polishing.

f) Lapping/Polishing of  $N^+$ -GaAs substrates

Once the photolithographic sequence is completed, the laser wafers are ready to be thinned down to 100 $\mu$ m in thickness. The technique used for the thinning of GaAs substrates is called lapping/polishing. The primary factor in lapping/polishing the  $n^+$ -GaAs substrate is to make the cleavage of laser bars more feasible, since the initial thickness of GaAs substrate are generally 400 $\mu$ m to 500 $\mu$ m. Prior to the preparation of lapping/polishing, the wafers are covered with a protective layer of photoresist onto the  $p^+$  GaAs contact to prevent any buildup of contaminants that occurs during this stage of processing. Figure 3.6 is an example of buildup contaminants that occurs if the protective photoresist is not used after polishing.



Figure 3.6 The effect of buildup contaminants and wax residue when photoresist layer is not used prior to polishing.

After depositing a layer of photoresist, the wafer are bonded p-side down onto a glass substrate (83mm diameter x 6mm nominal thickness) by an excess of wax. All excess wax should be scraped away from around the edges of the wafer and the glass substrate. It is of the utmost importance for the operation of lapping/polishing to ensure that all traces of exposed wax have been removed from the wafer/glass substrate assembly. There is the risk, once lapping/polishing has begun, any remaining wax might gather together to form a wax ball which could badly damage the surface of the wafer if it were to pass between the wafer and the surface of the glass lapping/polishing plate. Figure 3.7 is an example of how a wafer is bonded to a glass substrate

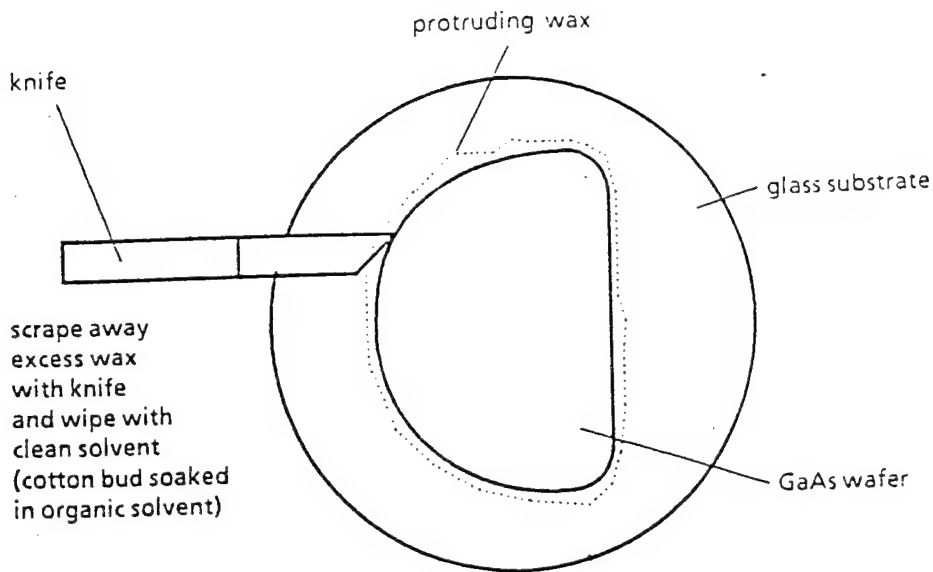


Figure 3.7 Wafer/glass substrate assembly prior to lapping/ polishing procedure.

The glass substrate along with the bonded wafers are then mounted onto a vacuum jig apparatus. The jig apparatus has the facility of increasing or decreasing the amount of load to be applied when lapping/polishing. The jig apparatus is then placed onto a glass lapping plate, however, before placing the jig and wafer/glass substrate assembly on the glass lapping plate, ensure that the surface of the plate is free from accumulation of dried aluminum oxide abrasive powder. The simplest way to remove this is to spray or rinse the surface of the plate with deionized water.

Place the jig on the glass lapping plate, as shown in Figure 3.8, and rotate the plate slowly (10 rpm) using the speed control knob so that the jig describes ten complete revolutions. The purpose of this is to thin down all the wafers evenly.

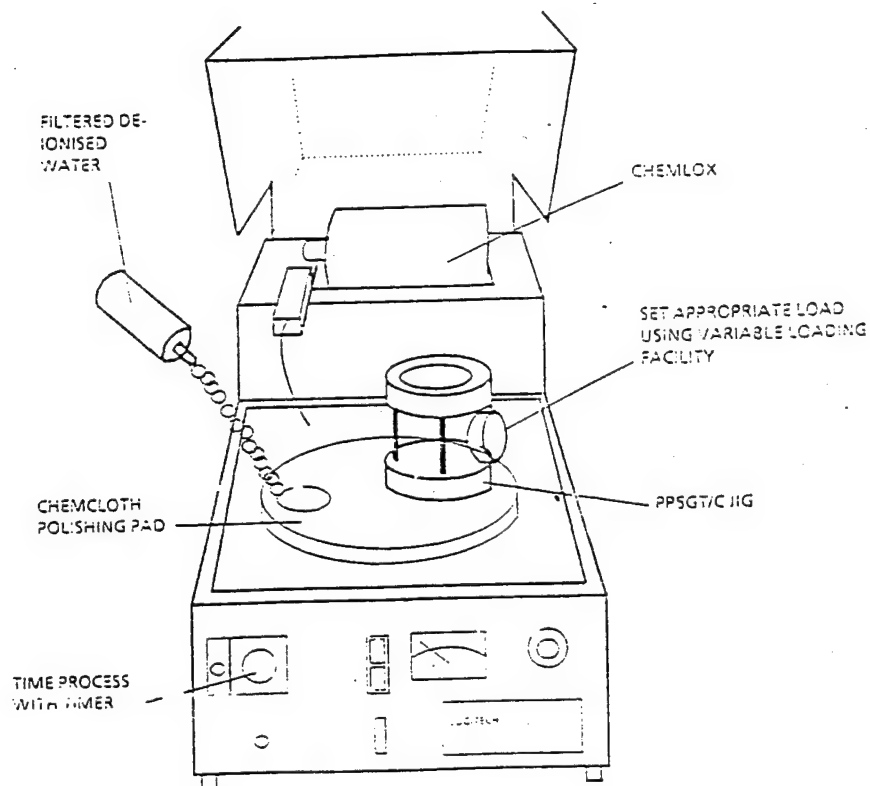


Figure 3.8 Lapping/polishing machine.

The lapping procedure can begin by setting the rotational glass plate to 10 rpm to lap the entire GaAs substrate surface uniformly and to adjust the jig apparatus at low pressure. In order lap the GaAs substrate, a  $3\ \mu\text{m}$  (abrasive size) solution of aluminum oxide abrasive powder is used. The lapping speed can then be increased to 40 rpm, and the jig pressure can be increased slightly to obtain a lapping rate of  $2.0\ \mu\text{m}/\text{min}$ . The lapped wafer is subjected to a visual and thickness examination to ensure that a satisfactory lapped have been achieved. This inspection can be made every 10 or 15 minutes. Once the

lapped wafer reaches a thickness of  $130\text{ }\mu\text{m}$ , the polishing stage is then proceeded by replacing the aluminum oxide abrasive powder from  $3.0\text{ }\mu\text{m}$  to  $0.3\text{ }\mu\text{m}$  granite and replacing the lapping glass plate with a polishing cloth plate. The polishing stage is to further reduce the GaAs substrate thickness down to  $100\text{ }\mu\text{m}$ , and to obtain a final mirror surface. Before moving on to the polishing stage of the process, it is of the utmost importance to ensure that all traces of  $3\text{ }\mu\text{m}$  abrasive have been removed from the wafer/glass substrate assembly, as this might cause considerable surface damage during polishing. A suitable method of achieving this is to wipe the entire glass plate with trichloroethylene or alcohol. As before, adjust the variable pressure jig to the desired setting and mount the jig assembly onto the lapping/polishing machine.

The polishing process is also sensitive to both the polishing rate and the pressure applied to the substrate. Excessive pressure or a high polishing rate will cause damage to the GaAs in the form of dislocations which may propagate into the active region of the laser device during operation and cause premature failure. Proper and improper polishing effects are shown in Figure 3.9 and Figure 3.10. Figure 3.9 is an example of a laser sample, which is polished at 50 rpm and a relatively high pressure. The amount of high pressure and speed can result in defects on the GaAs surface. Several tests can be done to find an appropriate setting to eliminate these defects. The polishing speed for these lasers is 30 rpm to 40 rpm with a jig pressure relative to a polishing rate of  $0.08\text{ }\mu\text{m}$  to  $1.0\text{ }\mu\text{m}/\text{min}$ . Further reduction in speed is sometimes necessary when the thickness is about  $118\text{ }\mu\text{m}$ . Figure 3.10 is an example of a polished  $100\text{ }\mu\text{m}$   $n^+$ - substrate. The wafer thickness should be  $100\text{ }\mu\text{m}$ -thick to cleave the wafer into laser bars.

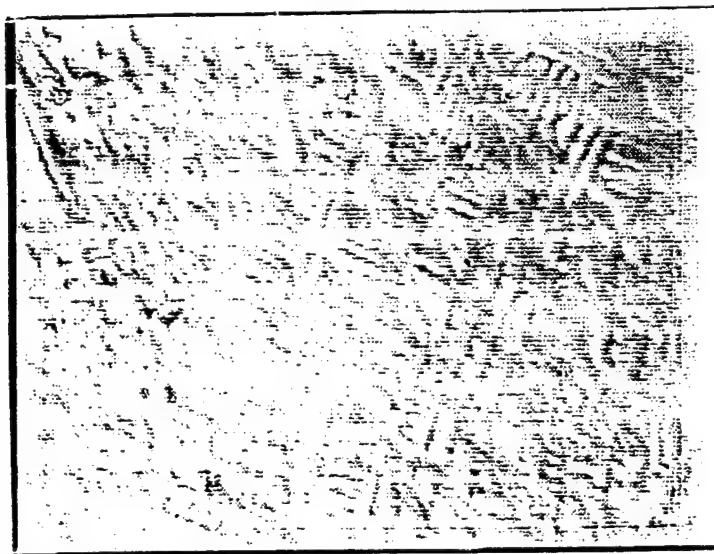
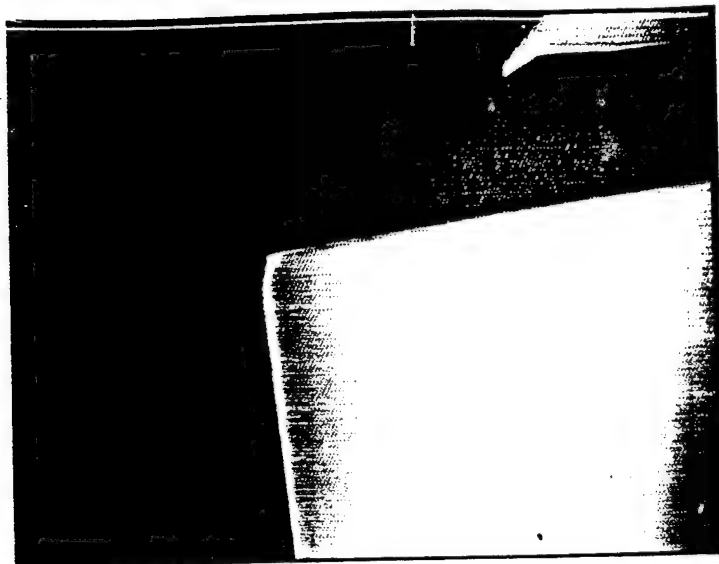
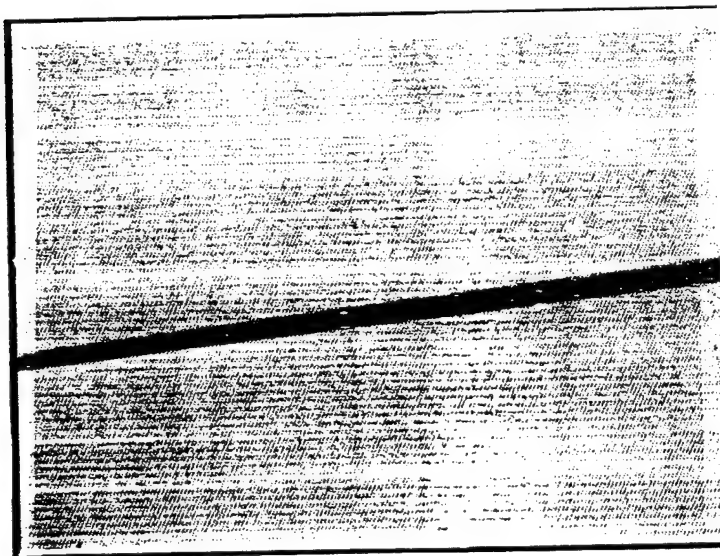


Figure 3.9 Strained surface due to improper polishing of  $n^+$  substrate.



(a)



(b)

Figure 3.10 (a) Lapping and polishing of a  $100\mu\text{m}$ -thick  $n^+$ -GaAs substrate.

### g) Evaporation and Annealing of $n^+$ Contacts

The last processing sequence for the broad-area lasers is the evaporation and the annealing of the  $n^+$  contacts. The  $n^+$  GaAs ohmic contact can be accomplished by utilizing AuGe/Ni/Au. The selected ohmic contacts are required to form low contact resistance, to improve the wettability of the substrate surface, and to provide better adherent to the bonding of indium heatsinks. The deposition of these multilayer film is accomplished by the same format as the deposition of  $p^+$  contacts, that is, with an electron-beam evaporator. The film deposition for the  $n^+$  GaAs layer contacts are as follows: AuGe(700-800Å)/Ni(350-380 Å)/Au(18000-2300Å). The alloying procedure is carried out in a flowing 10%  $H_2$ - $N_2$  ambient at 400°C for approximately one minute. The incorporation of nickel alloy to the AuGe and Au is to enhance the diffusion of germanium and gold into the lattice. An appreciable improvement of the contact resistance between the  $p^+$  and  $n^+$  GaAs has been achieved by adopting a Au/AuZn/Au and AuGe/Ni/Au multilayer structure, respectively. Thus, achieving a series resistance of 0.01  $\Omega$  and 0.03 $\Omega$  for TiPt/Au and AuZn/Au, respectively as shown in Figure 3.11.

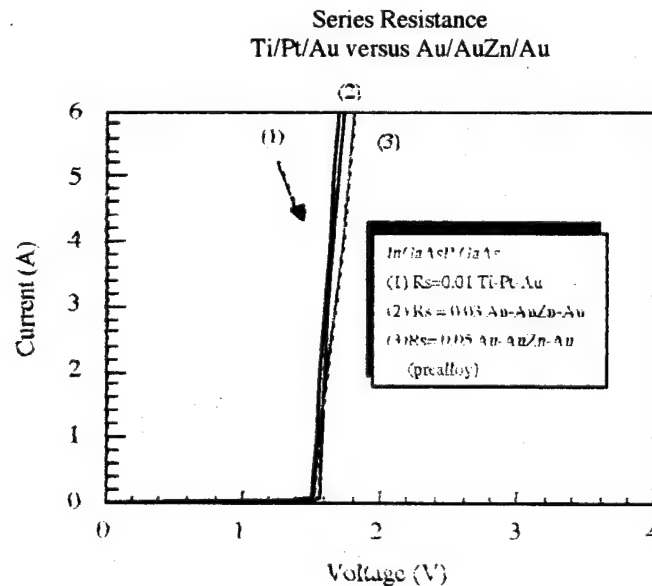
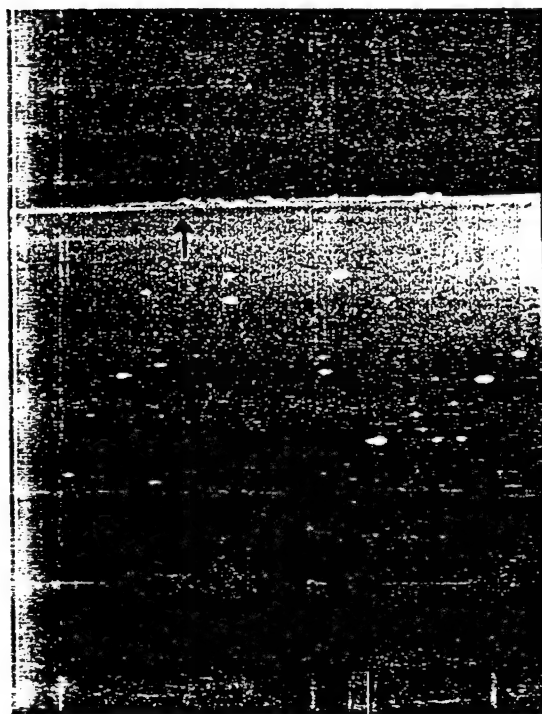
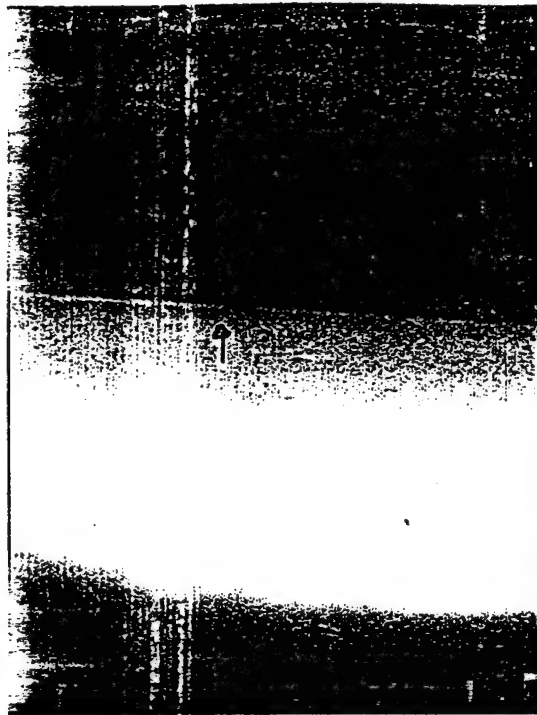


Figure 3.11 Series resistance of 0.01 $\Omega$  (TiPt/Au) and 0.03 $\Omega$  (AuZn/Au) for 808nm laser diodes.

The final stages of laser processing is the deposition of a Schottky Au contact (1000Å of Au) onto the  $p^+$  contact in order to form a current-blocking Schottky barrier outside the 100  $\mu\text{m}$  stripes. The additional Schottky barrier permits suitable laser diodes to be bonded p-side on indium-coated copper heatsinks to sustain high current measurements. The deposition of the Schottky Au thickness have been optimized considerably from 2000 Å to 1000 Å to reduce the effect of Au overlapping onto the epitaxial layer. This Au overlapping is created when the wafers are cleaved into laser bars which can lead to device leakages when the laser die are bonded p-side down, this can be seen in Figure 3.12..



(a)



(b)

Figure 3.12 (a) The effect of Au overlap onto the epitaxial layer with 2000Å of Schottky Au over the p-side after cleaving the wafers into laser bars, and (b) no Au overlap with 1000Å of Schottky Au after cleaving.

#### h) Cleaving of Laser Bars

A semiconductor laser diode consists of a stripe contact of width  $W$ , and two cleaved mirrors of cavity length  $L$ . These cleaved mirrors are formed by scribing lines at the edge of the laser wafer (perpendicular to the stripe contacts) with a diamond tip scriber system. Once the scribe lines are induced, an amount of pressure is applied to the wafer causing the semiconductor crystal to cleave along its cleavage plane. The laser bars should be cleaved perfectly to obtain good mirrors as shown in Figure 3.13.



(a)



(b)

Figure 3.13 (a) Laser bar of cavity length,  $L$ , and (b) Cleaved mirror.

### i) Bonding of Laser Diodes

The bonding of laser diodes is very critical for high power operation. The removal of excess heat from a laser diode is done by mounting a laser die onto a indium coated copper heatsink as shown in Figure 3.14.

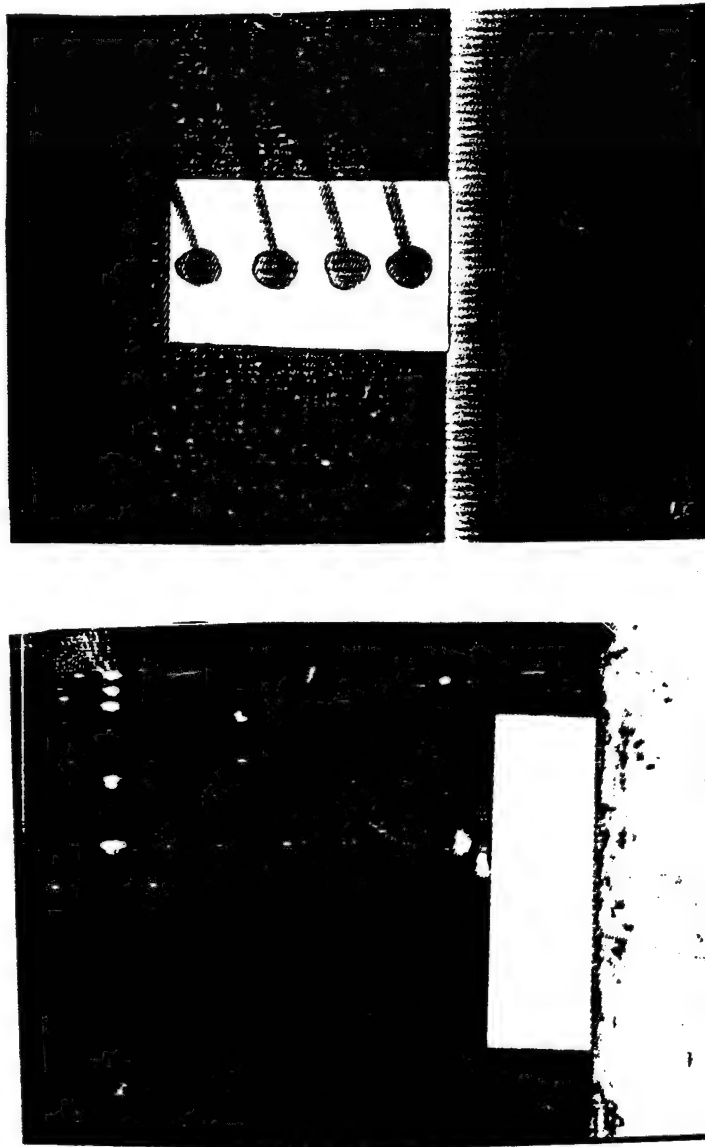


Figure 13.4 Mounting of a p-side laser diode on indium coated copper heatsink.

The process mounting a laser die onto a heatsink consists of the following:

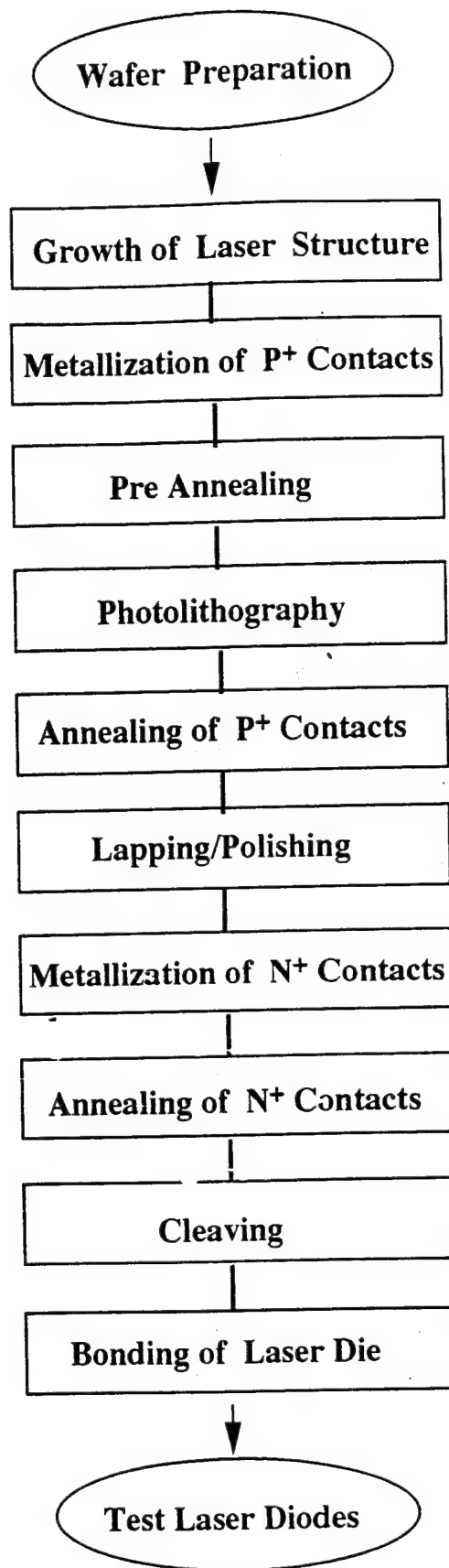
1. Select suitable laser die with no defects on the  $p^+$  and  $n^+$  contacts.
2. Lift the laser die by a vacuum tip.
3. Position the laser die at the edge of the heatsink, and slowly position the laser die onto the indium film.
4. Apply heat to the copper heatsink. The melting point of indium is  $150^{\circ}\text{C}$ .
5. Remove bonded laser, when melting and freezing of indium is completed. This can be visual observed through a microscope.

When bonding laser diodes onto a indium coated copper heatsink, leakages may arise, especially when mounting the diodes p-side down. These leakages are caused by three factors and there are:

1. Cleaving defects in the corners of the dies
2. Au overlap on the epitaxial layer
3. Indium whiskers at the edge of the heatsink

These three factors can be eliminated by: (1) scribing the laser die toward the central part of the laser bar; (2) reducing the Schottky film from  $2000\text{\AA}$  to  $1000\text{\AA}$  -thick; and (3) reducing the indium thickness from  $3\text{ }\mu\text{m}$  to  $2.0\text{ }\mu\text{m}$  and applying high nitrogen pressure to the heatsink. Using proper techniques, the laser diode can perform excellent during high power measurements.

The complete fabrication sequence for  $0.808\mu\text{m}$  InGaAsP/GaAs lasers is summarized in Figure 13.5.



*CHAPTER IV*

*LASER DIODE CHARACTERIZATION*

## Table of Contents

<b>Introduction</b>	2
• MOCVD-grown InGaP/GaAs heterostructures	3
• InGaAs/InGaP/GaAs 0.98 $\mu\text{m}$ lasers	4
• Conclusion	4
 <b>Section 1. Studies of the radiative efficiency of 0.8 <math>\mu\text{m}</math> InGaAsP laser material</b>	 6
• 1.1. Studies of spontaneous emission in double heterostructure laser diodes	6
• Calculation of maximum absolute value of external efficiency of spontaneous emission ( $\eta_e$ ) for double heterostructure	7
• Analysis of internal efficiency dependencies on injection current and temperature	8
• Experiments on Double Heterostructure Laser Diodes	10
• 1.2 Studies of spontaneous emission in separate confinement heterostructure laser diodes	16
• Calculation of maximum absolute value of external efficiency of spontaneous emission ( $\eta_e$ ) for separate confinement heterostructure	16
• Spontaneous emission measurements	17
• 1.3 Conclusions	20
 <b>Section 2. Uniformity of MOCVD-grown InGaAsP/GaAs heterostructures</b>	 21
 <b>Section 3. Optimization of laser structure parameters</b>	 30
• 3.1 Effect of active region thickness	30
• 3.2 Effect of waveguide-cladding layer bandgap discontinuity	37
• 3.3 Transverse far-field measurements and effect of waveguide thickness	41
• 3.4 Lateral far-field measurements	49
• 3.5 Effect of number of quantum wells in MQW lasers	55

This report summarizes the results of experimental research work on laser characterization performed at the Center for Quantum Devices under ARPA/US Army contract #DAAH 04-93-G-0044 "InGaAsP Diode Laser for Nd:YAG pumping". The introduction gives a background information about relevant laser materials and devices based on previous research. Section 1 describes the first stage of experiments aimed at the evaluation of the radiative properties of MOCVD-grown InGaAsP materials and laser heterostructures. Section 2 presents experimental data on the uniformity of MOCVD-grown laser structures obtained from the spectra of broad-area lasers. Section 3 gives an extensive overview of the experimental optimization of laser structure parameters. High-power operation and reliability data are the subject of Section 4. Finally, Section 5 gives a conclusion and underscores the results of laser measurements.

## **Introduction**

High-power diode lasers emitting in the wavelength range of  $0.8\mu\text{m}$  are of great importance as a pumping light source for solid state lasers [1]. AlGaAs/GaAs material system used conventionally for fabrication of  $0.8\mu\text{m}$  laser diodes is attractive due to the close lattice match between AlGaAs ternary compounds and GaAs substrate; considerable progress has been achieved during last decade in the fabrication of high-power  $0.8\mu\text{m}$  AlGaAs/GaAs lasers [2]. At the same time, strong evidence has been accumulating which argued that aluminum-free indium-containing InGaP, InGaAs and InGaAsP compounds had a number of advantages for the fabrication of high-power laser diodes. Those advantages mainly stem from the following features of this material system:

- The absence of easily oxidized Al-containing compounds allows lower growth temperature and facilitates post-growth processing and re-growth of etched mesas for buried structures and corrugation gratings. Additionally, a wide range of selective etchants exists for InGaAsP materials, further simplifying the laser fabrication;

- Al-free In-bearing materials demonstrate a resistance to dark line defect formation at high optical densities which slows gradual degradation dramatically thus increasing the operation lifetime;
- Low surface and interface recombination rates decrease nonradiative current leakage and reduces mirror facet overheating responsible for catastrophic optical damage (COD).

Potential of Al-free materials for higher device reliability and simplified processing has been confirmed by the results obtained on InGaAs/InGaP/GaAs 0.98  $\mu\text{m}$  lasers and LPE-grown InGaAsP/InGaP/GaAs 0.8  $\mu\text{m}$  lasers. Studies of MOCVD-grown GaAs-GaInP heterojunctions, quantum wells and superlattices exposed a capability of this growth technique to produce high-quality heterostructures suitable for optoelectronic device fabrication.

### **MOCVD-grown InGaP/GaAs heterostructures**

The advantages of Al-free material as well as the applicability of MOCVD growth technique for its preparation has been confirmed by the studies of GaAs/InGaP heterostructures, quantum wells and superlattices grown by low-pressure MOCVD [3-8]. Extremely high electron mobility of 780 000  $\text{cm}^2/(\text{Vs})$  due to high purity of the material has been demonstrated in GaAs/InGaP heterostructure [3]. Another feature important for electronic device fabrication is a relatively high valence band offset ( $\Delta E_v/\Delta E_c=0.41$ ) [4] at InGaP/GaAs heterojunction by comparison with the known value for AlGaAs/GaAs ( $\Delta E_v/\Delta E_c=1.5$ ). This indicates that better confinement for holes exists at InGaP/GaAs heterointerface [5]. DLTS studies of InGaP layers showed the absence of DX centers known to be responsible for non-radiative recombination and dislocation growth in AlGaAs/GaAs structures [6].

Recent works on MOCVD-grown GaAs/InGaP quantum wells and superlattices [7,8] illustrate good interfaces and uniform layer thickness crucial for quantum well laser structures. These studies presented a strong evidence of potential use of MOCVD as the growth method capable of producing InGaAsP/InGaP/GaAs heterostructures for reliable 0.808 $\mu$ m high-power diode lasers.

### **InGaAs/InGaP/GaAs 0.98 $\mu$ m lasers**

Very high quality Al-free InGaAs/InGaP/GaAs 0.98 $\mu$ m broad stripe and buried ridge lasers has been fabricated by metalorganic chemical vapor deposition (MOCVD) and gas-source molecular beam epitaxy [9-17]. These lasers exhibit high internal quantum efficiency ( $>90\%$ , [13]), low internal waveguide losses ( $\sim 1\text{cm}^{-1}$ , [13]) and low threshold current densities ( $58\text{A/cm}^2$ , [15]). Continuous wave (CW) output power of 500 mW per facet has been achieved for 130  $\mu$ m -wide stripe with uncoated mirrors [10]. Buried ridge [12], ridge waveguide [14,17], and buried heterostructure [16] lasers have been fabricated recently demonstrating the ease of etching and re-growth advantageous for mass production purposes. The COD limit has been extended to  $16\text{MW/cm}^2$  in pulse operation and  $8\text{MW/cm}^2$  in CW for coated mirrors [17].

### **Conclusion**

The encouraging results of implementation of Al-free materials for laser applications and the demand for highly reliable pump sources for Nd:YAG lasers stimulated the studies of MOCVD-grown 0.8  $\mu$ m InGaAsP/InGaP/GaAs diode lasers performed at the Center for Quantum Devices and attracted the funding for the project aimed at MOCVD fabrication of high-power high-reliability 0.808  $\mu$ m InGaAsP/InGaP/GaAs diode lasers with CW output power of 1W per facet and CW operation lifetime at room temperature substantially better than that for commercial AlGaAs/GaAs lasers emitting at this wavelength. At the initial stage, main attention was focused on the investigation of

radiative recombination efficiency in the InGaAsP quaternary active regions of double heterostructure (DH) separate confinement heterostructure (SCH) laser diodes prepared by MOCVD in InGaAsP/GaAs Al-free material system. The subject is of special importance because there are published data arguing that non-radiative channels may give a considerable input into the total recombination rate in case of MBE [22] and MOCVD-grown [23] AlGaAs/GaAs structures.

## Section 1. Studies of the radiative efficiency of 0.8 $\mu\text{m}$ InGaAsP laser material

### 1.1 Studies of spontaneous emission in double heterostructure laser diodes

The first step of the investigation of parameters of MOCVD-grown 0.8 $\mu\text{m}$  InGaAsP/InGaP/GaAs lasers was the evaluation of the internal efficiency of spontaneous radiative recombination in their quaternary active region ( $\eta_i$ ). This value is one of the main factors determining threshold current density as can be seen from equation (1.1) where  $I_0$  is transparency current density, corresponding to zero gain,  $d$  is thickness of the active region,  $\beta$  is a factor relating optical gain  $g$  to the current density as  $g=\beta(I-I_0)$  (for linear region),  $\Gamma$  is optical confinement factor indicating a fraction of optical wave propagating inside the active region,  $\alpha_i$  is internal optical loss in the structure, and  $R$  is reflection coefficient of a laser mirror.

$$I_{th} = \frac{I_0 d}{\eta_i} + \frac{d}{\eta_i \Gamma \beta} \left( \alpha_i + \frac{1}{L} \ln \frac{1}{R} \right) \quad (1.1).$$

Value of  $\eta_i$  represents a fraction of injected carriers that recombine emitting a photon and may be expressed through radiative and non-radiative lifetimes  $\tau_r$  and  $\tau_{nr}$  as  $\eta_i = \tau_{nr} / (\tau_r + \tau_{nr})$ .

A direct estimate of the absolute value of  $\eta_i$  from experimental measurements of external efficiency of emission through the laser mirror ( $\eta_e$ ) is prevented by self-absorption of the emitted radiation in the active region (absorption coefficient  $\alpha(E)$  varies from  $5 \times 10^3 \text{ cm}^{-1}$  to  $10 \text{ cm}^{-1}$  in the range of wavelengths corresponding to the spontaneous emission spectrum). This process is especially intense in DH lasers where major part of the radiation is propagating through the absorbing material of the active region. A possibility of re-radiation further precludes direct assessment of the data on  $\eta_i$ . However, it was

important to make this calculation for double heterostructure and compare the obtained rough upper estimate with experimental values.

### Calculation of maximum absolute value of external efficiency of spontaneous emission ( $\eta_e$ ) for double heterostructure

The following estimation of the fraction of spontaneously emitted radiation that can be coupled out from mirror facet of a short-cavity DH laser diode is made under several simplifying assumptions:

- angular distribution of spontaneous emission is spherically isotropic;
- only the radiation totally reflected from cladding layers is propagating in the active region (waveguide);
- the radiation is propagating in the waveguide without self-absorption or internal losses.

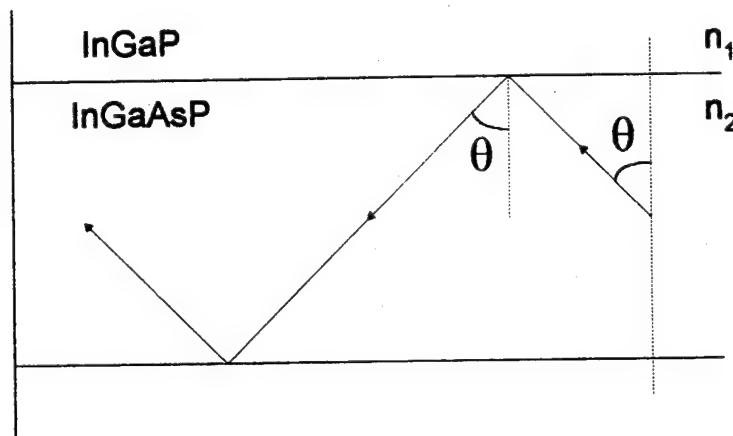


Fig. 1.1. Waveguide geometry model used for the calculation of the coupling efficiency of spontaneous emission.

The configuration of the model waveguide is shown in Figure 1.1. The angle of incidence of the emitted ray on the waveguide boundary is given as  $\theta$ . Total reflection from the interface occurs under condition:

$$\theta_i < \theta < \pi - \theta_i \quad (1.2),$$

where the angle of total reflection may be calculated from the refractive indices  $n_1$  for cladding InGaP and  $n_2$  for InGaAsP ( $E_g \sim 1.55\text{eV}$ ) as

$$\theta_i = \arcsin n_1/n_2 \quad (1.3)$$

Transmission factor  $T$  for the mirror facet should be also taken into account as given in [24a]:

$$T = \left( \frac{2}{n_2 + 1} \right)^2 \quad (1.4).$$

Combining (1.3) and (1.4) we can now obtain the relation between  $\eta_e$  and  $\eta_i$  as

$$\eta_e = \frac{4 \eta_i}{\pi} \frac{1}{(n_2 + 1)^2} \sqrt{\frac{2 \Delta n}{n_2}} \quad (1.5).$$

With the values of refractive indices for the active and cladding layers taken from [24b] as  $n_1=3.38$ ,  $n_2=3.61$ ; (1.5) gives  $\eta_e \sim 0.017\eta_i$ , which means that for 100% internal radiative efficiency in the active region, maximum external efficiency of spontaneous radiation is  $\sim 1.7\%$  in the absence of self-absorption and internal optical losses. As mentioned before, this result should be viewed as a rough upper estimate, since the effect of self-absorption in the active region is considerable even for very short cavity diodes.

### **Analysis of internal efficiency dependencies on injection current and temperature**

Qualitative data on the internal efficiency of spontaneous emission may be obtained through measurements of the radiation coupled out in the growth direction [25]. The laser

diode structure used in this experiment provides an opportunity to perform this kind of experiments since the heavily doped GaAs contact layer between the stripes is removed. The radiation emitted through the structure surface does not undergo self-absorption in the active region and measured values of external efficiency  $\eta_e$  should be directly proportional to the internal efficiency  $\eta_i$ .

Total rate of spontaneous recombination through both radiative and non-radiative channels as a function of excess carrier concentration ( $n$ ) is given by

$$R_{\text{spont}} = -dn/dt = An + Bn^2 \quad (1.6),$$

where  $A=1/\tau_{nr}$  and  $B$  is a band-to-band radiative recombination constant of the material. In the absence of current leakage from the active region total recombination rate is equal to the carrier injection rate  $I = dn/dt$  under steady-state conditions. Internal efficiency of spontaneous recombination may be calculated as a function of  $I$ :

$$\eta_i = 1 - \frac{A^2}{2BI} \left( \sqrt{1 + \frac{4BI}{A^2}} - 1 \right) \quad (1.7).$$

$I$  is related to the current density  $J$  (A/cm<sup>2</sup>) as  $I=J/qd$ , where  $q$  is elementary charge. As can be seen from (1.7), at high currents ( $I \gg A^2/2B$ ),  $\eta_i$  is close to unity and spontaneous radiation intensity grows linearly with current. At low currents, however, this dependence may be linear only in the absence of non-radiative recombination channels, that is for  $\eta_i=100\%$ . In the opposite case a competition of two channels takes place leading to superlinear light-current characteristic and varying external efficiency.

Equation (1.7) is also helpful to understand the temperature dependence of  $\eta_i$ . Radiative recombination rate decreases with temperature as  $T^{-3/2}$  [26] while non-radiative recombination normally increases. As a result, in a presence of significant non-radiative

recombination at room temperature  $\eta_i$  should rise substantially under cooling as non-radiative channel is suppressed. On the contrary, for  $\eta_i=100\%$  when all the injected carriers already recombine radiatively,  $\eta_i$  should hardly change with temperature.

In conclusion, the observation of spontaneous emission emitted through the structure surface as a function of injection current and temperature provides a tool for evaluation of the comparative contribution of radiative and non-radiative processes to the total recombination rate. These data, together with the results on the absolute value of  $\eta_i$  calculated through eq. 1.5 may give a conclusive estimate of the radiative quality of InGaAsP material of the active region.

### **Experiments on Double Heterostructure Laser Diodes**

Integrating sphere with silicon photodetector was utilized for the measurements of light-current characteristics of the DH laser diodes fabricated as described above under pulse operation and in continuous wave regime. Figure 1.2 shows a schematic of the experimental setup. For each structure, several laser diodes with cavity length varying from 300 $\mu\text{m}$  to 1.5mm were mounted n-side down on copper heatsinks and tested for threshold currents under pulse operation. Using  $\sim 1\text{mm}$ -long mounted laser diodes, spontaneous emission as a function of current and temperature was measured in the direction perpendicular to the structure plane. Major part of the radiation is absorbed in stripe contact metallization but even visible component of the part emitted from the surface outside the stripes is intense enough to be seen as red light. Stable 100 $\mu\text{m}$ -wide near field recorded by CCD camera shows the absence of current spreading from stripe contact. In addition, several short-cavity diodes ( $L=100\text{-}200\mu\text{m}$ ) were mounted n-side down for the measurement of spontaneous radiation coupled out through one of the laser diode mirrors.

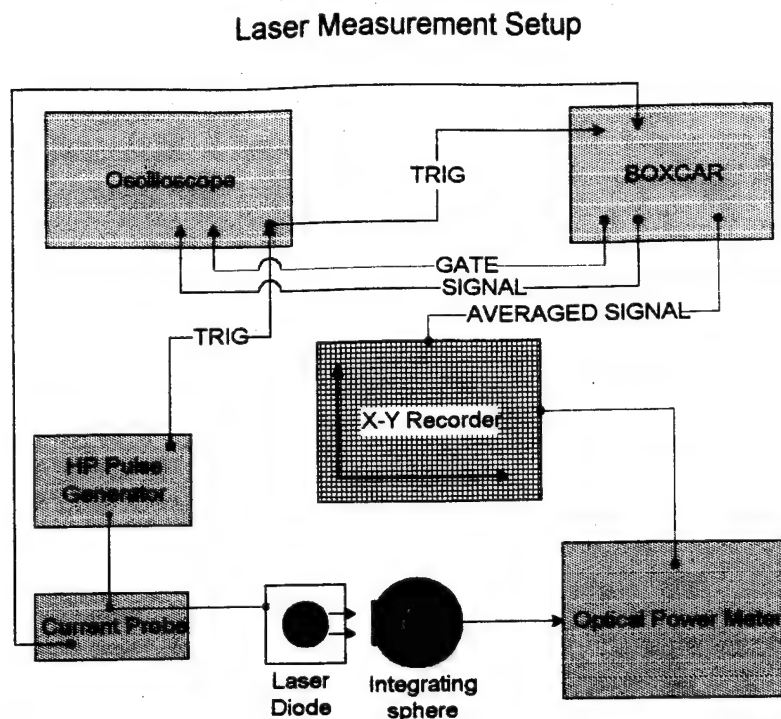


Fig. 1.2. Experimental setup for room-temperature laser measurements.

Figure 1.3 presents the current dependence of efficiency of spontaneous emission from the top surface of 0.9mm-long laser measured up to the pulse current density corresponding to the threshold for this cavity length. According to the data of electrochemical capacitance-voltage profiling (POLARON) shown in Figure 1.4, background carrier concentration in undoped active region is  $\sim 4 \times 10^{16} \text{ cm}^{-3}$ , while excess carrier concentration at threshold is known to be  $\sim 10^{18} \text{ cm}^{-3}$ . This implies that at the current densities approaching the threshold excess carriers are injected at the level well above the background and radiative recombination may be considered as a bimolecular process. Despite this fact, the efficiency plotted in Fig. 1.3 is nearly constant within the range of current below threshold. After the results of analysis presented earlier, this behavior indicates that radiative recombination is the dominant process and nonradiative channels do not give any considerable contribution to the total rate of recombination in the active region. In this case, a weak temperature dependence for spontaneous radiation output may be expected, as was discussed above.

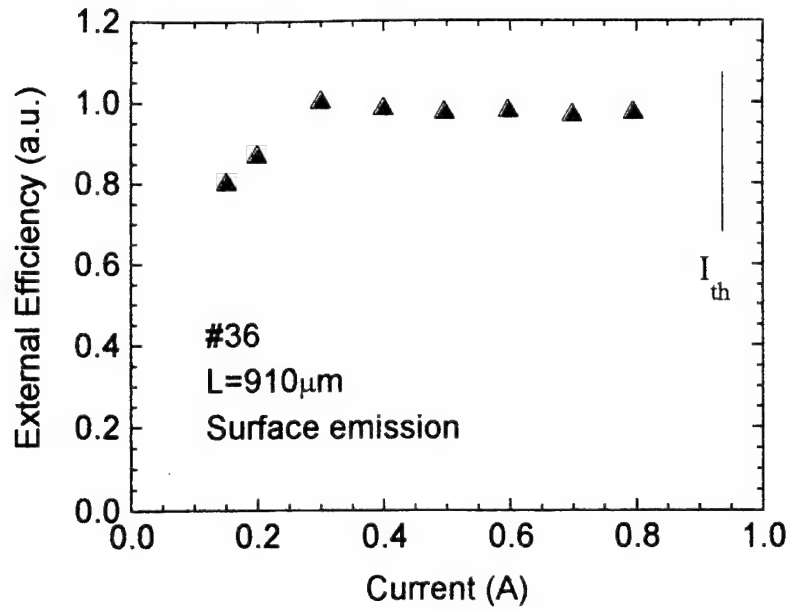


Fig. 1.3. Efficiency of spontaneous emission vs injection current for InGaAsP/GaAs double heterostructure laser. Radiation coupled out from the surface of the laser chip.

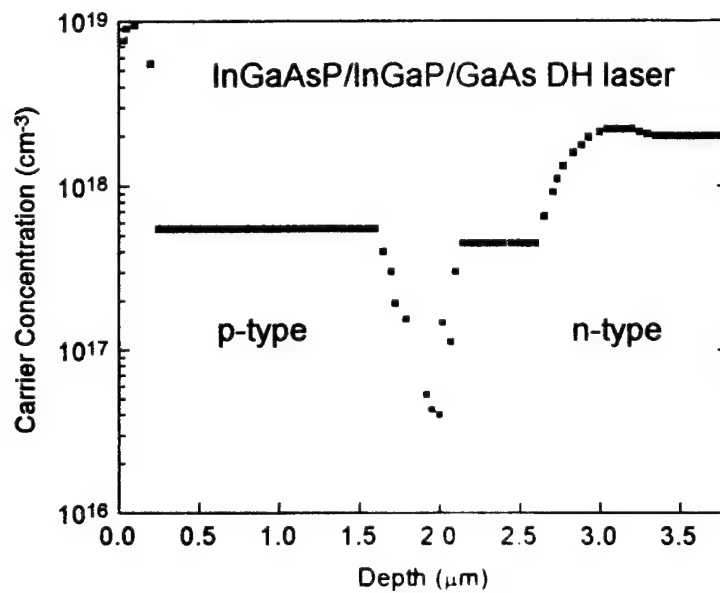


Fig. 1.4. Typical C-V profile of InGaAsP/GaAs double heterostructure laser.

Figure 1.5 shows the temperature dependence of spontaneous emission coupled out perpendicular to the structure plane under CW current density of  $300\text{A/cm}^2$ . A 1mm-long sample mounted on heatsink was fixed inside the Janis VPR-1 liquid nitrogen cryostat in order to obtain the low-temperature part of this characteristic. Emission output varies by less than 25% per 100K temperature change, becoming constant below 300K. Following the qualitative estimate based on eq. 1.7, this weak dependence confirms that at 300K the spontaneous internal efficiency is close to 100% for our InGaAsP/GaAs diodes.

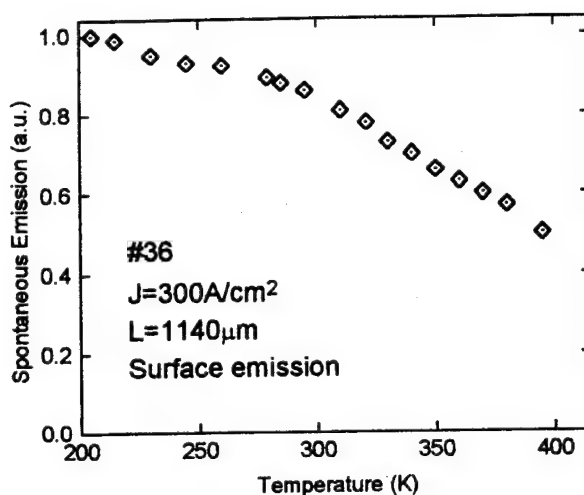


Fig. 1.5. Temperature dependence of spontaneous emission for InGaAsP/GaAs double heterostructure laser.

Figure 1.6 presents the results of measurement of absolute value of  $\eta_e$  for radiation coupled out through the mirror of a very short diode with cavity length of  $\sim 110\mu\text{m}$ . A value of  $\eta_e=0.45\%$  remains constant in the range of CW current density  $10\text{-}300\text{A/cm}^2$ . Slight saturation above this value may be attributed to thermal heating of the sample mounted n-side down and having relatively high series resistance. Our estimate showed that the maximum value of  $\eta_e$  is 1.7% for DH diodes with  $\eta_i\sim 100\%$  and negligible self-absorption. The absorption curve for the active region material is unknown, which prevented more accurate calculation. However, keeping in mind that for  $0.1\mu\text{m}$ -thick

active region self-absorption of radiation should be considerable even in very short diodes, it may be concluded that the observed value of  $\eta_e=0.45\%$  does not contradict to the condition of  $\eta_i\sim 100\%$ .

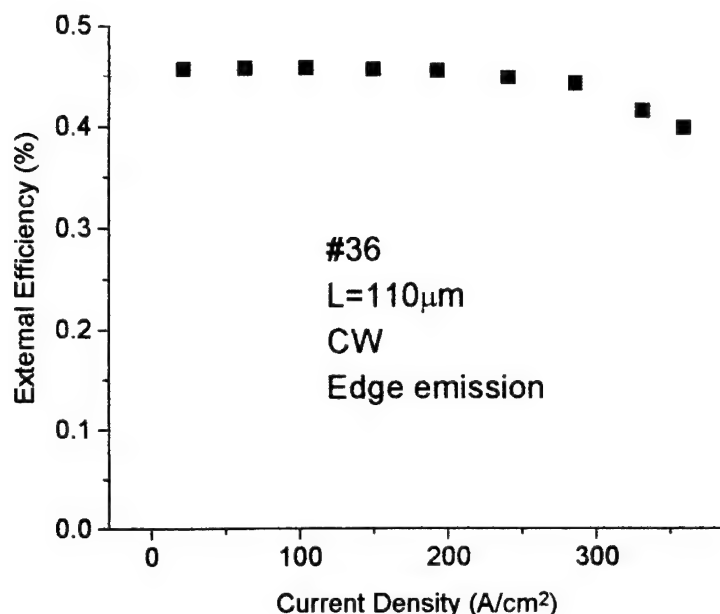


Fig. 1.6. Absolute value of external efficiency of spontaneous emission for short-cavity InGaAsP/GaAs double heterostructure laser.

The data on threshold current density for bonded and unbonded diodes with different cavity lengths prepared from two wafers (#36 and #43) are shown in Figure 1.7. Theoretical dependence of  $J_{th}$  on reciprocal cavity length from [27] is also given. The curve was calculated for a similar laser structure under the assumption of  $\eta_i\sim 100\%$  and the absence of internal losses. Energy-independent optical matrix element and conservation of momentum for radiative transitions were assumed in the calculation [27].

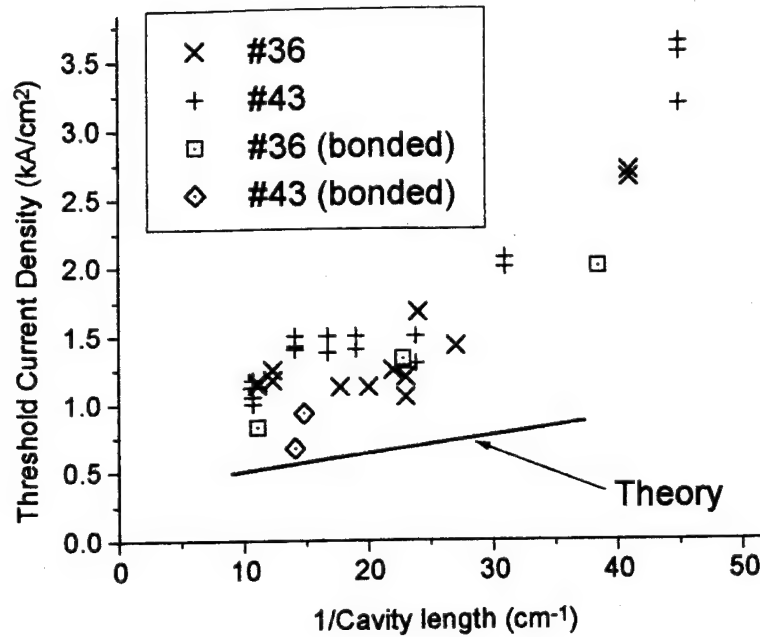


Fig. 1.7. Threshold current density vs reciprocal cavity length for InGaAsP/GaAs double heterostructure lasers.

As one can see in Figure 1.7, experimental data on threshold for long-cavity bonded diodes are slightly higher than the calculated values. We assume relatively high internal losses and/or spontaneous spectrum broadening to be the main reasons for this deviation. For laser diodes with  $L < 500 \mu\text{m}$ , rapid increase in  $J_{\text{th}}$  may be related to the carrier leakage from the active region due to relatively low confinement barrier. Nevertheless, the minimum values of  $J_{\text{th}} = 700 \text{ A/cm}^2$  obtained for long-cavity diodes are superior than the data published for both LPE-grown InGaAsP/GaAs DH diodes [28] and for AlGaAs diodes with the same energy band diagram [29].

In conclusion, we obtained the current and temperature dependencies of spontaneous radiation emitted through the surface of DH laser structure. Experimental data are in qualitative agreement with the speculations based on the analysis of rate equation and indicate that at room temperature and currents below threshold non-radiative recombination channels give only minor input in the total recombination rate.

Measurements of the absolute value of spontaneous external efficiency yield a lower value than theoretical estimate made under assumption of zero self-absorption. The difference is attributed to the fact that this assumption does not stand for 0.1 $\mu\text{m}$ -thick active region of the structure studied.

Results of our studies of spontaneous emission efficiency in DH laser diodes argue that at the current densities below 1kA/cm<sup>2</sup> almost all the injected carriers recombine radiatively in the 0.1 $\mu\text{m}$ -thick InGaAsP active region. This ensures the threshold current density for long-cavity double heterostructure laser diodes to be as low as 700 A/cm<sup>2</sup> which is better than the values for similar AlGaAs DH lasers and approaches the theoretical limit.

### **1.2 Studies of spontaneous emission in separate confinement heterostructure laser diodes**

#### **Calculation of maximum absolute value of external efficiency of spontaneous emission ( $\eta_e$ ) for separate confinement heterostructure**

An estimate of  $\eta_e$  as function of  $\eta_i$  in the absence of self-absorption and internal losses has been made in the previous section for double heterostructure and compared with experimental data. The observed discrepancy has been attributed to inherently high absorption of radiation in the thick active region ( $\alpha(E) \sim 5 \times 10^3 \text{cm}^{-1}$  to  $10 \text{cm}^{-1}$ ). On the contrary, in SCH-SQW (separate confinement heterostructure-single quantum well) structures active region is typically 10-20 times as thin as the waveguide layers and the effective value of  $\alpha(E)$  may be as low as 1 to  $100 \text{cm}^{-1}$ . The characteristic absorption length becomes comparable with cavity length of short laser diodes that can be fabricated (100-200 $\mu\text{m}$ ). In these diodes self-absorption may be considered negligible and theoretical estimation of  $\eta_e$  made under the same assumptions should be more accurate.

The waveguide geometry is still illustrated by Figure 1.1, but the refractive index of the waveguide should now correspond to the composition of InGaAsP optical confinement layers ( $E_g \sim 1.7\text{eV}$ ):  $n_2 = 3.50$ . Substitution of this value in equation (1.5) yields  $\eta_e = 0.016\eta_i$  and the maximum possible external efficiency of spontaneous emission is now 1.6% in case of non-absorbing waveguide.

### Spontaneous emission measurements

The studies of spontaneous emission of SCH laser diodes with 300Å-thick active region were performed with the same experimental setup as described in the previous section. Figure 1.8 shows a spectrum of spontaneous emission for one of the diodes. The absence of emission bands corresponding to shorter wavelengths demonstrates that only radiation originating in the active region is registered.

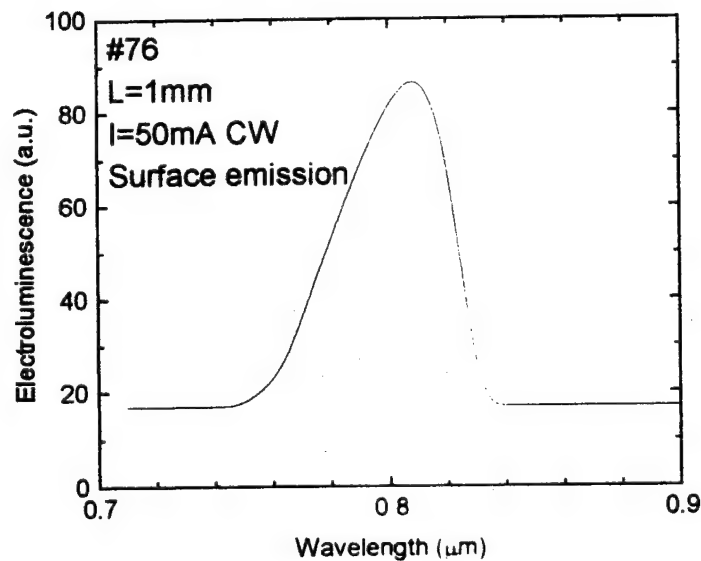


Fig. 1.8. Spontaneous emission spectrum for InGaAsP/GaAs separate confinement heterostructure laser. Radiation coupled out from the surface of the laser chip.

As discussed above, the external efficiency of spontaneous emission for very short-cavity SCH laser diodes may be expected to be close to the calculated maximum value. However, the absolute value of  $\eta_e$  measured for the radiation coupled out of one of the mirrors of 100 $\mu\text{m}$ -long SCH diode proved to be  $\sim 1.3\%$ , that is about 20% less than the calculated value of 1.6%. This difference may be explained by free-carrier absorption in highly doped InGaP cladding layers and residual self-absorption in 300 $\text{\AA}$ -thick active layer.

In order to determine whether this discrepancy can be explained by absorption in the structure, a dependence of external efficiency on cavity length has been investigated (Figure 1.9). With decreasing cavity length external efficiency grows sharply in 1mm cavity length range and stays nearly constant below  $L \sim 0.5\text{mm}$ . This behavior agrees well with the estimate of the effective absorption coefficient  $\alpha(E) \sim 10\text{--}100\text{cm}^{-1}$ . Extrapolation of the dependence for the shortest cavities shows that absorption loss is negligible and cannot be the reason for the observed 20% difference with the calculated values.

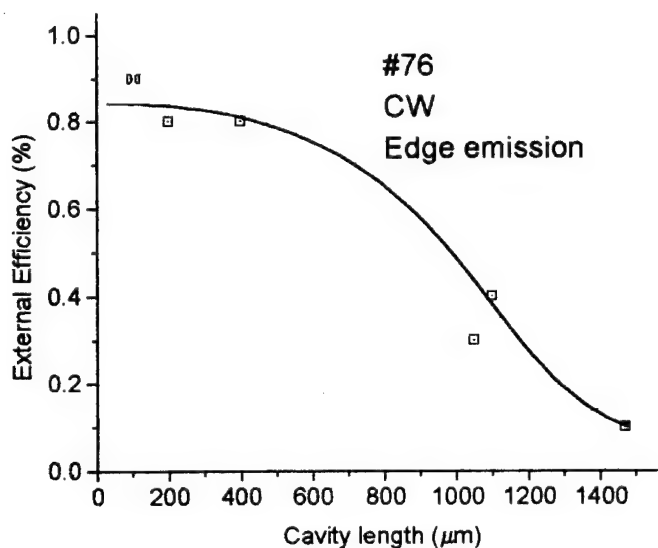


Fig. 1.9. External efficiency of spontaneous emission vs cavity length for InGaAsP/GaAs separate confinement heterostructure lasers.

Apart from the absorption effect, there may be two plausible explanations. One of them is a non-radiative recombination on the interfaces adjacent to the thin active layer. This assumption, however, does not concert with the experimental data on external efficiency versus current density, plotted in Figure 1.10. External efficiency is constant within a wide range of current densities confirming the absence of competing non-radiative recombination channel, as shown above. Another explanation is related to the inaccuracy of the estimate of  $\eta_e(\eta_i)$  made in the ray optics approximation which is accurate only for linear dimensions substantially exceeding the light wavelength. In our case when layer thicknesses are comparable or smaller than the wavelength, this approach yields only a rough estimate which may be responsible for somewhat lower values of  $\eta_e$  observed in the experiments.

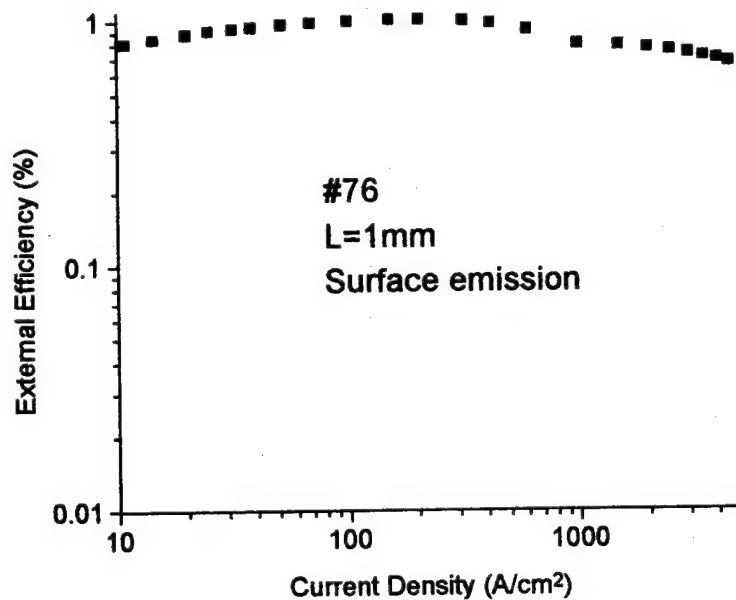


Fig. 1.10. External efficiency of spontaneous emission vs current density for InGaAsP/GaAs separate confinement heterostructure laser.

### **1.3 Conclusions**

Efficiency of spontaneous radiative recombination has been studied in double heterostructure laser diodes. Data on internal efficiency dependence on injection current density and temperature has been assessed from the measurements of radiation output in the direction perpendicular to the structure plane and compared with theoretical predictions based on rate equation analysis. External efficiency has been measured for the radiation coupled out of mirror facet of 0.1mm-long diode. Experimental value proved to be 0.45% compared to the maximum possible value of 1.7%. The difference between the experiment and theory is attributed to a strong self-absorption in the thick active region which was neglected in this calculation. A conclusion about near-100% internal efficiency of spontaneous recombination in the InGaAsP quaternary active region is confirmed by threshold current densities in these lasers being close to theoretical values and superior than those for LPE-grown or AlGaAs-based lasers of the same geometry.

Similar studies has been made on the external radiative efficiency in separate confinement heterostructure lasers. Validity of the assumption of negligible absorption for short-cavity SCH diodes has been confirmed by the study of external efficiency as a function of cavity length. The data on current density dependence of spontaneous emission from short diode argue for relative weakness of non-radiative channels in the range of threshold current densities for long-cavity lasers. This result confirms the applicability of MOCVD growth technique for the manufacturing of laser quality InGaAsP/GaAs heterostructures and provides a basis for further studies of structure uniformity and optimization of laser parameters.

## **Section 2. Uniformity of MOCVD-grown InGaAsP/GaAs heterostructures**

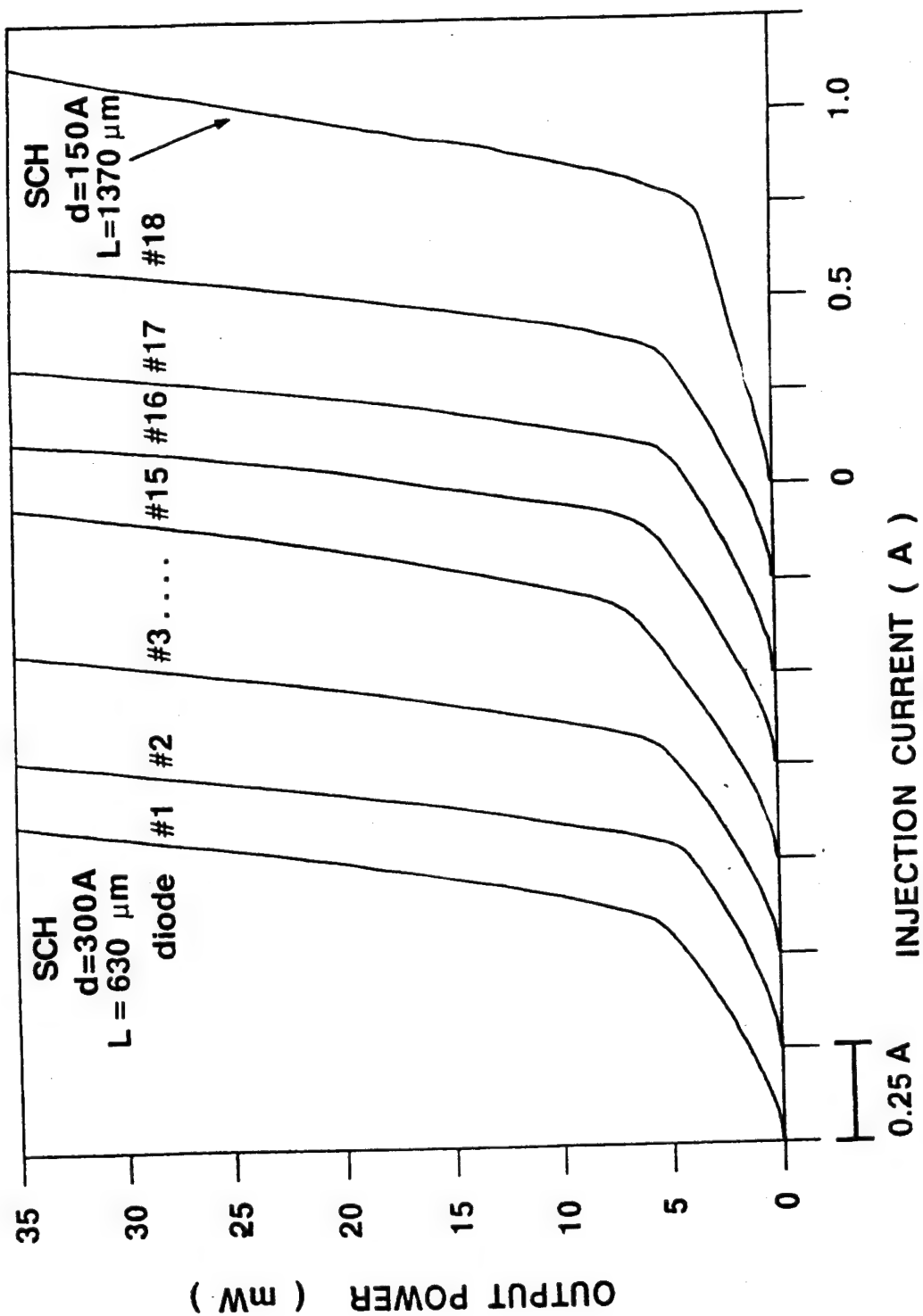
InGaP/InGaAsP/GaAs lasers with a 0.8 $\mu$ m emission wavelength were previously grown by liquid phase epitaxy (LPE) and it was shown that lasers had a number of benefits in comparison to conventional AlGaAs/GaAs devices [18, 28]. The most important of these are lower mirror facet temperature and resistance to dark line defect formation [18], promising a longer device lifetime when operating at high optical power densities. However, the LPE growth method has disadvantages for preparation of quantum-well structures which prevented the further development and application of LPE-grown InGaAsP/GaAs lasers. Inherent non-uniformity of LPE-grown layers is a major obstacle to systematic studies and optimization of laser structures, especially those with quantum-well active regions. At the same time, low-pressure metalorganic chemical vapor deposition (LP-MOCVD) [10,12] and gas-source molecular beam epitaxy [11,17] have been successfully used for epitaxial growth of highly uniform aluminum-free InGaAs/InGaP/GaAs laser structures and InGaP/GaAs superlattices for electronic devices [30]. Therefore, at this stage of the project, our attention was focused on the investigation of uniformity of the grown structures on the scale comparable to the laser dimensions (typically, 100 $\mu$ m-wide and 1mm-long), across the wafer as well as wafer-to-wafer reproducibility.

A rapid test of the wafer homogeneity could be made by recording light-current characteristics for various laser diode stripes along a cleaved bar. No mirror facet coating was applied to the diodes. Near-field patterns for bonded diodes were observed with the help of a CCD camera while an ADVANTEST Q8344A Optical Spectrum Analyzer was used to record emission spectra. The laser diodes were driven by current pulses with 50ns to 1ms width and 100Hz to 200kHz repetition rate during these measurements.

Measurements of I-V characteristics showed that these MOCVD-grown diodes have series resistance 2-3 times lower than high CW power LPE-grown InGaAsP/GaAs diodes [18] with a similar band diagram and geometry. The lowest value of series resistance was  $0.12\Omega$  for diodes with cavity length 1.37mm at currents higher than 300mA.

Figure 2.1 demonstrates the reproducibility of laser operation parameters for laser diodes with 300Å-thick active layer. The scatter of threshold current values did not exceed 5% for the 18 tested diodes of the same bar. Average threshold current density ( $J_{th}$ ) for diodes with cavity length  $L=0.63\text{mm}$  was  $0.80\text{kA/cm}^2$ . For laser diodes with a longer cavity length of  $L=1.1\text{mm}$  the value of  $J_{th}$  decreased to  $0.64\text{kA/cm}^2$ . Laser diodes with thin active region had a lower value of  $J_{th}$ ;  $0.47\text{kA/cm}^2$  for cavity length 1.37 mm (see Figure 2.1). The maximum value of differential efficiency ( $\eta_d$ ) for bonded diodes with the same cavity length was  $\sim 0.5\text{W/A}$  per two facets. Figure 2.1 shows pulse light-current characteristic of a bonded diode driven up to output power of 1.55W per facet.

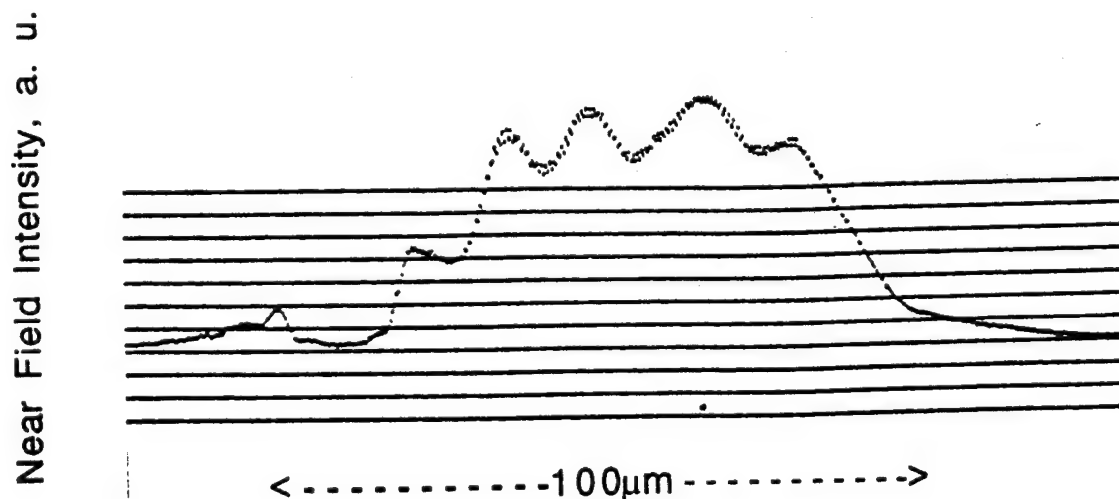
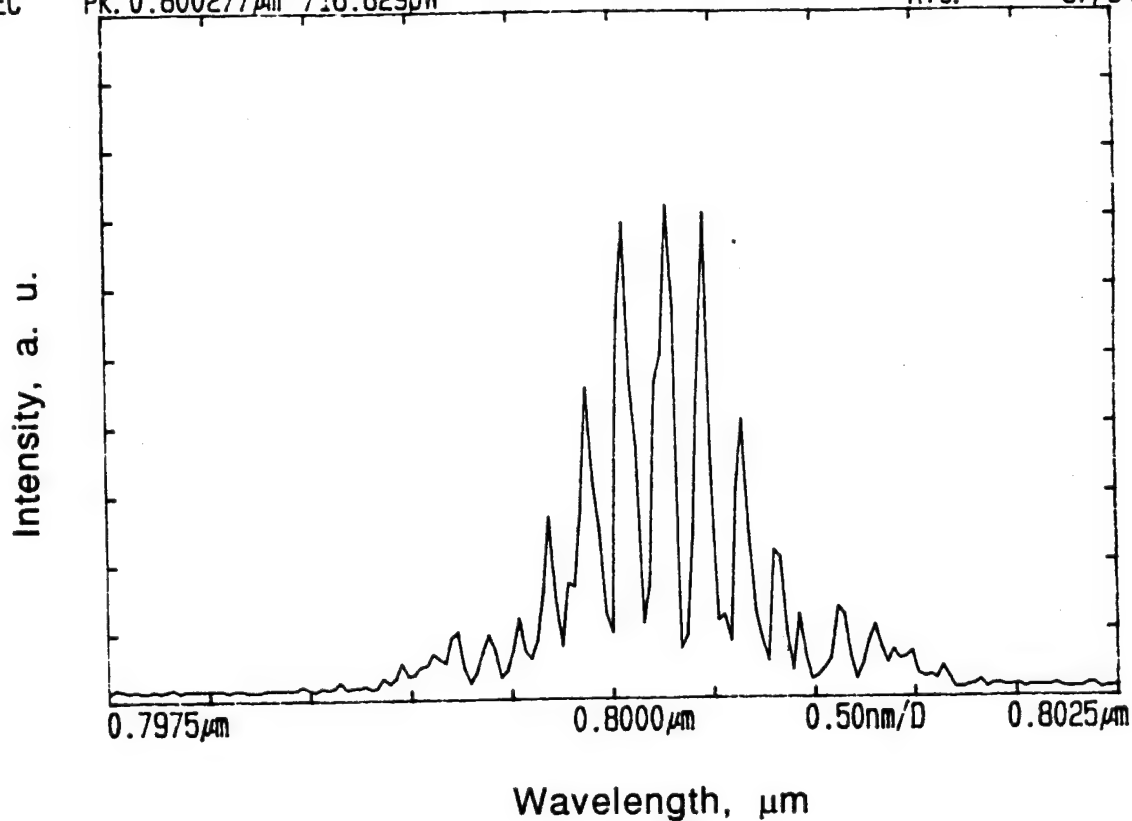
Fig. 2.1 Pulse light-current characteristics of unbonded diodes with active layer thicknesses  $d=300\text{\AA}$  and  $150\text{\AA}$  (a) and of a bonded diode with  $d=300\text{\AA}$  (b).



A typical near-field patterns and emission spectra for one of the diodes ( $d=300\text{\AA}$ ) with cavity length  $L=1.1\text{mm}$  just above the threshold and at a current of  $I=3\times I_{th}$  are shown in the Figures 2.2a and 2.2b, respectively. At currents less than  $1.3-1.5\times I_{th}$ , the lasing spectrum has a narrow envelope (FWHM about  $1\text{nm}$ ) and consists of several discrete lines (see Fig. 2.2a). A set of equidistant maxima was observed in the near-field distribution in this current range (Fig. 2.2a). An increase of current over  $1.5\times I_{th}$  resulted in a flattening of the near-field pattern with hardly resolved trace of equidistant maxima seen previously (Fig. 2.2b). This near-field pattern can be attributed to the formation of a system of self-focusing phase-locked filaments rather than to the contribution of high-order lateral modes. Formation of these filaments is a feature of highly uniform broad-area AlGaAs/GaAs stripe lasers prepared by MBE [31] or MOCVD [32].

**Fig. 2.2** Far-field patterns and lasing spectra of a diode with 300Å-thick active layer and cavity length 1.1mm under driving currents of  $I=1.1I_{th}$  (a) and  $I=3I_{th}$  (b).

\*\* ADVANTEST Q8344A Optical Spectrum Analyzer \*\* 1993- 9- 1 18: 49: 54  
 SPEC Pk: 0.800277 $\mu$ m 716.829pW AVG: 57/64

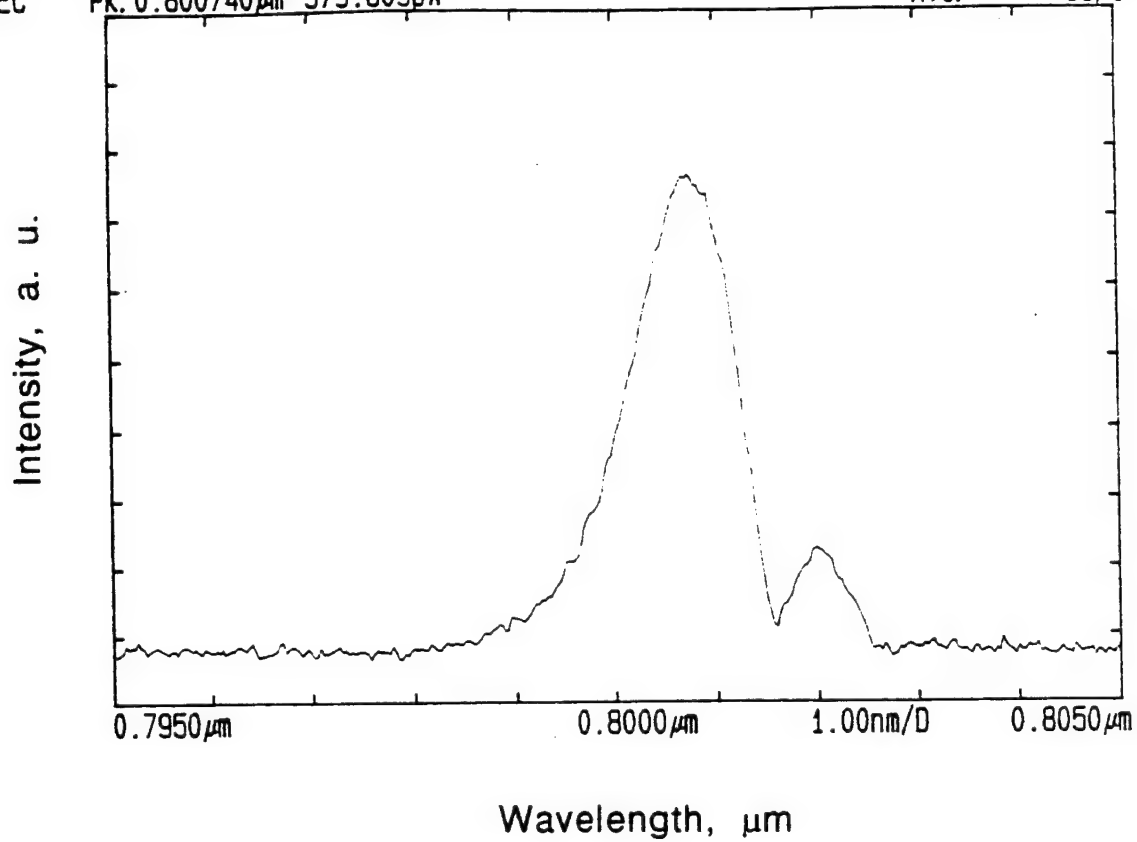


\*\* ADVANTEST Q8344A Optical Spectrum Analyzer \*\*

1993- 9- 7 16: 52: 56

SPEC Pk: 0.800740  $\mu\text{m}$  379.809pW

AVG: 63/64



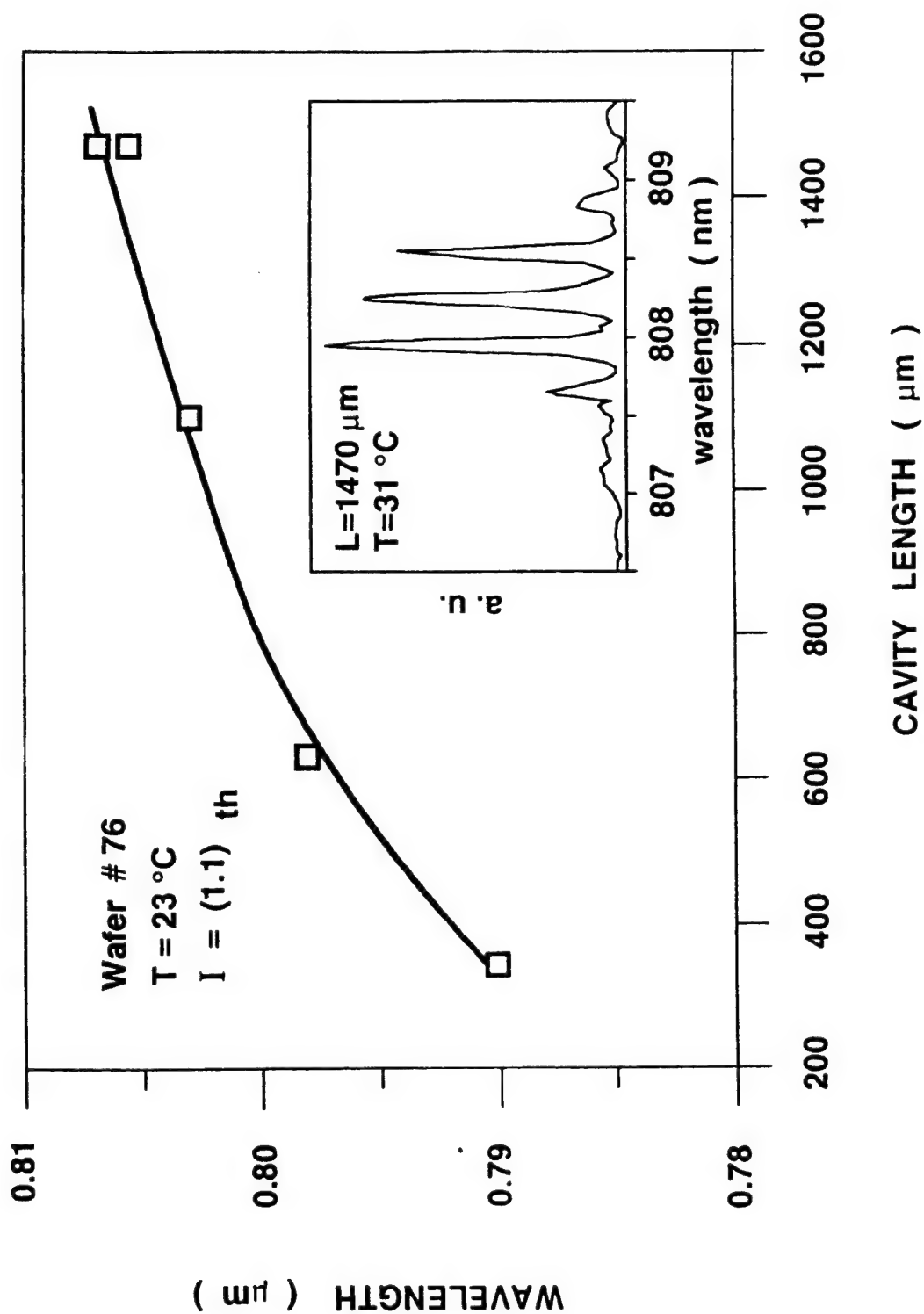
Near Field Intensity, a. u.



The increase of current also results in a broadening of the emission spectrum with discrete spectral lines gradually merging into a single band with FWHM of 2nm (see Fig. 2.2b). This linewidth is maintained up to the maximum current values of  $4 \times I_{th}$  and this feature is important for application as a laser diode pump source.

The composition of quaternary material of the active regions in the fabricated laser diodes is well-suited for Nd:YAG pumping, since the long-wavelength shift of emission after mirror facet coating should lead to the lasing with wavelength of 0.808 $\mu$ m. This was confirmed by the measured dependence of lasing wavelength on cavity length, shown in Figure 2.3.

**Fig. 2.3** Lasing wavelength dependence on cavity length for diodes with 300Å-thick active layer at 23°C. Inset: Lasing spectrum for a diode from the same wafer with cavity length 1.47mm at 31°C.



As in the case of AlGaAs pumping laser diodes, fine tuning of the emission wavelength can be also accomplished by changing the heatsink temperature. We have found a long-wavelength temperature shift of the lasing line of 0.2nm/K. For example, the lasing spectrum for a diode with cavity length of 1.47mm can be shifted to 808 nm position by increasing the temperature from ambient to 31°C, as shown in Figure 2.3.

In conclusion, at this stage it has been demonstrated that LP-MOCVD growth can ensure the fabrication of highly uniform Al-free InGaAsP/InGaP/GaAs separate-confinement 808 nm laser diode structures. The experimental results showed that the lasing spectrum width, near-field uniformity and series resistance were no worse than those for AlGaAs/GaAs pumping lasers. This achievement provided a solid base for thorough optimization of threshold current density and efficiency of InGaAsP/InGaP/GaAs lasers for high-power operation. A systematic approach to this problem called for experimental determination of the interdependence between structure parameters (layer thicknesses, composition and doping) and laser characteristics (threshold current density, differential efficiency and  $T_0$ ).

### Section 3. Optimization of laser structure parameters

#### 3.1 Effect of active region thickness

This section of the report presents the results obtained for two laser structures: #226 (active layer thickness 150 Å) and #228 (active layer thickness 300 Å). A schematic band diagram of the structures studied is shown in Figure 3.1. Undoped quaternary active region and waveguide were sandwiched between Si-doped ( $N_d \sim 5 \times 10^{17} \text{ cm}^{-3}$ ) and Zn-doped ( $N_a \sim 6 \times 10^{17} \text{ cm}^{-3}$ ) InGaP cladding layers. Other parameters not mentioned above were identical to the structures described in the previous report.

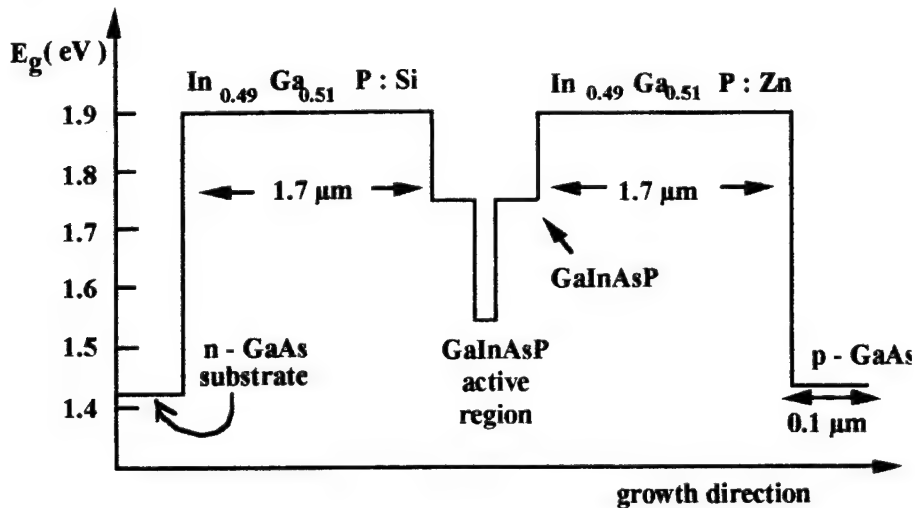


Fig. 3.1. Schematic band diagram of single quantum well separate confinement heterostructure InGaAsP/GaAs diode laser.

Broad-area contact laser diodes with a stripe width of 100 μm diodes and cavity length varying from 100 to 4300 μm were prepared from both wafers and studied. No mirror facet coating was applied. Diode chips were mounted on copper heatsinks by indium bonding. Dependencies of lasers parameters on cavity length were measured in pulsed mode (pulse width 100–400 ns) using an integrating sphere with a Si photodiode. Light-current characteristics were also measured in CW and in quasi-CW mode (pulse width 200 μs, repetition rate 10 Hz).

Figure 3.2a shows a complete view of the dependence of  $J_{th}$  on cavity length for the diodes prepared from wafers #226 and #228. Two regions may be distinguished in the dependence for wafer #228: the range of cavity lengths ( $L$ ) less than 0.5 mm where  $J_{th}$  increases very fast with decreasing cavity length and the range of  $L$  longer than 0.5 mm where the increase of  $J_{th}$  is relatively slow (Figure 3.2a). In case of wafer #226, the dependence has the same shape but the rapid increase of  $J_{th}$  starts at the cavity lengths as long as 1 mm. Figure 3.2b presents part of the data in Figure 3.2a related to long-cavity diodes and plotted versus reciprocal cavity length. This figure will be discussed after considering differential efficiency for the lasers studied.

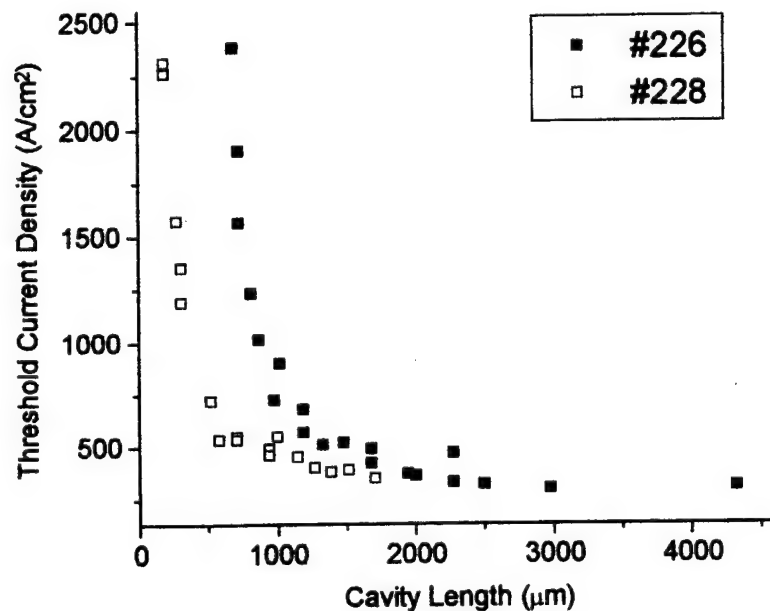


Fig. 3.2a. Threshold current density vs cavity length for laser diodes with active layer thickness 150 Å (#226) and 300 Å (#228).

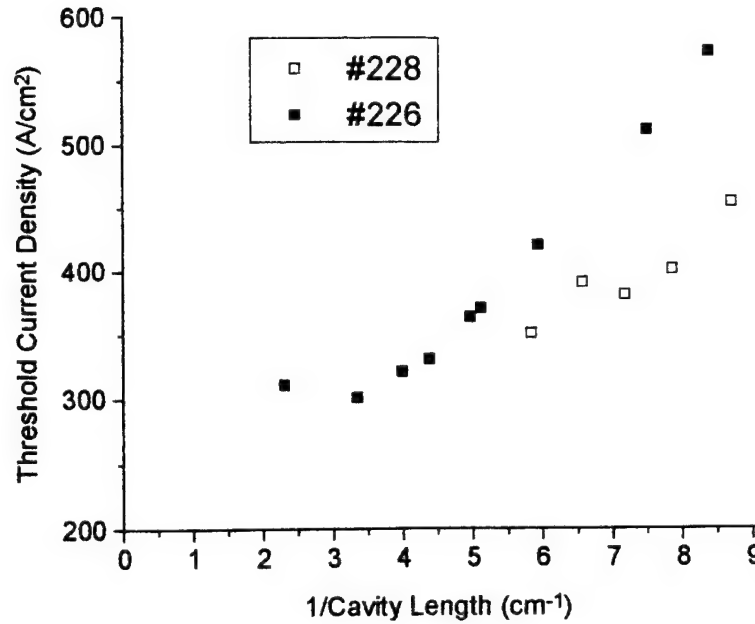


Fig. 3.2b. Threshold current density vs reciprocal cavity length for long-cavity laser diodes with active layer thickness 150Å (#226) and 300 Å (#228).

The dependence of reciprocal differential efficiency ( $1/\eta_d$ ) on cavity length for diodes of the same wafers is presented in Figure 3.3. Both dependencies have a similar shape. The differential efficiencies have the maximum values in the range of medium cavity lengths where their dependence on cavity length is very weak. For longer diodes  $\eta_d$  decreases with increasing  $L$  demonstrating conventional behavior. The decrease of  $\eta_d$  occurring at shorter cavity lengths as well as the plateau at medium cavity lengths cannot be explained within the frame of traditional theory assuming the internal losses to be constant. The curves for the two wafers are shifted with respect to each other corresponding to the shift in threshold current dependencies.

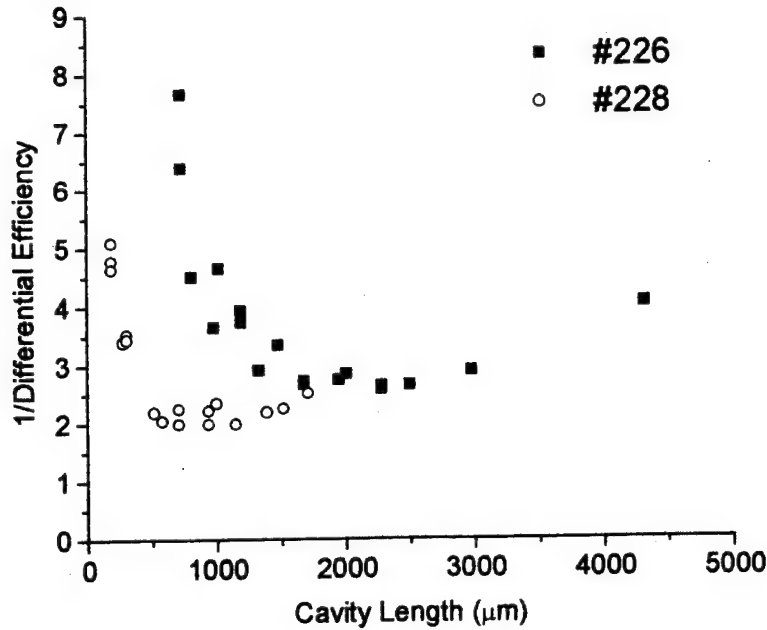


Fig. 3.3. Reciprocal differential efficiency vs cavity length for laser diodes with active layer thickness 150 Å (#226) and 300 Å (#228).

The results discussed above demonstrate that the values of differential efficiency in the studied samples are closely connected with the values of threshold current density. Apparently, internal losses may be considered as independent from current only for the diodes with longest cavity lengths. Regular differential efficiency dependence for the diodes longer than 1 mm enabled us to determine internal quantum efficiency and internal losses in the structure from cutoff point on  $1/\eta_d$  axis and slope of the line according to the known relation

$$\eta_d = \eta_i \left( 1 + \frac{\alpha_i L}{\ln(1/R)} \right)^{-1}$$

which may be also rewritten as

$$1/\eta_d = 1/\eta_i (\alpha_i + \alpha_{out}/\alpha_{out}) = 1/\eta_i (1 + \alpha_i L),$$

assuming output losses close to  $1/L$  for mirror facet reflectivity  $R \sim 0.3$ .

The interpolation shown in Figure 3.3 gives the same value of internal losses  $\alpha_i \sim 4.5 \text{ cm}^{-1}$  for structures #228 and #226. In accordance with our previous studies of spontaneous emission from this type of laser diodes [33] this interpolation yields high values of internal efficiency  $\eta_i \sim 80\%$ .

The deviation from normal dependence of  $\eta_d$  in the range of medium and short cavity lengths has been previously ascribed to excess carrier leakage to the waveguide and p-cladding layers [18]. Data shown in Figure 3.2b reflects the enhancement of the influence of carrier leakage in the diodes of wafer #226. Despite having the active region thinner than #228, diodes of wafer #226 exhibit higher threshold current densities for cavity lengths shorter than 2 mm. Only diodes of wafer #226 with extremely long cavities ( $L > 2 \text{ mm}$ ) have the lowest  $J_{th} = 290 \text{ A/cm}^2$  which is smaller than expected for wafer #228 with the same cavity length. Data for the diode with  $L \sim 4 \text{ mm}$  shows that non-homogeneous current distribution due to the problem of uniform mounting of extremely long chips can affect the measured values of  $J_{th}$  for the longest diodes and make them unsuitable for interpolation. As for the data for wafer #228, shown in Figure 3.2a, these appears to be more reliable. The value of zero-gain current density ( $J_0 = 220 \text{ A/cm}^2$ ) and slope of the corresponding interpolation curve are approximately two times higher than it is expected from the simplest radiative model [34] disregarding any factors increasing thresholds in real conditions. The broadened emission and gain spectra seem to be the main factors which cause the inferiority of the parameters of the long-cavity diodes compared to the ideal model.

In order to reveal the influence of spillover of carriers for shorter-cavity diodes, electroluminescence spectra were registered in the direction normal to the structure plane for two diodes made from wafers #228 and #226 (Figure 3.4). Comparison of these spectra shows that quantization effect shifts the position of active region emission

maximum by  $\sim 20$  meV to shorter wavelengths for the diode of wafer #226 in comparison with the diode of wafer #228. In addition to the main (active region) emission band these spectra contain a short-wavelength band of radiation from the waveguide with the relative intensity increasing with injection current density above  $20\text{--}40\text{ A/cm}^2$ . The current dependence of the ratio of waveguide radiation intensity to that of the active region ( $\zeta$ ) is shown in Figure 3.5. As can be expected for the narrower active region, the value of  $\zeta$  for the diodes of structure #226 is 4 times higher than that for structure #228 and approaches 0.1 in the range of currents typical for lasing threshold.

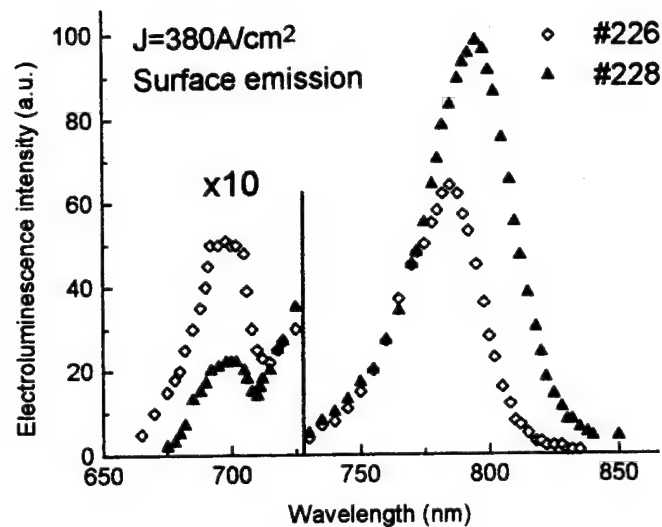


Fig. 3.4. Electroluminescence spectra for laser diodes with active layer thickness  $150\text{ \AA}$  (#226) and  $300\text{ \AA}$  (#228). Radiation coupled out perpendicular to the junction plane.

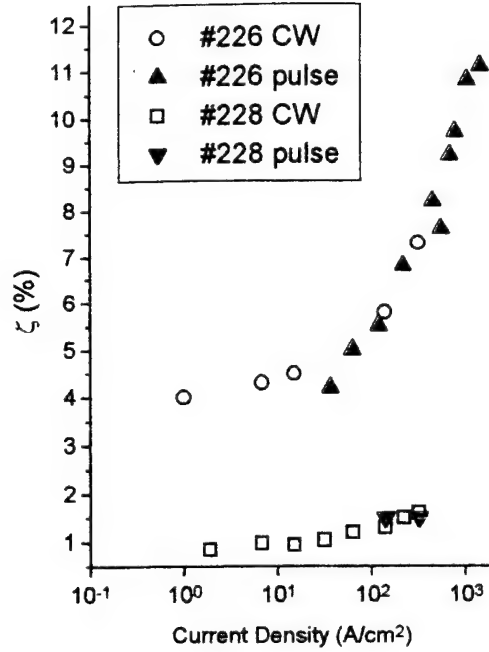


Fig. 3.5. Ratio of radiation intensities from the waveguide and active region vs current density for laser diodes with active layer thickness 150Å (#226) and 300 Å (#228).

It should be emphasized that the measured value of  $\zeta$  is significantly lower than actual fraction of carriers recombining out of the active region. The first reason for this is that  $\zeta$  was measured for the radiation emitted from the periphery of the stripe where current density is lower than the average over all the stripe width. Thus, the actual contribution of waveguide recombination is expected to be higher corresponding to the higher average current density. Secondly, the total value of losses due to recombination out of the active region exceeds the waveguide recombination because the enhancement of carrier spillover to the waveguide should be accompanied by current overflow to the cladding layers. This effect is studied in more detail in the next section of this report. It should be also noted that earlier data [35] as well as the results of this work show that the intensity of waveguide radiation continues to grow with current above the threshold. Combining this observation with the results discussed above, it may be concluded that the peculiarities of both threshold current density and differential efficiency dependencies on cavity length for

the studied laser diodes may be explained by carrier spillover to the waveguide and current overflow to the cladding layers which is the stronger the smaller is the active region thickness.

### **3.2 Effect of waveguide-cladding layer bandgap discontinuity**

The experiments described above showed that increasing threshold current density in laser diodes with high output losses (short cavity length) leads to excess carrier spillover from active region to waveguide layers which results in increased internal loss due to free carrier absorption. However, the observed drastic drop of differential efficiency for short-cavity diodes cannot be explained exclusively by this mechanism because no reasonable concentration of carriers in the waveguide can result in a value of internal loss necessary to account for this effect. It has been previously attributed to electron spillover from waveguide to p-cladding layer leading to the leakage current that decreases the internal efficiency of radiative recombination in the active region [18]. This effect is pronounced for laser structures with relatively small bandgap discontinuity between waveguide and cladding layers. Therefore, the influence of the leakage current on laser parameters may be demonstrated and investigated by comparative study of laser structures differing by waveguide-cladding layer bandgap step only.

Two types of laser structures were used in this work: #228 and #342-345 series. Band structure parameters for the four wafers are given in Table 3.1. Information on the bandgaps of active region and waveguide layers was extracted from electroluminescence spectra registered under very low excitation level (current density  $\sim 20 \text{ A/cm}^2$ ) to eliminate the effects of band filling or thermal heating. Emission peak from the cladding layer could not be seen in these experiments because of low excess carrier concentration and low radiative efficiency in highly doped InGaP material. Values of bandgap of the cladding layers were obtained from the position of the related peak in photoluminescence spectra. As it can be seen from the Table, band structure of the waveguiding region is almost the

same for all four wafers and  $E_{\text{waveguide}}^g - E_{\text{active}}^g = 230 \pm 5$  meV. At the same time, bandgap discontinuity  $\Delta = E_{\text{cladding}}^g - E_{\text{waveguide}}^g$  varies from  $\sim 80$  meV for #228 ("low  $\Delta$ ") to 130-140 meV for ##342-345 ("high  $\Delta$ ").

**Table 3.1**

Energy gaps of each layers for the lasers used in this work. Electron-volts (eV) are used for energy gap unit.

Sample Number	226,228	342	344	345
Eg, active	1.55	1.52	1.525	1.525
Eg, wave guide	1.78	1.75	1.75	1.76
Eg, cladding	1.86	1.89	1.89	1.89

Laser diodes were prepared and light-current characteristics for the four structures were recorded in short pulse operation under conditions described in the previous section. Figure 3.6 shows cavity length dependence of reciprocal differential efficiency for the diodes with low (#228) and high  $\Delta$  (##342-345). As can be seen in the figure, for cavity length longer than 1 mm values of  $\eta_d$  for two types of laser structures are very close (within the experimental data scatter). However, instead of stabilization of  $\eta_d$  at the level  $\sim 0.85$  W/A happening at  $L=600-1200$   $\mu\text{m}$  for #228, the efficiency continues to grow for the diodes with high  $\Delta$  and stabilizes at the level  $\sim 1.1$  W/A for cavity length 400-900  $\mu\text{m}$ . Sharp drop of  $\eta_d$  that occurs for cavity length shorter than 500  $\mu\text{m}$  for #228, does not become significant for the structures with high  $\Delta$  until the cavity lengths as short as 200  $\mu\text{m}$ . This difference indicates that the loss mechanism responsible for stabilization and subsequent drop of efficiency is enhanced by the decrease in  $\Delta$  and therefore is connected with the distribution of carriers between the waveguide and cladding layers.

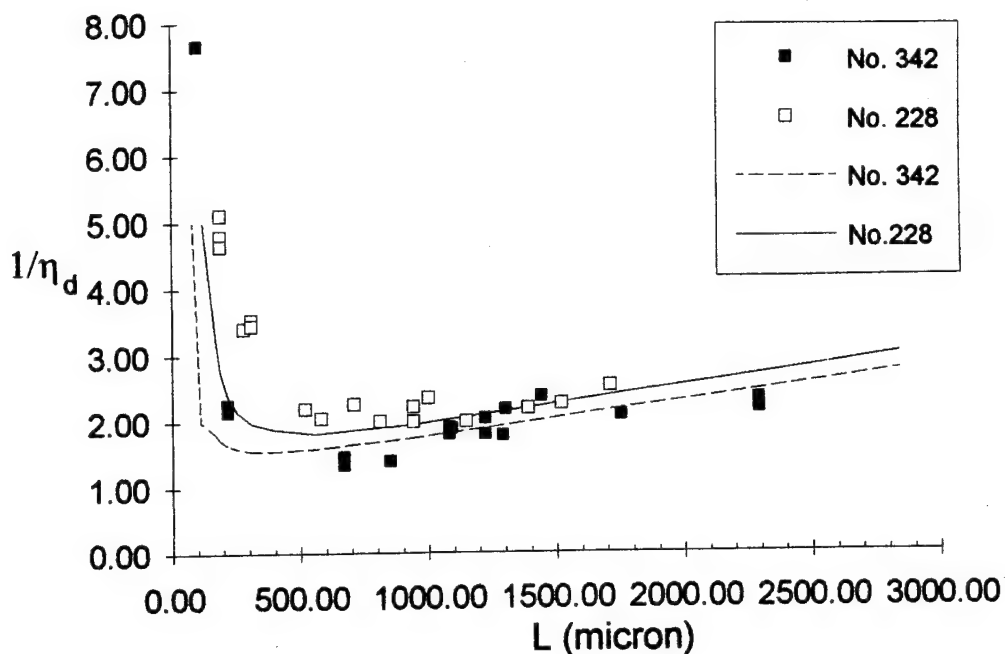


Fig.3.6 Differential efficiency vs. cavity length for lasers with high (#342) and low (#228) waveguide-cladding layer band discontinuity. Scattered dots are experimental data, lines are theoretical results.

This conclusion is further supported by the data on threshold current density as function of output losses ( $\alpha_m \sim 1/L$ ) for the two types of structures presented in Figure 3.7. Similar to the differential efficiencies discussed above,  $J_{th}$  for long-cavity lasers ( $\alpha_m < 20 \text{ cm}^{-1}$ ) seems to be the same for diodes with high and low  $\Delta$  within the experimental scatter. For shorter cavities,  $J_{th}$  dependence on output loss for low  $\Delta$  (#228) starts to deviate from linearity predicted by conventional theory assuming constant internal efficiency and internal loss (see previous report). On the contrary, the dependence for the diodes with high  $\Delta$  (##342-345) is linear up to the output loss as high as  $50 \text{ cm}^{-1}$  ( $L=200 \text{ }\mu\text{m}$ ). Characteristically, for both structures the deviation from linear dependence of  $J_{th}$  and the sharp drop in differential efficiency occur at the same cavity length.

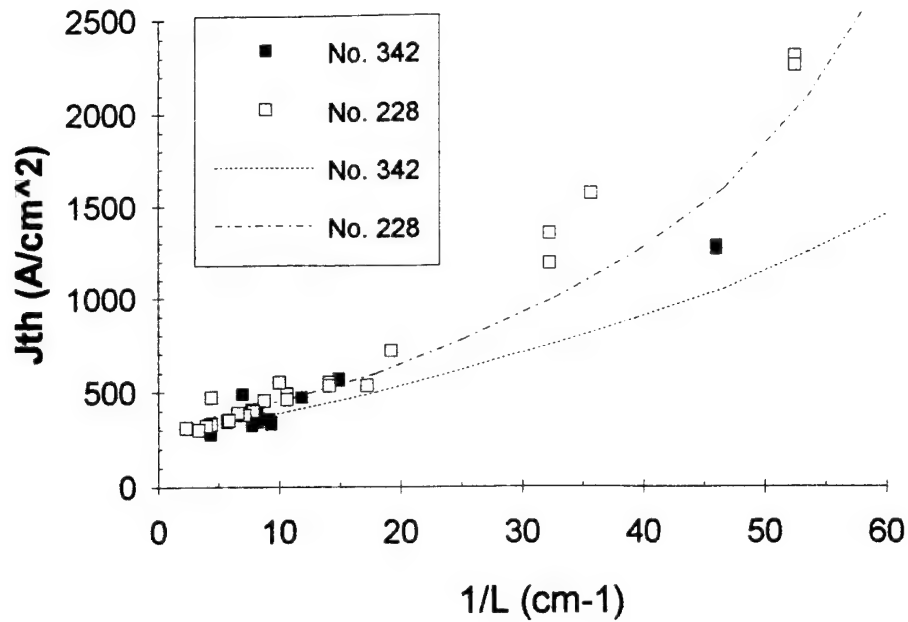


Fig. 3.7. Threshold current density ( $\text{A/cm}^2$ ) vs. reciprocal cavity length for lasers with high (#342) and low (#228) waveguide-cladding layer band discontinuity. Scattered dots are experimental data, lines are theoretical results.

Qualitatively, the observed influence of the  $\Delta$  value on the deterioration of  $\eta_d$  and  $J_{th}$  for short-cavity diodes, may be explained as follows. For long diodes with low output losses ( $L > 1000 \mu\text{m}$ ) excess carrier concentration is relatively low in the waveguide and negligible in the cladding layers. Internal loss and internal efficiency do not depend on cavity length and the experimental dependencies  $\eta_d(L)$  and  $J_{th}(1/L)$  demonstrate a traditional linear behavior independent of  $\Delta$ . However, as the output losses increase, excess carrier concentration in the active region at threshold increases as well, entailing a thermal spillover of excess electrons to the waveguide and cladding layers. Excess electron concentration in p-cladding layer is determined by thermal equilibrium with the carriers in waveguide and therefore is an exponential function of  $\Delta = E_{cladding}^g - E_{waveguide}^g$ . Hence, leakage current created by excess electrons recombining in the p-cladding and contact layers should be suppressed considerably in the structures with high  $\Delta$ , in agreement with

experimental results discussed above. The comparison of theoretical and experimental data clearly demonstrates that current leakage to p-cladding layer affects the laser parameters significantly only in the range of cavity lengths below 500  $\mu\text{m}$ . For cavity lengths longer than 500  $\mu\text{m}$  the current leakage results in no more than 10-15% change in the values of efficiency and threshold.

In conclusion, comparative experimental studies of the diodes with varying thickness of the active region and waveguide-cladding layer bandgap discontinuity provided input information for the formulation of a theoretical model attempting to describe accurately the observed laser behavior. This approach was instrumental in understanding the critical phenomena affecting laser performance, namely gain saturation and minority carrier leakage into the cladding layers.

### **3.3 Transverse far-field measurements and effect of waveguide thickness**

Relatively low band gap difference between the active region corresponding to 0.8  $\mu\text{m}$  lasing wavelength and InGaP cladding layers requires special band gap engineering approach to the design of high-efficiency 0.8  $\mu\text{m}$  InGaAsP/GaAs separate confinement heterostructure (SCH) lasers. Previously, we have demonstrated that high differential efficiency may be achieved for lasers with InGaAsP waveguide composition close to InGaP due to suppressed excess carrier spillover from the active region to the waveguide layers. This design also results in weak optical confinement corresponding to the small refractive index step between the waveguide and cladding layers. Attractive features of the lasers with weak waveguide confinement include narrow transverse far-field pattern (as low as  $27^\circ$  compared to  $35\text{--}45^\circ$  typical for AlGaAs lasers) and large beam spot on the laser mirror providing low optical density beneficial for high-power operation limit.

We investigated experimentally the laser diodes with 300 Å wide active region and varying thickness of the weakly confined waveguide and compared the characteristic features of

these lasers with conventional AlGaAs laser diodes emitting in the same wavelength range. The relevant parameters of the SCH structures studied are given in Table 3.2.

Table 3.2. Parameters of 0.8  $\mu\text{m}$  InGaAsP/GaAs SCH laser structures

Active Layer				Waveguide Layer		
Wafer #	Thickness ( $\text{\AA}$ )	$E_{\text{active}}^g$ (eV)	$\Gamma_{\text{act}}$	Thickness ( $\text{\AA}$ )	$E_{\text{waveguide}}^g$ (eV)	$\Gamma_{\text{wg}}$
367	300	1.50	6.3	4300	1.76	0.70
364	300	1.49	6.0	5600	1.76	0.80
387	300	1.49	5.6	6900	1.78	0.86
384	300	1.50	5.2	8200	1.76	0.90

Undoped quaternary active region  $\text{In}_{0.13}\text{Ga}_{0.87}\text{As}_{0.74}\text{P}_{0.26}$  and waveguide  $\text{In}_{0.37}\text{Ga}_{0.63}\text{As}_{0.25}\text{P}_{0.75}$  were sandwiched between Si-doped ( $N_d \sim 5 \times 10^{17} \text{ cm}^{-3}$ ) and Zn-doped ( $N_a \sim 6 \times 10^{17} \text{ cm}^{-3}$ ) InGaP cladding layers. The composition of the quaternary active region of the SCH structures corresponds to the band gap energy  $1.495 \pm 0.005 \text{ eV}$ , while the composition of the waveguide layers corresponds to the energy  $1.77 \pm 0.01 \text{ eV}$ . The thickness of the active region for all structures is  $300 \text{ \AA}$ , while the thickness of the confinement (waveguide) region  $d_{\text{wg}}$  for the structures varied from 4300 to 8200  $\text{\AA}$ . The post-growth processing of the wafers followed the procedure outlined in the previous report. After cleaving, the individual diodes were mounted p-side down on copper heat sinks by indium bonding. Uncoated diodes with cavity length varying from 500 to 2500  $\mu\text{m}$  were prepared.

Threshold current density and differential efficiency for the mounted diodes were measured at  $20^\circ\text{C}$  in pulsed mode (pulse width 100–400 ns, repetition rate 5–1.25 kHz) using an integrating sphere with a Si photodiode. Figs. 3.8 and 3.9 show the experimental values of threshold current density  $J_{\text{th}}$  and reciprocal differential efficiency  $1/\eta_d$  for the

laser diodes with waveguide thickness  $d_{wg}$  varying from 4300 to 8200 Å. Threshold current density and reciprocal differential efficiency are independent of waveguide thickness in all the range of cavity lengths.

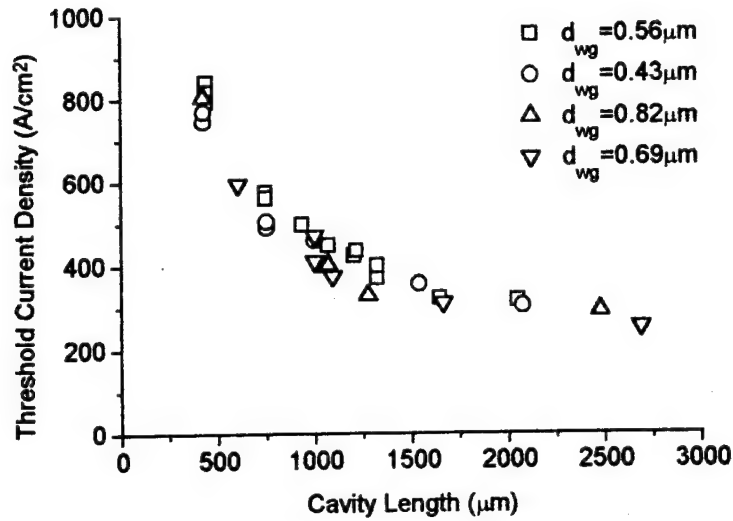


Fig. 3.8. Threshold current density vs cavity length for 0.8  $\mu m$  SCH-SQW InGaAsP/GaAs laser diodes with varying waveguide thickness.

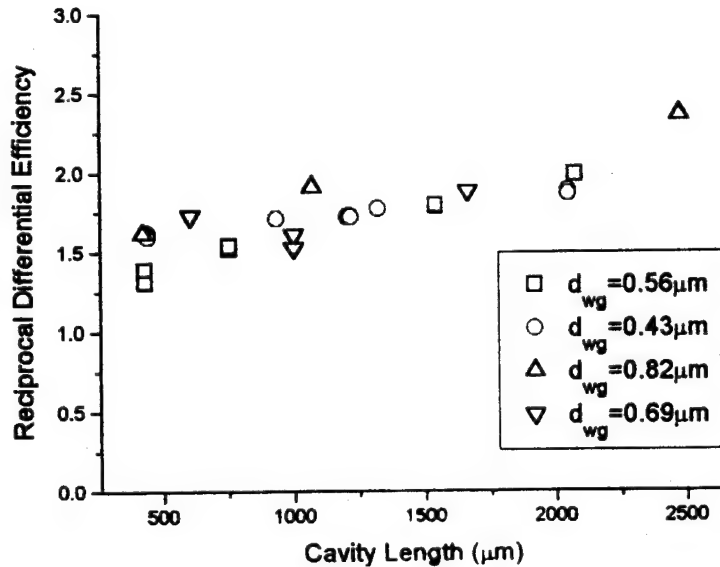


Fig. 3.9. Reciprocal differential efficiency vs cavity length for 0.8  $\mu m$  SCH-SQW InGaAsP/GaAs laser diodes with varying waveguide thickness.

For the measurement of characteristic temperature  $T_0$  value, threshold current was measured under pulse operation with the heat sink temperature varying from 16°C to 105°C. Laser diodes with cavity lengths 1.3 mm were used for these experiments in order to avoid any effect of carrier leakage to the cladding layers [39]. Experimental data of threshold current were plotted against temperature in logarithmic scale and interpolated by linear curve in the range of temperatures 16°C to 60°C. The value of  $T_0$  was calculated according to the equation,

$$T_0 = \frac{T_1 - T_2}{\log J_1 - \log J_2}$$

where  $J_1$  and  $J_2$  are threshold current densities corresponding to the heat sink temperatures  $T_1$  and  $T_2$ , respectively. Characteristic temperature  $T_0$  varies slightly with waveguide thickness in the range of 132° to 146° showing a tendency to increase with decreasing waveguide thickness.

Experimental setup for far-field measurements consisted of water-cooled heat sink holder fixed on two horizontal translation stages providing for an accurate alignment of the system. A rotation stage coaxial with the heat sink holder was used for rotating an adjustable-length arm with a Si photodiode. The active area of the photodiode was limited by 1 mm-wide vertical slit. Rotation stage was driven by UR80 stepping motor with CC1.1 stepping motor controller (Klinger). Signal from the photodiode was detected by lock-in amplifier. The data acquisition system used in these experiments is described in the previous section. This setup insured a reproducible assessment of far-field patterns with resolution as high as 0.01° for lasers driven in CW and quasi-CW regime. Typical transverse far-field pattern measured in CW at room temperature is presented in Fig. 3.10.

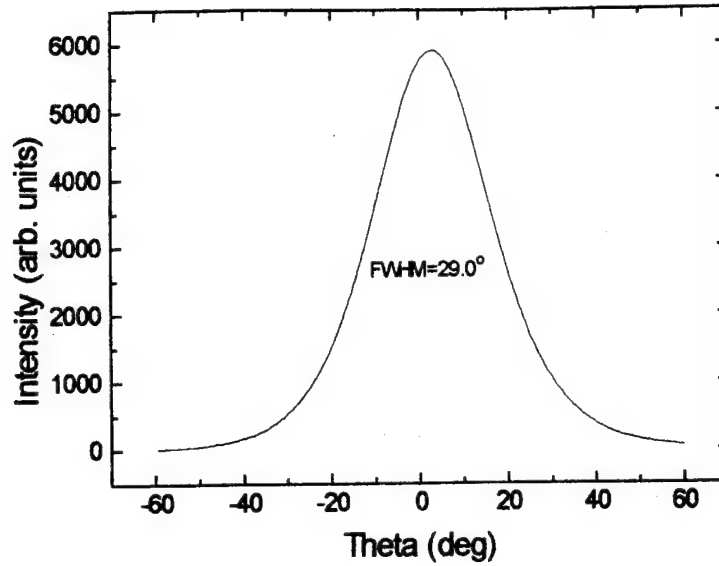


Fig. 3.10. Transverse far-field pattern of 0.8 $\mu$ m SCH-SQW InGaAsP/GaAs laser diode.

The far-field pattern is single-lobe and Gaussian up to the current densities  $3xJ_{th}$  independently of cavity length and waveguide thickness indicating stable fundamental transverse mode operation for all the lasers under experimental conditions. Halfwidth of the far-field pattern is shown in Fig. 3.11 as function of the waveguide thickness. Transverse beam divergence of the lasers fabricated increases slightly with waveguide thickness from  $29^\circ$  for  $d_{wg}=4300 \text{ \AA}$  to  $31.3^\circ$  for  $d_{wg}=8200 \text{ \AA}$ .

Optical intensity distribution in the lasing mode was calculated for 5-slab waveguide model [40] and transverse far-field pattern was obtained by Fourier-transforming the intensity profile at the mirror facet [41]. Small refractive index step between the waveguide and the cladding layer required an accurate approximation of the refractive indices for InGaAsP alloys lattice-matched to GaAs. Therefore, the difference between the refractive indices of the active layer and the cladding layer was taken to be approximately 0.14 to make best fitting of the experimental data. This value is very close to the calculated data available in the literature [42]. Refractive index of the waveguide

layer was linearly extrapolated corresponding to the energy gap values determined by photoluminescence measurements (see Table 3.2). Fig. 3.11 presents the theoretical and experimental values of the transverse far-field divergence for the lasers with strong (squares), intermediate (crosses) and weak (diamonds) confinement. As mentioned before, lasers with weak confinement demonstrate low beam divergence beneficial for optical coupling into single-mode fibers or optical transfer systems for solid-state laser pumping. Calculated values of the far-field halfwidth show the same weak dependence of the beam divergence on the waveguide thickness that has been observed in the experiment (solid circles). For comparison, the same dependence for InGaAsP/GaAs lasers with weak confinement is shown in Fig. 3.12 together with the curve for a typical AlGaAs laser structure with strong optical confinement in the waveguide ( $\text{Al}_{0.3}\text{Ga}_{0.7}\text{As}$  waveguide,  $\text{Al}_{0.5}\text{Ga}_{0.5}\text{As}$  cladding barrier) [43].

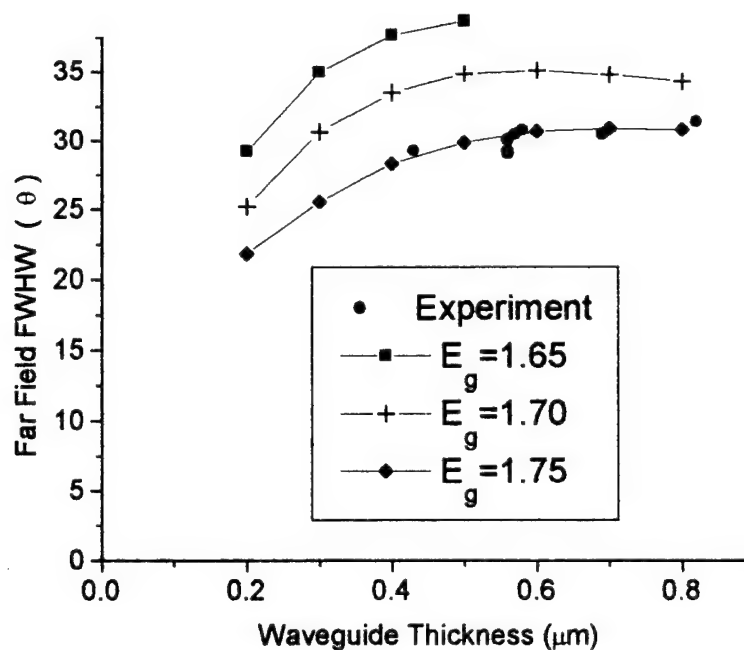


Fig. 3.11. Transverse far-field divergence vs waveguide thickness for  $0.8\mu\text{m}$  SCH-SQW InGaP/InGaAsP/GaAs laser diodes with varying bandgap of waveguiding layers.

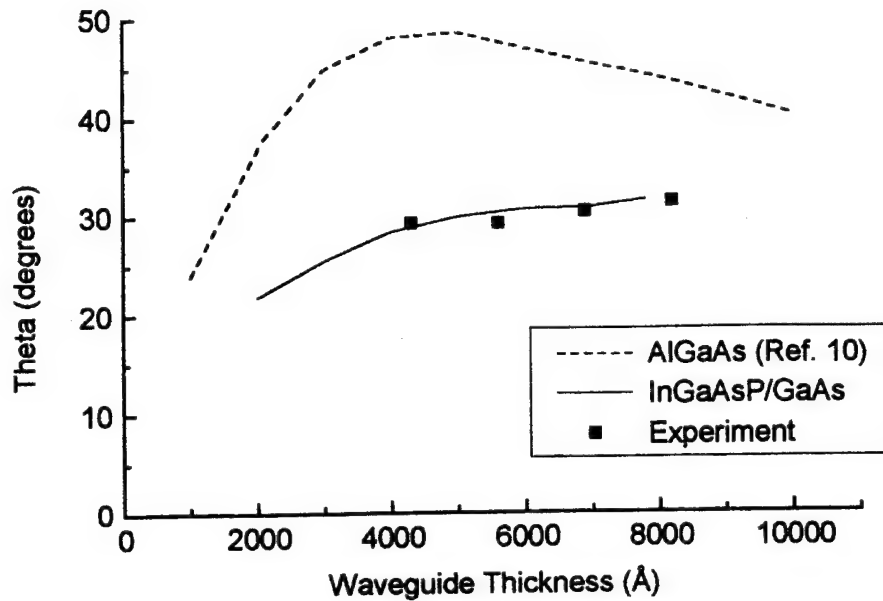


Fig. 3.12. Transverse far-field divergence vs waveguide thickness for 0.8 $\mu$ m SCH-SQW InGaP/InGaAsP/GaAs laser diodes (solid curve) and AlGaAs laser diodes (dashed curve).

As can be seen in Fig. 3.12, beam divergence is considerably higher (usually above 40°) for AlGaAs lasers with comparable waveguide thickness although it exhibits a decrease with  $d_{wg}$  increasing above 5000 Å as optical wave profile broadens in strongly confined waveguide. Beam divergence below 35° may be achieved in AlGaAs lasers only by reducing waveguide thickness below 1500 Å and allowing the optical wave to “leak” into the cladding layers. The negative consequences of this “leakage” in AlGaAs lasers are discussed further. On the contrary, narrow beam divergence of 27-31° or lower is supported by weakly confined InGaAsP/InGaP waveguide of any thickness. Independence of the far-field halfwidth on  $d_{wg}$  indicates that optical intensity distribution in the waveguide hardly changes with  $d_{wg}$  varying from 4000 to 8000 Å. This conclusion has two important implications.

1) Optical confinement factor  $\Gamma_{act}$  in the active region (quantum well) varies slowly with the waveguide thickness. Calculated values of  $\Gamma_{act}$  for the fabricated laser structures are

given in Table 3.2 and, indeed, show insignificant variation (less than 20%). Independence of  $\Gamma_{act}$  on  $d_{wg}$  is in good agreement with the observed threshold current densities being close for structures with different waveguide thickness (Fig. 3.8). On the contrary, strong optical confinement in conventional AlGaAs lasers entails a strong dependence of  $\Gamma_{act}$  on the waveguide thickness and requires a careful optimization of the waveguide parameters to achieve low threshold current densities, especially for lasers with quantum well active regions [44].

2) Fraction of the optical power propagating through the waveguide  $\Gamma_{wg}$  rather than through the cladding layers reduces considerably with decreasing waveguide thickness (see Table 3.2). Corresponding “leakage” of the optical field to the cladding layers is a subject of major concern in AlGaAs lasers because of the high absorption loss in the indirect band gap AlGaAs material with high Al composition [44]. Deep-level impurities and growth defects also contribute to the high absorption in wide band gap AlGaAs [45]. On the opposite, free carrier absorption in high quality direct band gap InGaP cladding barriers do not incur any significant increase in the internal losses in Al-free laser structures, as evidenced by the experimental data on threshold current densities as well as by the values of differential efficiency observed for long-cavity laser diodes. For lasers with cavity lengths 1.5-1.7 mm from the four wafers with different  $d_{wg}$ , differential efficiencies varied from 0.85 to 0.75 W/A yielding the values of internal loss  $5.5 \pm 0.5 \text{ cm}^{-1}$  despite the fact that the penetration of the optical field into the cladding layers given by

$$\Gamma_{cl} = 1 - \Gamma_{wg}$$

increased by approximately a factor of 3 (see Table 3.2). Differential efficiencies as high as 1-1.2 W/A has been observed for the lasers with cavity length 0.7-0.9 mm.

The only experimental value which demonstrated any noticeable variation with the waveguide thickness is the characteristic temperature  $T_0$ . Slight decrease of the  $T_0$  value with increasing waveguide thickness may be attributed to temperature-dependent

absorption losses in the waveguide due to the excess carrier spillover from the active region to the waveguiding layers [38]. At elevated temperatures, free carrier absorption in the waveguide may become significant and result in  $T_0$  reduction with increasing  $\Gamma_{wg}$ .

In conclusion, the experimental investigation of Al-free SCH InGaAsP/InGaP/GaAs laser diodes with varying waveguide thickness revealed the new and attractive features of these devices stemming from relatively weak optical confinement in the InGaAsP/InGaP waveguide with low refractive index step. Narrow transverse beam divergence, independence of optical confinement factor on the waveguide thickness and low absorption loss in the InGaP cladding layers were demonstrated experimentally and found in good agreement with theoretical predictions. As will be shown in Section 4, large beam spot on the laser mirror and resistance of Al-free material to non-radiative recombination-induced catastrophic damage resulted in the achievement of optical power density on the uncoated mirror facet as high as  $1.6 \text{ MW/cm}^2$  in CW and  $2.5 \text{ MW/cm}^2$  in quasi-CW.

### **3.4 Lateral far-field measurements**

Low lateral far-field divergence close to the diffraction limit is required for high-power lasers used in fiber amplifier pumping or solid-state laser pumping systems. Typically, single lateral mode should be supported by the laser waveguide, therefore, one of the following laser structures is employed in order to achieve near-diffraction limit high-power operation:

- narrow stripe index-guiding laser in ridge waveguide, buried ridge, or buried heterostructure configuration;
- phase-locked array of index guided or anti-guided stripes optimized for single-mode operation;
- master-oscillator power amplifier (MOPA) structure.

Of the three choices, the first one seems to be advantageous for large-scale high power laser fabrication as it does not require the detailed calculation and precise control of the refractive indices and optical wave distribution as single-mode array, neither the ultra-low reflectivity front facet coating as MOPA. In AlGaAs-based lasers, however, the implementation of narrow-stripe single-mode lasers is hindered by low COD limit and relatively high resistance associated with this material system as well as by their short-lifetime under high current density operation. On the opposite, high COD limit, low series resistance and extreme stability under high current density together with the ease of high-quality mesa stripe etching and regrowth, make the narrow stripe structure extremely attractive for high-power single-mode Al-free laser fabrication. Output power as high as 800 mW in near-diffraction limit beam has been obtained from MBE-grown Al-free ridge waveguide lasers emitting at 0.98  $\mu\text{m}$  wavelength [17].

Despite the fact that high-power single lateral mode operation is not expected from broad-area lasers, the studies of lateral far-field patterns can provide some useful information for future development of narrow-stripe single-mode lasers or MOPAs. With this in mind, lateral far-field distribution has been recorded for broad-area lasers with various cavity length, waveguide thickness and doping under a wide range of pulse widths and current densities.

Fig. 3.13 shows the lateral far-field pattern observed at the onset of lasing ( $J=1.01$ - $1.05J_{\text{th}}$ ). Single-lobe pattern with narrow divergence of  $\sim 1^\circ$  (2 times the diffraction limit) indicates a uniform current distribution across the stripe typical for high-quality MOCVD-grown structures.

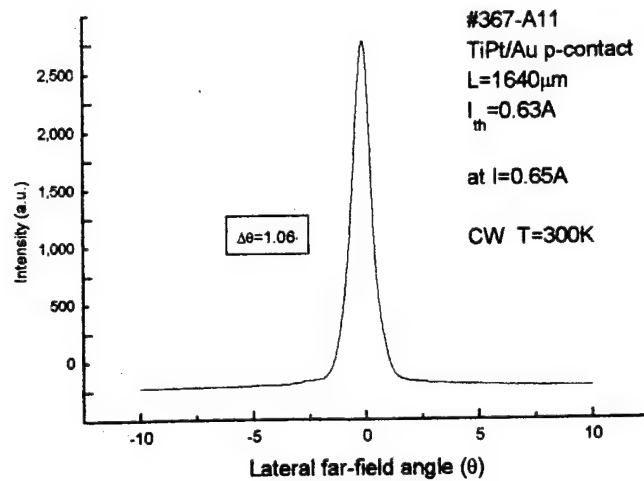


Fig. 3.13. Lateral far-field pattern of 0.8 $\mu$ m SCH-SQW InGaP/InGaAsP/GaAs laser diode at the onset of lasing.

However, as current density increases above the threshold, the far-field pattern broadens splitting into multiple peaks and steering from the initial beam direction (Fig. 3.14).

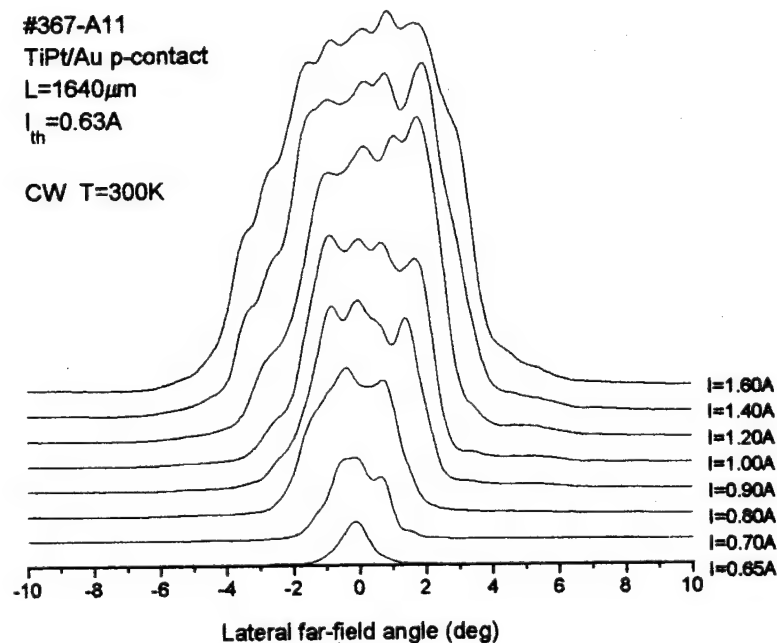
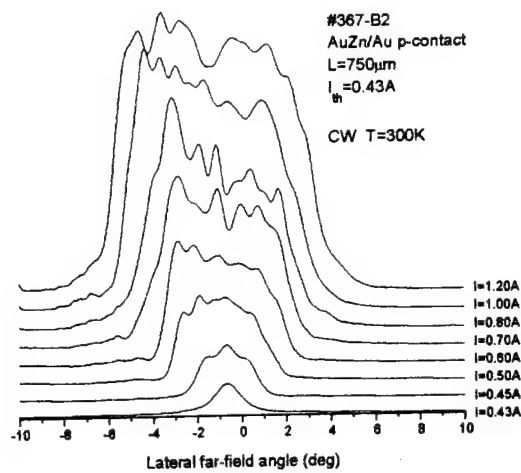


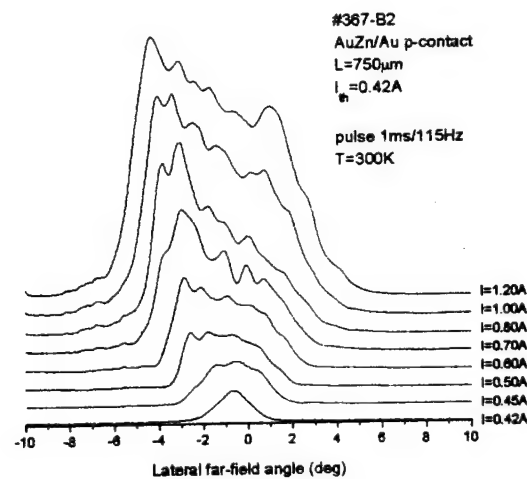
Fig. 3.14. Lateral far-field pattern of 0.8 $\mu$ m SCH-SQW InGaP/InGaAsP/GaAs laser diode under varying injection current density.

This type of behavior has been consistently observed for broad-area lasers with varying cavity length and waveguide thickness, under CW and pulse current conditions (Fig. 3.15a-c). According to the calculations presented in Part 3 of this report, it indicates that current filamentation occurs soon after the onset of lasing due to a strong positive dependence of the refractive index of InGaAsP material on the carrier concentration in the waveguide layers. It is well known [46], that this dependence may be made weaker by the appropriate doping of the waveguide at the expense of threshold current density. In order to confirm experimentally that this effect is responsible for the observed behavior, a laser structure has been grown with waveguiding region p-doped with Zn up to the acceptor concentration of  $\sim 5 \times 10^{17}$ . As shown in Fig. 3.16, waveguide doping indeed resulted in the improvement of the beam stability and divergence confirming the initial assumption about the reason for current filamentation.

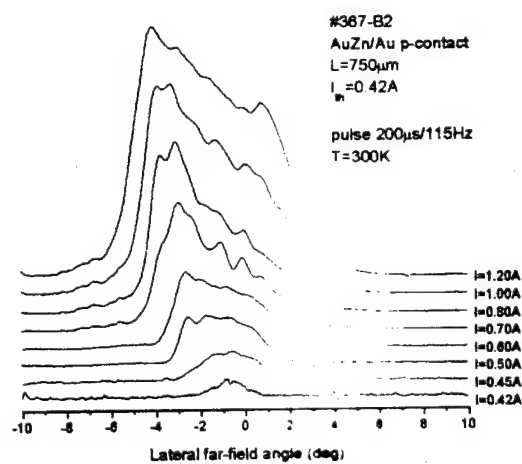
It should be noted that the observed refractive index dependence on the carrier concentration by no means prevents the achievement of single lateral mode operation in narrow stripe lasers. At the same time, this phenomenon should be taken into account during the optimization of narrow stripe laser and MOPA structures and especially for accurate evaluation of spatial hole burning effect on the fundamental mode stability.



(a)

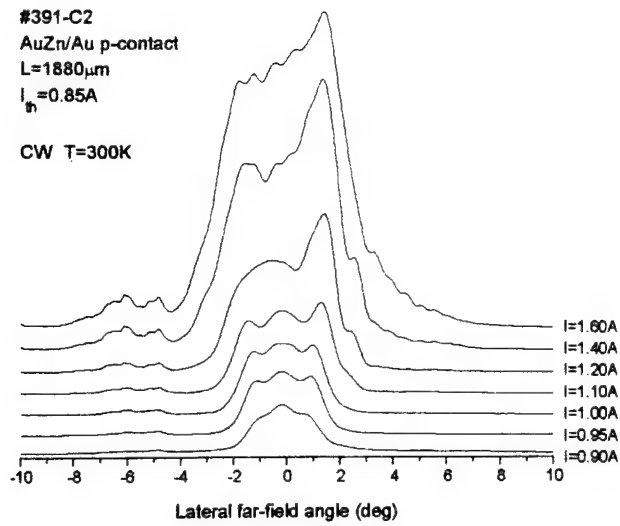


(b)

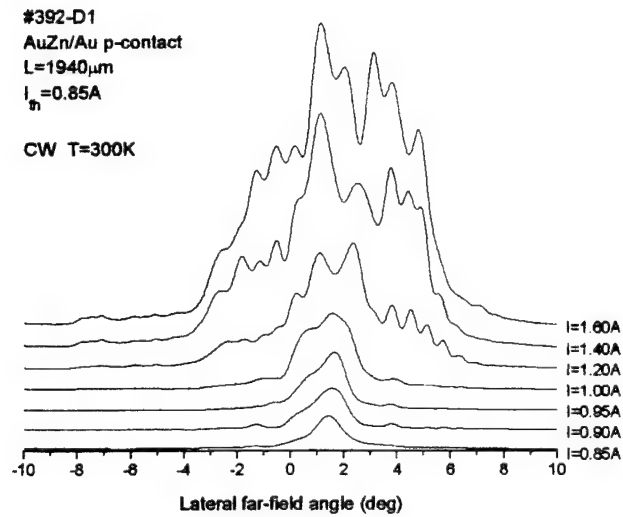


(c)

Fig. 3.15. Lateral far-field patterns of 0.8 $\mu$ m SCH-SQW InGaP/InGaAsP/GaAs laser diode under varying density of (a) continuous wave, (b) pulse 1ms/115Hz, and (c) pulse 200 $\mu$ s/115Hz current.



(a)



(b)

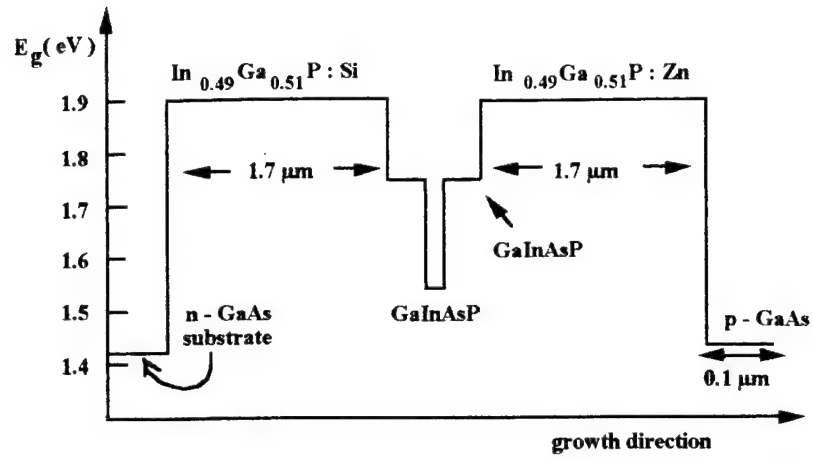
Fig. 3.16. Lateral far-field patterns of 0.8 $\mu$ m SCH-SQW InGaAsP/GaAs laser diodes with  
(a) Zn-doped up to  $p \sim 5 \times 10^{17}$ , and (b) undoped waveguiding layers.

### **3.5 Effect of number of quantum wells in MQW lasers**

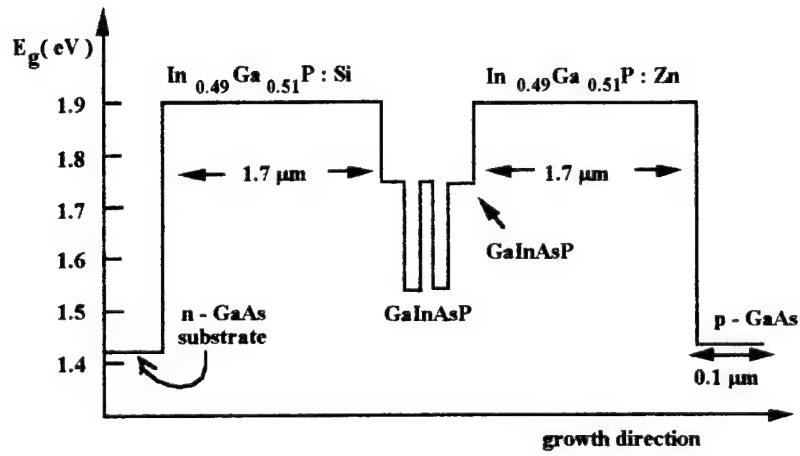
In order to complete the optimization of the SCH laser structure for high-power  $0.8\mu\text{m}$  SCH-SQW InGaAsP/GaAs laser diodes, we have performed the studies of the laser parameter dependence on the number of quantum wells in the active region. Here, we present the experimental results of this work.

We have examined three laser structures with different numbers of quantum wells and with total active layer thickness of  $300\text{ \AA}$  in order to maintain the optical confinement factor constant. These structures allow us to investigate the effects resulting from quantum confinement in the active region, on the threshold current density ( $J_{th}$ ). The ultimate question addressed here is whether multiple narrow quantum wells can provide any advantage as active region material for high-power lasers when compared to single well of the same total width.

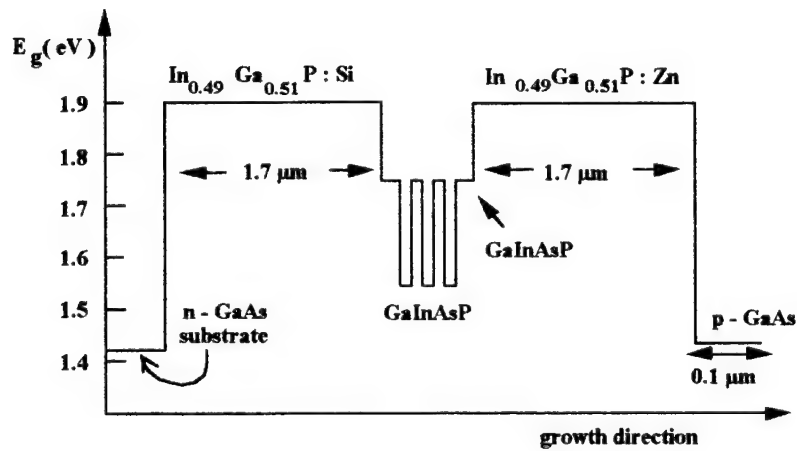
The schematic band diagram of three separate confinement heterostructure (SCH) InGaAsP/GaAs laser structures under study are shown in Fig. 3.17a-c. The three laser structures have different active layer thickness and number of wells:  $300\text{ \AA}$  single quantum well,  $150\text{ \AA}$  double quantum well, and  $100\text{ \AA}$  triple quantum well separated by  $100\text{ \AA}$ -thick InGaAsP barriers between the wells. The active layer for all three SCH structures corresponds to the band gap energy  $1.495\pm 0.005\text{ eV}$ , while the composition of the waveguide layers corresponds to the energy  $1.77\pm 0.01\text{ eV}$ .



a)



b)



c)

Fig. 3.17. Band gap diagrams of a) single quantum well, b) double quantum well, and c) triple quantum well separate confinement heterostructures.

Specific features of  $J_{th}(L)$  dependence for single 300Å well active region have been discussed in the previous report. Experimental results (Fig. 3.18) show that  $J_{th}$  reveals no significant difference between the laser structures with one, two and three quantum wells.

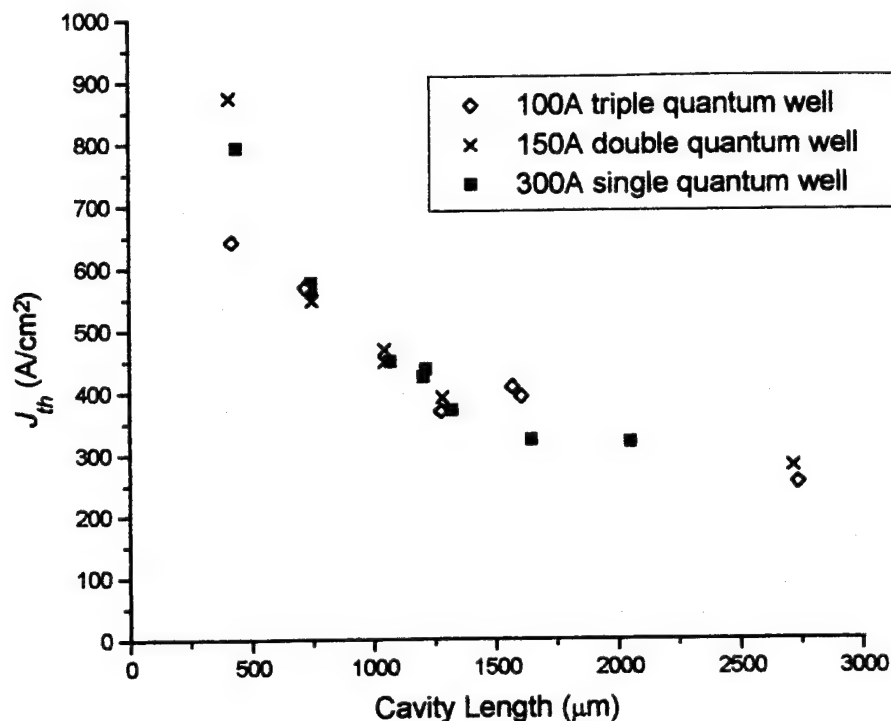


Fig. 3.18. Cavity length dependence of threshold current density for 0.8μm SCH laser diodes with varying active region structure..

Such laser parameters as differential efficiency and characteristic temperature  $T_0$  are also independent on the inner structure of the active region. This can be understood by considering the gain of the laser, since this is the only physical parameter that is affected by the energy level structure depending on the quantum well thickness. Even though narrow quantum well (100 Å-thick) has a higher material gain at injection carrier concentration above  $2.5 \times 10^{18} \text{ cm}^{-3}$  due to the 2-dimensional nature of density of state, the difference is less than 5%. The reason is that in the given range of excess carrier concentrations ( $1 - 4 \times 10^{18} \text{ cm}^{-3}$ ), the only significant transition for 100 Å quantum well is

e1-hh1. Otherwise, the gain would be much larger than that of a thicker (300Å) quantum well. Small difference in the material gain combined with the total active layer thickness being constant, results in the modal gain independent on the number (thickness) of the quantum wells in the active region. According to the obtained experimental results as well as to the theoretical considerations, the usage of multiple quantum wells (MQW) in the active region does not result in any significant advantage for high-power lasers when compared to single well active region with the same total thickness. This conclusion is important for practical purposes because it eliminates a necessity of precise thickness control essential for the growth of MQW structures and helps to achieve lower production costs while maintaining the same high laser efficiency.

In conclusion, the experimental studies of the influence of laser structure parameters on the performance of broad-area high-power 0.8µm SCH InGaAsP/GaAs laser diodes were instrumental in designing the optimized multi-layer laser structure for high-power operation. Differential efficiency of 1.3 W/A for the lasers with cavity length about 800 µm and 1 W/A for cavity length 1 mm is as good as the best values reported for AlGaAs lasers [51]. For high power lasers operating under injection currents far exceeding the threshold value, this parameter is the most significant. The value of  $T_0$  is critical for continuous wave operation when laser is likely to be overheated.  $T_0$  values of 175 K obtained for 0.8 µm Al-free lasers are better than those typical for commercial AlGaAs lasers (130-160 K [52]). Proper design of laser structure insured excellent high-power performance reported in detail in Section 4.

## **Appendix I. Automatization of the experimental setup**

High volume of the accumulated measurement data and the necessity of numerical analysis of the experimental results prompted the efforts aimed at the automatic data acquisition from all the devices used for laser characterization. This goal has been achieved through the implementation of PC-based data acquisition system consisting of the National Instruments Signal Conditioning Extensions assembly (SCXI) and a plug-in data acquisition board installed in Hewlett-Packard 486/33VL computer running LabView software. The configuration of this system provides for simultaneous monitoring of 32 current, voltage and thermocouple signals, signal conditioning (amplification, filtering, averaging, electrical isolation and multiplexing), analog-to-digital conversion, data display and storage, and data export to such applications as Excel, Origin, Mathematica etc. In addition, a number of devices featuring the IEEE-488 interface have been configured for data acquisition and measurement control (Klinger stepping motor controller CC1.1 for far-field measurement system, Acton SpectraPro®-275 monochromator, EG&G 5209 lock-in amplifier and ADVANTEST Q8344A Optical Spectrum Analyzer).

An example of setup configuration for computerized high-power laser measurement is given in Figure A.1.

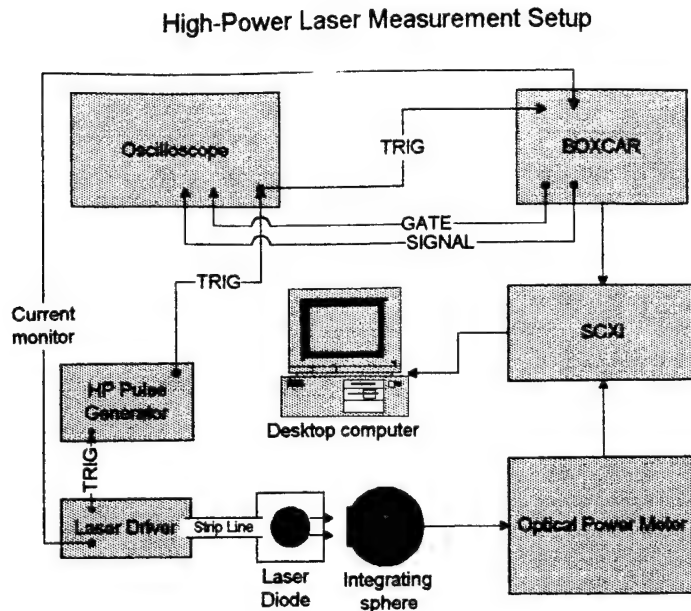
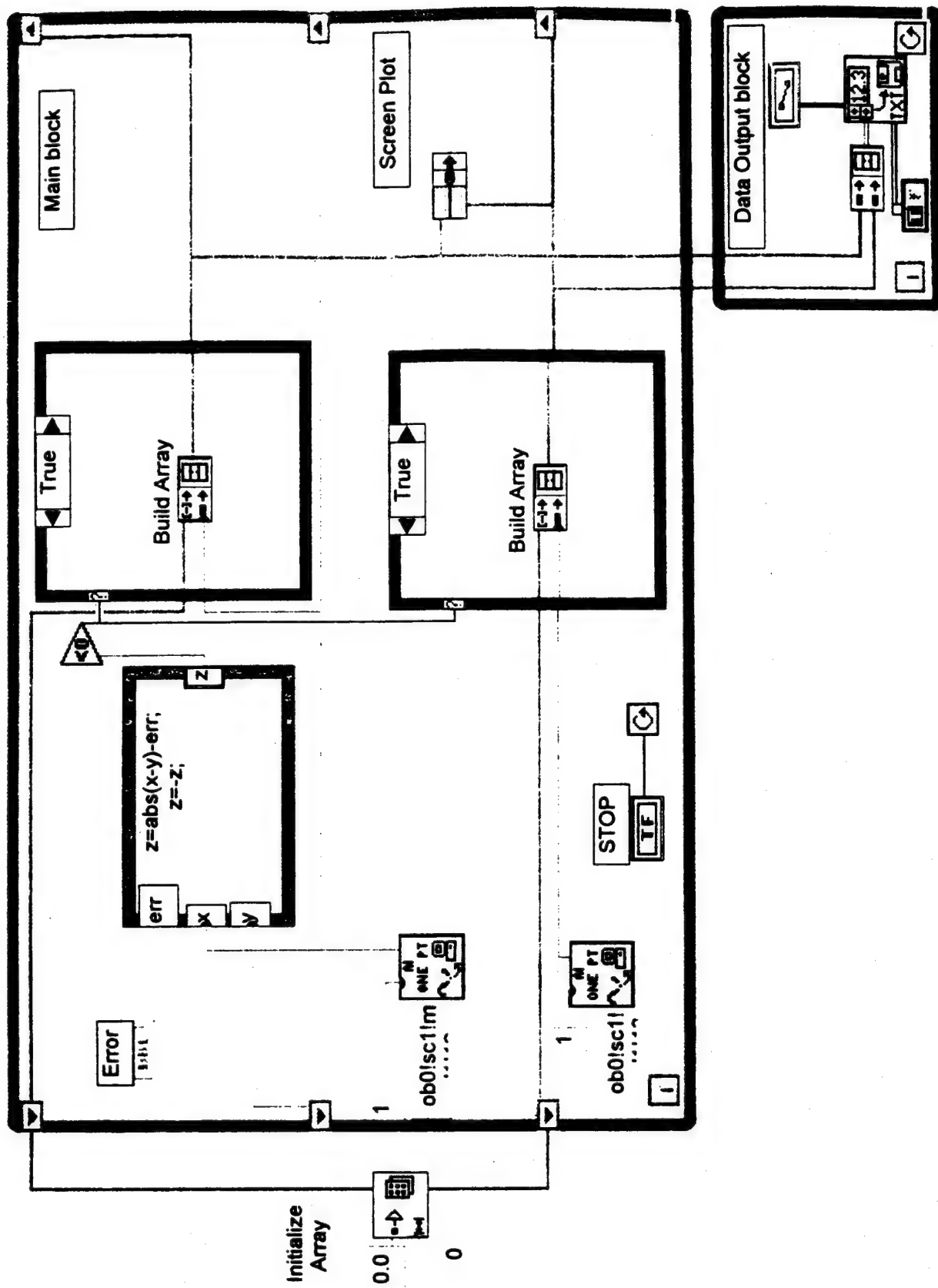


Fig. A.1. Setup configuration for computerized high-power laser measurements.

Current monitoring signal from SDL 820 laser driver (for CW measurements) or Stanford Research Gated Boxcar Averager (for pulse measurement) and output power signal from UDT S380 optometer are conditioned by the SCXI unit, digitized and acquired by the LabView Virtual Instrument (VI) which builds the array of data according to the specified format (TAB-delimited ASCII columns). Fig. A.2 shows the block-diagram of data acquisition and storage VI. This VI simultaneously displays the light-current graph on the computer monitor (Screen Output block) and exports the data file to the computer memory (Data Output block).

As a result, such basic laser characteristics as light-current dependence, optical spectrum, transverse and lateral far-field patterns and electroluminescence spectrum, may be recorded, stored and exported for numerical analysis or graphic presentation. For the sake of security, hard copies of the characteristics are routinely recorded or printed out as a backup protection from computer faults or data corruption.

Block Diagram



## Section 4. High power measurements and reliability testing

### 4.1 High-power measurements

Optimization of laser efficiency through the design of laser structure with minimal current leakage and internal loss stimulated the effort to obtain high power output from relatively short laser diodes corresponding to the maximum values of differential efficiency. The highest differential efficiency of 1-1.3 W/A has been typically observed for single-well laser diodes with cavity length 0.6-0.8 mm. As shown in Fig. 4.1, the best result has been observed for the laser with cavity length 0.78 mm which delivered the output power about 7 W limited by the current driver rather than COD of the facet. This result corresponds to optical power density on the laser mirror as high as 6 MW/cm<sup>2</sup>.

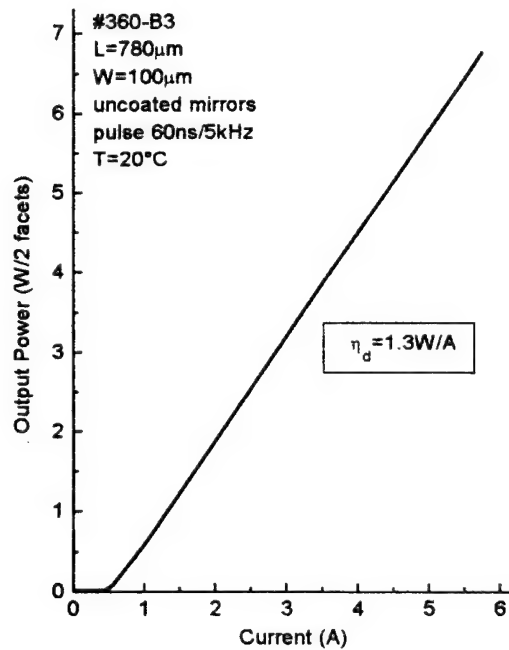


Fig. 4.1. Output power vs. current for high-power InGaAsP/GaAs diode laser with uncoated facets

After mirror coating, pulse output power as high as 4.6W has been delivered from one facet with 100  $\mu\text{m}$  - wide aperture under driving current as low as 4.5 A. High power

measurements for single-well laser diodes were performed in continuous wave (CW) and quasi-CW (pulse width 200  $\mu$ s, frequency 10 Hz) operation. The light output power versus CW current curve for one of these lasers is illustrated in Fig. 4.2. Catastrophic degradation of the uncoated laser mirror does not occur at power level of 2.17 W per facet in CW-regime and maximum power has been limited by thermoelectric cooler capacity. Total quasi-CW output power as high as 7 W has been obtained from single 200  $\mu$ m-wide stripe, corresponding to the optical power density of 2.5 MW/cm<sup>2</sup>.

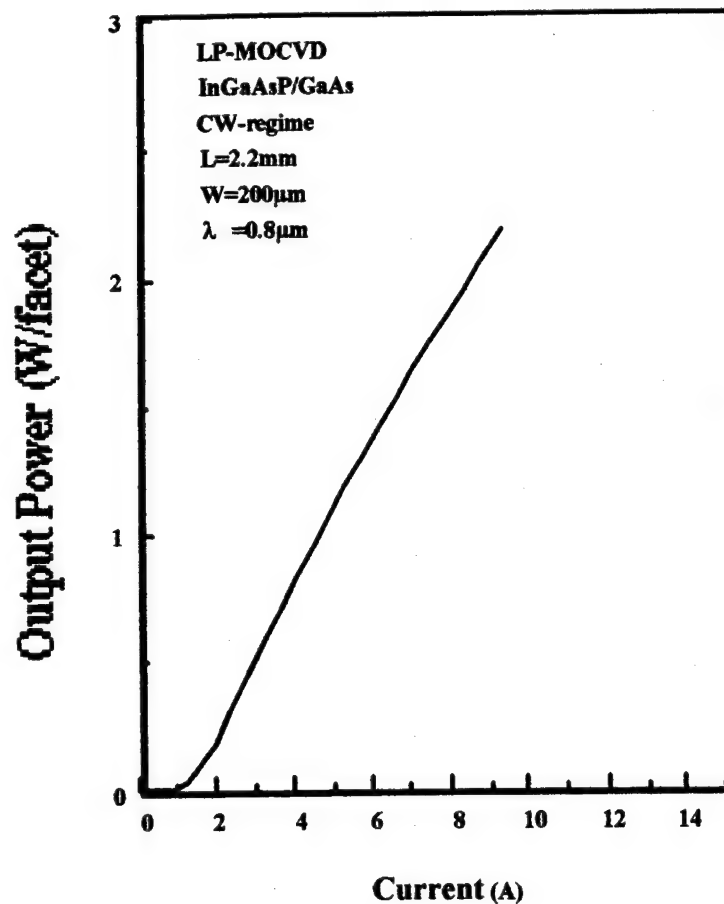
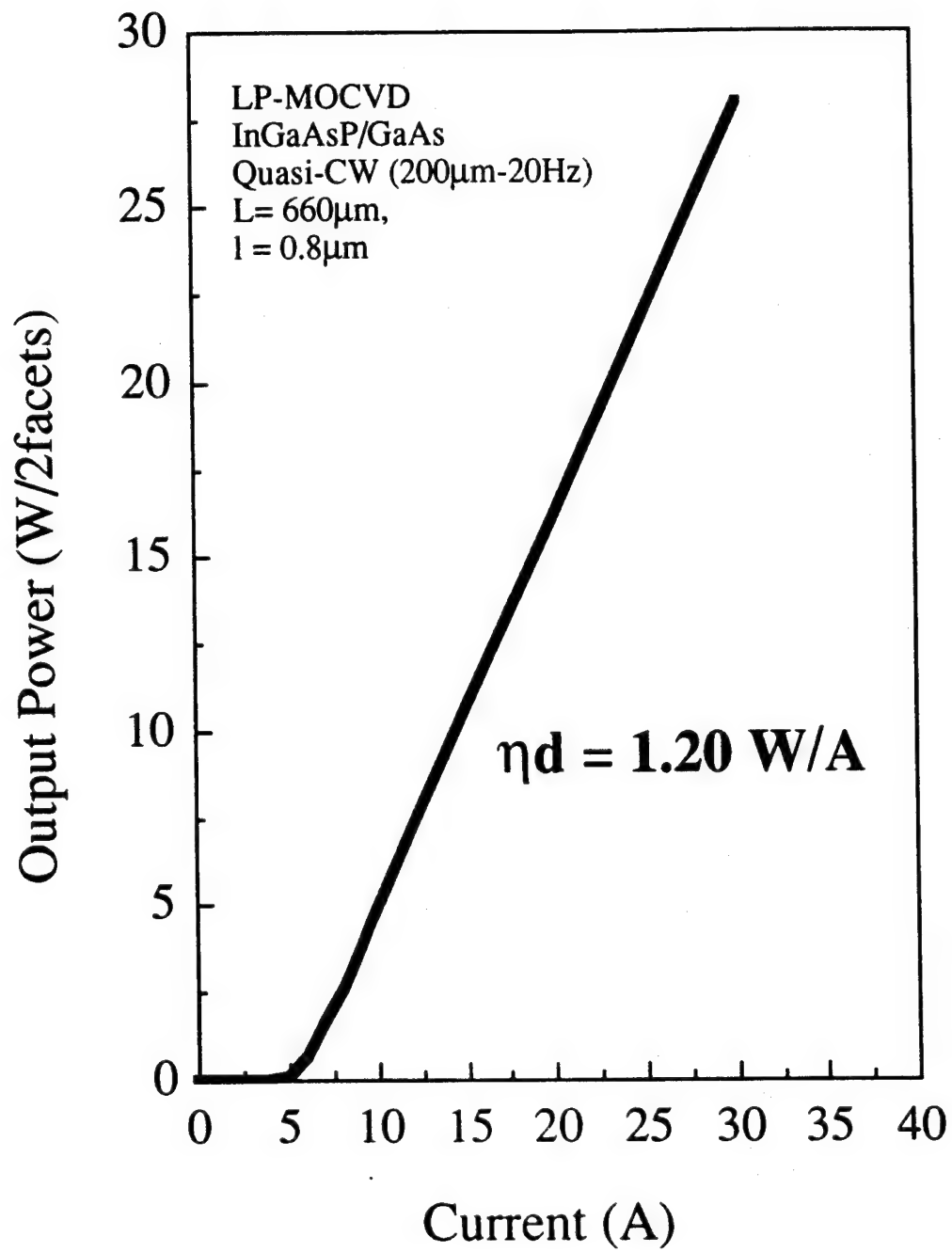


Fig. 4.2. Output power vs. current for high-power InGaAsP/GaAs diode laser with uncoated facets

High optical output may be achieved from laser bars consisting of several separate gain-guided stripes under condition of high uniformity of current density and thermal flow from the active region of different stripes. This requirement has been satisfied by increasing the temperature of indium-bond formation from 160°C to 220-240°C. However, this temperature is only suitable for the lasers with TiPt/Au p-type contact. Lasers with AuZn/Au contact demonstrated a rollover of light-current characteristic at low power level, originating from contact degradation and consequent current leakage through the p-n junction. On the contrary, the same laser structure with TiPt/Au contact mounted under the same conditions featured high contact uniformity and operated in high current density and high output power regime. Excellent uniformity of indium-bond formed under high temperature provided for mounting and testing of the laser bars as wide as 4.5 mm consisting of 15 100  $\mu\text{m}$ -wide stripes on 300  $\mu\text{m}$  centers (filling factor 33%). Experiments with high-amplitude current pulses were performed using a specially designed setup consisting of 100 A Q-CW laser driver (Advance Modules), low-impedance strip transmission line and a cooling circuit. Quasi-CW output power as high as 27 W has been obtained in this setup from a device with the highest differential efficiency of 1.2 W/A (Fig. 4.3).



This result stimulated an attempt to fabricate and test a laser bar with increased emitting aperture and filling factor, capable of higher power operation. The following progress in this direction has been made by far:

- New heatsink design has been developed and implemented suitable for laser bars with total aperture as wide as 1 cm;
- Liquid-cooled temperature-controlled test stage has been developed and assembled. The projected capacity of the stage amounts to 100 A Q-CW current (200  $\mu$ s/20 Hz);
- Test sample consisting of several separate bars has been fabricated of structure #344 with 200  $\mu$ m contact stripes on 300 $\mu$ m centers (filling factor 66%). Total emitting aperture was close to 9 mm (30 stripes).

The bars were mounted on the new type of heatsink and tested under Q-CW driving current (200  $\mu$ s/20 Hz) up to the limit of the current driver (100 A). At the highest point total output power reached 46W (Fig.4.4).

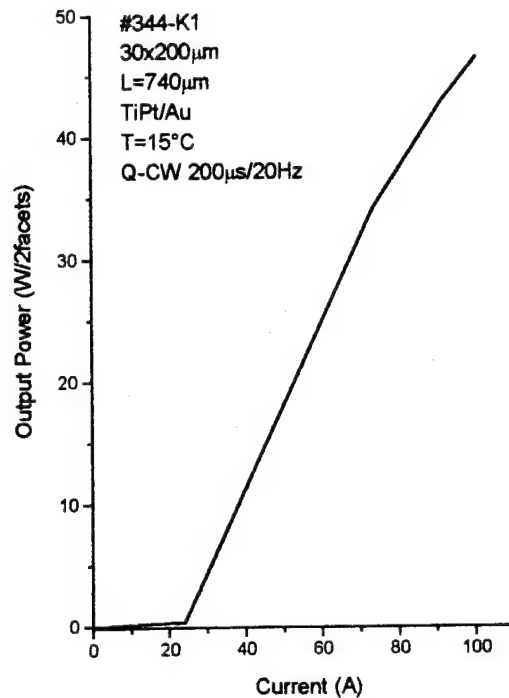


Fig. 4.4. Output power vs. current for high-power InGaAsP/GaAs diode laser bar with uncoated facets.

After a few seconds of operation the power dropped to 45W and stabilized at this level. Operation temperature of 15°C was reliably supported by the cooling stage. Differential efficiency observed in this experiment was close to 0.7 W/A. The sample was turned off and on several times and reached the 45 W power level without further degradation. Microscopic inspection of the mirrors revealed local mirror damage of 3 stripes while the rest of the facet was intact.

The following conclusions have been drawn as a result of this preliminary test:

- New designs of heatsink and cooling stage are efficiently supporting the laser bar operation up to the Q-CW driving current of 100 A;
- Single bar fabricated of a laser structure similar to #387 should be used to increase the differential efficiency;

- Output power may be increased by reducing the number of stripes in the laser bar. Along with lower threshold current, this should result in higher optical density on the laser mirror.

Indeed, output power as high as 67 W has been obtained from laser bar consisting of 32 100  $\mu\text{m}$ -wide stripes with lower threshold current of 15 A (Fig. 4.5).

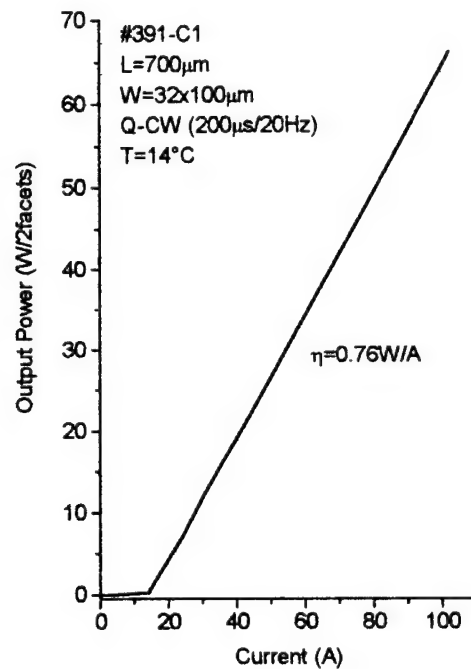


Fig. 4.5. Output power vs. current for high-power InGaAsP/GaAs diode laser bar with uncoated facets.

Lower estimate for COD limit of InGaAsP/GaAs material can be made based on the highest output power values observed for uncoated 100 $\mu\text{m}$ -wide broad-area lasers in Q-CW ( 2.5 MW/cm<sup>2</sup>) and pulse (6 MW/cm<sup>2</sup>) modes. COD-limited output power from 1 cm-wide uncoated laser bar may be estimated as 150 W/facet. It is interesting to compare this value with the available data on COD limit values for AlGaAs-based lasers and arrays. To the best of our knowledge, the record data published for 1 cm-wide array

and 100 $\mu$ m-wide array are 3.4MW/cm<sup>2</sup> [2] and 8MW/cm<sup>2</sup> Q-CW [47], respectively. Comparing these values with the measured data for Al-free 808nm material, it is necessary to keep in mind two important considerations ("compare apples and apples"). First, the reported data for AlGaAs lasers refer to the COD limits for coated facets while the values obtained in the absence of coating are typically an order of magnitude lower [48]. Second, broad area lasers tend to display lower COD limits when compared to the arrays of narrow current-confining stripes as those reported in [47] due to current filamentation. Therefore, much higher COD limits may be expected for narrow-stripe Al-free laser structures with coated facets. As an example, COD limits as high as 8 MW/cm<sup>2</sup> in CW and 16 MW/cm<sup>2</sup> in Q-CW have been reported for 4  $\mu$ m-wide stripe Al-free lasers with coated facets emitting at 980nm [17]. More or less sensible comparison may be made with the data quoted in [48] for uncoated 10  $\mu$ m-wide stripe AlGaAs lasers as shown in Table 4.1 which shows that higher COD limits have been obtained for Al-free lasers despite the adverse effect of current filamentation.

Table 4.1. COD limits for AlGaAs and Al-free lasers

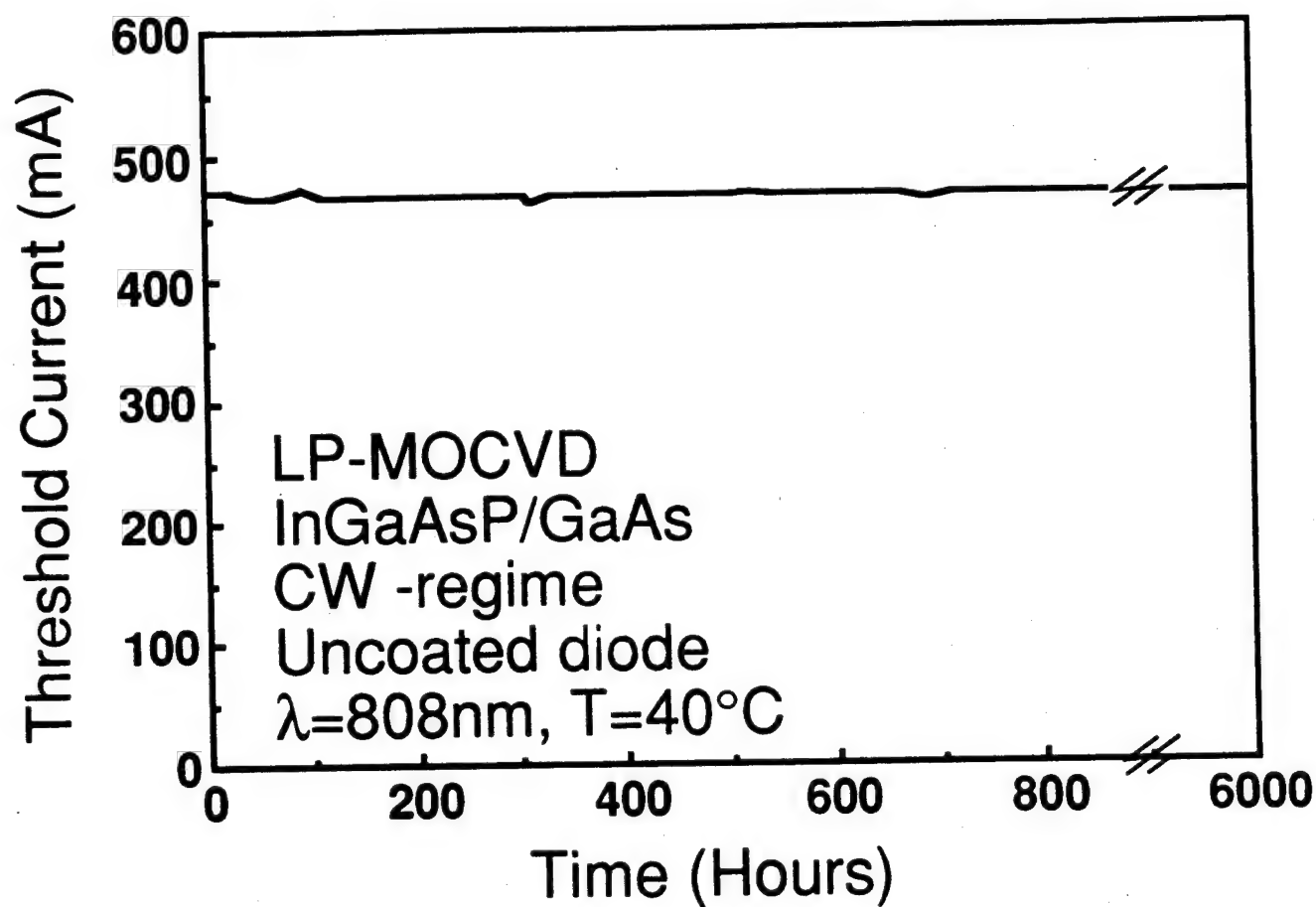
	InGaAsP 100 $\mu$ m-wide	AlGaAs 10 $\mu$ m-wide [48]
pulse	6MW/cm <sup>2</sup>	3MW/cm <sup>2</sup>
Q-CW	2.5MW/cm <sup>2</sup>	1MW/cm <sup>2</sup>

#### **4.2 Reliability testing**

A rapid degradation test has been performed on 5 identical uncoated lasers with a 100  $\mu$ m - wide aperture and a cavity length  $\sim$ 1 mm. After 40 hours of testing under a constant CW current of 1.5 A, corresponding to the optical output power of about 400†mW per facet, the output power was either stable or increased by  $\sim$ 1%. No degradation of the

laser parameters or change of the emission wavelength was observed. The increase of the optical power may be attributed to current-induced annealing of the indium bond resulting in a more uniform current distribution across the contact stripe.

A diode laser with a 100  $\mu\text{m}$ -wide stripe bonded p-side down has been subjected to lifetime testing under a constant current of 1.5 A CW. The laser emitting 800 mW total power operated for 6000 hours in the CW-regime at 40°C as illustrated in Fig. 4.6. After more than 6 months of aging, the laser diode continues to operate without any increase of threshold current density and wavelength shift. The testing was interrupted  $\sim 10$  times for threshold current and lasing wavelength monitoring and the laser survived the corresponding thermal cycling without any damage. This result may be compared to the recent experiments with uncoated AlGaAs lasers performed by IBM [49,50]. Ridge-geometry lasers with 5  $\mu\text{m}$ -wide stripes were operated at a CW power of 40 mW corresponding to the same optical power density. Typical lifetime observed in these experiments was about 20 minutes and resulted in catastrophic degradation. After pretreatment under inert ambient, the lifetime increased by almost 3 orders of magnitude but still remained close to 200 hours [49]. This comparison vividly demonstrates the superior reliability of aluminum-free lasers and corroborates the effect of low mirror facet-temperature previously reported for InGaAsP lasers [18] as well as the resistance of In-based materials to dark-line defect propagation [48]. A more detailed lifetime testing of the lasers with mirror facet coatings should give additional information about the comparative reliability of InGaAsP and AlGaAs high-power 808 nm lasers.



Six laser diodes have been randomly selected without burn-in testing or any selection. All the lasers are 100  $\mu\text{m}$ -wide broad-area devices with a cavity length of 1 mm. No facet coating has been applied to the laser mirrors. The diodes are mounted junction side down on copper heatsinks by indium bonding. The lifetime testing is performed under a constant flow of dry nitrogen in computer-controlled Laser Reliability System (LRS) custom designed and manufactured by EMS Development Corp. in collaboration with the Center.

In the first stage of experiment, all laser diodes were tested at room temperature and constant optical output power of 500 mW. After 2000 hours, no degradation was observed for 5 of the tested lasers, while one showed a slight increase of the operating current values(#387-F3 in Fig. 4.7).

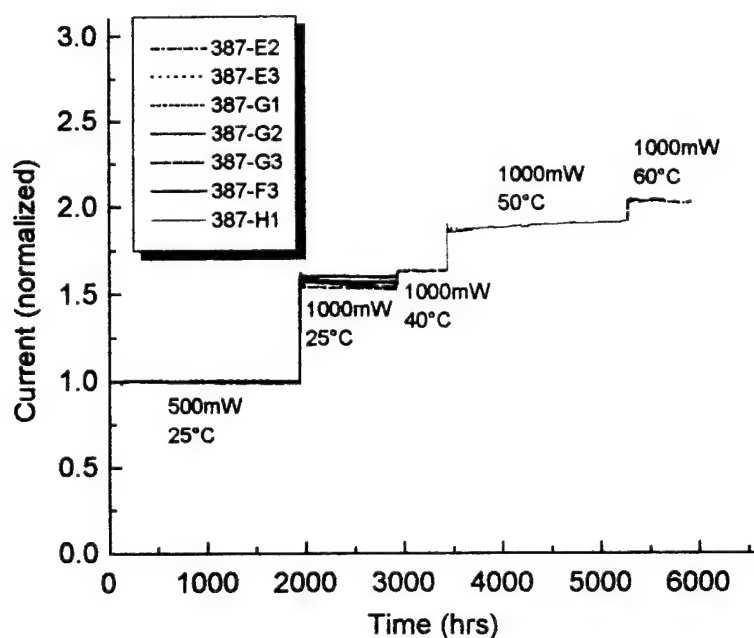


Fig. 4.7 Reliability of 6 randomly selected InGaAsP/GaAs 808 nm laser diodes. Constant power @ 500 mW & 1000 mW (uncoated facets).

Assuming a linear degradation rate and a lifetime criterion of 20% increase in the operating current, the minimum projected lifetime was estimated as  $2 \times 10^6$  hours. Following this initial test period, the lasing wavelengths has been measured for all the lasers under test and compared to the initial values. No change of the lasing wavelength has been observed within the accuracy of measurement ( $5 \text{ \AA}$ ).

The output power was then increased to 1 Watt and the test continued for the same set of samples. Again, after an additional 1000 hours of testing 5 lasers showed no degradation, while the same #387-F3 showed an increase of the operating current, corresponding to the lifetime of  $1.65 \times 10^6$  hours (188 years). Comparison of the sample #387-F3 with the other laser samples showed that in this case laser chip had been shifted out of the heatsink edge by  $\sim 25\text{-}30 \text{ \mu m}$  which evidently resulted in the laser mirror overheating and gradual degradation.

At this point, the batch testing was temporary terminated to determine the temperature limit at which the degradation becomes visible. One laser diode was operated at 1 W output power for 500 hours at  $40^\circ\text{C}$  for 2000 hours at  $50^\circ\text{C}$  and for 1000 hours at  $60^\circ\text{C}$  without noticeable degradation, and the testing currently continues.

Figure 4.7 shows that most of the lasers exhibit a slight improvement of their characteristics resulting in the decrease of the operating current. Similar behavior has been previously reported for high-quality MOCVD-grown aluminum-free InGaAsP/InP lasers with lifetime in excess of  $10^7$  hours [46]. This effect is attributed to the gradual annealing of the laser contacts and indium bond leading to some decrease in electrical and thermal resistance of the device.

### **4.3 Diode-pumped Nd:YAG solid state laser.**

We have demonstrated a diode pumped Nd:YAG laser utilizing an aluminum-free laser diodes fabricated at the Center for Quantum Devices. The diode pumped laser operated in a round Gaussian ( $\text{TEM}_{00}$ ) transverse mode with a sub-angstrom spectral width at  $1.064$

$\mu\text{m}$  (Fig. 4.8). The aluminum-free InGaAsP laser diodes are 100  $\mu\text{m}$  wide broad stripe devices without facet coatings in a triple quantum well arrangement. The solid-state laser efficiency of 25% was comparable to typical commercial devices pumped with AlGaAs laser diodes. This was expected since a comparison of divergence and spectral characteristics between pump diodes of either material system are virtually identical. The main advantage of the quaternary material system is expected to be in extended lifetime since it is an aluminum-free system. This advantage is particularly important for telecommunication applications in which the diode pumped laser can be used as a pump source for a fiber amplifier.

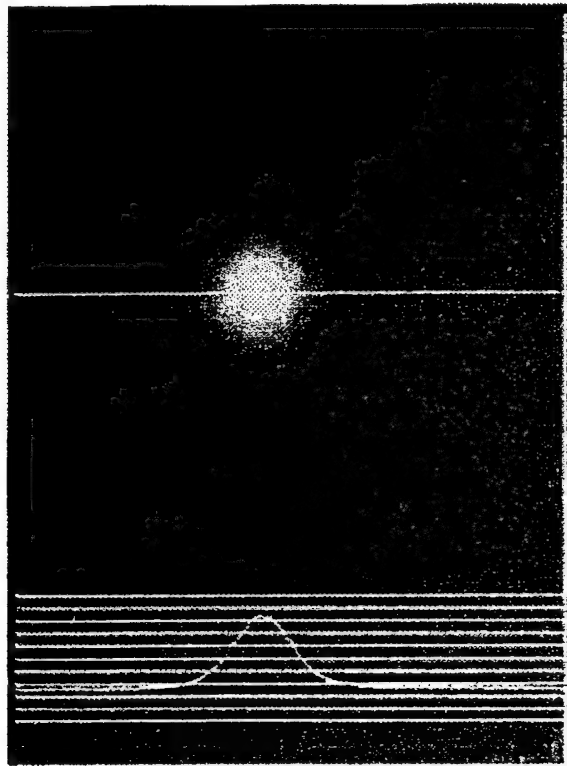


Fig. 4.8. Far-field pattern of Nd:YAG solid state laser pumped with InGaAsP/GaAs laser diode.

## Section 5. Conclusions and future research

It may be interesting to compare the key laser parameters for Al-free InGaAsP/GaAs and AlGaAs 0.8 $\mu$ m laser diodes. Table 5.1 summarizes the results of Center for Quantum Devices and data on AlGaAs lasers available in literature.

Table 5.1 Comparison of AlGaAs versus Aluminum-free InGaAsP/GaAs  
High Power Laser Diodes (aperture 100  $\mu$ m)

	AlGaAs	InGaAsP (results of CQD)
$\lambda$ (nm)	800	800
$J_{th}$ (A/cm <sup>2</sup> )	230 <sup>Ref.51</sup> -400 <sup>Ref.52</sup>	240-500
$\eta_d$ (W/A)	1.3 <sup>Ref.51</sup> -0.8 <sup>Ref.52</sup>	1.3
$T_0$ (°C)	130-160 <sup>Ref.52</sup>	170-175
Series resistance ( $\Omega$ )	0.25 <sup>Ref.52</sup>	0.1
Thermal resistance (K/W)	10 <sup>Ref.52</sup>	~1
Transverse beam divergence	32-48 <sup>Ref.52</sup>	26°
COD limit for uncoated facets (MW/cm <sup>2</sup> )	0.5-1 <sup>Ref.48</sup>	6
Lifetime under 1MW/cm <sup>2</sup> (hours)	200 (uncoated facets <sup>Ref.50</sup> )	>1,650,000 (uncoated facets)
Degradation under 1 Watt (uncoated facets)	Immediate	No degradation after 2000hrs at 500mW + 1000hrs at 1W + 500hrs at 1W, 40°C + 2000hrs at 1W, 50°C + 1000hrs at 1W, 60°C (test continues)

As can be seen from the Table, optimized Al-free InGaAsP/GaAs lasers demonstrate a performance comparable with the best commercially available AlGaAs lasers in terms of threshold current density, differential efficiency, series resistance and  $T_0$  while significantly outperforming AlGaAs in transverse beam divergence, thermal resistance, mirror damage resistivity and lifetime for uncoated lasers. Al-free lasers are therefore a viable replacement for AlGaAs 808 nm devices used in solid state pumping systems. Their implementation promises a considerable increase of overall system performance and reliability.

Future research should focus on the achievement of

- high-power single lateral mode operation of buried ridge lasers,
- optimization of mirror facet coating,
- continuation of lifetime testing at higher power level, and
- lifetime testing of buried ridge lasers with coated facets.

## References

- [1] B. Zhou, T. J. Kane, G. J. Dixon, and R. L. Byer, *Opt. Lett.*, vol. 10, p. 62, 1985.
- [2] J. G. Endriz, M. Vakili, G. S. Browder, M. DeVito, J. M. Haden, G. L. Harnagel, W. E. Plano, M. Sakamoto, D. F. Welch, S. Willing, D. P. Worland, and H. C. Yao, "High Power Diode Laser Arrays", *IEEE J. Quantum Electron.*, vol. QE-28, pp. 952-965, 1992.
- [3] M. Razeghi, M. Defour, and F. Omnes, *Appl. Phys. Lett.*, vol. 55 (5), p. 457, 1989.
- [4] U. Ekenberg and M. Altarelli, *Phys. Rev. B*, vol. 35, p. 7585, 1987.
- [5] Y. J. Chan, D. Pavlidis, M. Razeghi, and F. Omnes, *IEEE Trans. Electron. Devices*, vol. ED-37, p. 2141, 1990.
- [6] S. L. Feng, J. C. Bourgoin, F. Omnes and M. Razeghi, *Appl. Phys. Lett.*, vol. 59, (8), p. 941, 1991.
- [7] X. He and M. Razeghi, *Appl. Phys. Lett.*, vol. 61, pp. 1703-1705, 1992.
- [8] X. He and M. Razeghi, "Well resolved room-temperature photovoltage spectra of GaAs-GaInP quantum wells and superlattices", *Appl. Phys. Lett.*, vol. 62, pp. 618-620, 1993.
- [9] T. Ijichi, M. Ohkubo, N. Matsumoto, and H. Okamoto, in *Tech. Dig. IEEE 12th International Semiconductor Laser Conf.*, Davos, Switzerland, p. 44, 1990.
- [10] K. Mobarhan, M. Razeghi, G. Marquebielle, and E. Vassilaki, "High power,  $0.98\mu\text{m}$ , Ga<sub>0.8</sub>In<sub>0.2</sub>As/GaAs/Ga<sub>0.51</sub>In<sub>0.49</sub>P multiple quantum well laser," *J. Appl. Phys.*, vol. 72, pp. 4447-4448, 1992.
- [11] G. Zhang, J. Näppi, K. Vanttinen, H. Asonen, and M. Pessa, *Appl. Phys. Lett.*, vol. 61, p. 96, 1992.
- [12] K. Mobarhan, M. Razeghi, and R. Blondeau, "Ga<sub>0.8</sub>In<sub>0.2</sub>As/GaAs/Ga<sub>0.51</sub>In<sub>0.49</sub>P buried ridge structure single quantum well laser emitting at  $0.98\mu\text{m}$ ", *Electron. Lett.*, vol. 28, pp. 1510-1511, 1992.
- [13] S. H. Groves, J. N. Walpole, and L. J. Missagia, *Appl. Phys. Lett.*, vol. 61, p. 255, 1992.

- [14] W. T. Tsang, R. Kapre, M. C. Wu, and Y. K. Chen, *Appl. Phys. Lett.*, vol. 61, p. 755, 1992.
- [15] C. J. Chang-Hasnain, R. Bhat, H. Leblanc and M. A. Koza, *Electron. Lett.*, vol. 29, pp. 1-2, 1993.
- [16] Y. K. Sin, H. Horikawa, and T. Kamijoh, *Electron. Lett.*, vol. 29, pp. 240-242, 1993.
- [17] H. Asonen, J. Näppi, A. Ovtchinnikov, P. Savolainen, G. Zhang, R. Ries, and M. Pessa, *IEEE Photon. Technol. Lett.*, vol. 5, p. 589, 1993.
- [18] D. Z. Garbuzov, N. Yu. Antonishkis, A. D. Bondarev, A. B. Gulakov, S. N. Zhigulin, N. I. Katsavets, A. V. Kochergin, and E. V. Rafailov, *IEEE J. Quantum Electron.*, vol. QE-27, p. 1531, 1991.
- [19] Zh. I. Alferov and D. Z. Garbuzov, in *Proc. 18th Int. Conf. Phys. Semiconductors*, vol. 1, Stockholm, Sweden, p. 203, 1986.
- [20] D. K. Wagner, R. G. Waters, P. L. Tihanyi, H. J. Vollmer, A. J. Roza, D. S. Hill, M. M. Leopold, *IEEE J. Quantum Electron.*, vol. QE-24, p. 1258, 1988.
- [21] P. S. Zory, J. J. Coleman, G. Costrini, M. A. Emanuel, M. E. Givens, L. J. Mawst, A. R. Reisinger, C. A. Zmudzinski, *Electron. Lett.*, vol. 22, p. 475, 1986.
- [22] P. Blood, A. I. Kucharska, J. P. Jacobs, and K. Griffiths, "Measurement and calculation of spontaneous recombination current and optical gain in GaAs-AlGaAs quantum-well structures", *J. Appl. Phys.*, vol. 70, (3) pp. 1144-1156, 1991.
- [23] R. K. Ahrenkiel, B. M. Keyes, and D. J. Dunlavy, "Intensity-dependent minority-carrier lifetime in III-V semiconductors due to saturation of recombination centers", *J. Appl. Phys.*, vol. 70, (1) pp. 225-231, 1991.
- [24a] T. Ikegami, *IEEE J. Quantum Electron.*, vol. QE-8, p. 470, 1972.
- [24b] M. A. Afromowitz, *Solid State Comm.*, vol. 15, p. 59, 1974.
- [25] C. H. Henry, R. A. Logan, and K. A. Bertness, *J. Appl. Phys.*, vol. 52, (7) p. 4453, 1981.
- [26] T. S. Moss, G. J. Burrell, B. Ellis, "Semiconductor Opto-Electronics", John Wiley and Sons, NY, 1973.

- [27] D. Z. Garbuzov, V. B. Khalfin, In: "Quantum Well Lasers", ed. P. Zory, Academic Press, NY, 1993.
- [28] Zh. I. Alferov, I. N. Arsent'ev, D. Z. Garbuzov, E. Tulashvili, "Low-threshold pulsed and CW InGaAsP/InGaP/GaAs double-heterojunction lasers emitting visible radiation in the 0.73-0.79  $\mu\text{m}$  range ( $T=300\text{K}$ ,  $I_{\text{th}}=3.5\text{-}1.3\text{ kA/cm}^2$ )", *Sov. Phys. Semicond.* vol. 18 (1), pp. 99-101, 1984.
- [29] J. C. Dymant, F. R. Nash, C. J. Hwang, G. A. Rozgonyi, R. L. Hartman, H. M. Marcos, and S. E. Haszko, "Threshold reduction by the addition of phosphorus to the ternary layers of double-heterostructure GaAs lasers", *Appl. Phys. Lett.*, vol. 24, pp. 481-484, 1974.
- [30] X. He and M. Razeghi, *J. Appl. Phys.*, vol. 62, p. 4447, 1992.
- [31] A. Larsson, J. Salzman, M. Mittelstein, and A. Yariv, *J. Appl. Phys.*, vol. 60 (1), p. 66, 1986.
- [32] M. Sakamoto and Y. Kato, *Appl. Phys. Lett.*, vol. 50, p. 869, 1987.
- [33] M. Razeghi, J. Diaz, I. Eliashevich, K. Mobarhan, X. He, E. Kolev, L. Wang, and D. Garbuzov, "MOCVD-grown GaInAsP-GaAs laser for Nd:YAG pumping", *Proceedings of IEEE/LEOS Conference, San Jose, CA, November 15-18, 1993, Post-Deadline Papers*, pp. 27-28, paper PD2.4.
- [34] P. Zory (ed.), "Quantum Well Lasers" (Academic Press Inc., San Diego, CA, 1993), p.310.
- [35] W. Rideout, W. F. Sharfin, E. S. Koteles, M. O. Vassell, and B. Elman, *IEEE Photon. Technol. Lett. PTL-3*, 784 (1991).
- [36] M. Razeghi, *Nature*, **369**, 631 (1994).
- [37] J. Diaz, H. J. Yi, M. Erdtmann, X. He, E. Kolev, D. Garbuzov, E. Bigan, and M. Razeghi, *J. Appl. Phys.* **76**, 700 (1994).
- [38] J. Diaz, I. Eliashevich, X. He, H. Yi, L. Wang, E. Kolev, D. Garbuzov, and M. Razeghi, *Appl. Phys. Lett.* **65**, 1004 (1994).
- [39] J. Diaz, I. Eliashevich, H. J. Yi, X. He, M. Stanton, M. Erdtmann, L. Wang, and M. Razeghi, , *Appl. Phys. Lett.* **65**, p. 2260 (1994).
- [40] H. C. Casey, Jr., M. B. Panish, W. O. Schlosser, and T. Paoli, *J. Appl. Phys.* **45**, 322 (1974).

- [41] J. Butler and J. Zoroofchi, IEEE J. Quantum Electron. **QE-10**, 809 (1974).
- [42] N. S. Takashi, A. Fukushima, T. Sasaki, J. Ishikawa, K. Ninomiya, H. Narui, and Sh. Kurita, J. Appl. Phys. **59**, 761 (1986).
- [43] H. C. Casey, Jr., M. B. Panish, and J. L. Merz, J. Appl. Phys. **44**, 5470 (1973).
- [44] M. E. Givens, L. M. Miller, and J. J. Coleman, J. Appl. Phys. **71**, 4583 (1992).
- [45] R. J. Deri and E. Kapon, IEEE J. Quantum Electron. **QE-27**, 626 (1991).
- [46] M. Razeghi, "MOCVD Challenge" (Adam Hilger, Bristol and Philadelphia, 1989).
- [47] D. F. Welch et al., Electron. Lett. **24**, p.113 (1988)
- [48] M. Fukuda, "Reliability and Degradation of Semiconductor Lasers and LEDs", Artech House, Boston, London, 1991, pp.179-181
- [49] F. R. Gfeffer and D. J. Webb, J. Appl. Phys. **68**, p. 14 (1990).
- [50] W. C. Tang, E. H. Altendorf, H. J. Rosen, D.J. Webb, P. Vettiger, Electron. Lett. **30**, p. 143 (1994).
- [51] A. Yariv et al. *Electron. Lett.* **22**, p. 79 (1986)
- [52] Spectra Diode Labs, 1994 Product Catalog

## *CHAPTER V*

### *THEORETICAL ANALYSIS OF 808nm InGaAsP/GaAs LASERS*

## I. Introduction

High-power diode lasers of wavelength  $\lambda=808$  nm are attractive source for pumping solid-state lasers. Laser diodes provide very high power conversion efficiency as well as effective coupling to the solid-state laser, incomparable to conventional flash lamps.

Until the recent introduction of quaternary InGaAsP/GaAs material as an alternative [1], most of the research on this category of lasers have been based on the Al-containing materials, that is, AlGaAs/GaAs. Even though Al-based material possesses benefits such as easier epitaxial growth compared to the quaternary material due to inherently good lattice-match, it has fundamental limit for high power due to the catastrophic optical damage [2] and dark line defect formation [3]. InGaAsP material has shown much higher catastrophic optical damage limit,  $2.2 \text{ MW/cm}^2$  for uncoated laser at CW operation (compared to  $0.5 \text{ MW/cm}^2$  for AlGaAs lasers) and more than  $9 \text{ MW/cm}^2$  for coated laser at CW operation [4]. This higher optical damage limit may be attributed to the much lower surface recombination rate, about two orders of magnitude less than for AlGaAs system [4a]. Very strong resistance to dark line defect formation [3] and degradation by metal ohmic contact [5] is attributed to dislocation pinning by large In atoms [6]. In addition, good etching selectivity between GaInP and GaAs heterostructure and immunity to oxidation greatly facilitate the regrowth procedures [7]. Recent lifetime test revealed that a diode without mirror coating did not show any degradation after 6000 hours of operation at  $40^\circ\text{C}$  while emitting 800 mW of CW power [8]. This result is a large contrast to the AlGaAs counterpart which endured only about 200 hours even after special treatment when operated at the same condition [9]. All of the above facts strongly suggest the use of the InGaAsP/GaAs as an alternative of AlGaAs for high power lasers and laser amplifiers.

### *Necessity of Theoretical Analysis*

Semiconductor laser is a subject requiring various inter-disciplinary studies ranging from quantum field theory for photon and electrons to chemical engineering. During last decades most of basic mechanisms for semiconductor laser operation have been understood through numerous theory and experiment from each area, including detailed mechanism for lasing [11], degradation [12], various dynamic properties [13-15] and even non-classical light generation (as squeezed states) [16] by semiconductor lasers. Nevertheless, there are several reasons that it still remains very difficult job to predict the characteristics of the lasers made of new material system such as InGaAsP/GaAs, from a first principle.

First of all, the laser characteristics include many unsolved physical problems. For example, there is no universal agreement on the most dominant mechanism for intraband momentum relaxation during high-power operation. The momentum relaxation strongly affects optical gain, laser spectrum as well as heating. Another challenging problem is understanding of hetero-interfaces. Still band calculation including interfaces remains difficult problem. Whether interface has intrinsic interface-state acting as DX-center is not fully understood [16a]. Interface-state would strongly influence electric field distribution in multiple quantum well structures through charge accumulation.

In this respect, it is very crucial to perform theoretical analysis on the new material system in parallel to experiment. In this work, we tried to obtain accurate physical models for radiative and non-radiative recombination, intraband momentum relaxation, quantum-size and strain effect on stimulated emission (gain) for the InGaAsP/GaAs material system. Our theoretical analysis was compared with the experimental results and feedback was derived to the theory to elaborate our physical model.

In most cases the experiment and theoretical analysis presented in this work were motivated from optimization of the laser structure. Almost in every experiment for optimization, we found that the experimental results were inexplicable or sometimes contrary to the conventional theory and could be explained only when we elaborated some factors that had not been considered in detail so far. This clearly vindicates our above argument that theory that models semiconductor lasers should be developed case by case for an enough accuracy to “engineer” this highly sophisticated device, high-power laser.

In the following, we report our theoretical analysis given on

- ◇ radiative recombination efficiency
- ◇ minority carrier leakage to barrier layers
- ◇ quantum-size effect on gain and threshold current density
- ◇ momentum relaxation
- ◇ strain effect on density of states and gain
- ◇ linewidth enhancement factor  $\alpha$  on near- and far-field pattern

At a first glance, these topics look unrelated to each other. It will be obvious, however, that all of the research stemmed from one purpose: optimal engineering of the laser diodes. The physical understanding derived in this work was directly used in design of optimal operation and structure for high power laser diodes as stated in conclusion of each section and at the final section. In the final section we suggest a possible direction for further investigation based on this work and recent progress.

## **II. Radiative recombination efficiency of InGaAsP/GaAs lasers grown by MOCVD *-spillover to waveguide, and absence of non-radiative recombination center***

### ***Introduction***

Radiative recombination efficiency is the ratio of radiative energy generated from a photonic device to the total energy injected to the device. Numerous research has been focused on this factor since the radiative recombination efficiency is strongly dependent on both material quality and device structure [17-20]. Commonly the radiative recombination efficiency is degraded by such as point defects, dislocation and surface related recombination, or insufficient capturing of carriers to active layers. The interest of the study on the radiative recombination efficiency for Al-free InGaAsP/GaAs stems from following reasons. Firstly it was found that for Metal-Organic Chemical Vapor Deposition (MOCVD) or Molecular Beam Epitaxy (MBE)-grown AlGaAs material has significant non-radiative recombination presumably due to oxidation of Al-containing layers [19,20]. The InGaAsP known to be immune to such oxidation is expected to have much lower non-radiative recombination due to absence of oxidation-related defects. Secondly control of excess carrier spillover into the waveguide and cladding layer is very crucial in quantum well structures. These spillover can degrade the laser performance in large extent via free-carrier optical loss and minority carrier-leakage current especially at high excitation level and high temperature.

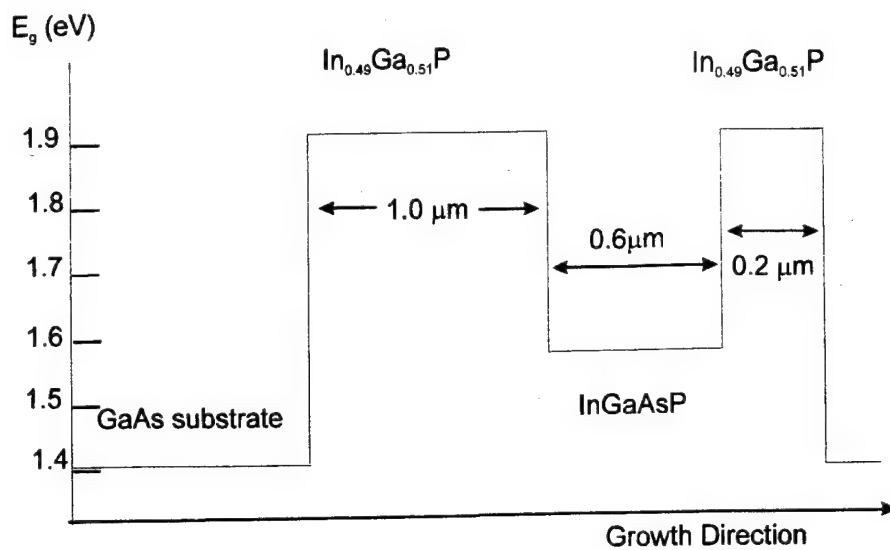
The results presented in this work demonstrate that the efficiency of radiative recombination at 300 K for both MOCVD-grown InGaAsP/GaAs double heterostructures (DH) and separate confinement

heterostructures (SCH) with active layer thickness of 300 Å are close to 100%, and that nonradiative recombination is not significant over a wide range of excitation level from  $1 - 10^3 \text{ W/cm}^2$ .

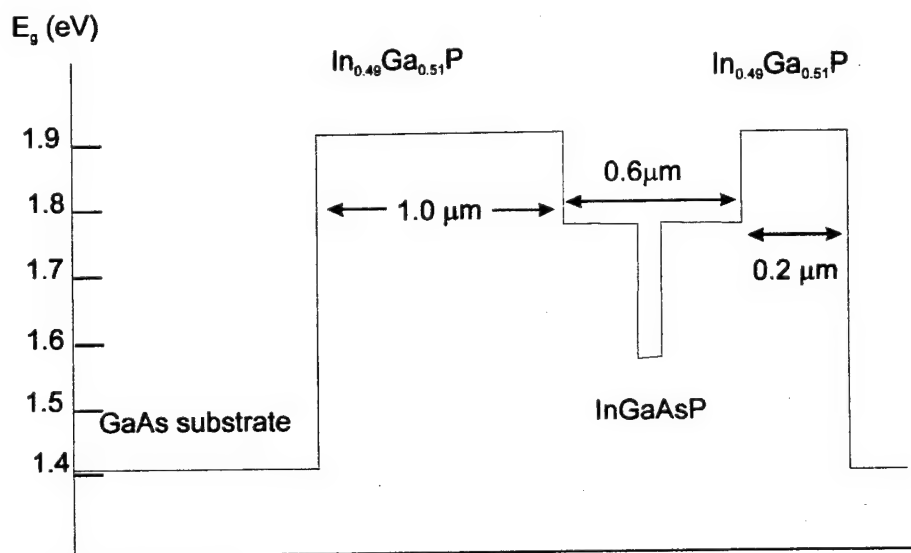
### ***Samples and Experimental details***

Double and Separate Confinement InGaAsP/GaAs Heterostructures specially intended for Photoluminescence (PL) measurements have been grown by the Low Pressure-MOCVD. The optimal growth condition has been reported in Ref. 21. The band diagrams of the SCH and DH structures are shown in Fig. 2-1 (a) and (b), and the main parameters of the structures studied are given in Table 2-1. Compositions of the quaternary materials in the active regions of SCH-structures were varied over the range corresponding to band gap energies from 1.52 to 1.57 eV, while the compositions of the confinement layers for the structures studied correspond to energies from 1.78 to 1.81 eV. The thickness' of the active and confinement (waveguide) regions were 300 Å and 6000 Å respectively. In the case of DH, the band gap energy of the 6000 Å thick active region was about 1.51 eV (Table 2-1). The thickness of the upper  $\text{In}_{0.49}\text{Ga}_{0.51}\text{P}$  cladding layer in all the structures was less than 1000 Å to minimize absorption of the excitation radiation in the cladding layer. The layers were not intentionally doped and residual donor concentration was about  $10^{16} \text{ cm}^{-3}$ .

Besides the MOCVD-grown structures, an SCH structure grown by Liquid Phase Epitaxy (LPE) with the method described in Ref. 22, 23 was also examined in this experiment. As seen in Table 2-1, the parameters of LPE-grown structures are very similar to those of SCH-structures grown by MOCVD.



(a)



(b)

Fig. 2-1. The Schematic of (a) DH structure and (b) SCH structures

**Table 2-1.** The structure parameters of the studied samples: MOCVD-SCH (no. 122, 214, 120), LPE-SCH (LPE, LPE2), MOCVD-DH (no. 127, 225).  $\Delta E_g$  is the difference of the band gap of the active layer and the waveguide layer, and  $\xi$  is the ratio of the luminescence intensity from the active layer and the waveguide layer and  $\eta$  is the internal efficiency determined by PL experiment.

		Active Layer			Waveguide Layer		$\Delta E$	$\xi$
		Thickness (Å)	Band gap	$\eta$	Thickness (Å)	Band gap		
SCH	LPE	300	1.525	>70 %	6000	1.822	0.297	2800
	122	300	1.519	>70 %	6000	1.818	0.299	2100
	214	300	1.577	>70 %	6000	1.781	0.204	110
	120	300	1.579	>70 %	6000	1.808	0.229	480
	LPE2	300	1.558	>70 %	6000	1.829	0.271	1600
	128	300	1.569	>70 %	6000	1.737	0.168	20
	269	300	1.61	>70 %	6000	1.768	0.158	16
DH	127	6000	1.511	>70 %				
	225	6000	1.790	~ 15 %				

The measurement of the absolute values of external efficiency for this LPE-grown structure has been carried out earlier as reported in Ref. 18, 23. In this experiment, SCH structures were mounted on glass slides and the GaAs substrates were removed. The 670 nm line of a  $\text{Kr}^+$ -laser whose photon energy was less than the  $\text{In}_{0.49}\text{Ga}_{0.51}\text{P}$  band gap and more than the InGaAsP-waveguide band gap energy was used in this experiment. The absorption and luminescence intensity measurements were performed in the "transparent" geometry utilizing a silicon photodiode with a large enough active area to collect at least 95 % of the luminescence radiation emitted in a  $2\pi$  solid-angle. After this measurement and the calculation of the external efficiency, these samples with removed substrates have been used as a standard for determination of luminescence efficiency of samples on substrates in a conventional "reflectance" geometry. The values of external efficiency obtained for samples with substrate were used to calculate internal efficiency from a simple relation neglecting multi-pass and re-radiation effects and taking into account only reflection at the air-structure interface with the refractive index of the waveguide material assumed to be 3.45. The result of this experiment was that the internal efficiency for this structure as well as for other similar LPE-grown structures is greater than 70% in the excitation range of 10-100  $\text{W}/\text{cm}^2$  at 300 K [23].

In the present work, the 488 nm line of a Spectra Physics  $\text{Ar}^+$ -laser was used for the PL excitation both for spectral measurement and for measurement of the total (integrated) intensity of emission in the spectral bands. A specially modified Carl Zeiss (Axioskop 50) microscope with the photodetector mounted in its collimator was utilized for integrated measurement of luminescent intensity. The excitation beam was focused at the sample surface by the microscope objectives and luminescence radiation was collected by the same objectives. Several thin foil diaphragms with diameters between 100 and 200  $\mu\text{m}$  were used to confine the area of the illuminated spot. The optical power density within the spot was calibrated using two photodiodes, with one of them measuring input laser power before the microscope and the second

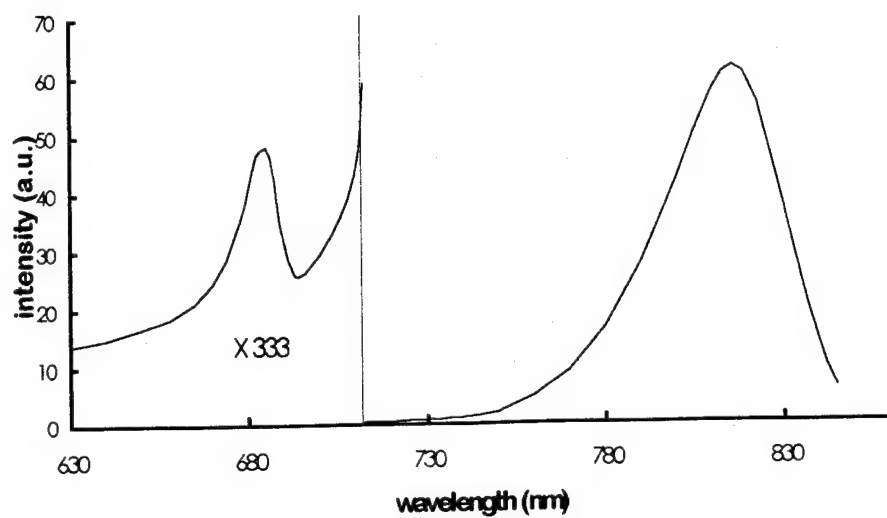
measuring power coming through the hole of the diaphragm placed in the plane of focus of the microscope objective. The uniformity of the excitation radiation within the spot was checked with a CCD camera positioned in place of the photodiode. The resulting power density at these spots could be varied from  $0.1 \text{ W/cm}^2$  to  $2 \cdot 10^3 \text{ W/cm}^2$  by adjusting the output power of the  $\text{Ar}^+$ -laser from 30 mW to 6 W, and with appropriate optical filters. The conventional scheme including the monochromator and the photomultiplier was adapted for the PL spectrum measurement. All measurements were performed at room temperature.

### ***Results and Discussion***

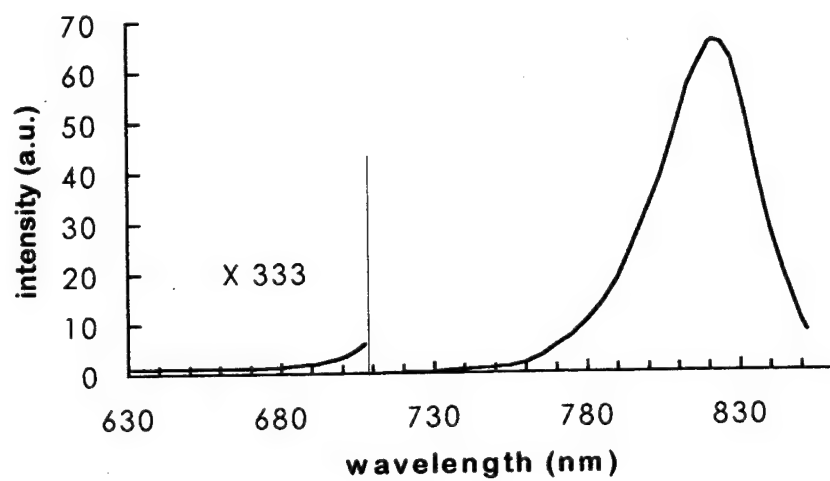
Fig. 2-2 (a) and (b) demonstrate typical PL spectra for MOCVD-grown SCH and DH structures at an excitation level of about  $1 \text{ W/cm}^2$ . In the case of SCH structures, besides the main luminescence band from the active region, the spectra contain a second low intensity short-wavelength band that is due to the recombination in the waveguide layer. The spectrum of the LPE-grown SCH structure has the same character.

The ratios of the integrated intensity of the emission from the active region to that from the waveguide (denoted by  $\xi$  below) at a low excitation level vary from 100 to 3000 for SCH structures with different compositions for the active and waveguide regions (Table 1). The value of  $\xi$  as a function of excitation level for MOCVD-grown SCH structure No. 214 is shown in Fig. 2-3. This ratio is almost constant in the low excitation range ( $P < 10 \text{ W/cm}^2$ ) and decreases by one order of magnitude when the excitation level reaches  $5 \cdot 10^2 \text{ W/cm}^2$ .

The results of the measurement of the integrated luminescence intensity ( $L_{int}$ ) versus excitation level ( $P$ ) are given in Fig. 2-4 (a) and (b). Considering the data of Fig. 2-4. (a), it should be emphasized that



(a)



(b)

Fig. 2-2 The PL spectrum of (a) MOCVD-grown SCH structure, (b) MOCVD-grown DH structure, at  $T=300$  K, excitation power density  $P=1$  W/cm<sup>2</sup>

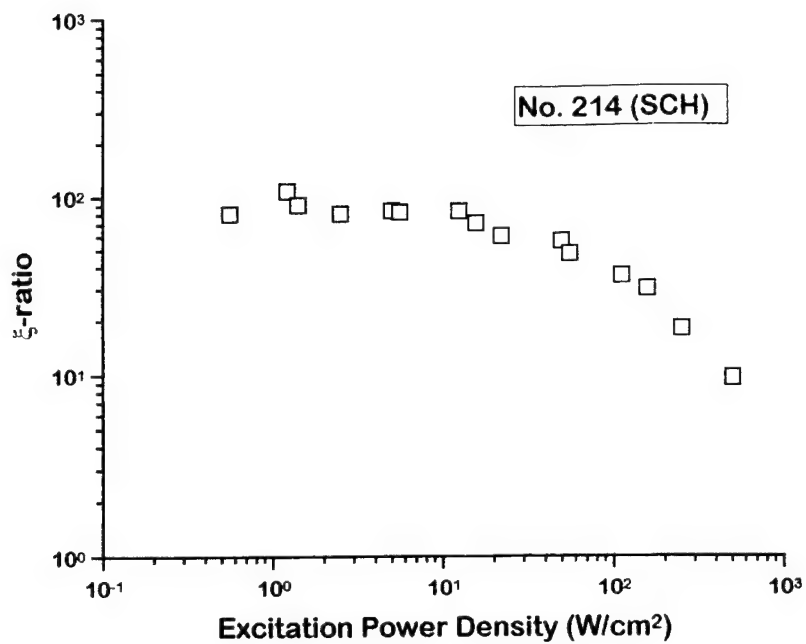
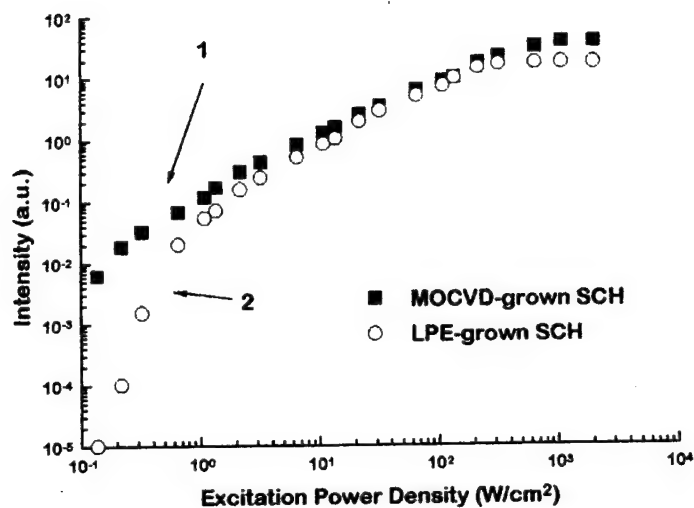
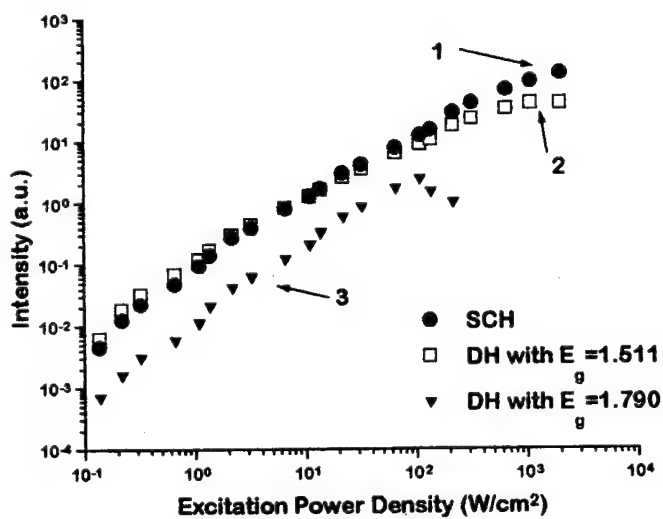


Fig. 2-3. The dependence of  $\xi$  (the ratio of the PL intensity from the active layer to that from the waveguide layer on the excitation power density  $P$ , for the SCH structure No. 225 (see Table 2-1)



(a)



(b)

Fig. 2-4. The PL integral intensities of various structures: (a) curve 1: MOCVD-grown SCH (no. 122), curve 2 : LPE-grown SCH (no. LPE); (b) all MOCVD-grown, curve 1: SCH structure (no. 122), curve 2: DH with the active-layer material (no. 127), curve 3: DH with the waveguide material used for its active layer (no. 225)

MOCVD-grown  $\lambda = 0.8 \mu\text{m}$  SCH structures demonstrate the same luminescence efficiency as the LPE-grown SCH wafers in a range of excitation levels from 10 to  $2 \cdot 10^2 \text{ W/cm}^2$ . The dependence of  $L_{int} = f(P)$  for these structures is close to linear in the excitation range from 1 to  $50 \text{ W/cm}^2$  and the internal efficiency is more than 70%.

The super-linear decrease of  $L_{int}$  at excitation levels less than  $1 \text{ W/cm}^2$  is related to the enhancement of the contribution of non-radiative recombination at the low excitation level. This decrease is much more pronounced for LPE-grown structure as shown in Fig. 2-4 (a) (curve 2). Curve 3 of Figure 2-4 (a) refers to DH structure no. 225, which was grown with an active region of InGaAsP with a composition corresponding to 1.8 eV, close to that of the waveguide layer of the SCH structures. For this sample, the influence of non-radiative recombination within or out of the active region is considerable through the range of excitation levels studied. In spite of the super-linear increase of the intensity for this structure, its efficiency is three times lower than that of the  $0.8 \mu\text{m}$ -emitting DH-structures, even at  $P=10^2 \text{ W/cm}^2$ . Further increase of the excitation level for this structure only resulted in irreversible reduction of the luminescence output, apparently due to surface damage. For  $0.8 \mu\text{m}$  emitting DH and SCH structures, the irreversible change of the luminescence output did not exceed 5-10 % of the initial efficiency even after being exposed to optical power densities around  $10^3 \text{ W/cm}^2$ . As for the form of the dependence of luminescence intensity on excitation, these were different for SCH and DH structures at high excitation levels (Fig. 2-4 (b) curve 1 and curve 2). The tendency of the luminescence intensity to saturate for DH structures was observed only at the highest excitation level ( $P > 10^3 \text{ W/cm}^2$ ) while the deviation from the linearity for SCH structures began to appear at excitation levels as low as  $50 \text{ W/cm}^2$ . The comparison with the result of the Fig. 2-3 makes it possible to conclude that such behavior of  $L_{int}=f(P)$  dependence of SCH structures can be ascribed to the super-linear increase of the waveguide emission intensity at excitation levels higher than  $50 \text{ W/cm}^2$ .

Fig. 2-5 shows the value of  $\xi$  characterizing the ratio of the intensity from the waveguide region and the active region plotted as a function of the difference in the energy positions ( $\Delta E_g$ ) of the waveguide and the active region emission peaks for the SCH structures studied. The good correlation between the values of  $\xi$  and  $\Delta E_g$  implies that excess carriers recombining in the waveguide are in thermal equilibrium with the carriers in the active region of SCH structures. The values of  $\xi$  that have been used for the plotting of the Fig. 2-5 were measured in the range of the low excitation level where  $\xi$  is shown to be approximately constant ( $\xi = \xi_c$ ). In this case, the band scheme shown in the Fig. 2-6 can be applied and neglecting the difference in the electron effective mass in the active and waveguide region, one can obtain a simple relation for  $\xi_c$

$$\xi_c = \frac{L_z}{W} e^{\Delta E_g / kT} \quad (2-1)$$

where  $L_z$  and  $W$  are the thickness' of the active layer and the total waveguide layer respectively. The good fit of the experimental and calculated values of  $\xi$  confirms the validity of the proposed model. The main point of this model is that the excess hole density and the intensity of the radiative recombination in the waveguide region is determined by the total band gap difference ( $\Delta E_g$ ) of the active and the waveguide materials rather than by the discontinuity of the valence band.

The value of the  $\xi$  is not equal to the ratio of the *total* recombination rates in the active and the waveguide regions (denote by  $\beta$  below) since the internal efficiency of the radiative recombination in both regions should be taken into account to get this ratio: i.e.  $\beta = \xi / (\eta_a / \eta_w)$  where the subscripts  $a$ ,  $w$  mean their association with the active and the waveguide material respectively. It should be mentioned that the excess carrier density in the waveguide region is always considerably smaller than in the active region and when evaluating  $\beta$ , the value of the  $\eta_w$  should be taken from the corresponding low excitation condition. Using the data of Fig. 2-4 (b) (curve 3), one can find the appropriate value of  $\eta_w$  to be around 10-20 %. It means that at excitation level for more than  $10^2 \text{ W/cm}^2$  for this SCH structure under study values of  $\beta$  can approach one and spillover of the excess carrier into the waveguide can leak to the saturation of the active

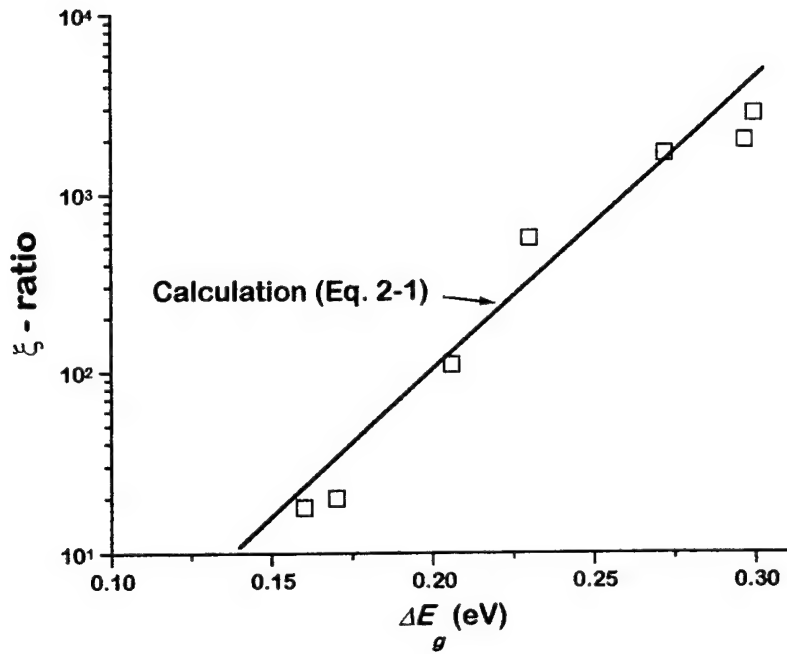


Fig. 2-5. The ratio  $\xi$  of the PL intensity from the active layer to that from the waveguide layer for the studied SCH structures as a function of  $\Delta E_g$ .

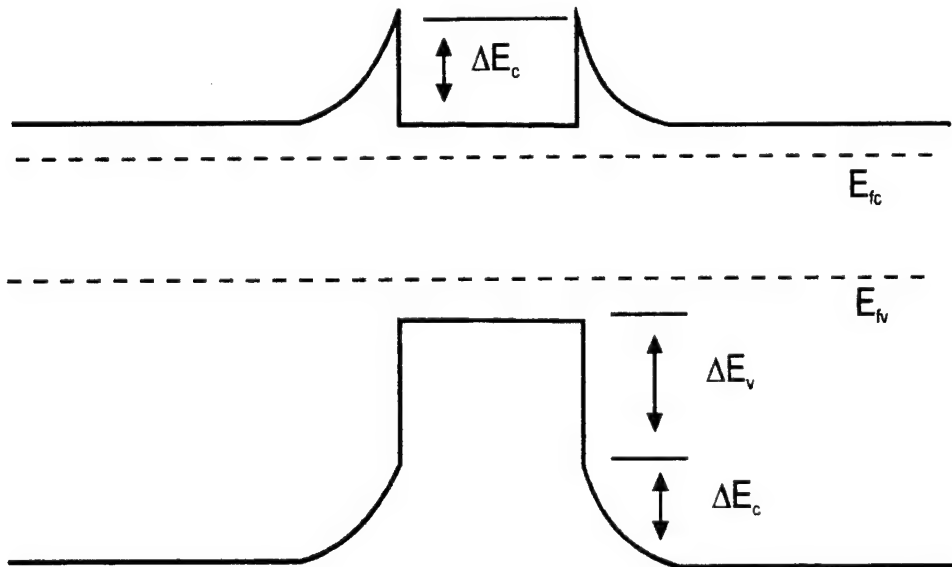


Fig. 2-6. Scheme of confinement barrier at low excitation level for heterostructure with low donor concentration in the confinement layer and the active layer.

region radiation intensity. This was observed experimentally for SCH structures studied [Fig. 2-4 (b) curve 2].

### ***Conclusion***

The results obtained in this work can be formulated as follows:

- 1) MOCVD-grown DH and SCH InGaAsP/GaAs structures with an active region band gap of 1.5 eV have a radiative recombination efficiency exceeding 70% over a very wide range of excitation level from 1 to  $10^3$  W/cm<sup>2</sup>.
- 2) In the case of SCH structures, the populations of the excess holes in the waveguide region are in the thermal equilibrium with those in the active region, and at low excitation levels, the intensity of the radiation in the waveguide depends only on the difference in the band gap of the active region and the waveguide region materials ( $\Delta E_g$ ), not on the valence band or conduction band discontinuity separately.
- 3) For SCH structure under study with  $\Delta E_g = 200-300$  meV, the spill-over of excess carriers under excitation higher than 50-100 W/cm<sup>2</sup> can influence the efficiency of the radiative recombination in the active region.

### III. Dependence of minority carrier leakage

#### on active layer volume for the InGaAsP lasers

##### *-effect of strong minority leakage on electric field in cladding layer*

#### *Introduction*

In the previous section we found that the spillover to waveguide is given by a thermal Boltzman distribution and is quite significant at high injection level for separate confinement heterostructure (SCH). Consequently one may question as to how significant the effect of the spillover will be on actual laser operation. Expecting that the narrower the quantum well thickness of SCH structure is, the higher spillover takes place, we compared laser characteristics of two kinds of lasers with different quantum well (QW) thickness, 150 Å and 300 Å.

In this comparative experiment we found that lasers with 150 Å QW thickness give indeed significantly poor threshold condition and efficiency. We analyzed this result by calculating minority leakage carrier (spillover to the cladding layers). In our theoretical calculation it was found that the approximation for the leakage current calculation normally employed in the literature [24,25] is not appropriate when the leakage current is comparable to the majority carrier current. We will show that the experimentally observed abnormal characteristics can be only explained when a more accurate model for the leakage current is employed for calculation.

#### *Sample preparation and Experiment*

We fabricated separate confinement heterostructure (SCH) with an active layer  $\text{In}_{0.13}\text{Ga}_{0.87}\text{As}_{0.74}\text{P}_{0.26}$  of energy gap 1.55 eV, and waveguide layers  $\text{In}_{0.37}\text{Ga}_{0.63}\text{As}_{0.25}\text{P}_{0.75}$  of energy gap 1.80 eV, sandwiched

between Si-doped ( $N_d \sim 5 \times 10^{17} \text{ cm}^{-3}$ ) and Zn-type ( $N_a \sim 6 \times 10^{17} \text{ cm}^{-3}$ ) InGaP cladding layers of energy gap 1.90 eV on Si-doped (100) GaAs substrate by low-pressure metalorganic chemical vapor deposition (LP-MOCVD). A schematic energy gap diagram under a forward bias is shown in Fig. 3-1. Broad-area laser diodes with a 100  $\mu\text{m}$  wide stripe were fabricated and mounted on copper heatsinks by indium bonding. Uncoated diodes with cavity length varying from 100 to 4300  $\mu\text{m}$  were prepared. Two different laser structures were grown with 150 Å and 300 Å thick active layers, respectively.

Measured dependencies of  $J_{th}$  on the cavity length for the two different laser structures with 150 Å and 300 Å thick active layers are plotted in Fig. 3-2 as a function of inverse cavity length. If only radiative recombination is considered for calculation of current, threshold current density  $J_{th}$  is inversely proportional to the cavity length  $L$  as plotted in the Fig. 3-2 by a dotted line. What is experimentally observed is quite different from this simple prediction. First, the dependencies of  $J_{th}$  on cavity length  $L$  of the lasers are significantly deviating from the linear dependence on the inverse cavity length. What is more interesting is the notably different dependencies of  $J_{th}$  on cavity length  $L$  between the 150 Å and 300 Å active layer lasers unlike the prediction of the theory. A similar behavior is observed in differential efficiency measurement as shown in Fig. 3-3. A simple theory without non-radiative recombination ( $\eta_i=1$ ) predicts that the reciprocal differential efficiency ( $1/\eta_d$ ) is linearly proportional to the cavity length  $L$  as plotted in the Fig. 3-3 by a dotted line. Again the experiment shows the deviation of  $1/\eta_d(L)$  from the linear dependence for short cavity lasers and strong difference between the two types of laser structures as shown in Fig. 3-3. To explain these effects properly, a more realistic model is required, taking into account non-radiative recombination such as Auger recombination [26], non- $\Gamma$  valley recombination, or leakage current [25]. As shown below we found that the leakage current, the current due to the recombination of excess carriers in cladding and contact layers, is the principal reason of the observed dependencies of  $J_{th}$  and  $\eta_d$ .

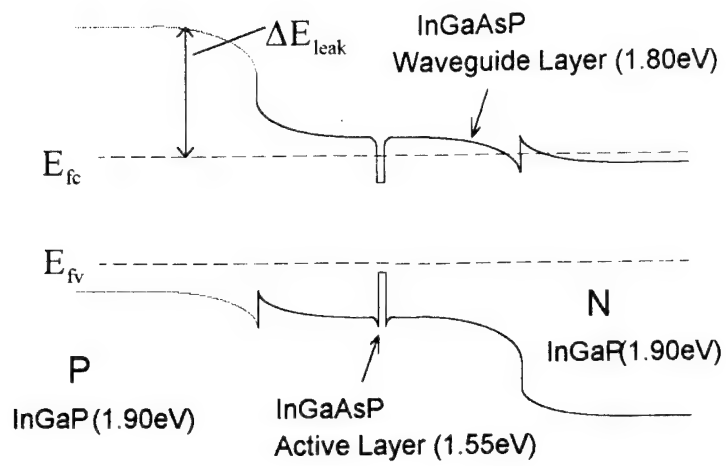


Fig. 3-1. Schematic energy diagram for the laser structures used in this work. Two horizontal dotted lines represent the Quasi-Fermi levels for the electrons and holes.

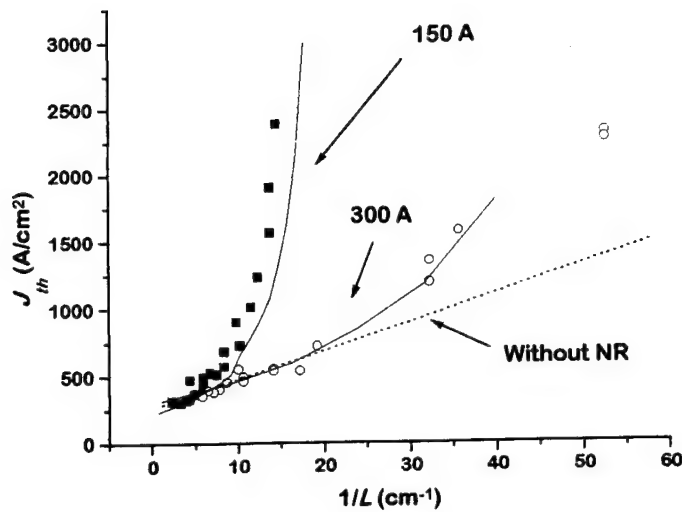


Fig. 3-2 Threshold current ( $J_{th}$ ) vs. Reciprocal Cavity Length ( $L$ ) for QW lasers with active layer thickness of 150 Å and 300 Å. Solid and dotted lines represent the theory with and without non-radiative recombination, while scattered points are the experimental data.

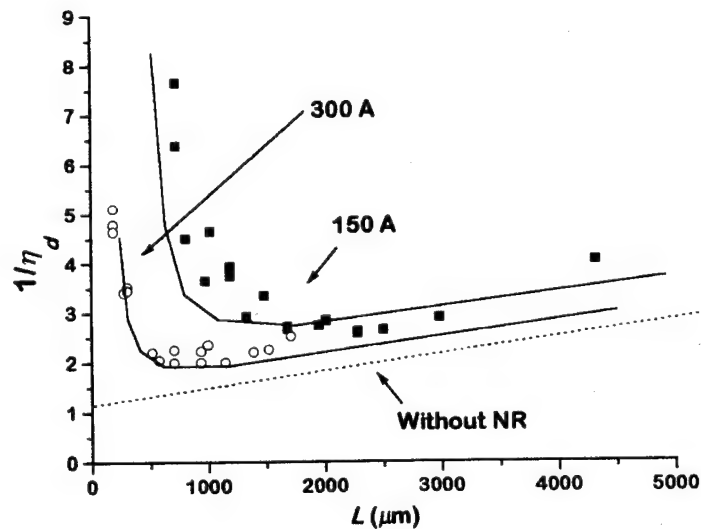


Fig. 3-3 Reciprocal Differential Efficiency ( $\eta_d$ ) vs. Cavity Length ( $L$ ) for QW lasers with active layer thickness of 150 Å and 300 Å. Solid and dotted lines represent the theory with and without non-radiative recombination, while scattered points are the experimental data.

As confirmed in section II, excess carrier concentration in the cladding layer near the waveguide region is given by the thermal equilibrium distribution, with the energy barrier  $\Delta E_{leak}$  indicated in Fig. 3-1. The energy barrier  $\Delta E_{leak}$  is related to  $\Delta E_g$ , the energy gap difference between the active layer and the cladding layers [27]. This difference of energy gap  $\Delta E_g$  in the InGaAsP/GaAs material system with  $\lambda=0.808 \mu\text{m}$  is about 350 meV. This can be compared to a laser made of GaAs active layer ( $\lambda=0.860 \mu\text{m}$ ) with  $\text{Al}_{0.55}\text{Ga}_{0.45}\text{As}$  barrier heterostructure in which  $\Delta E_g$  is 100 meV greater. This lower  $\Delta E_g$  leads to much higher carrier leakage to cladding layer. Another factor that contributes to the high leakage current in the InGaAsP/GaAs is the relatively small refractive index difference between the active layer and the cladding layer ( $\Delta n=0.14$ ) compared to the GaAs/  $\text{Al}_{0.55}\text{Ga}_{0.45}\text{As}$  ( $\Delta n \sim 0.30$ ). The small refractive index difference requires higher quasi-Fermi level separation due to smaller optical confinement, further reducing the energy barrier  $\Delta E_{leak}$ . These differences change the excess carrier concentration in the cladding layer by over two orders of magnitude and the leakage current is increased correspondingly. In this situation, an accurate model suitable to the case of high leakage current should be developed to minimize errors of the approximation used for AlGaAs lasers ( $\lambda=0.860 \mu\text{m}$ ).

### ***Leakage current calculation***

An accurate formula for electric field in the cladding layer for a large leakage current is derived from continuity of current in the cladding layers [28]:

$$E_o \cong \frac{I}{q\mu_p P_o} (J_{majority} + \frac{D_p}{D_n} J_{leakage}) \quad (3-1)$$

where the majority carrier current in the cladding layer ( $J_{majority}$ ) originated from the carrier recombination in the active layer,  $J_{act}$ , and in the waveguide layer,  $J_{wg}$ , and Auger recombination,  $J_{Auger}$ , that is,

$$J_{majority} = J_{act} + J_{wg} + J_{Auger} \quad (3-2)$$

while the minority carrier current in the cladding layer  $J_{leakage}$  is related to the electric field by [25]

$$J_{leakage} = qD_n n \left[ \sqrt{\frac{1}{L^2} + \left(\frac{kT}{2qE_o}\right)^2} \coth \sqrt{\frac{1}{L^2} + \left(\frac{kT}{2qE_o}\right)^2} + \frac{kT}{2qE_o} \right] \quad (3-3)$$

The three terms in RHS of Eq. (3-2) are obtained from the standard approach [24]. Equation (3-1) is somewhat different from the formula used in the literature [24,25,29] for the electric field in the cladding layer:

$$E_o \cong \frac{I}{q\mu_p P_o} (J_{majority} + J_{leakage}) \quad (3-4)$$

The terms in the parenthesis correspond to the total current. Difference is factor of  $D_p/D_n$  (diffusion coefficient ratio) which is less than one tenth for most materials [30]. When the leakage current becomes comparable to the majority carrier currents as in this case, use of Eq. (3-4) will overestimate both the electric field and  $J_{leakage}$  significantly. To verify the validity of the Eq. (3-1) and the approximation used here, a complete equation set including Poisson equation and current continuity was solved numerically using finite element method. The numerical result shows that the electric field given by Eq. (3-1) is indeed very accurate approximation except very close to the space charge region. The difference of Eq. (3-1) from the electric field calculated by the Poisson equation is less than  $10^{-6}$ , while the Eq. (3-4) used in the literature has more than 30 % error in highly leaky conditions. Equations (3-1) and (3-3) were solved self-consistently for the total current needed for lasing. Internal efficiency  $\eta_i$  was obtained for calculation of the differential efficiency  $\eta_d$  [31] by considering all of the non-radiative-recombination-induced currents using

$$\eta_i = \frac{J_{rad}}{J_{rad} + J_{non-rad}} = \frac{J_{Act}}{J_{Act} + J_{wg} + J_{Auger} + J_{leakage}} \quad (3-5)$$

### Results and Discussion

Calculated  $J_{th}$  are shown in Fig. 3-2 by solid lines, demonstrating good agreement with the experiment for the lasers with both 150 Å and 300 Å active layers. The physical reason of the sharper increase for 150 Å active layer laser compared to for 300 Å is explained by the leakage current mechanism as follows: The 150 Å active layer laser has two times smaller optical confinement than for 300 Å, due to 2 times thinner

active layer. Since two times higher gain in the active layer is required to compensate same optical loss of the lasers, the quasi-Fermi level should be higher for the 150 Å structure, resulting in much larger leakage to the cladding layer. Same principle applies to the differential efficiency (Fig. 3-3). The solid lines represent our calculation. Sharply dropped differential efficiency for the 150 Å active layer laser for short cavity originated from higher carrier leakage due to the too small optical confinement. It should be noted that any non-radiative recombination may result in the non-linear dependence of  $J_{th}$  and  $\eta_d$  on  $1/L$  and  $L$ , respectively. However the observed notably different dependencies on the cavity length between 150 Å and 300 Å (Figs. 3-2 and 3-3) are not explained by other mechanisms but the minority carrier leakage since only the latter is exponentially dependent on the quasi-Fermi level, unlike other non-radiative recombination mechanisms.

In summary, we have analyzed the InGaAsP lasers grown on GaAs substrate with the emitting wavelength of 0.808  $\mu\text{m}$  using an accurate model for the case of large leakage current. Our model could provide an excellent quantitative explanation of the observed  $J_{th}$  and  $\eta_d$  dependence on the cavity length. For short cavity lasers, a thinner active layer (150 Å) resulted in higher threshold current and lower differential efficiency than for thicker one (300 Å) due to the too small optical confinement, high Quasi-Fermi level separation, and high leakage current. Our theoretical and experimental study clearly demonstrates the effect of narrow quantum well active layer (consequently small optical confinement factor) on the change of laser characteristics due to carrier spillover to cladding layer.

#### IV. Comparison of Gain and Threshold

current density for diodes with different

QW thickness -*quantum-size effect of QW lasers*

In previous section, it was found that for InGaAsP/GaAs ( $\lambda=808$  nm) laser diodes, 300 Å is the optimal thickness for the active layer. A theoretical calculation and experimental investigation revealed that laser diodes with active layers thinner than 300 Å had a significantly large minority carrier leakage to the cladding layer, degrading the threshold condition and internal efficiency. This was primarily due to too small optical confinement.

However, in that work, we considered only single quantum wells (QW) of various thickness. Given that 300 Å is the optimal thickness in this case, a question naturally arises as to whether a multiple quantum well with total thickness 300 Å is superior to a single quantum well with 300 Å thickness. Our investigation was motivated by the fact that in AlGaAs/GaAs lasers, narrow QW's are known to have better performance (less temperature dependence and wavelength stability) than thicker active layer lasers [32]. Arakawa and Yariv [33] attributed the lower threshold current density of thinner QW's to the lower current for transparency (the current at which gain is zero.) Their calculation indicates that threshold current density for the lasers with 100 Å active layer can be even 2 times lower than that of 300 Å active layer for low loss ( $\alpha \sim 10$  cm<sup>-1</sup>).

However, the argument of their work [33] may not be a general conclusion when other factors are considered. Firstly, the effective-mass energy band approximation used in their work fails to describe the

mixing of heavy holes and light holes, which makes significant difference in optical transition properties [34]. Since this mixing becomes more prominent in the narrow quantum wells, comparison of optical properties for QW's with different well thickness without considering the mixing effect would not give a valid conclusion. Secondly, a relatively high intraband relaxation rate usually found in the InGaAsP quaternary material due to alloy scattering [35] may deform the gain spectra significantly. Even though lasers with higher relaxation rate are favored for the single longitudinal mode operation due to the homogeneous broadening of the gain spectrum [36], the high relaxation rate may lower the difference of the gain for the lasers with different QW thickness by smoothing the gain spectra.

The above question, that is, whether the lasers composed of narrow QW's show better performance compared with lasers with thicker QW's when they have same optical confinement (same total active layer thickness) taking these two effects into account, is addressed in this work. We compared characteristics of three different QW structures with same total QW active layer thickness of 300 Å ( the optimal thickness according to the work of the previous section ), in theory and experiment.

We have grown three laser diodes with (1) triple 100 Å QW's, (2) double 150 Å QW's, and (3) single 300 Å QW for the active layer. Detailed sample preparation and experimental procedure for measurement of  $J_{th}$  and  $\eta_d$  were described in previous sections. The experimental results (Dots) for  $J_{th}$  as function of cavity length  $L$  show no significant difference of  $J_{th}$  between the laser structures with one, two and three quantum wells. Differential efficiency  $\eta_d$  was also found independent on the inner structure of the active region.

To determine whether this result comes from the intrinsic effects such as valence-band mixing or high relaxation rate as mentioned earlier, or from extrinsic effect such as interface-induced degradation, we compared the experiment with theory, taking the valence-mixing and high relaxation rate into account. The energy levels of the valence-bands was calculated by employing Luttinger-Kohn Hamiltonian [37]

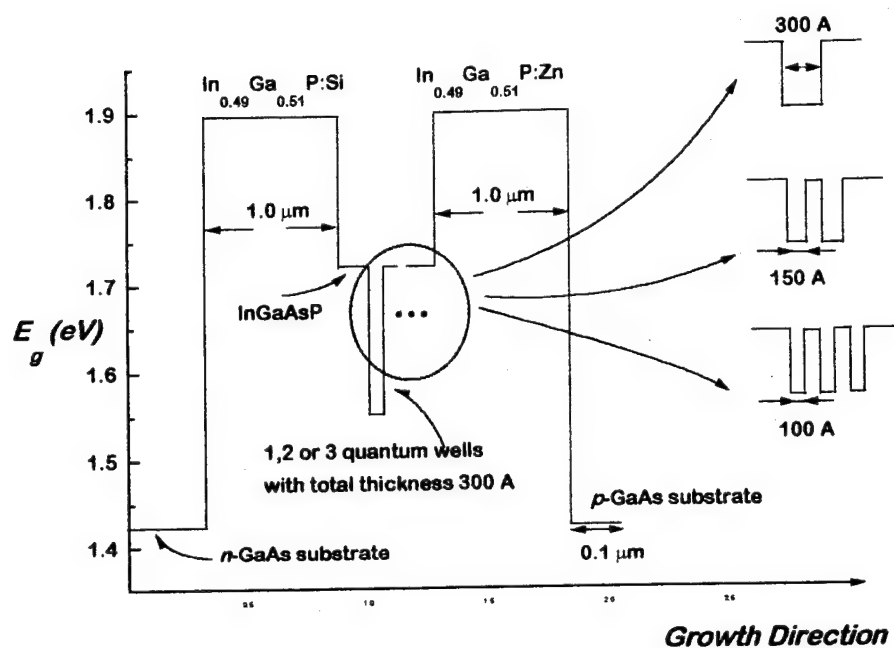


Fig. 4-1. Schematic diagram of three kinds of lasers with triple 100 Å QW, double 150 Å QW and single 300 Å QW thicknesses that were used for this experiment.

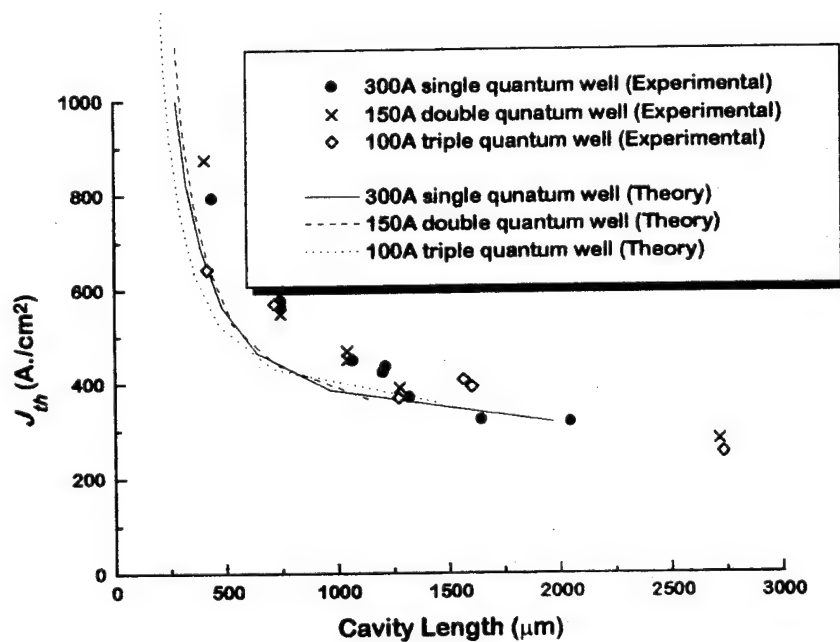


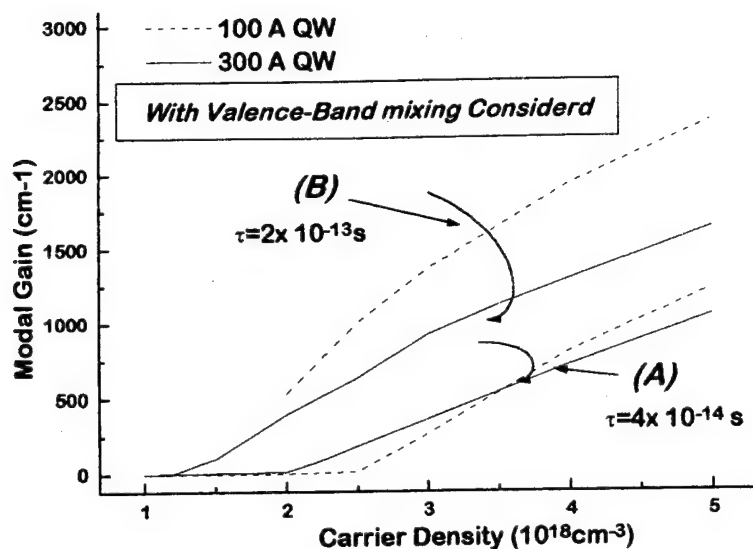
Fig. 4-2. The threshold current densities of the three lasers shown in Fig. 1. The Dots represent Experiment while Solid Lines represent Theoretical results.

with the envelope function approximation [38]. Material parameters such as Luttinger parameter and the energy gap are linearly interpolated from the values of binary materials [39,40]. After an unitary transformation for further simplification, the Hamiltonian matrix becomes

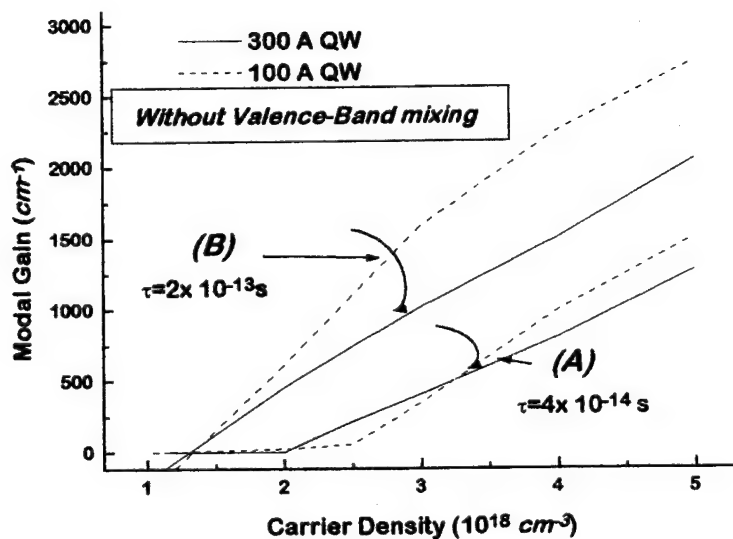
$$H_v = \frac{1}{2} \left( \frac{\hbar^2}{m_o} \right) \begin{pmatrix} (\gamma_1 + \gamma_2)k_\rho^2 + (\gamma_1 - 2\gamma_2)k_z^2 & \sqrt{3}\gamma_2 k_\rho (k_\rho + i2k_z) \\ \sqrt{3}\gamma_2 k_\rho (k_\rho + i2k_z) & (\gamma_1 - \gamma_2)k_\rho^2 + (\gamma_1 + 2\gamma_2)k_z^2 \end{pmatrix} + V(z) \quad (4-1)$$

where  $\gamma_1, \gamma_2$  are Luttinger parameters,  $k_\rho, k_z$  are operators for wave numbers parallel and perpendicular to the well planes and  $V(z)$  is the potential profile of the valence band. In Eq. (4-1), we assumed  $\gamma_3 = \gamma_2$  for a simpler comparison with the effective mass Hamiltonian as discussed below. The heavy hole (upper row) and light hole (lower row) are mixed due to the non-zero off-diagonal elements of the Hamiltonian. The space-dependent Hamiltonian was solved using the eigenfunction expansion method [40]. The energy band and the envelope functions obtained from the Hamiltonian (Eq. (4-1)) are used in calculation of the optical gain [38]. In the gain calculation, we used  $\tau=0.04$  ps for the relaxation time as determined from photoluminescence measurement described in section V. The calculated gains for 100 Å QW and 300 Å QW vs. injection current density are shown in Fig. 4-3 (a) (Curve A). The two curves (in Curve A) show remarkably similar dependence on the injection carrier density. As discussed above, this is quite contrary to the work of Arakawa, and Yariv [33] where significantly less transparency carrier density and higher gain were obtained from thinner QW. The difference may come from either of two effects considered here: valence band mixing, or high intraband relaxation rate. To clarify the origin, we re-calculated the gain without either of them. Curve B in Fig. 4-3 (a) is the gain vs. carrier density without considering high relaxation rate. Instead of  $\tau=0.04$  ps,  $\tau=0.2$  ps was assumed. In this case, the quantum-size effect of QW is evident: 100 Å QW lasers would have more than 30% higher gain than 300 Å QW lasers. This difference was almost absent for  $\tau=0.04$  ps case.

To estimate the effect of mixing of valence-bands, the effective-mass approximation (non-mixing) was applied to gain calculation. For a systematic comparison, we made following change on Hamiltonian, while keeping the form of Eq. (4-1):



(a)



(b)

Fig. 4-3 (a) Calculated Modal Gains for 100 Å QW lasers (Dashed Lines) and 300 Å QW lasers (Solid Lines) when the Valence-Bands Mixing was considered. Curve A is related to the relaxation time  $\tau = 4 \times 10^{-14} \text{ s}$ , while Curve B is for  $\tau = 2 \times 10^{-13} \text{ s}$ . (b) Same with (a) except that the Valence-Band Mixing was not taken into account for the calculation.

$$H_v \rightarrow H_v^{non-mixing} = \frac{1}{2} \left( \frac{\hbar^2}{m_o} \right) \begin{pmatrix} (\gamma_1 - 2\gamma_2)(k_z^2 + k_p^2) & 0 \\ 0 & (\gamma_1 + 2\gamma_2)(k_z^2 + k_p^2) \end{pmatrix} + V(z) \quad (4-2)$$

In this way, we could see the difference of mixing and non-mixing directly without being affected by other parameters change. Note that Eq. (4-1) and Eq. (4-2) would give same eigen-energies when  $V(z)=0$  (i.e. bulk material). Figure 4-3 (b) shows the calculated gains when energies and wavefunction for the holes are calculated with the effective-mass Hamiltonian (Eq. (4-2)) for  $\tau=0.04$  ps (Curve A) and  $\tau=0.2$  ps (Curve B). This calculation also indicates the absence of difference of gains for 100 Å and 300 Å QW lasers when the relaxation rate is high (Curve A). Thus it is not the valence-band mixing that makes the gains for the two QW lasers less different but the high relaxation rate.

In order to directly verify whether the calculated gain correctly models experiment, we performed calculation of  $J_{th}$  using the model conventionally used in literature [41] except for leakage current calculation. Since the injection efficiency is strongly dependent on the QW width for high-loss lasers (i.e. short cavity lasers) [41], the minority-carrier leakage to the cladding layer (which is most responsible for the injection efficiency degradation [42]) was calculated with an improved model for leakage current as illustrated in section III. The parameters needed for  $J_{th}$  calculation were obtained as follows: Background optical loss  $\alpha \sim 2 \text{ cm}^{-1}$  was obtained from differential efficiency measurement as in [43] and  $\Delta E_c/\Delta E_v \sim 0.4$  was assumed for our system as in GaAs/InGaP [44]. The optical confinement factor  $\Gamma=0.057$  was calculated from waveguide model using  $\Delta n=0.14$ , the refractive index difference between the active layer ( $\text{In}_{0.13}\text{Ga}_{0.87}\text{As}_{0.74}\text{P}_{0.26}$ ) and cladding layer (InGaP) that was obtained by fitting the far-field pattern with the diffraction-theory calculation [45]. None of the variables were used as fitting parameters in the present work. The calculation reveals almost same threshold current densities for all the three laser structures. This was expected so since the three lasers have same gain, optical confinement, active layer volume, and loss. Figure 4-2 shows the comparison of the calculation (Solid Lines) with the experiment (Dots). The agreement is excellent for entire investigated range of cavity length.

The excellent matching of experiment and theory indicates that the interfaces between well layers and barrier layers do not contribute to loss or non-radiative recombination in a detectable level. If this is not so, the triple 100 Å QW lasers, having 3 times more hetero-interfaces than single 300 Å QW lasers, would have shown higher threshold current due to the higher loss and non-radiative recombination. Absence of additional loss due to the interface is consistent with the recent work on hall mobility measurement [46]. In that work, it was shown that the interface roughness should be less than two monolayers. This small fluctuation does not cause any detectable optical loss according to light-scattering calculation [47].

In conclusion, we showed that the absence of quantum-size effect of narrow InGaAsP/GaAs QW lasers on  $J_{th}$  and  $\eta_d$  obtained in our experiment can be attributed to their high relaxation rate. The valence-mixing effect itself does not reduce the difference of the gains for narrow QW (100 Å) and thick QW (300 Å) lasers as far as the relaxation rate is kept low ( $\tau=0.2$  ps). An excellent agreement of theory and experiment corroborates the state-of-art growth of InGaAsP/GaAs lasers that eliminates the undesirable effects of hetero-interfaces.

## V. Temperature dependence of Laser characteristics

### *-Origin of carrier relaxation*

In this section, experimental and theoretical study on temperature dependence of  $J_{th}$  and  $\eta_d$  was carried out in order to understand the detailed mechanism of increase of  $J_{th}$  and decrease of  $\eta_d$  at high temperature. The major reason of such a temperature dependence is the thermal broadening of the gain spectrum which results in reduction of gain peak. However, calculation performed in this section shows that this effect cannot fully explain the experimental data of  $J_{th}$  and  $\eta_d$ . In this work, we investigated the temperature dependence of momentum relaxation rate  $\hbar/\tau$  in InGaAsP active layer through photoluminescence study. It was shown that the theoretical model of the temperature dependence of  $\hbar/\tau$  provides an explanation of the observed temperature dependence of  $J_{th}$  and  $\eta_d$ .

The dependence of  $J_{th}$  and  $\eta_d$  on temperature were measured under pulse operation (pulse width 100-400 ns, repetition rate 5-2.5 kHz) using an integrating sphere with a Si photodiode in the temperature ranging from 15 °C to 120 °C. The measured data are shown in Fig. 5-1 and Fig. 5-2 by square dots. We already have calculated the variation of  $J_{th}$  and  $\eta_d$  as function of cavity length, considering the thermal broadening of the gain spectrum with momentum relaxation rate ( $\hbar/\tau_0$ ,  $\tau_0=4 \cdot 10^{-14}$  sec) in the previous section. The gain thermal broadening effect originates from the microscopic gain expression: [32]

$$g(\hbar\omega) = \frac{q^2 |M|^2}{\hbar\omega\epsilon_0 m^2 c_0 \hbar n L_z} \sum_{ij} m_{r,ij} A_{ij} C_{ij} [\tilde{f}_c - (1 - \tilde{f}_v)] \theta(\hbar\omega - E_{ij}) \quad (5-1)$$

where  $|M|^2$  is bulk momentum transition matrix element,  $\epsilon_0$  is permittivity,  $m$  is free electron mass,  $c_0$  is vacuum speed of light,  $N$  is effective refractive index,  $i, j$  are conduction electron, valence heavy hole quantum numbers,  $m_{r,ij}$  is reduced mass for transition  $i, j$ ,  $C_{ij}$  is spatial overlap factor between states  $i$  and

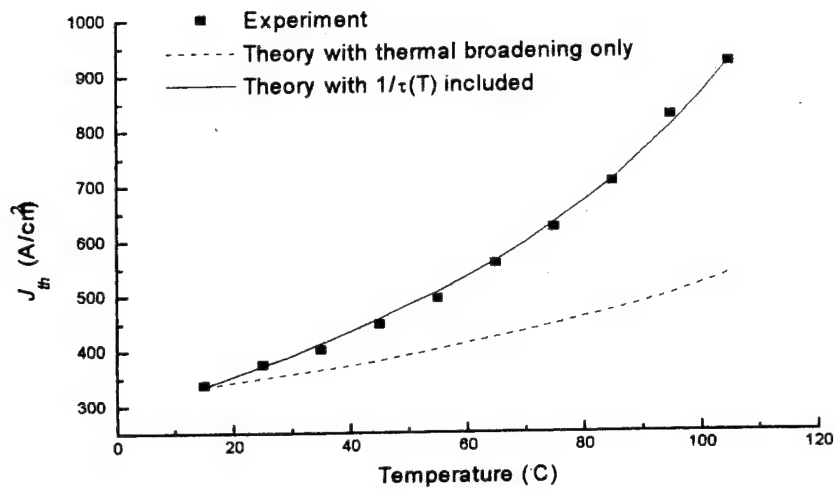


Fig. 5-1. The threshold current density ( $J_{th}$ ) of the lasers with cavity length  $L = 1090 \mu m$  for different operating temperature ( $T$ )

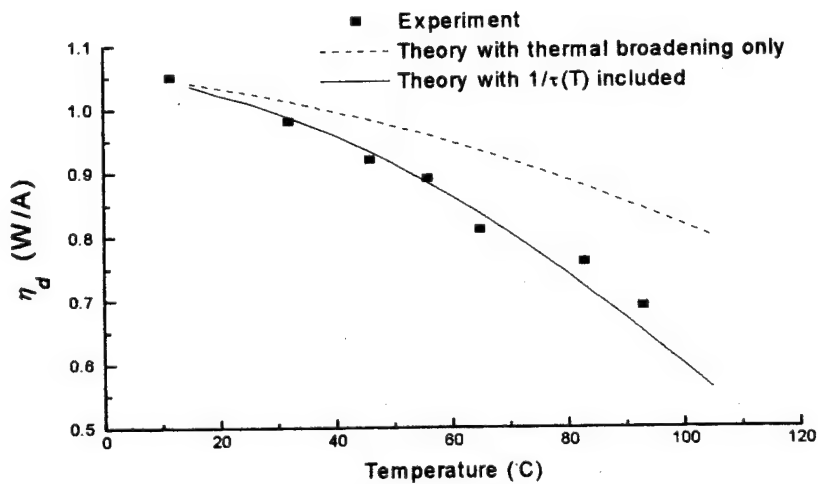


Fig. 5-2. The Differential efficiency ( $\eta_d$  (W/A) ) of the lasers with cavity length  $L = 1090 \mu m$  for different operating temperature ( $T$ )

$j$ ,  $\theta(x)$  is step function, and  $E_{ij}$  is transition energy between stages  $i$  and  $j$ .  $A_{ij}$  is anisotropy factor for transition  $i,j$  given by

$$A_{ij} = (3/4)(1 + \cos^2 \Theta_{ij}) \quad (\text{for TE})$$

$$A_{ij} = (3/2)\sin^2 \Theta_{ij} \quad (\text{for TM})$$

The angular factor  $\Theta_{ij}$  is given by  $\cos^2 \Theta_{ij} = E_{ij}/E$ .  $\tilde{f}_c(E)$  and  $\tilde{f}_v(E)$  are convoluted quasi-Fermi distribution functions, e.g.

$$\tilde{f}_c(E) = \int_{E_g}^{\infty} d\xi \left[ \frac{1}{\pi} \frac{\hbar/\tau}{(\xi - E)^2 + (\hbar/\tau)^2} \right] \{ \exp[(\xi - E_{fc})/kT] + 1 \}^{-1}, \quad (5-2)$$

where  $E_{fc}$  is quasi-Fermi level of electron carriers in active medium, determined by injection carrier density, and  $\hbar/\tau$  is momentum relaxation rate (= scattering rate of carriers).  $\tilde{f}_c(E)$  and  $\tilde{f}_v(E)$  have broader distribution over energy level at high temperature, causing broader gain spectrum.

Numerical calculation of  $J_{th}$  and  $\eta_d$  was carried out as described in Section III. The theoretical results are shown in Fig. 5-1 and Fig. 5-2 with dotted lines, showing that the experimental data has a much stronger temperature dependence than this effect alone could explain. This led us to consider the temperature dependence of momentum relaxation rate  $\hbar/\tau$  and the way it affects  $J_{th}$  and  $\eta_d$ .

Theoretical calculations [48-50] show that major mechanisms contributing to the momentum relaxation rate  $\hbar/\tau$  are (i) carrier-carrier scattering [48], (ii) carrier-phonon scattering [49] and (iii) alloy scattering [50] and their temperature dependencies have been well known. Since the three major origins of the momentum relaxation have comparable magnitude in the temperature range of our investigation, it is difficult to theoretically predict the temperature dependence of the relaxation rate  $\hbar/\tau$  when the mechanisms are combined. In this work, we obtained the temperature dependence of  $\hbar/\tau$  by measuring photoluminescence spectrum and comparing them with the theoretically calculated spectrum, as done in Yamada, et al [51]. The dotted lines in Fig. 5-3 show the experimental photoluminescence spectrum

obtained from the studied laser structure in the temperature range from 15 °C to 105 °C. Detailed set-up for this measurement was described in section II. The solid lines in Fig. 5-3 represent the theoretical calculation of spontaneous emission spectrum  $R(E)$  obtained as follow: [32]

$$R(E) = \frac{16p^2 Nq^2 E |M|^2}{e_0 m^2 c_0^3 h^4 L} \sum_{i,j} m_{r,ij} C_{ij} [\tilde{f}_c \cdot \tilde{f}_v] q(E - E_{ij}) \quad (5-6)$$

At several temperatures between 15 °C to 105 °C, we fitted the theoretical spectrum to experimental data by adjusting two parameters,  $E_g$  and  $\hbar/\tau$ , as was done in Fig. 5-3. Roughly speaking,  $E_g$  determines the peak position, and  $\hbar/\tau$  gives the half width of the spectrum. In this way, we obtained  $E_g$  and  $\hbar/\tau$  of the active-layer material at each temperature and the results are shown in Fig. 5-4.

Both  $E_g$  and  $\tau$  decrease from 1.51 eV to 1.45 eV and from  $4 \cdot 10^{-14}$  sec to  $1.8 \cdot 10^{-14}$  sec, respectively, as temperature varies from 20 °C to 105 °C. Fig. 5-4 shows that  $E_g(T)$  is an almost linear function of temperature, while  $\tau(T)$  has sub-linear dependence approximately as  $T^{-1/2}$ . It is well known that alloy scattering time (= momentum relaxation time  $\tau$ ) has  $T^{-1/2}$  dependence, from mobility measurement and first principle calculation [50,52], while polar optical phonon scattering has approximately  $T^{-2}$  dependence [49] and carrier-carrier scattering (mainly from hole-hole scattering) has very small temperature dependence [48]. Therefore our photoluminescence experiment data imply that the alloy scattering may be the dominant mechanism of the momentum relaxation for the studied active-layer material.

The experimental temperature dependence of momentum relaxation time  $\tau(T)$  given in Fig. 5-4 is best fitted with the following formula:

$$\tau(T) = \tau_0 \left( 1 + \beta \left( \frac{T - T_0}{T_1 - T_0} \right) \right)^{-1} \quad (5-7)$$

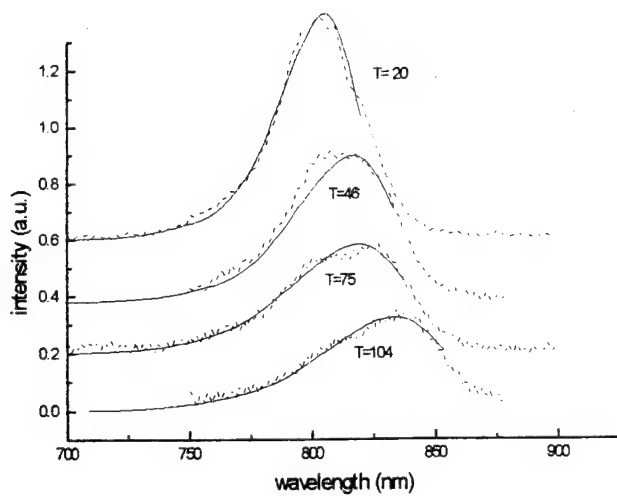


Fig. 5-3. Measured Photoluminescence Spectrum of the studied laser structure at different temperatures (dotted curve). The Spectrum was reproduced by calculation with best fitting parameters for (i) Momentum Relaxation rate and (ii) Energy Gap, at each temperature (solid curve).

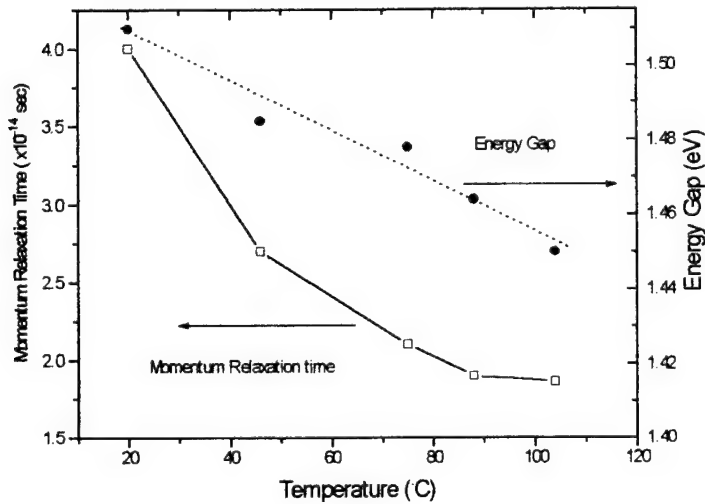


Fig. 5-4. Temperature dependence of Momentum Relaxation Time and Energy Gap, obtained from best fitting of the calculated photoluminescence spectrum to the experimental spectrum (The best fitting of calculation to experiment is shown in Fig. 5-3.)

where  $T_0=15^\circ\text{C}$ ,  $T_1=105^\circ\text{C}$ ,  $\beta \approx 1.1$ , and  $\tau_0=4 \cdot 10^{-14}$  s. With this  $\pi(T)$ , the gain  $g(E)$  was recalculated through Eq. (5-1) and (5-2). Decrease of  $\pi(T)$  at high temperature (increase of relaxation rate  $\hbar/\tau$ ) makes  $\tilde{f}_{e(v)}(E)$  and  $g(E)$  broader and reduces their peak heights. Besides the additional gain broadening,  $1/\pi(T)$  affects our theoretical model in two more ways. First, hole mobility decreases at high temperature because it is inversely proportional to the scattering rate [52]: (electron mobility does not play crucial role in calculation of  $J_{th}$  and  $\eta_d$  as discussed in section III)

$$\mu(T) = \mu_0 \left( \frac{\tau_0}{\tau(T)} \right) \quad (5-8)$$

where  $\mu_0=300 \text{ cm}^2/\text{Vs}$  was used for InGaP cladding layer. The mobility of the cladding layer is an important parameter affecting the minority carrier leakage current which was shown previously to be anomalously large in non-optimized structures. The other effect is on the free-carrier absorption in waveguide layer. It is because the free-carrier absorption originates from the scattering of photo-excited free-carriers, and therefore the absorption rate is linearly proportional to the scattering rate. Thus free-carrier absorption loss  $\alpha_{fc}(T)$  is given by

$$\alpha_{fc}(T) = \alpha_{fc,0} \left( \frac{\tau(T)}{\tau_0} \right) \cong [3 \cdot N_{wg} + 7 \cdot P_{wg}] \cdot 10^{-18} \left( \frac{\tau(T)}{\tau_0} \right) [\text{cm}^{-1}] \quad (5-9)$$

where  $\alpha_{fc,0}$ , the room temperature free-carrier absorption loss was obtained from Ref. 17, and  $N_{wg}$ ,  $P_{wg}$  are non-equilibrium electron and hole concentrations in the waveguide layer in  $\text{cm}^{-3}$  unit. All temperature dependencies of the  $g(T, \pi(T))$ ,  $\mu(T)$  and  $\alpha_{fc}(T)$  which originated from  $\pi(T)$ , force  $J_{th}$  higher and  $\eta_d$  lower than in the case when only thermal broadening  $g(T)$  was considered. The results calculated using the Eq. (5-1), (5-2), (5-4)-(5-6) are shown in Fig. 5-1 and Fig. 5-2 by solid lines, showing an excellent quantitative agreement.

In conclusion, it has been demonstrated that the increase of  $J_{th}$  and the decrease of  $\eta_d$  of InGaAsP ( $\lambda=0.8 \mu\text{m}$ ) lasers at high temperature are mainly due to the thermal broadening of gain spectrum, and the

increase of momentum relaxation rate  $\hbar / \tau$  , presumably originating from alloy scattering. The understanding of the origin of the observed temperature dependence of  $J_{th}$  and  $\eta_d$  can be utilized in optimization of the investigated high-power lasers through proper structure designs.

## VI. Strain effect on 808 nm lasers

Strain effect on band-structures has been intensively researched on 0.98  $\mu\text{m}$  and 1.3-1.5  $\mu\text{m}$  long wavelength lasers [38, 53]. Theoretical band-calculation using envelope wave function approximation shows that strain induces significant shift of heavy-hole and light-hole energies in opposite directions, reducing degeneracy of the valence-band. Enhancement of gain and spontaneous emission have been observed experimentally as well as reduction of threshold current density [54]. A recent calculation shows that the linewidth enhancement factor  $\alpha$  can be tuned to zero when the strain and modulation-doping level are properly chosen [55]. Since the  $\alpha$  factor is one of the most crucial parameters for laser dynamics and high-power operation, the effect of strain need to be examined more closely.

In this section we describe the calculated results of stain effect on  $\lambda=808$  nm InGaAsP/GaAs lasers. We used the Luttinger-Kohn hamiltonian which was used for description of the valence-band mixing in section IV. The strain effect can be easily incorporated into the Luttinger-Kohn hamiltonian as done in [39].

$$H_{total} = H_v + H_{strain} \quad (6-1)$$

where

$$H_v = \frac{1}{2} \left( \frac{\hbar^2}{m_o} \right) \begin{pmatrix} (\gamma_1 + \gamma_2)k_\rho^2 + (\gamma_1 - 2\gamma_2)k_z^2 & \sqrt{3}\gamma_2 k_\rho(k_\rho + i2k_z) \\ \sqrt{3}\gamma_2 k_\rho(k_\rho + i2k_z) & (\gamma_1 - \gamma_2)k_\rho^2 + (\gamma_1 + 2\gamma_2)k_z^2 \end{pmatrix} + V(z) \quad (6-2)$$

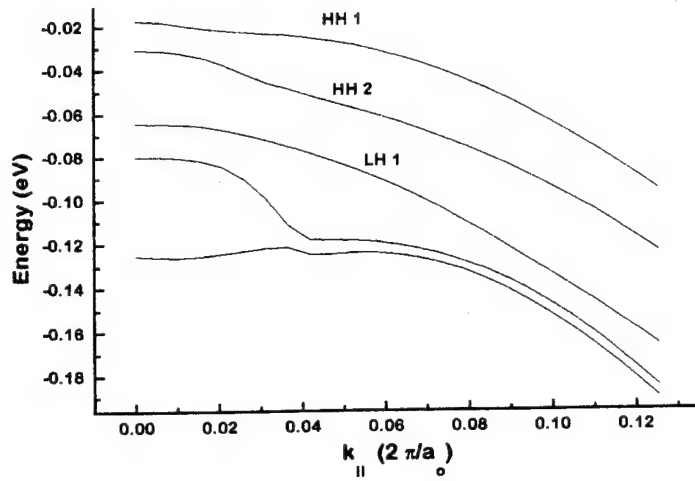
as defined in section IV.  $H_{strain}$ , the hamiltonian describing the energy shift on  $|J=3/2, J_z=\pm 3/2\rangle$  and  $|J=3/2, J_z=\pm 1/2\rangle$  is written in the following form:

$$H_{strain} = \begin{pmatrix} -\delta\epsilon_H - \frac{1}{2}\delta\epsilon_S & 0 \\ 0 & -\delta\epsilon_H + \frac{1}{2}\delta\epsilon_S \end{pmatrix} \quad (6-3)$$

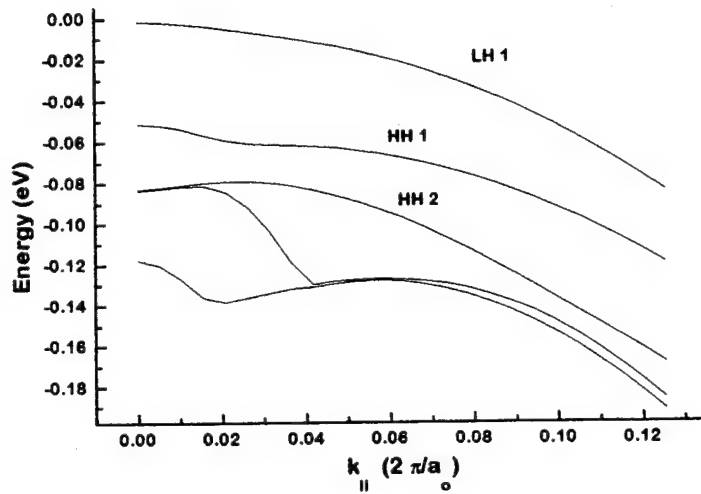
where  $\delta\epsilon_H$ ,  $\delta\epsilon_S$  are termed hydrostatic and shear energies, respectively.  $\delta\epsilon_H$  and  $\delta\epsilon_S$  are related to lattice-mismatch parameters via elastic constants  $C_{11}$ ,  $C_{12}$  and hydrostatic and shear deformation potentials  $a_1$ ,  $a_2$  by  $\delta\epsilon_H = 2a_1e_o(C_{11}-C_{12})/C_{11}$ ,  $\delta\epsilon_S = a_2e_o(C_{11}+2C_{12})/C_{11}$ . The material parameters such as elastic constants, Luttinger parameters and deformation potential for our quaternary material were interpolated from values of related binary compounds.

Figure 6-1 compares the band-structures of  $\text{In}_{0.13}\text{Ga}_{0.87}\text{As}_{0.74}\text{P}_{0.26}$  active layer sandwiched by  $\text{In}_{0.37}\text{Ga}_{0.63}\text{As}_{0.25}\text{P}_{0.75}$  waveguide layer with and without strain. The increased separation of  $hh1$  band and  $lh1$  band is clearly shown in this figure. Obviously this enhanced separation comes from the shear energy incorporated in Eq. (6-3). The large separation of  $hh1$  and  $lh1$  is beneficial for lowering threshold current density due to lower density of state and/or lighter effective mass for holes.

Figure 6-2 shows the optical gains when injection carrier density in active layer reaches  $2.7 \times 10^{18} \text{ cm}^{-3}$  with and without strain incorporation in the active layer. Enhancement of gain for strained layer by about factor of 2 is evident in this figure. Considering higher gain with less quasi-Fermi energy separation, we derive another benefit from strained QW structures, that is, reduced minority carrier leakage to cladding layers. Therefore we expect much less threshold current density, especially in  $\lambda=808 \text{ nm}$  InGaAsP/GaAs laser by employing strains in the active layers because of significant decrease of leakage current to which the lasers are vincible due small optical confinement as discussed in section III.



(a)



(b)

Fig. 6-1 (a) The valence-subband structures for a 100 Å  $\text{In}_{0.13}\text{Ga}_{0.87}\text{As}_{0.74}\text{P}_{0.26}/\text{InGaP}$  quantum well surrounded by InGaP barriers for (a) without strain (b) with 2.0 % compressive strain. Shift of light hole above heavy hole is clearly shown.

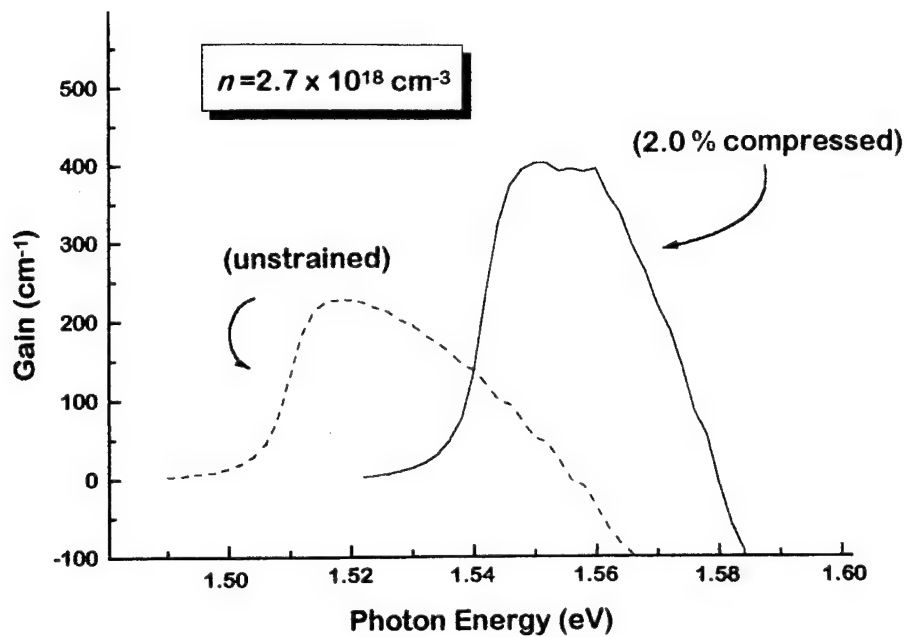


Fig. 6-2. Gain spectra of unstrained quantum well shown in Fig. 6-1 (a) (Dotted Line) and of strained quantum well shown in Fig. 6-1 (b) (Solid Lines) when injection carrier density  $n = 2.7 \times 10^{18} \text{ cm}^{-3}$ .

## VII. Beam propagation in MOPA

### *- Linewidth enhancement factor effect*

#### *Introduction*

Recent high demand on coherent, high power laser for such advanced area as optical fiber [56,57] or free-space communication [58], optical data processing [59] or storage and solid state laser pumping [60,61], has stimulated the research on stable high power lasers emitting in a broad wavelength range. However these demands include not only high power but also spectrally pure light source (coherence), and this has been an unsolved problem for long time.

Even though high power lasers with relatively broad spectrum and the pure-spectrum lasers with moderate power range have been fabricated with good quality, there had been a paradigm that designing of the laser possessing both features is not realistic. The reason is that for pure-spectrum laser (single transverse and longitudinal mode, diffraction-limited narrow far-field pattern, narrow emission linewidth only limited by spontaneous emission noise [62] ), one needs to use complicated design and fabrication technology such as distributed bragg reflector (DBR) [63], Buried heterostructure or antiguiding laser arrays, all of which enhance the optical loss and heat dissipation on the laser medium, preventing high power operation. Therefore so far the highest power was available from the lasers with the simplest geometry such as broad-area laser or amplifier with 100  $\mu\text{m}$  or wider stripe width up to 600  $\mu\text{m}$  [64], in which it is inherently difficult to control the lateral and longitudinal mode selection, spectrum width, and uniform optical field distribution .

Researchers from various groups have started merging the two separate developments by employing concept of the laser amplifier to a high power light source [65-67]. In this concept, one integrates two lasers with distinctive features, one totally devoted to the spectral aspect, the other devoted to high power. DBR or DFB lasers with spectral excellence are used as input source for broad-area (or tapered) lasers that amplify it for output. The beam quality offered from the former (master oscillator) remains excellent even after power amplification through the latter (power amplifier). So far the best result among monolithically integrated laser source was obtained from the design where a DBR laser is employed for master oscillator and a tapered broad-area amplifier is used for power amplifier ( thus named Monolithically integrated Flared Amplifier-Master Oscillator Power Amplifier (MFA-MOPA) ) [65] using AlGaAs/GaAs material system. 2 W CW was obtained with the laser linewidth as low as 4 MHz and diffraction-limited lateral far-field angle ( $0.28^\circ$ ) without any chirping in laser modulation. The laser possesses the best beam quality of the DBR lasers [63] while still achieving very high CW power. However the life-time issue of the laser amplifier has not not been dealt with yet. It is speculated that the Al-contained MOPA would show similar degradation observed in AlGaAs laser diodes due to inherent oxidation problem and replacement and that replacement by Al-free material is highly desirable.

In this section, as a first step toward the embodiment of the MOPA by InGaAsP material system, we developed a numerical simulator for MOPA using beam propagation method [68]. This method has been successfully applied to MFA-MOPA [69], Resonant-optical-waveguide power amplifier [66], and various laser structures [68,70,71]. Brief description on beam propagation method is given, followed by the numerical results for various linewidth enhancement factor  $\alpha$  and the pumping current density  $J$ .

### ***Theoretical model***

When a single longitudinal TE mode oscillating at the frequency  $\omega$ , propagating in  $z$  direction is considered, the electric field can be written as:

$$\vec{E} = \hat{x} \psi(x, z) e^{-i(\omega t - kz)} \quad (7-1)$$

Here field profile on  $y$  direction is not considered since the beam profile in the perpendicular direction to the junction plane remains the fundamental mode and does not affect the dynamics of the lasers. When the beam width  $w$ , and the cavity length  $L$  are much larger than wavelength  $\lambda$ , Maxwell's wave equation can be converted to a simpler form, by employing paraxial approximation [70]:

$$2ik \frac{\partial \psi}{\partial z} + \frac{\partial^2 \psi}{\partial x^2} + (n_{eff} - k^2) \psi = 0 \quad (7-2)$$

where  $n_{eff}(x, z) = n_o + \frac{i}{k_o} \{g(1 + i\alpha) - \alpha_{loss}\}$  and the gain

$$g = \frac{\beta \Gamma (J - J_{th})}{I + P / P_{sat}} \quad (7-3)$$

is used in this approximation to incorporate the gain saturation effect. The differential gain  $\beta \Gamma = 0.1 \text{ cm/A}$ , the back-ground optical loss  $\alpha_{loss} = 5 \text{ cm}^{-1}$  and  $P_{sat} = \frac{hc}{\lambda q} \frac{\eta_{int}}{\Gamma \beta} \sim 150 \text{ mW}/\mu\text{m}$  are assumed in our calculation. The linewidth enhancement factor  $\alpha \equiv -(1/2k_o) dn/dg$  (sign may be different from literature), and the pumping current  $J$  are used as a varying parameters in the simulation. Equation (7-2) is rewritten as

$$\frac{\partial \psi}{\partial z} + (\mathbf{A} + \mathbf{B}) \psi = 0, \quad (7-4)$$

where  $\mathbf{A} = \frac{i}{k_o} \frac{\partial^2}{\partial x^2}$ , the diffraction operator and  $\mathbf{B} = \frac{i}{2k_o} (n_{eff}(x, z) - k^2)$ , the complex-gain operator. The

approximate solution of Eq. (7-4) with minimal error [70] is given by

$$\psi(x, z + \delta z) = e^{\frac{1}{2} \mathbf{A} \delta z} e^{\int_z^{z+\delta z} \mathbf{B}(z') dz'} e^{\frac{1}{2} \mathbf{A} \delta z} \psi(x, z) \quad (7-5)$$

Here  $\delta z$  should be chosen so that in this interval the change of gain-loss is small, that is,  $\delta z \Delta n_{eff} \ll k w^2 n_{eff}$  [70]. If  $\Delta n_{eff} \sim 0.01$ ,  $w = 100 \text{ nm}$ ,  $k = 6 \cdot 10^4 \text{ cm}^{-1}$ , then  $\delta z \ll 1000 \text{ nm}$  should be

satisfied for Eq. (7-5) to be valid solution. The operator  $e^{\frac{1}{2} \mathbf{A} \delta z}$  has the physical meaning of free-diffraction propagation of the wave and it can be rewritten as

$$\psi(x, z + \delta z) \equiv e^{\frac{1}{2} A \delta z} \psi(x, z) = (\mathbf{F}^{-1} e^{i \frac{q^2}{2k} \delta z} \mathbf{F}) \psi(x, z) \quad (7-6)$$

where  $q$  is the Fourier space variable,  $\mathbf{F}$  represents the Fourier transform operator in  $x$  space. Using Eq. (7-1), (7-5) and (7-6), we can evaluate  $E(x, z)$  for all  $x$  and  $z$ , given a input field at the input aperture supplied from the external source (such as DBR lasers). We assumed 10 mW Gaussian light for the input external light source.

In this work, this method is applied to MFA-MOPA to demonstrate the effect of parameters such as linewidth enhancement factor  $\alpha$ , and the pumping current density  $J$  on the amplifier gain, near-field and far-field pattern of the amplified beam so that optimized pumping level for a given material parameters can be determined. This device is chosen for our study since first so far it demonstrates the best experimental results ( 21W pulse wave [64] diffraction-limited beam, 2W CW [65] ), and also it has the simplest structure to analyze. This simulator can easily be converted to study of other structure such as antiguiding array MOPA or laser diodes. Studies on those topics will be reported in separate papers. The schematic diagram of the MFA-MOPA analyzed in this work is shown in Fig. 7-1.  $J$  in Eq. (1) was varied from 0.5 kA/cm<sup>2</sup> to 5 kA/cm<sup>2</sup> for study of both weakly saturated and strongly saturated cases. The current is confined inside the contact boundary shown in Fig. 7-1. The importance of the linewidth enhancement factor  $\alpha$  in stabilizing the lateral mode has been recognized by many authors [72,73]. This effect was given special emphasis in this work. Calculated amplified beams from MFA-MOPA with  $\alpha=0$  (no dispersion due to carrier density variation),  $\alpha = + 2.0$  (positive dispersion) and  $\alpha = - 2.0$  (negative anomalous dispersion) are compared in the next section.

### ***Results and Discussion***

Solid line and dotted line of Fig. 7-2 (a) represent the far-field pattern from the power amplifier with  $\alpha = 0$  at  $J = 500$  A/cm<sup>2</sup> and  $J = 5000$  A/cm<sup>2</sup>, respectively. Near-diffraction-limited beam is obtained in both cases in far-field pattern when proper correction lens is inserted to make the best collimated beam.

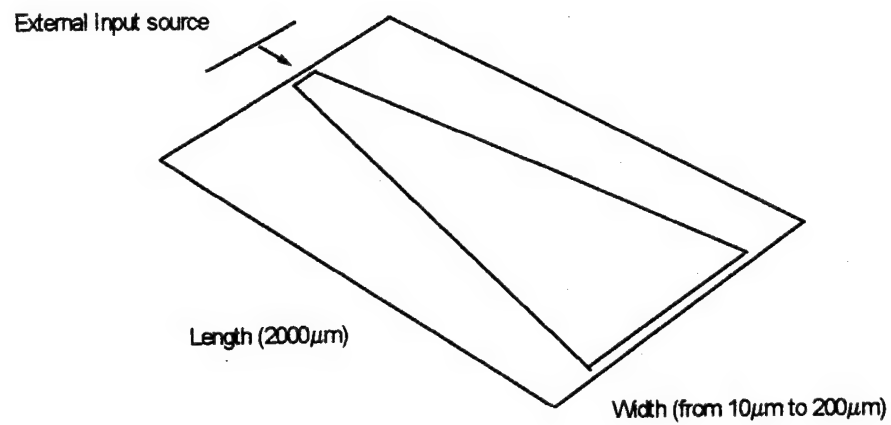


Fig.1 Schematic diagram of MCPA. The amplifier broadens from 10  $\mu$ m at the input to 200  $\mu$ m at the output.

The effect of lens is incorporated into the calculation using spherical lens approximation [74]. Small satellites far-field pattern around the main central lobe in high power operation indicate that the phase front of the amplified beam has been distorted even when  $\alpha = 0$ , and cannot be easily recovered by corrective lens. Fig. 7-2 (b) shows the calculated near-field pattern of output power from the MOPA with  $J=5000 \text{ A/cm}^2$ . Higher intensity remains near the central region, indicating that still the gain is not completely saturated over whole region.

If the refractive index  $n_{\text{eff}}$  increases as the carrier density increases (i.e. positive  $\alpha$ ), the beam tends to be self-focused and becomes filamentary [73], causing the far-field pattern to be wide and multi-lobed. The effect of positive  $\alpha$  on the far-field and near-field pattern is shown in Fig. 7-3 (a) and 7-3 (b), respectively, where formation of filament is obvious in high current injection. The resulting far-field at high current pumping ( $J = 5000 \text{ A/cm}^2$ ) has very wide and large number of satellites as often observed in the experiment of highly injected laser diodes. Spacing between the filaments is approximately  $15 \mu\text{m}$ , as observed in the laser diodes [75].

Negative  $\alpha$  has the defocusing effect, contrary to positive  $\alpha$  case. The resulting far-field and near-field patterns are shown in Fig. 7-4 (a),(b), respectively. As expected, the near-field pattern becomes much more uniform than  $\alpha = 0$  case since the central higher intensity part in Fig. 7-2 (b) has been spread due to the defocusing effect. Also far-field pattern has much wider beam spread, about 3-4 times wider than  $\alpha = 0$  case due to the same effect. This fact indicates that phase front becomes again distorted in the negative  $\alpha$  case, not corrected by a simple spherical lens.

In terms of the total output power, the three  $\alpha$  cases generate almost same output. When  $J=5000 \text{ A/cm}^2$  (corresponding to total current  $I = 10 \text{ A}$ ) is applied, Fig. 7-2 (b), 7-3 (b), 7-4 (b) show that almost 14 W is generated in each case from the input power 10 mW. The amplifier gain reaches to 140, that is, 21dB. Total conversion quantum efficiency is about 1.4 W/A or 93%, showing that only small fraction of beam

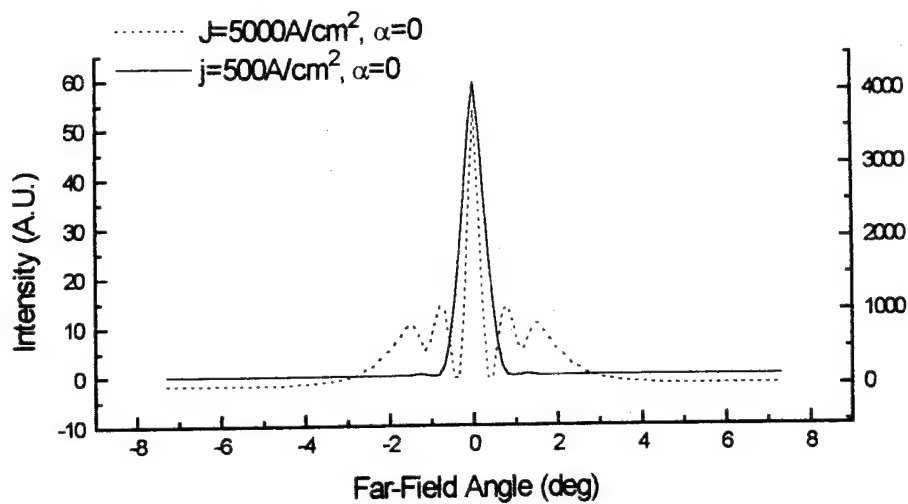


Fig 2 (a) Far-field pattern of the MOPA with  $J=500\text{A/cm}^2$  and  $J=5000\text{A/cm}^2$  and  $\alpha=2$ . High gain results in the number of satellites around the central lobe, due to the phase front distortion by the non-uniform gain.

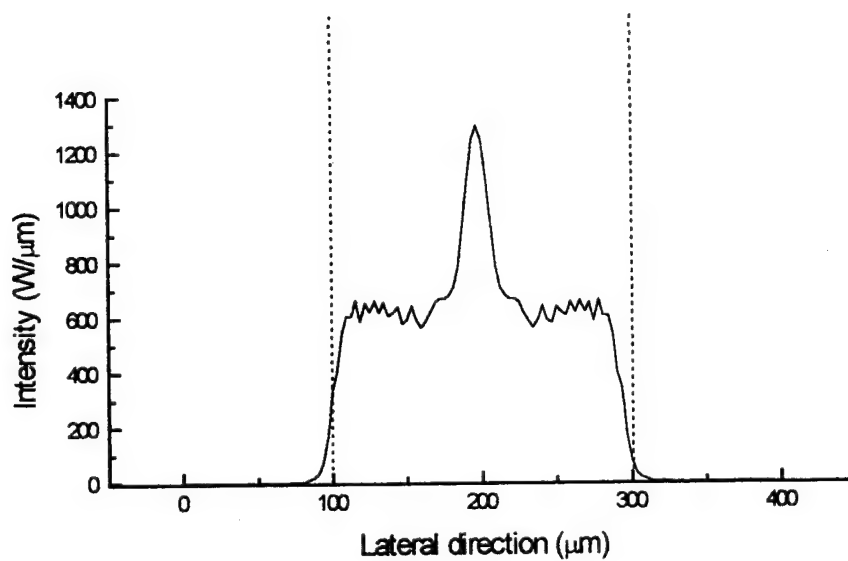


Fig 2 (b) Near-Field Pattern of output power from MOPA with  $J=5000\text{A/cm}^2$  and  $\alpha=0$ . There is non-uniform unsaturated region near the center. Dotted lines represent the output side gain-guided aperture boundaries.

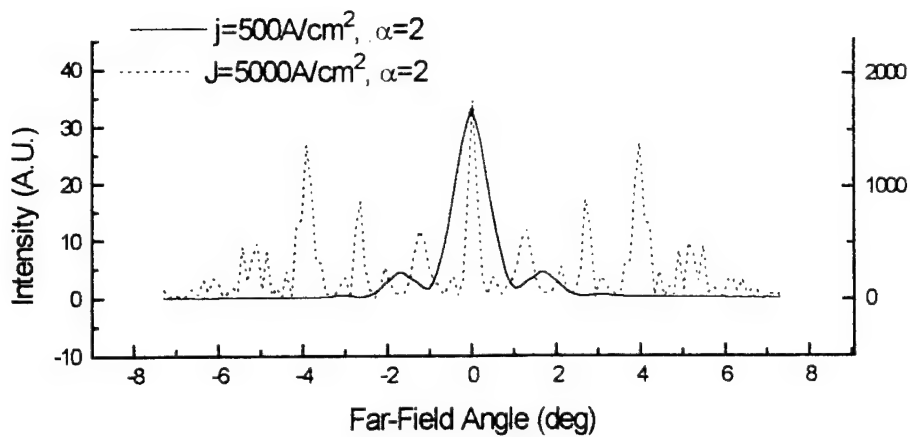


Fig 3 (a) Far-field pattern of the MOPA with  $J=500A/cm^2$  and  $J=5000A/cm^2$  and  $\alpha=2$ . Half-width becomes much wider and/or multi-lobed, resulting from the nonlinear self-focusing effect by the positive linewidth enhancement factor  $\alpha$ .

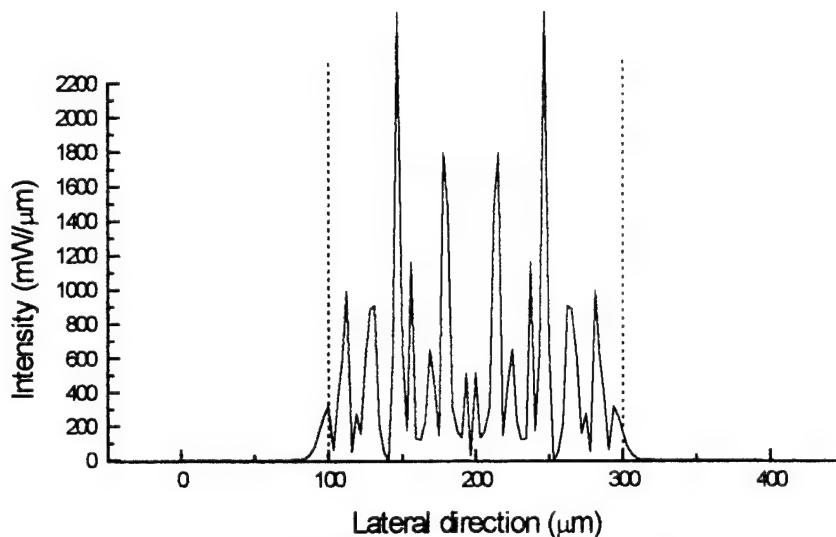


Fig 2 (b). Near-Field Pattern of the MOPA with  $J=5000A/cm^2$ , with  $\alpha=2.0$ . Filaments with spacing of approximately  $15\mu m$  are formed due to self-focusing effect. Dotted lines represent the gain-guided output aperture boundary.

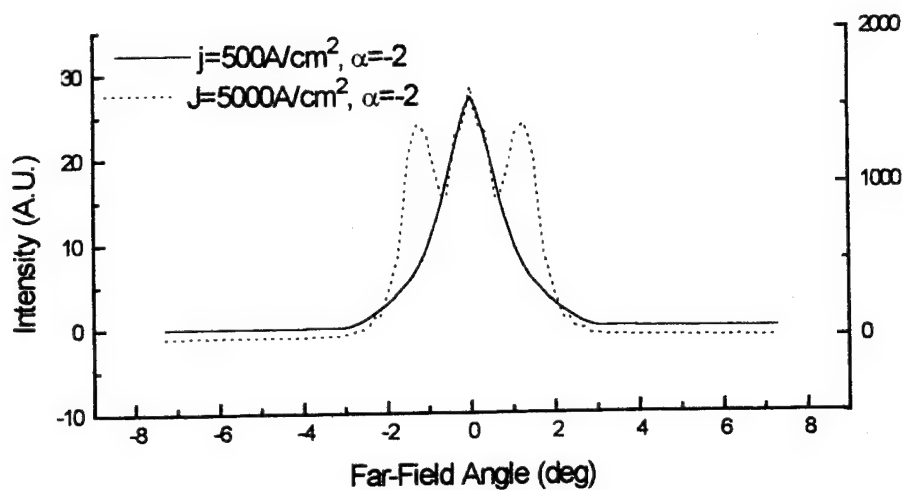


Fig 4 (a) Far-field pattern of the MOPA with  $J=500\text{A/cm}^2$  and  $J=5000\text{A/cm}^2$  and  $\alpha=-2$ . Half-width becomes much wider compared to the  $\alpha=0$  case, resulting from the defocusing effect of the negative anomalous dispersion (negative  $\alpha$ )

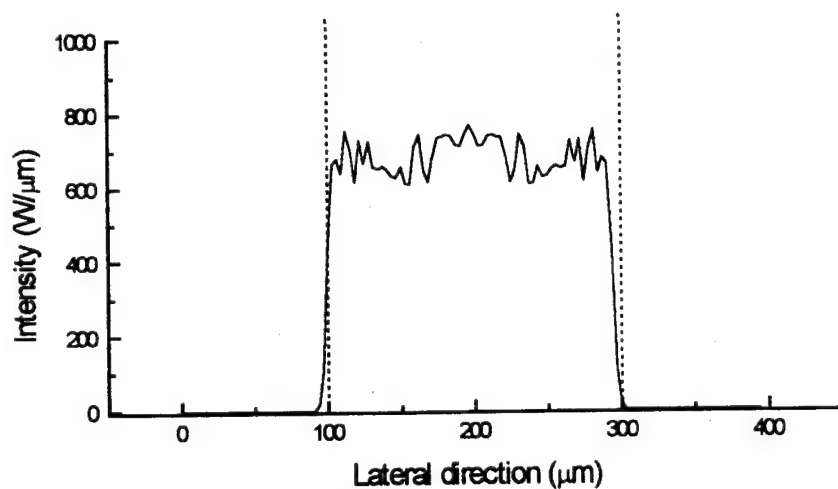


Fig 4 (b) Near-Field Pattern of the MOPA with  $J=5000\text{A/cm}^2$ , with  $\alpha=-2.0$ . Filaments are nearly unseen. Dotted lines represent the gain-guided output aperture boundary.

was lost by the optical loss inside the pumped region and in the outside lossy region, and by the spontaneous emission to which current below the threshold is consumed.

In conclusion, through a numerical simulation we clearly demonstrated the effect of the linewidth enhancement factor  $\alpha$  to the lateral optical distribution. In order to achieve the narrowest beam divergence, the linewidth enhancement factor  $\alpha$  should be a small negative number to avoid filamentary lasing.

## VIII. Conclusion

### *Optimization of the InGaAsP/GaAs laser diodes*

In this work, we reported a detailed experiment and theoretical analysis for various properties of the laser diodes. In section II, it was found that the LP-MOCVD-grown InGaAsP has no detectable non radiative recombination center at high excitation and that spillover to waveguide layer is determined purely by thermal distribution. It enabled us to model the device in the later sections. Observation made in section III that 300 Å thick active layer gives the optimal optical-confinement, below which the minority carrier leakage increases rapidly, stimulated us to further investigate whether multiple quantum well lasers with a 300 Å total thickness for active layer has better performance than the 300 Å single well lasers. In that experiment (section IV) we found that making multiple quantum wells for the total 300 Å active layer volume does not lower  $J_{th}$  nor increase  $\eta_d$  due to alloy-scattering-induced high momentum relaxation rate. Thus the 300 Å single quantum well SCH lasers is favored for the most efficient high power laser structure, requiring only a minimum complexity of fabrication. We attributed the major reason of degradation of threshold condition at high temperature to alloy scattering in active layer (section V). Control of proper alloy composition to minimize the potential fluctuation would improve the temperature characteristics. However, we should note that high momentum relaxation rate is a beneficial factor when we consider high-speed modulation properties. Capturing time, which is a limiting factor for modulation rate, is known strongly dependent on the momentum relaxation and is often bottle-neck of high-speed modulation lasers. Alloy scattering may be an ideal solution to this since it enhances momentum relaxation without degrading radiation efficiency (not creating non-radiative recombination center).

### *Direction for further investigation*

Our study cast a few perspectives for further study. Our numerical simulation of beam-propagation on MOPA clearly indicated the linewidth enhancement factor  $\alpha$  is the single most important factor governing

the beam-quality. This result stimulates us to further investigate on this topic as to how to control the linewidth enhancement factor. There are a number of report that modulation-doping and strain can shift the  $\alpha$  factor [54,55]. However, no detailed transport mechanism inside the quantum well with doping and strain at high power operation (high current) has been understood. Therefore it is an very interesting and also urgent topic to investigate this effect with consideration of electric field, many body interaction and interface state for the high performance laser device design.

## References

- [1] M. Razeghi, "High-power laser diodes based on InGaAsP alloys", *Nature*, vol. 369, 631, 1994.
- [2] C.H. Henry, P.M. Petroff, R.A. Logan, and F.R. Merritt, "Catastrophic damage of AlGaAs double-heterostructure laser material", *J. Appl. Phys.* 50, 3721, 1979.
- [3] S.L. Yellen, A.H. Shepard, C.M. Harding, J.A. Baumann, R.G. Waters, D.Z. Garbuzov, V. Pjataev, V. Kocherigin, and P.S. Zory, "Dark-line-resistant, Aluminum-free diode laser at 0.8  $\mu\text{m}$ ", *IEEE Photon. Tech. Lett.*, PTL-4, 1328, 1992.
- [4] Jae S. Yoo, Sang H. Lee, Gueorgui T. Park, Yong T. Ko, and Taeil Kim, "Peculiarities of catastrophic optical damage in single quantum well InGaAsP/InGaP buried-heterostructure lasers", *J. Appl. Phys.* 75, 1840, 1994.
- [4a] M. Fukuda, "Current drift associated with surface recombination current in InGaAsP/InP optical devices", *J. Appl. Phys.*, 59, 4172, 1986.
- [5] O. Ueda, S. Yamakoshi, T. Sanada, I. Umebu, and T. Kotani, "Mechanism of catastrophic degradation in InGaAsP/InP double-heterostructure light emitting diodes and GaAlAs double-heterostructure light emitting diodes applied to pulsed large current", *J. Appl. Phys.*, vol. 53, 9170, 1982.
- [6] P. A. Kirkby, "Dislocation pinning in GaAs by the Deliberate Introduction of Impurities", *IEEE J. Quantum Electron.*, vol. QE-11, 562, 1975.
- [7] N. Chand, N.K. Dutta, and S.N.G. Chu, A.V. Syrbu, A.Z. Mereutza, and V.P. Yakovlev, "High performance strained InGaAs/AlGaAs buried-heterostructure quantum-well lasers fabricated by in situ etching and regrowth", *Appl. Phys. Lett.*, vol. 62, 1818, 1993.
- [8] I. Eliashevich, J. Diaz, H. Yi, L. Wang, and M. Razeghi, to be published in *Appl. Phys. Lett.*, (Ms# L-3379), accepted on January 17, 1995.
- [9] W. C. Tang, E. H. Alterndorf, H.J. Rosen, D. J. Webb, P. Vettiger, "Lifetime extension of uncoated AlGaAs single-quantum-well lasers by high-power burn-in in inert atmospheres", *Electron. Lett.*, vol. 30, 143-145 (1994).

- [11] W. Chow, S. Koch and M. Sargent III, *Semiconductor-Laser Physics*, (Springer Verlag, Berlin, 1994) p. 203
- [12] M. Fukuda, *Reliability and Degradation of Semiconductor Lasers and LEDs* (Artech House, Boston, 1991)
- [13] N. Jensen, H. Olesen, and K. Stubkjar, "Partition Noise in Semiconductor Lasers under CW and pulsed operation", *IEEE J. Quantum Electron.*, QE-23, 71 (1987)
- [14] P. Szczepanski, A. Mossakowska, and D. Dejnrowicz, "Relaxation Oscillations in Waveguide Distributed Feedback Lasers", *J. Light Wave Technology* 10, 220 (1992)
- [15] H. Li, J. Ye, and J. McInerney, "Detailed Analysis of Coherence Collapse in Semiconductor Laser", *IEEE J. Quantum Electron.* QE-29, 2421 (1993)
- [16] Y. Yamamoto and S. Machida, "Amplitude squeezing in a pump-noise-suppressed laser oscillator", *Phys. Rev. A* 34, 4025 (1986)
- [16a] S. Luryi, "Hot-Electron Transistors" in *High-Speed Semiconductor Devices*, S. M. Sze, Ed., John Wiley & Sons Inc., New York, 1990, p. 410
- [17] R.J. Nelson and K.G. Sobers, *J. Appl. Phys.*, 49, 6103(1978)
- [18] D.Z. Garbuzov, *J. Lumin.*, 27, 109 (1982)
- [19] R.K. Ahrenkiel, B.M. Keyes, and D.J. Dunlavy, *J. Appl. Phys.*, 70, 225 (1991)
- [20] P. Blood, A.I. Kucharska, J.P. Jacobs, and K. Griffiths, *J. Appl. Phys.*, 70, 1144 (1991)
- [21] X. He and M. Razeghi, *J. Appl. Phys.* 62, 4447 (1992)
- [22] D.L. Garbuzov, N.Y. Antoishkis, A.D. Bondarev, S.N. Zhigulin, A.V. Kochergin, N.I. Katsavets and E.V. Rafailov, *IEEE J. Quantum Electron.*, 27, 1531 (1991)
- [23] Zh. I. Alferov and D.Z. Garbuzov, 18th Int. Conf. on Phys. of Semicond. V.I., Stockholm, Sweden, 203 (1986)

- [24] A. R. Reisinger, P. s. Zory, and R. Waters, IEEE J. Quantum Electron., QE-23, 993 (1987).
- [25] N.K. Dutta, J. Appl. Phys., 52, 70 (1981).
- [26] N. K. Dutta, J. Appl. Phys., 54, 1236 (1983).
- [27] Casey and Panish, "*Heterostructure Laser*" (Academic, New York, 1978).
- [28] J. Diaz, I. Eliashevich, H. Yi, M. Stanton, M. Razeghi, Appl. Phys. Lett., 65, 2260 (1994).
- [29] S. Chinn, P. Zory, A. Reisinger, IEEE J. Quantum Electron., QE-24, 2191 (1988).
- [30] C. M. Wolfe, N. Holonyak, Jr., and G. E. Stillman, "*Physical properties of semiconductors*" (Prentice Hall, Englewood Cliffs, NJ, 1989), p.340.
- [31] J.R. Biard, W.N. Carr, and B.S.Reed, Trans. AIME, 230, 286 (1964)
- [32] R. Chin, N. Holonyak, Jr., B. A. Vojak, K. Hess, R. D. Dupuis, and P. D. Dapkus, Appl. Phys. Lett. 36, 19 (1980)
- [33] Y. Arakawa, A. Yariv, IEEE J. Quantum Electron. QE-21, 1666 (1985)
- [34] P. A. Chen and C. Y. Chang, J. Appl. Phys. 76, 85 (1994)
- [35] H. J. Yi, J. Diaz, I. Eliashevich, M. Stanton, M. Erdtmann, X. He, L.J. Wang, and M. Razeghi, Appl. Phys. Lett. 66, 253 (1995)
- [36] B. Zee, IEEE J. Quantum Electron. QE-14, 727 (1978)
- [37] J. M. Luttinger, Phys. Rev. 102, 1030 (1956)
- [38] D. Ahn, S. L. Chuang, IEEE J. Quantum Electron. QE-30, 350 (1994)

- [39] W. Chow, S. Koch and M. Sargent III, *Semiconductor-Laser Physics*, (Springer Verlag, Berlin, 1994) p. 203
- [40] D. Gershoni, C. H. Henry and G. A. Baraff, IEEE J. Quantum Electron. QE-29, 2433 (1993)
- [41] H. Hirayama, Y. Miyake, and M. Asada, IEEE J. Quantum Electron. QE-28, 68 (1992)
- [42] J. Diaz, I. Eliashevich, H. Yi, M. Stanton, and M. Razeghi, Appl. Phys. Lett. 65, 2260 (1994)
- [43] H. J. Yi, J. Diaz, L. J. Wang, I. Eliashevich, S. Kim, R. Williams, M. Erdtmann, and M. Razeghi, to be published in Appl. Phys. Lett., (Ms # L-2832), accepted on March 7, 1995
- [44] D. Biswas, N. Debbar, P. Bhattacharya, M. Razeghi, M. Defour, and F. Omnes, Appl. Phys. Lett. 56, 833 (1990)
- [45] J. Bulter, J. Zoroofchi, IEEE J. Quantum Electron. QE-10, 809 (1974)
- [46] W. C. Mitchel, G. J. Brown, I. Lo, S. Elhamri, M. Ahoujja, K. Ravindran, R. S. Newrock, M. Razeghi, and X. He, Appl. Phys. Lett. 65, 1578 (1994)
- [47] C. Henry, R. Logan, F. Merritt, IEEE J. Quantum Electron. QE-17, 2196 (1981)
- [48] M. Asada, A. Kameyama, Y. Suematsu, IEEE J. Quantum Electron. QE-20, 745 (1984).
- [49] A. Fortini, D. Diguët, J. Lugand, J. Appl. Phys. 41, 3121 (1978).
- [50] K. Masu, El. Tokumitsu, M. Konagai and K. Takahashi, J. Appl. Phys. 54, 5785 (1983).
- [51] M. Yamada, H. Ishiguro and H. Nagato, Jpn. J. Appl. Phys. 19, 135 (1980).
- [52] D. Look, D. Lorange, J. Szelov, C. Stutz, K. Evans, and D. Whitson, J. Appl. Phys. 71, 260 (1992).
- [53] PR B on strain for band

- [54] F. Kano, T. Yamanaka, N. Yamamoto, H. Mawatari, Y. Tohmori, and Y. Yoshikuni, "Linewidth enhancement factor in InGaAsP/InP Modulation-Doped Strained Multiple-Quantum Well Laser", *IEEE J. Quantum Electron.* QE-30, 533 (1994)
- [55] T. Yamanaka, Y. Yoshikuni, W. Lui, K. K. Yokoyama, and S. Seki, "Theoretical analysis of extremely small linewidth enhancement factor and enhanced differential gain in modulation-doped strained quantum-well lasers", *Appl. Phys. Lett.* 62, 1191 (1993)
- [56] Y. Yamamoto, "Noise and error rate performance of semiconductor laser amplifiers in PCM-IM optical transmission systems", *IEEE J. Quantum Electron.*, 16, 1073, 1980.
- [57] S.B. Alexander, E.S.Kintzer, J.C.Livas, J.N.Walpole, C.A.Wang, and L.J. Missaggia, and S.R.Chinn, "1 Gbit/s coherent optical communication system using a 1W optical power amplifier", *Electron. Lett.*, vol.29, 114-115,1993.
- [58] T.L.Koch, "Semiconductor lasers for coherent optical fiber communications", *J. Lightwave Tech.*, 8, 274, 1990.
- [59] P.R.Prucnal, "Optically processed self-routing, synchronization, and contention resolution for 1-D and 2-D photonic switching architectures", *IEEE J. Quantum Electron.*, 29, 600, 1993.
- [60] J. G. Endriz, M. Vakili, G. Browder, M. DeVito, J. Haden, G. Harnagel, W. Plano, M. Sakamoto, D. Welch, S. Willing, D. Worland, and H. Yao, "High Power Diode Laser Arrays", *IEEE J. Quantum Electron.*, vol. 28, 952-965, 1992.
- [61] J. Kasinski, W. Hughes, D. DiBiase, P. Bournes, and R. Burnham, "One Joule Output From a Diode-Array-Pumped Nd:YAG Laser with Side-Pumped Rod Geometry", *IEEE J. Quantum Electron.*, vol. 28, 977-985, 1992.
- [62] C.H. Henry, "Theory of the linewidth of semiconductor lasers", *IEEE J. Quantum Electron.*, 18, 259, 1982.
- [63] S. O'Brien, R. Parke, D.F.Welch, D.Mehuys and D.Scifres, "high power singlemode GaInAs Lasers with distributed bragg reflectors", *Electron. Lett.*, 28, 1272, 1992.

- [64] L. Goldberg, D. Mehuys, "21W broad area near-diffraction-limited semiconductor amplifier", *Appl. Phys. Lett.*, vol. 61, 633-635, 1992.
- [65] S. O'Brien, D. Welch, R. Parke, D. Mehuys, K. Dzurko, R. Lang, R. Waarts, and D. Scifres, "Operating Characteristics of a High-power monolithically integrated flared amplifier master oscillator power amplifier", *IEEE J. Quantum Electron.*, 29, 2052, 1993.
- [66] D. Botez, M. Jansen, C. Zmudzinski, L. J. Mawst, P. Hayashida, C. Tu, and R.F. Nabiev, "Flat-phasefront fanout-type power amplifier employing resonant-optical-waveguide structures", *Appl. Phys. Lett.*, vol. 63, 3113-3115, 1993.
- [67] F. Koyama, K.-Y. Liou, A.G. Dentai, T. Tanbun-ek, and C.A. Burrus, "Multiple-Quantum-well GaInAs/GaInAsP Tapered Broad-Area amplifier with monolithically integrated waveguide lens for high-power applications", *IEEE Photon. Technol. Lett.*, vol. 5, 916-919, 1993.
- [68] G.P. Agrawal, W.B. Joyce, R.W. Dixon, and M. Lax, "Beam-propagation analysis of stripe-geometry semiconductor lasers: Threshold behavior", *Appl. Phys. Lett.*, vol. 43, 11, 1983.
- [69] R.J. Lang, A. Hardy, R. Parke, D. Mehuys, S. O'Brien, J. Major, D. Welch, "Numerical analysis of flared semiconductor laser amplifiers", *IEEE J. Quantum Electron.*, 29, 2044, 1993.
- [70] M. Lax, J.H. Batteh, and G.P. Agrawal, "Channeling of intense electromagnetic beams", *J. Appl. Phys.*, vol. 52, 109-125, 1981.
- [71] G. R. Hadley, J. P. Holimer, and A. Owyong, "Comprehensive modeling of diode arrays and broad area devices with applications to lateral index tailoring", *IEEE J. Quantum Electron.*, vol. 24, 2138-2152, 1988.
- [72] F. Nash, "Mode guidance parallel to the junction plane of double- heterostructure GaAs lasers", *J. Appl. Phys.*, vol. 44, 4696, 1973.
- [73] D. Mehuys, R.J. Lang, M. Mittelstein, J. Salzman, Amnon Yariv, "Self-stabilized nonlinear lateral modes of broad area lasers", *IEEE J. Quantum Electron.*, vol. 23, 1909-1920, 1987.
- [74] M. Klein and T. Furtak, "Optics", John Wiley & Sons, 1986.

[75] A. Larsson, M. Mittlestein, Y. Arakawa, A. Yariv, "High efficiency broad area single quantum well lasers with narrow single-lobed farfield pattern prepared by MBE", *Electron. Lett.*, vol.22, 79-91, 1986.

## *CHAPTER VI*

### *808 nm InGaAsP/GaAs BURIED RIDGE LASERS*

## CHAPTER VI

### 808nm InGaAsP/GaAs Buried Ridge Lasers

#### 1. Introduction

InGaAsP alloys, lattice matched to GaAs, are of interest in diode lasers emitting at 0.7-0.9 $\mu$ m because of their superior resistance over AlGaAs alloys to rapid degradation by dark line defect propagation<sup>[1]</sup> and catastrophic mirror damage<sup>[2]</sup>. The aluminum free system also lends themselves more readily to the fabrication of advanced integrated device structures by epitaxial regrowth. The center has demonstrated the growth of high quality InGaAsP-GaAs separate-confinement heterostructures with InGaP cladding layers by low-pressure metalorganic chemical vapor pressure (LP-MOCVD) and the fabrication of this material into broad-area devices.<sup>[3-13]</sup> The major advantage of broad-area lasers are their high reliability and the simplicity of fabrication; however, their disadvantages lies in the multimode operation.<sup>[14]</sup> In reducing the current spreading, the threshold current density, and to obtain single-mode, buried-ridge lasers (BRS) are of interests. These BRS lasers provides excellent optical and electrical confinement carriers, and reducing the nonradiative recombination centers at the sidewalls. In addition, it provides low threshold current density, stable guide modes, and near-circular far- field pattern. The complexity of fabricating index-guided lasers is that the internal waveguide is formed by etching certain portions of semiconductor material and regrowing a lower index material around the lasing stripe. The most essential concept in most junction lasers is that the laser should operate in a single-mode. The domination of the fundamental mode operation results in how the active region is localized.

This semi-report discusses the studies and evaluation that has been done over the past months on growth characterization, fabrication and cleaning preparation of buried ridge lasers. Two types of selective growth techniques (LP-MOCVD and GSMBE) for the III-V semiconductor materials are being considered for regrowth. The fabrication of index-guided 0.80 $\mu$ m lasers are divided into three stages of research. The first stage consists of fabrication technology, i.e., photolithography, cleaning, regrowth of GaAs or InGaP films by LP-MOCVD and GSMBE. Second stage is focused on the optical quality of the confinement layers after regrowth which will be reported elsewhere, and the third stage is the characterization of these buried ridge devices.

## 2. Growth Characterization of GSMBE Regrowth

### a. GSMBE Regrowth Review

The many variants of MBE: solid source MBE, gas-source MBE, and metalorganic MBE have all been used to achieve regrowth. Regrowth using MBE is desired because of its ability to reproducibly grow very thin layers in a controlled manner. (e.g. for vertical cavity surface emitting laser mirrors). At present, most MBE regrowth is done by metalorganic MBE (also known as CBE) because it is also possible to achieve selective area growth.

For MBE, typical growth rates on (100) surfaces are 0.5 to 1.5  $\mu\text{m/hr}$ . and this growth rate depends (approximately) only on substrate temperature and incident Ga flux, since the Ga atom is assumed to have a sticking coefficient of one. In regrowth, both the incident flux and the sticking coefficient depend on the angle a facet makes with the (100) reference plane. In addition, the effect of changing the growth temperature is different for different facet angle. Thus the growth rate is a strong function of the crystal angle and changes radically between facets.

The effective sticking coefficient depends on facet angle and the diffusion length of the incident atoms at the chosen growth temperature. If the facet angle relative to (100) is increased, the sticking coefficient is decreased relative to (100). If the diffusion length of the incident atoms is less than the dimension of the facet, then the relative effective sticking coefficient will be further reduced or enhanced as the atoms diffuse towards a more preferable facet.

In attempt to regrow high quality InGaP-GaAs on a 1  $\mu\text{m}$  etched ridge using GSMBE technique, several growth rates and growth conditions were investigated for several weeks. In doing so, InGaP regrown on InGaAsP demonstrated room temperature photoluminescence intensities on the order of 3 times weaker than that observed on unprocessed wafers grown simultaneously (Figure 6.1). No variation in the peak position or the full-width at half-maximum was observed between the two samples. Strong photoluminescence of the InGaAsP active layer (Figure 6.2) is seen on samples with regrown confinement layer, indicating excellent optical quality of the regrown InGaP.

Topophotoluminescence measurements of the regrown InGaP (Figure 6.3) show luminescence can occur from on top of the buried ridge, as well as from the 300  $\mu\text{m}$  spacings regions.

### 3. Experimental Studies of Buried Ridge

#### a. Growth Structure

The primary epitaxial layers for the buried-ridge laser is grown by low-pressure metalorganic chemical vapor deposition. Starting with an n-type (100) oriented Si-doped GaAs substrate, the following layers are grown: an n-type Si-doped ( $N_d \sim 5 \times 10^{17} \text{ cm}^{-3}$ ) InGaP cladding layer, an  $\text{In}_{0.37}\text{Ga}_{0.63}\text{As}_{0.25}\text{P}_{0.75}$  waveguide layer ( $E_g = 1.78 \pm 0.01 \text{ eV}$ ) with an undoped  $\text{In}_{0.13}\text{Ga}_{0.87}\text{As}_{0.74}\text{P}_{0.26}$  quaternary active region ( $E_g = 1.495 \pm 0.05 \text{ eV}$ ), and a final layer of  $\text{In}_{0.37}\text{Ga}_{0.63}\text{As}_{0.25}\text{P}_{0.75}$  waveguide layer ( $E_g = 1.78 \pm 0.01 \text{ eV}$ ) as shown in Figure 6.4.

#### b. Buried Ridge Processing

Once the structure is grown,  $1 \mu\text{m}$  mesas with  $300 \mu\text{m}$  center-to-center spacing are formed on the active layer. The BRS formation is greatly influenced by the total thickness of the InGaAsP layer and the substrate misorientation. The mesa sidewalls are performed by standard photolithography techniques. Unlike the broad-area lasers, the  $1 \mu\text{m}$  mesas requires separate set of conditions such as exposure time and developer ratio. To determine the processing conditions that is needed for this type of BRS lasers, several experiments were studied with non planar GaAs substrates. The proposed steps that are needed to form  $1 \mu\text{m}$  stripes are outlined below.

#### Processing Procedure

Following the growth of the top waveguide layer, the wafers are prepared for photolithography. The technique necessary to form  $1 \mu\text{m}$  buried ridge mesas is the application of a resist film layer onto the wafer surface. A positive photoresist is applied through a  $0.2 \mu\text{m}$  filtering hypodermic syringe to remove polymerized particles before it is placed onto the center of the semiconductor wafer. To acquire a linewidth of  $1 \mu\text{m}$  ridge and  $5 \mu\text{m}$  wide contact for the cap layer, it is necessary to select the type of resist needed that will minimize notching and maintain linewidth control when processing on highly reflective substrates. The resist material used in this study is Shipley Microsoft 1813J (for  $1 \mu\text{m}$  pattern) and 1827 (for  $5 \mu\text{m}$  pattern). The difference between the two types of resist is the viscosity of the resist. The basic requirement of photolithography is

to achieve the necessary resist thicknesses for the appropriate pattern formation. A spin speed curve for the Microsoft photoresist is shown in Figure 6.5 (a).

The film thickness versus spin speed plots provide the information required to properly select a Microsoft resist to meet process dependent thickness specifications. For a 1  $\mu\text{m}$  linewidth, Microsoft 1813 J resist is required. In applying the 1813J resist onto the semiconductor surface, the sample is placed onto a vacuum chuck that is held down by vacuum which it is then rapidly accelerated to 6000 rpm for 20 seconds to obtain a resist thickness of about 1.2  $\mu\text{m}$ . The thickness of the resist coating depend upon the viscosity of the resist and the rate of acceleration of the spinner as shown in Figure 6.5 (a). Control over the thickness and uniformity of the resist is very important in controlling the pattern dimension during exposure. Efforts are made to keep the semiconductor devices clean and free from dust during this stage of the processing. The resist work is done primarily in dust-free clean rooms in which dust count, temperature, and humidity are controlled. Often the resist is very sensitive to humidity which can prevent the pattern to be developed properly.

#### *Pre-Exposure Soft Bake:*

Once the wafers are completely coated with photoresist, the wafers are placed in a conventional oven at a temperature of 90°C. This SoftBake step is general necessary to prevent possible bubbling or peeling of the resist.

#### *Mask Exposure:*

As previously reported, the resist film thickness is critical in order to reduce photo speed and critical dimension variability. The amount of exposure light source is in the range of 350-450 nm. The exposure of the resist through the mask is accomplished by direct contact printing with a filtered ultra-violet light.

Several optimization have been made to successfully form 1  $\mu\text{m}$  ridges over the entire wafer. These optimizations consists of mask dimension, exposure time, and cleaning sequence prior to processing. It has been noted previously that to be able to operate the buried-ridge lasers in a single mode operation, the buried mesas is greatly influence upon the width of the ridge. Therefore, the amount of width tolerance that is

produced during photolithography and after etching is very critical to the operating optical spectra of the laser.

In determining the amount of tolerance after photolithography, several studies have been made using two types of masks. Mask one consists of  $1\mu\text{m}$  lines with  $300\mu\text{m}$  spacing and mask 2 comprises of  $2\mu\text{m}$  lines with  $300\mu\text{m}$  spacing. Following mask exposure, the exposed samples are immersed into a developer bath for a limited amount of time. It has been observed that the total linewidth of the buried ridge mesas for mask #1 is within  $1\mu\text{m}\pm 0.5\mu\text{m}$  and mask #2 can bear a linewidth of  $2\mu\text{m}\pm 0.6\mu\text{m}$ . This total linewidth is greatly dependent upon the amount of time the wafers are exposed to the UV light, developer, and etching. The following table comprises the exposure and the development time needed to form a  $1\mu\text{m}$  linewidth.

**Table 1**

Mask	Exposure (s)	Developing (s)
$1\mu\text{m} \times 300\mu\text{m}$	25 sec	1' 10"
$2\mu\text{m} \times 300\mu\text{m}$	15 sec	45"

#### *PostBake:*

Upon obtaining the desire linewidth, the wafers goes through a PostBake step at a temperature of  $120^\circ\text{C}$ . This additional heat treatment of the resist film further adhere the film and prevent the removal of the resist during etching. Figure 6.5 (b) - (d) shows the primary steps needed to create  $1\mu\text{m}$  resist lines.

#### *Etching:*

A second aspect of a successful patterned is a viable etching process. There are number of important factors to be considered in selecting an InGaAsP quaternary etch:

- resist to etch selectivity
- the etch selectivity has a direct impact upon the resist sidewall slope
- various etch parameters can affect whether residues are left behind following the chemical etch

Several etchant solutions have been studied intensively to chemically etch the InGaAsP quaternary material. Three types of etchants were investigated on several samples that best resemble to the InGaAsP energy gap material. The three etchants are  $\text{H}_2\text{SO}_4:\text{H}_2\text{O}_2:\text{H}_2\text{O}$ ,  $\text{H}_2\text{O}_2:\text{HCl}:\text{HBr}:\text{H}_2\text{O}$ , and Bromine/Glycol. By carefully studying the etching behavior over a wide temperature region and timing behavior as well as surface irregularities, we have been able to form  $1\mu\text{m}$  mesas with  $\text{H}_2\text{O}_2:\text{HCl}:\text{HBr}:\text{H}_2\text{O}$  and Bromine/Glycol successfully with no surface roughness as shown in Figure 6.6 (a) and (b). However, surface irregularities and surface roughness was observed with  $\text{H}_2\text{SO}_4:\text{H}_2\text{O}_2:\text{H}_2\text{O}$  as shown in Figure 6.7 (a) and (b).

An important feature of etching InGaAsP with narrow stripes is the substrate orientation. For stripes oriented along the  $\bar{1}\bar{1}0$  we found inverted v-shape groove, whereas for stripes along  $110$  resulted with v-shape grooves. The etched mesa profiles were examined by aligning the  $1\mu\text{m}$  stripes with respect to the vertical and lateral direction of growth defect by standard photolithography. As shown in Figure 6.8,  $\bar{1}\bar{1}0$  planes for the side walls are formed when using  $\text{H}_2\text{O}_2:\text{HCl}:\text{HBr}:\text{H}_2\text{O}$  or Bromine/Glycol as the primary etchant for InGaAsP material. The removal of the InGaAsP layer between the  $1\mu\text{m}$  linewidth is very critical since the linewidth is very narrow as compared to  $100\mu\text{m}$  linewidth. The amount of undercut expected after etching is within  $\pm 0.03\mu\text{m}$ . Table 2 lists two types of etchants that are possible candidates for the InGaAsP quaternary.

**Table 2**

Etchant Solution	Etchant Time ( $\mu\text{m}/\text{min.}$ )	Temperature ( $^{\circ}\text{C}$ )
$\text{H}_2\text{O}_2:\text{HCl}:\text{HBr}:\text{H}_2\text{O}$	$0.28\mu\text{m}/\text{min.}$	$20^{\circ}\text{C}$
Bromine/Glycol	$0.074\mu\text{m}/\text{min.}$	$25^{\circ}\text{C}$

Following the formation of the ridge mesas using wet chemical technique, the wafers under goes a cleaning process before selective regrowths are performed. The critical steps of such process are the transfers of the wafers from one technique to the next. In most cases the samples are exposed for a certain period of time to the ambient air which bears the danger of contaminating the semiconductor surface, thus affecting the epitaxial growth tremendously.

### *Pre-cleaning prior to regrowth*

Several cleaning and regrowth experiments were performed using low-pressure metalorganic chemical vapor deposition (LP-MOCVD) and gas-source molecular beam epitaxy (GSMBE) systems. Three types of cleaning procedures known as A, B, and C listed in Table 3 have been investigated as possible candidates to be used prior to regrowth of III-V material. All cleaning procedures and regrowth experiments were executed on GaAs and GaAs/GaInP samples with and without  $1\mu\text{m}$  stripes.

Following the formation of  $1\mu\text{m}$  mesas, the experimental samples undergoes a cleaning procedure to eliminate residues left on the surface prior to regrowth of InGaP and GaAs.

**Table 3**

A	B	C
TCE, TCA	AZ-Stripper + DI rinse	AZ-Stripper + DI rinse
Acetone	Acetone	Sulfuric Acid
Methanol	Methanol	DI rinse
Propanol	Methanol	

Three separate regrowth compositions, (GaAs, InGaP and GaAs-InGaP) were grown on different experimental samples by MOCVD and GSMBE techniques (equipped with gas lines), using the above cleaning procedure listed in Table 3.

In using procedure A and B as a post etchant removal prior to regrowth, can result in cloudiness and deterioration of the surface as shown in Figure 6.9. The surface resulted in numerous defects over the regrown  $1\mu\text{m}$  mesa. These defects is a direct result of mixing alcohol and acid during cleaning, and acid residues that are left along the mesa sidewalls. In understanding the direct cause of these defects and cloudiness, each element of procedure A and B had to be studied individually to pinpoint exactly which step was causing the abnormality on the surface. To eliminate cross linking of alcohol and acids, procedure C was implemented and studied. After etching portions of the quaternary layer, the samples were immersed into two baths (cold and hot) of AZ400K stripper solution to remove the remaining photoresist on the surface.

The samples were then immersed in acetone bath for at least 5 - 10 minutes and rinse thoroughly with deionized water. Prior to inserting the samples into the growth chamber, the samples were dipped into a diluted sulfuric acid for a few seconds to remove any form of film oxide on the surface. A smooth and defect-free regrowth layer of InGaP-GaAs was obtained using method C as shown in Figure 6.10.

Cross-section of the regrown layers by scanning electron microscope (SEM) was not performed in the beginning due to the lack of availability of the system at that time. However, since the arrival of the SEM, preliminary studies of the etching and regrown layers are being conducted. Further investigations are being continued to improve the quality of the InGaP-GaAs films both electrically and optically as well as the processing steps.

#### *Post Regrowth*

After regrowth of the upper GaInP cladding and GaAs cap layer using GSMBE growth technique, the laser structures are then processed into devices. The surface cleaning of these wafers consists of a chemical degreasing of trichloroethane (to remove wax and grease residues), acetone (to remove polymer particles), methanol and propanol (to remove particles from previous steps or water content). The wafers are then immersed into a 1% hydrofluoric (HF) solution for 20 seconds to remove any interfacial native oxides from the semiconductor surface prior to metal deposition. In order to localize the injection current through the active region, a  $5\mu\text{m}$  resist mask is properly align over the regrown  $1.0\mu\text{m}$  active region. This strip contact is formed by the combination of metallization technology (i.e. lift-off technique) and photolithographic techniques as shown in Figure 6.11.

The  $5\mu\text{m}$  wide metal contact to a  $p^+$ -type doped GaAs layer is formed by choosing Ti-Pt-Au as the metal contact. The evaporation rate required to deposit these multilayer metal films is 10-20 Å per minute. The removal of the Ti-Pt-Au between the  $5\mu\text{m}$  stripes consists of universal lift-off techniques. The lift-off procedure consists of placing the wafers into an acetone bath for an amount of time necessary to completely remove the metal film between the stripes.

In order to confine the current along the  $5\mu\text{m}$  stripe contact, chemical wet etching is applied to the laser processing. In general, the etching procedure should be

uniform across the wafer, consistent and reproducible from wafer to wafer. With the upper GaInP layer serving as an etch stop, the  $p^+$ -type GaAs cap layer between the  $5\mu\text{m}$  stripe contact is selectively etched using  $\text{NH}_4\text{OH}:\text{H}_2\text{O}_2:\text{H}_2\text{O}$  (Ammonia Hydroxide: Hydrogen Peroxide) mixture at pH level of 7 or  $\text{H}_2\text{SO}_4:\text{H}_2\text{O}_2:\text{H}_2\text{O}$ . The use of this selective etch solution provides tight tolerances of mask undercutting ( $\pm 0.02\mu\text{m}$ ) and uniform etch walls across the wafer. This is one additional advantage of using the InGaP/InGaAsP/GaAs material system.

The non-alloying heat treatment for the Ti-Pt-Au contact to the  $p^+$ -GaAs layer is accomplished by alloying the wafers to  $440^\circ\text{C} \pm 20^\circ\text{C}$  for few minutes in a controllable forming gas ambient of 10%  $\text{H}_2$ - $\text{N}_2$ . The system used to obtain the metallurgical composition of the metal layer to  $p^+$ -doped GaAs layer is done by open tube furnace rather than rapid thermal annealing. The next sequence of laser process is the lapping/polishing of the  $n^+$ -GaAs layer to a thickness of  $100\mu\text{m}$ . The primary factor in lapping/polishing the  $n$ -GaAs substrate is cleaving and packaging considerations, since the initial thickness of the GaAs substrate is generally  $400\mu\text{m}$  to  $500\mu\text{m}$ -thick. The procedure used to facilitate this material for the preparation of lapping/polishing consists of applying a protective layer of photoresist onto the  $p^+$ -GaAs contact layer to prevent any type of buildup contamination's that can occur during lapping/polishing. The wafers are bonded p-side down onto a glass substrate (83mm diameter x 6mm nominal thickness) by an excess of wax. The glass substrate along with the bonded wafers are mounted onto a commercialized Logitech lapping/polishing machine that polishes the wafers to a thickness of  $100\mu\text{m}$ . The final stages of laser fabrication is the metallization of the  $n^+$ -GaAs substrate and annealing of the  $n$ -contacts. The metallization used for  $n$ -type GaAs substrate consists of AuGe/Ni/Au. The alloying procedure to obtain the eutectic composition of AuGe-Ni-Au to the  $n$ -type GaAs layer is carried out in a flowing 10%  $\text{H}_2$ - $\text{N}_2$  ambient at  $400^\circ\text{C} \pm 10^\circ\text{C}$ . A final layer of Schottky Au ( $1000\text{\AA}$ ) is deposited over the entire  $p^+$ - contact surface in order to form a current-blocking Schottky barrier outside the  $5\mu\text{m}$  stripes and to permit cleaved laser chips to be bonded p-side down on indium-coated copper heatsinks. The overall process sequence for a buried ridge laser is shown in Figure 6.12 (a) - (c).

#### 4. Device Characterization

The InGaAsP/InGaP/GaAs buried ridge lasers resulted in peak power of 5mW (without antireflective coating) at a cavity length of 400 $\mu$ m under pulse operation (400ns - repetition rate 1.25kHz) as shown in Figure 6.13. These devices have exhibit single mode operation (Figure 6.14) under room temperature at 815nm wavelength, which can be tuned at 808nm. High contact resistance of  $\sim 60$  ohms were obtained from these devices which indicates further studies of annealing are needed. Further characterization of these devices are being continued.

#### 5. Summary

Index-guided lasers such as buried-ridge lasers are very important for many applications such as light sources for optical information processing devices because of low threshold current, minimal astigmatism, and fundamental transverse-mode operation. Most index-guided lasers reported to date use AlGaAs-InGaAs-GaAs, InGaAs-GaAs ( $\lambda=0.98\mu$ m), InGaAsP-InP on InP substrate for 1.3  $\mu$ m -1.5  $\mu$ m lasers. However, 0.808  $\mu$ m aluminum-free InGaAsP-InGaP-GaAs index-guided lasers have not been reported up to our knowledge. The superiority that aluminum-free systems (InGaAsP alloys) lends to the semiconductor lasers is their superior resistance over AlGaAs alloys to rapid degradation by dark line defect propagation and catastrophic mirror damage. Also, it lends to themselves more readily to fabrication of advanced integrated device structures by epitaxial regrowths unlike the AlGaAs lasers. Because of the problem with the removal of the stable oxide on the regrowth surface of aluminum alloy, it is difficult to fabricate high performance index-guided laser structures as buried-ridge laser.

Preliminary studies on buried-ridge lasers with InGaAsP alloys have reached its first stage of fabrication technology. In which photolithography, etching, and cleaning of the structure have been studied to produce 1 $\mu$ m InGaAsP ridges by etching away portions of the InGaAsP layer with H<sub>2</sub>O<sub>2</sub>:HCl:HBr:H<sub>2</sub>O or Bromine/Glycol. Epitaxial regrowth of GaAs, InGaP, and InGaP-GaAs on non-planar and on 1 $\mu$ m mesas ( $\bar{1}\bar{1}0$  and 110 orientation) was studied and compared using the three cleaning methods outlined in Table 3. Experimentally it was shown that utilizing method C resulted in smooth and defect-free surface after regrowth. However, both material and processing technology must be further improve to obtain low threshold, higher efficiency, and low contact resistance.

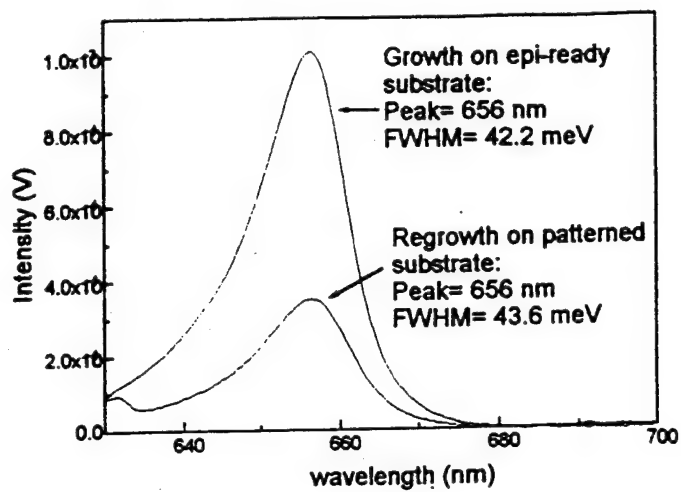


Figure 6.1 Photoluminescence of preprocessed and unprocessed samples.

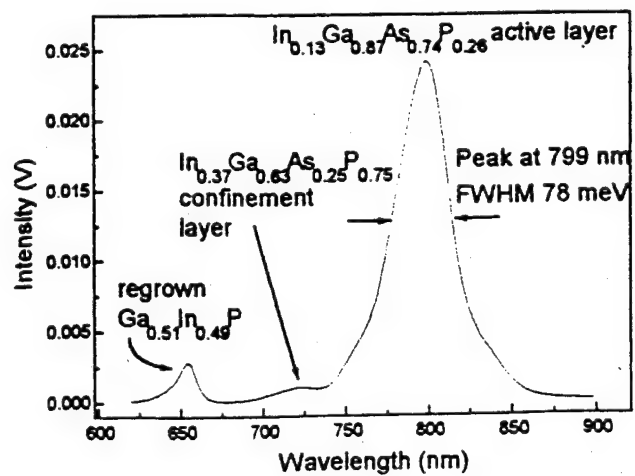


Figure 6.2. Room Temperature Photoluminescence of regrown laser structure.

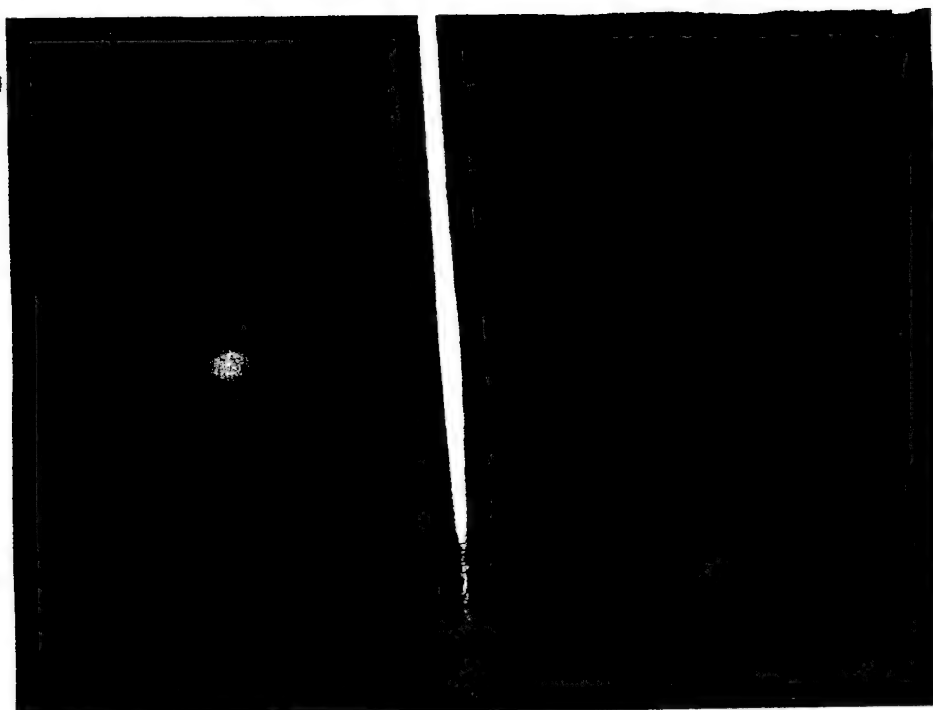


Figure 6.3. Topophotoluminescence photograph showing luminescence from InGaP on top of 1  $\mu\text{m}$  ridge.

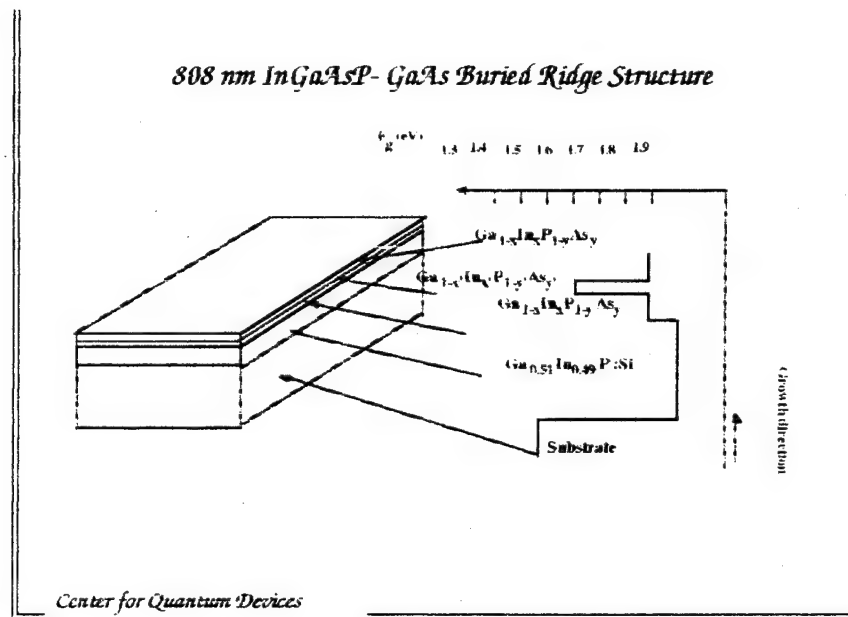


Figure 6.4. Initial BRS structure grown by LP-MOCVD.

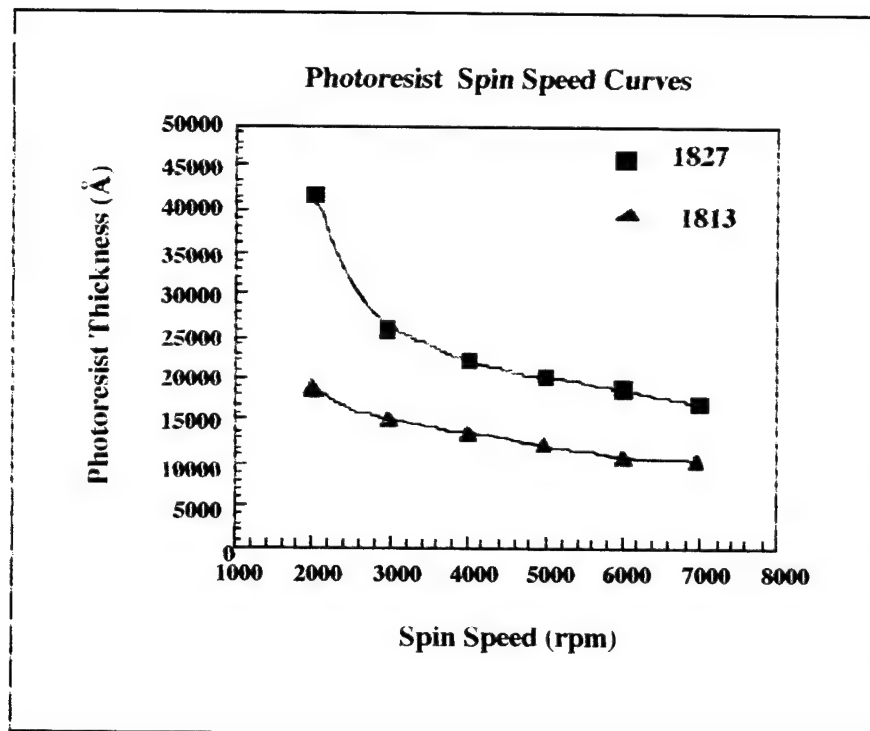
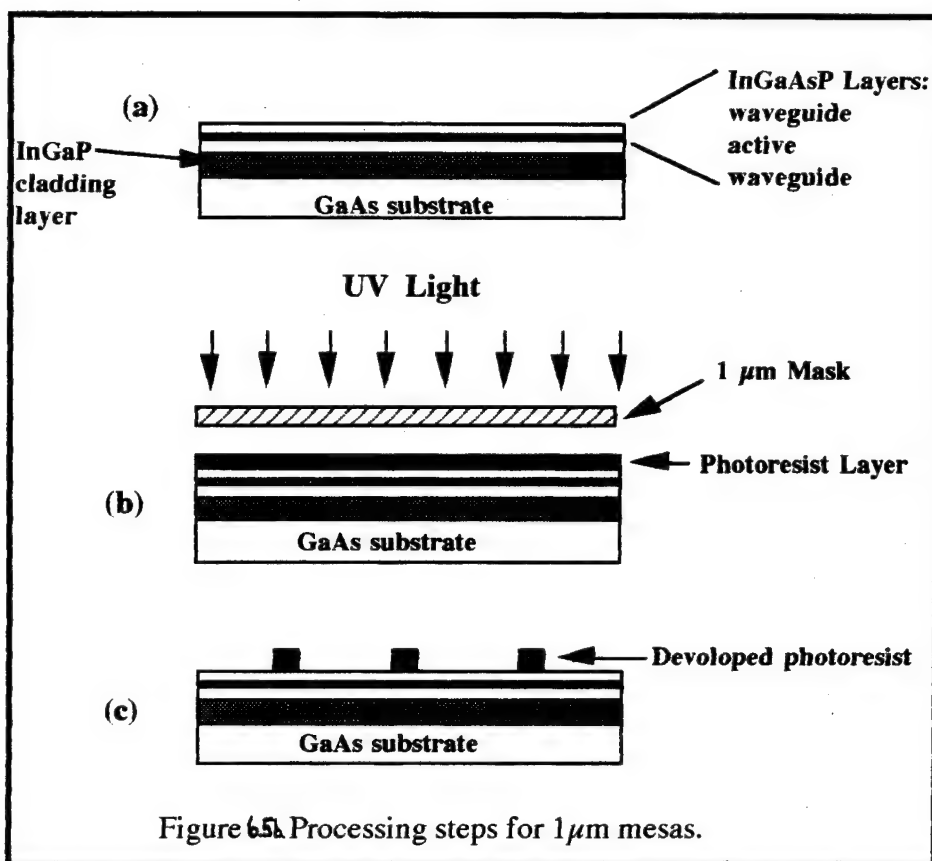


Figure 6.5 (a). Resist thickness versus spin speed for a 25 seconds spin.



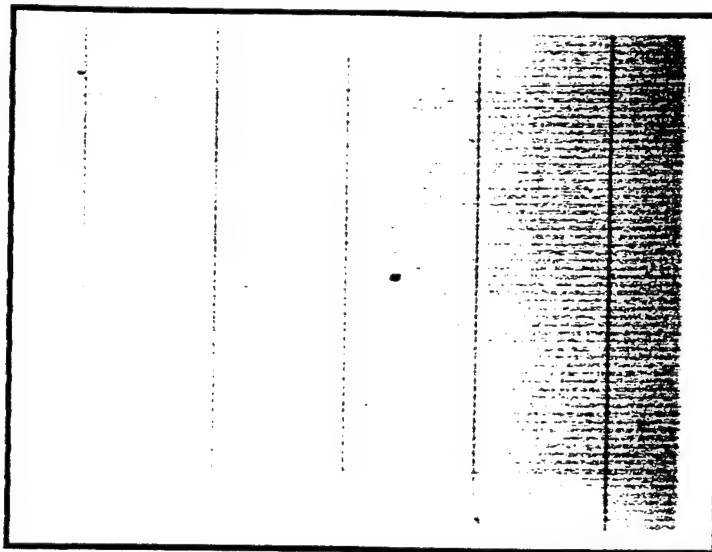


Figure 6.6 (a). Etched  $1\text{ }\mu\text{m}$  ridge mesas with  $\text{H}_2\text{O}_2\text{:HCl:HBr:H}_2\text{O}$  at room temperature.

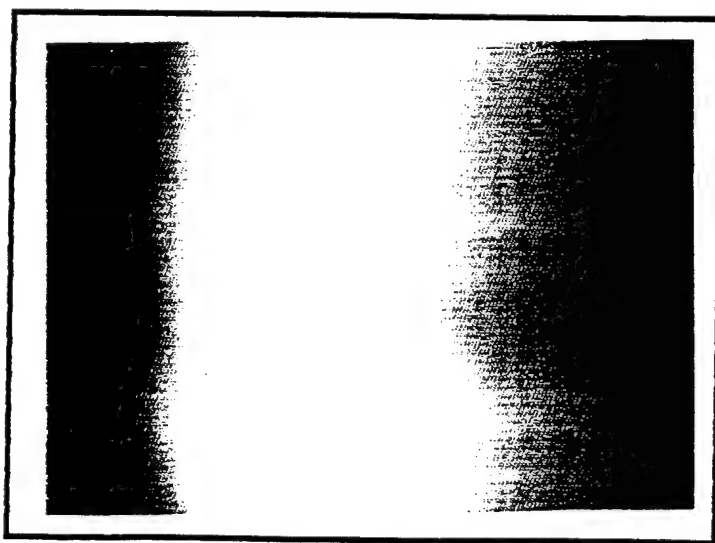


Figure 6.6 (b). Etched  $1\text{ }\mu\text{m}$  ridge mesas with Bromine/Glycol at room temperature.

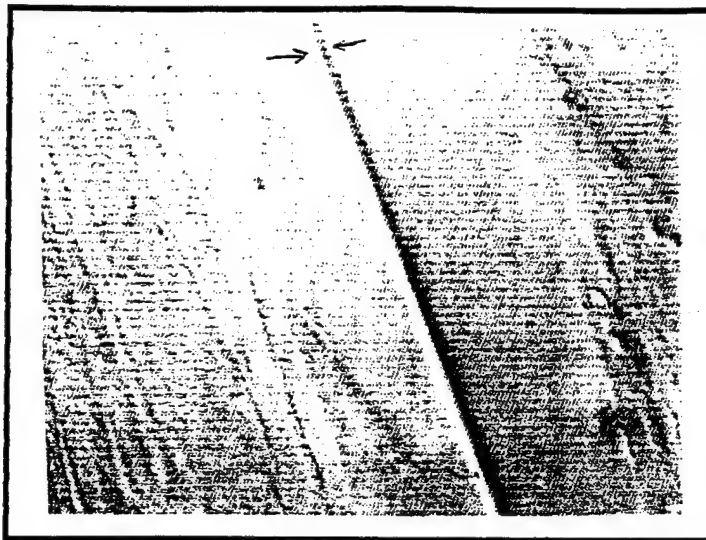


Figure 6.7. (a) Surface irregularities found with  $\text{H}_2\text{SO}_4:\text{H}_2\text{O}_2:\text{H}_2\text{O}$  when etching InGaAsP.

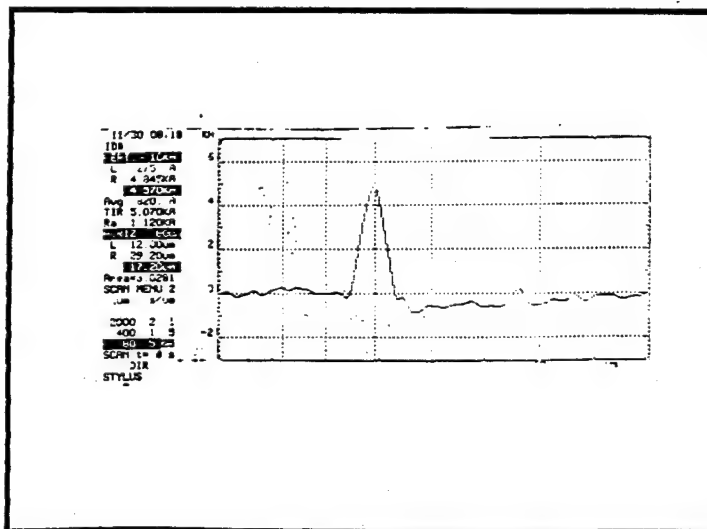


Figure 6.7. (b). Alpha step profile of an  $1\mu\text{m}$  etched ridge with  $\text{H}_2\text{SO}_4:\text{H}_2\text{O}_2:\text{H}_2\text{O}$ .

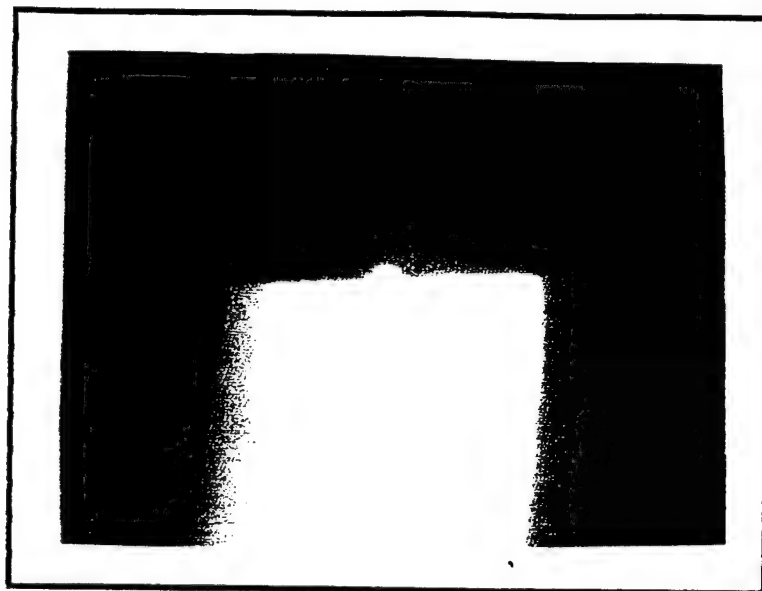


Figure 6.8. Experimentally found cross sections of the etched mesas at room temperature in the  $1\bar{1}0$  direction.

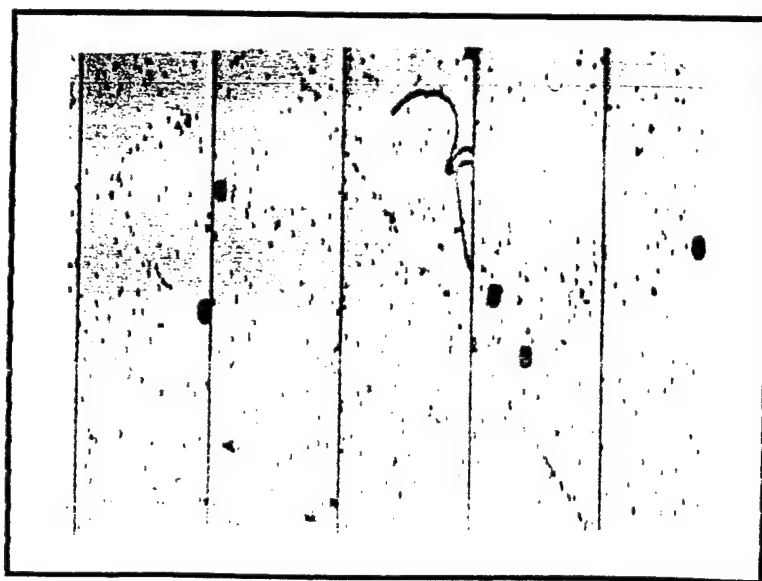


Figure 6.9. Experimentally regrowth of InGaP with Procedure A using MOCVD.

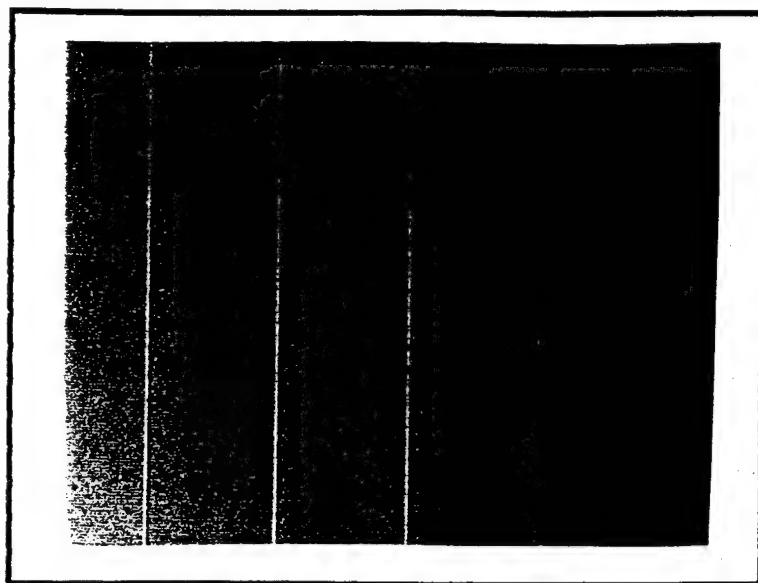


Figure 6.10. Experimentally regrowth of InGaP-GaAs with Procedure C using GSMBE.

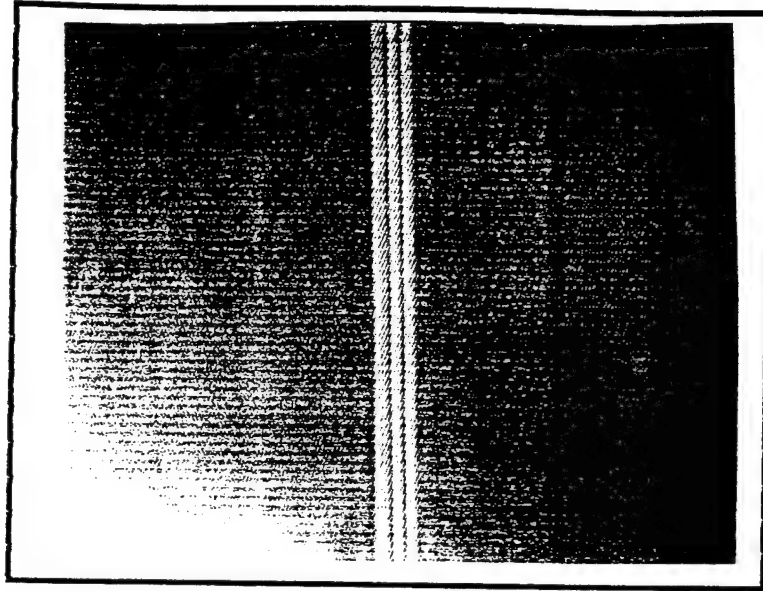


Figure 6.11. Top view of  $5\mu\text{m}$  contact properly aligned on top of the  $1\mu\text{m}$  regrown area.

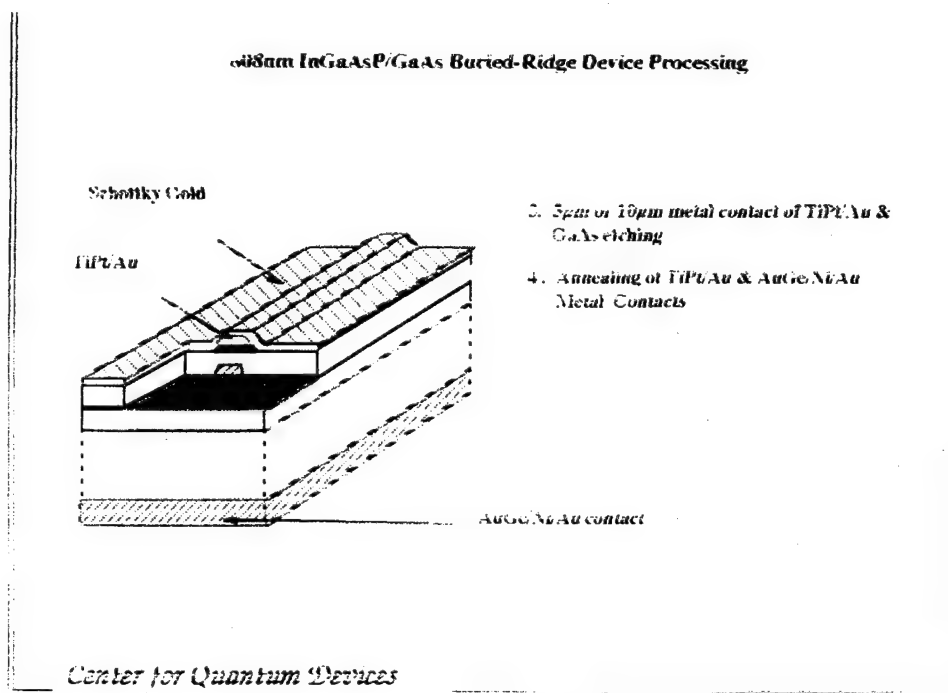
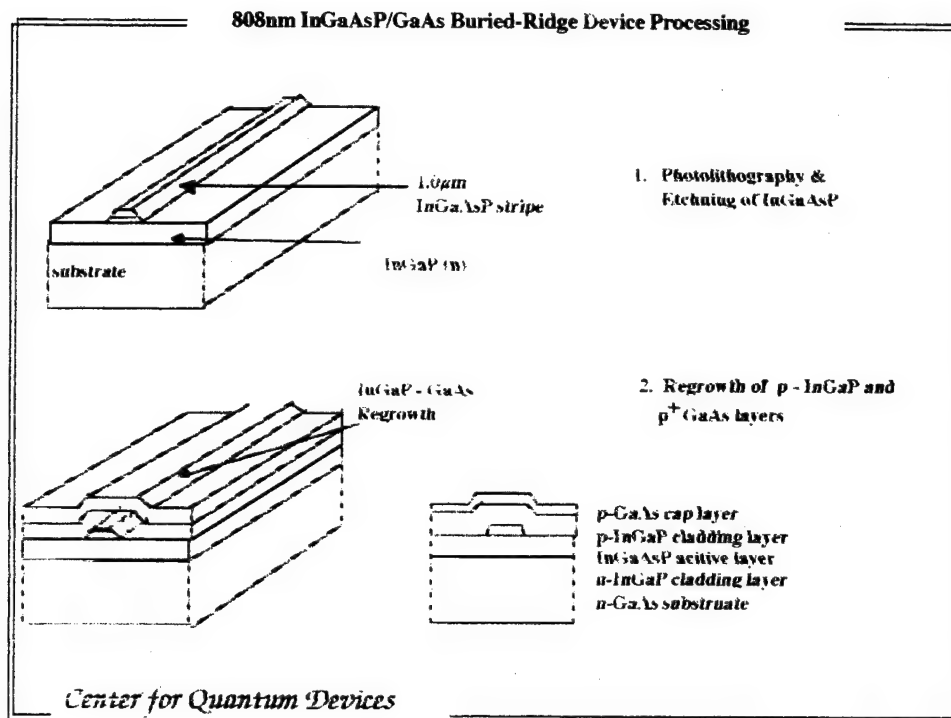


Figure 6.12 (a) - (b). Processing steps for a 808nm InGaP/InGaAsP/GaAs BRS laser.



**808nm InGaAsP/InGaP Buried-Ridge Diode Laser**  
**ONR #N0014-93-1-0176**

Threshold current  $I_{th}=0.24A$  and peak power of 4.5mW per two facets uncoated under room temperature have been obtained.

Calculated series resistance of 60 ohms between p- and n- contacts.

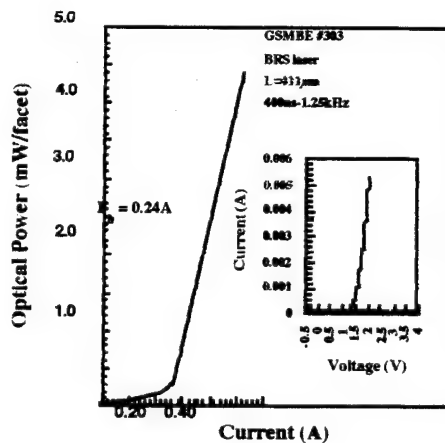


Figure 6.13. Light - Current characteristics of a BRS laser under pulse operation.

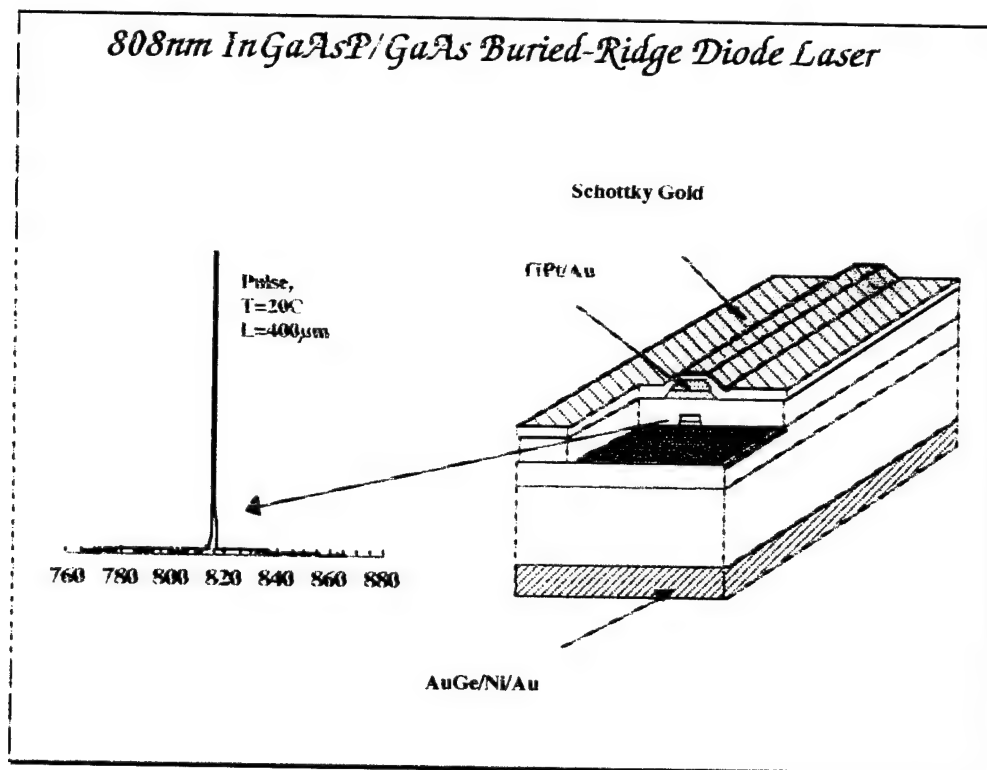


Figure 6.14. 808nm BRS laser diode spectrum laseing in single mode at room temperature.

- [1] D.Z Garbuzov, N.Y. Antonishkis, A. D. Bondarev, S.N. Zhigulin, A. V. Kochergin, N. I. Katsavets, and E. U. Rafailov, *IEEE J. Quantum Electron*, **27**, 1531, 1991.
- [2] T. Ijichi, M. Ohkubo, N. Batsumoto, and H. Okamoto, *Conference Digest 12th IEEE International Semiconductor Laser Conference Davos, Switzerland, 1990*, paper D-2.
- [3] M. Razeghi, M. Defour, and F. Omnes, *Appl. Phys. Lett.*, vol. 55 (5), p. 457, 1989.
- [4] X. He and M. Razeghi, *Appl. Phys. Lett.*, vol. 61, p. 1703-1705, 1992.
- [5] X. He and M. Razeghi, *Appl. Phys. Lett.*, vol. 62, p. 618-620, 1993.
- [6] M. Razeghi, J. Diaz, I. Eliashevich, K. Mobarhan, X. He, E. Kolev, L. Wang, and D. Garbuzov, *Proceedings of IEEE/LEOS Conference, San Jose, CA, November 15-18, 27-28*, paper PD2.4, 1993.
- [7] J. Diaz, H. Yi, M. Erdtmann, X. He, E. Kolev, D. Garbuzov, E. Bigan, and M. Razeghi, *J. Appl. Phys.*, vol. 76, p. 700-704, 1994.
- [8] M. Razeghi, J. Diaz, I. Eliashevich, X. He, E. Kolev, L. Wang, and D. Garbuzov, *Proceedings of Lasers and electroopt. CLEO '94, Anaheim, CA, May 1994*, p. 25-26 paper CHM5.
- [9] J. Diaz, I. Eliashevich, K. Mobarhan, E. Kolev, L.J. Wang, D. Garbuzov and M. Razeghi, *IEEE Photon. Technol. Lett.*, vol. 6, p. 132, 1994.
- [10] J. Diaz, I. Eliashevich, X. He, H. Yi, E. Kolev, D. Garbuzov, and M. Razeghi, *Appl. Phys. Lett.*, **65**, p. 1004, 1994.
- [11] J. Diaz, I. Eliashevich, H. Yi, M. Stanton, M. Razeghi, *Appl. Phys. Lett.*, vol. 65, No. 18, p. 2260-2262, 1994.
- [12] H. J. Yi, J. Diaz, I. Eliashevich, M. Stanton, M. Erdtmann, X. He, L.J. Wang, and M. Razeghi, *Appl. Phys. Lett.*, **66** (3), p. 253-255, 1995.
- [13] M. Razeghi, J. Diaz, I. Eliashevich, X. He, H. Yi, M. Erdtmann, E. Kolev, L. Wang, and D. Garbuzov, *Proceedings of IEEE/ISCL '94 Conference, Maui, Hawaii, September 19-23*, p. 159-160, paper P39, 1994.
- [14] Bohdan Mroziewicz, Maciej Bugajski, Wlodzimierz Nakwaski, *Physics of Semiconductor Lasers*, PWN, Amsterdam, 1991.

*CHAPTER VII*  
*PRESS RELEASES AND ARTICLES*

## PRESS RELEASES AND ARTICLES

"Razeghi accepts AIX 200 for SiC," III-Vs Review, Vol. 7 No. 4, June 1994, p. 4

"ARPA seeks cheaper, better laser weapons," Washington Report, Laser Focus World, July 1994, p. 53

"Indium Makes More Durable Semiconductor Laser," Inside R&D, July 6, 1994

"Aluminum-free high-power diodes have long lifetimes," Semiconductor Lasers, Laser Focus World, August 1994, p. 26.

"Quantum Force," Profile in Northwestern University Perspective Magazine, Summer 1994.

"InGaAsP laser diodes outperform AlGaAs," Opto & Laser Europe, October 1994

"Bienen is inaugurated as 15th President of Northwestern," Profile of Center in Northwestern Observer, May 22, 1995

"EMCORE Announces MOCVD sale and Collaboration Agreement with Northwestern's Professor Razeghi," Press Release June 16, 1995

"Society of Woman Engineering Achievement Award," Press Release July 1, 1995

"Korean Foundation announces collaborations with three U.S. Labs", Press Release Northwestern News, July 14, 1995

"Center for Quantum Devices chosen for collaboration", Press Release Northwestern News, July 28, 1995

*CHAPTER VIII*

*PATENTS*

## Patents

1. NU #9244-A & NU #9244-B " Intermetallic compound semiconductor thin film and method of manufacturing same" Granted # 5,421,910 6/6/95
2. NU #9301 "1.3  $\mu\text{m}$  Semiconductor Laser Grown by MOCVD"
3. NU #9321 " SLOW ( Semiconductor Laser Organic Waveguide) device for generating blue light"
4. NU #9322 "Aluminum free 650nm to 1100nm High Power Lasers Grown on GaAs, InP, and Si substrates" Granted #5,389,396 2/14/95
5. NU #9322-CIP "LW-SCAW-LD Large Waveguide Separate Confinement Quantum Well Laser Diodes for High Power Laser" Granted #5,384,151 1/24/95
6. NU #9435 " Aluminum Free GaInAsP Quantum Well Intersubband Photodetectors"
7. NU #9443 " Technology of Heatsink for GaAs-GaInAsP-GaInP High"
8. NU #9444 " Technology of GaInAsP-GaInP-GaAs High Power Laser Emitting at 808nm"
9. NU #9449 "Selective Epitaxy for Quantum Devices"

*CHAPTER IX*  
*PUBLICATION LISTS*

### *Publication Lists*

- [1] M. Razeghi, J. Diaz, I. Eliashevich, K. Mobarhan, X. He, E. Kolev, L. Wang, and D. Garbuzov, "MOCVD-grown GaInAsP-GaAs laser for Nd:YAG pumping", Proceedings of IEEE/LEOS Conference, San Jose, CA, November 15-18, 27-28, paper PD2.4, 1993.
- [2] J. Diaz, H. Yi, M. Erdtmann, X. He, E. Kolev, D. Garbuzov, E. Bigan, and M. Razeghi, "Efficiency of photoluminescence and excess carrier confinement in InGaAsP/GaAs structures prepared by metal-organic chemical-vapor deposition", J. Appl. Phys., vol. 76, 700-704, 1994.
- [3] M. Razeghi, J. Diaz, I. Eliashevich, X. He, E. Kolev, L. Wang, and D. Garbuzov, "InGaAsP/GaAs high power lasers for Nd:YAG pumping", Proceedings of Lasers and electroopt. CLEO '94, Anaheim, CA, May 1994, 25-26 paper CHM5.
- [4] J. Diaz, I. Eliashevich, K. Mobarhan, E. Kolev, L.J. Wang, D. Garbuzov and M. Razeghi, "InGaP/InGaAsP/GaAs 0.808mm Separate Confinement Laser Diodes Grown by Metalorganic Chemical Vapor Deposition", IEEE Photon. Technol. Lett., vol. 6, 132, 1994.
- [5] J. Diaz, I. Eliashevich, X. He, H. Yi, E. Kolev, D. Garbuzov, and M. Razeghi, "High-power InGaAsP/GaAs 0.8mm laser diodes and peculiarities of operational characteristics", Appl. Phys. Lett., 65, 1004, 1994.
- [6] J. Diaz, I. Eliashevich, H. Yi, M. Stanton, M. Razeghi, "Theoretical investigation of minority carrier leakages of high-power 0.8mm InGaAsP/InGaP/GaAs laser diodes", Appl. Phys. Lett., vol. 65, No. 18, 2260-2262, 1994.
- [7] H. J. Yi, J. Diaz, I. Eliashevich, M. Stanton, M. Erdtmann, X. He, L.J. Wang, and M. Razeghi, "Temperature dependence of threshold current density  $J_{th}$  and differential efficiency  $\eta_d$  of High Power InGaAsP/GaAs ( $\lambda=0.8\mu\text{m}$ ) lasers", Appl. Phys. Lett., 66 (3), 253-255, 1995.
- [8] M. Razeghi, J. Diaz, I. Eliashevich, X. He, H. Yi, M. Erdtmann, E. Kolev, L. Wang, and D. Garbuzov, "Peculiarities of operation characteristics of high-power InGaAs/GaAs  $0.8\mu\text{m}$  laser diodes", Proceedings of IEEE/ISCL '94 Conference, Maui, Hawaii, September 19-23, 159-160, paper P39, 1994.
- [9] J. Diaz, I. Eliashevich, M. Stanton, L. Wang, and M. Razeghi, "Performanc of High Power InGaAsP/GaAs Laser Diodes", CAM '94 Conference, Cancun, Mexico, September 1994.
- [10] J. Diaz, I. Eliashevich, H. Yi, L. Wang, and M. Razeghi, "Optimization of InGaAsP/GaAs laser diode processing for high power operation", in Proceedings of the IEEE Lasers and Electro Optics Society Annual Meeting, LEOS '94, Boston, MA, 1994 (IEEE, Piscataway, 1994), p. 65, Paper SL 13.3.

- [11] H. Yi, I. Eliashevich, J. Diaz, L.J. Wang, and M. Razeghi, "Theoretical Investigation of  $J_{th}$  and  $\eta_d$  vs. Cavity Length for InGaAsP/GaAs High Power Lasers", in Proceedings of IEEE Lasers and Electro Optics Society Annual Meeting, LEOS '94, Boston, MA, 1994 (IEEE, Piscataway, 1994), p. 65, Paper SL 13.4.
- [12] J. Diaz, H. Yi, S. Kim, M. Erdtmann, L.J. Wang, I. Eliashevich, E. Bigan, and M. Razeghi, "Investigation of 0.8 $\mu$ m InGaAsP-GaAs laser diodes with Multiple Quantum Wells", in Proceedings of SPIE-The International Society for Optical Engineering, *invited paper*, vol. 2397, p.350-362, Feb. 6-9, San Jose, CA, 1995.
- [13] H. Yi, I. Eliashevich, J. Diaz, X. He, M. Erdtmann, L.J. Wang, E. Kolev, and M. Razeghi, "The optimized structure for InGaAsP/GaAs 808nm high power lasers", submitted to Appl. Phys. Lett.
- [14] I. Eliashevich, J. Diaz, H. Yi, L. Wang, M. Razeghi, "Reliability of Aluminium-Free 808 nm high-power Laser Diodes with Uncoated Mirrors", Appl. Phys. Lett., 66 (23), p. 3087-3089 June 1995.
- [15] H. Yi, I. Eliashevich, J. Diaz, X. He, M. Erdtmann, L.J. Wang, and M. Razeghi, "Dependence of Laser Characteristics on Quantum Well Structures for InGaAsP/GaAs Laser diodes", submitted to Appl. Phys. Lett. 1995.
- [16] J. Diaz, I. Eliashevich, H.J. Yi, S. Kim, L.J. Wang, and M. Razeghi, "High Reliability High Power Aluminum-free Lasers", submitted to 22nd International Symposium on Compound Semiconductor, Korea '95.
- [17] J. Diaz, I. Eliashevich, L.J. Wang, H.J. Yi, M. Erdtmann, S. Kim, and M. Razeghi, "High-power temperature of 0.98 $\mu$ m GaInP/GaAs/GaInAs lasers" submitted to Appl. Phys. Lett., April 1995.
- [18] J. Diaz, I. Eliashevich, L.J. Wang, H.J. Yi, M. Erdtmann, S. Kim, and M. Razeghi, "High-power temperature of 0.98 $\mu$ m GaInP/GaAs/GaInAs lasers" submitted to Appl. Phys. Lett., April 1995.
- [19] M. Razeghi, "Aluminum-free diode lasers last longer", Laser Focus World, p. 36, November 1995.
- [20] M. Razeghi, "High Power Laser Diodes", Optics & Photonics News, p. 17-20, vol.6, No.8, 1995.
- [21] M. Razeghi, "Reliability of 808nm high power lasers, Optics & Photonics News, p. 6, vol.6, No.10, 1995.

- [22] M. Razeghi, "High-Power laser diodes based on InGaAsP alloys", *Nature*, p. 631, vol. 369, no. 6482, 1994.
- [23] C. Jelen, S. Slivken, J. Diaz, S. Kim, D. Wu, and M. Razeghi, "Characterization of InGaP Regrown on Patterned Wafers by Molecular Beam Epitaxy" MRS Boston 1995, EE Nov. 27 - Dec. 1, Dec Fall Meeting, 1995.
- [24] M. Razeghi, invited talk, "High Power Lasers", The Eighth International Conference on Superlattices, Microstructures and Microelectronics, August 20-25, 1995.
- [25] M. Razeghi, invited talk, "Novel Optoelectronic Materials and Their Device Applications", "Low Dimensional Structures and Devices", Pan Pacific Singapore, May 8-10, 1995.
- [26] H. Yi, J. Diaz, D. Wu, M. Erdtmann, S. Kim, I. Eliashevich, and M. Razeghi, "Optical Loss and Catastrophic Optical Damage Power-Limit of 980nm Al-free laser diodes" submitted to *Appl. Phys. Letters*.
- [27] H.J. Yi, J. Diaz, I. Eliashevich, G. Lucas, S. Kim, D. Wu, M. Erdtmann, C. Jelen, S. Slivken, and M. Razeghi, "Comparison of Gain and Threshold Current Density for InGaAsP/GaAs ( $\lambda=808\text{nm}$ ) Lasers with Different Quantum-Well Thickness" submitted to *Appl. Phys. Letts*.
- [28] M. Razeghi, "High Power Semiconductor Diode Laser" Center Nonlinear Optical Material (CNOM) Annual Affiliates Meeting at Stanford University (September 19-20 1995).